

2001

Effects of High Temperature Exposure on the Tensile Ductility of an Aged Metastable Beta Titanium Alloy

Mohammed Almesallmy
University of Rhode Island

Follow this and additional works at: <https://digitalcommons.uri.edu/theses>

Terms of Use

All rights reserved under copyright.

Recommended Citation

Almesallmy, Mohammed, "Effects of High Temperature Exposure on the Tensile Ductility of an Aged Metastable Beta Titanium Alloy" (2001). *Open Access Master's Theses*. Paper 1109.
<https://digitalcommons.uri.edu/theses/1109>

This Thesis is brought to you by the University of Rhode Island. It has been accepted for inclusion in Open Access Master's Theses by an authorized administrator of DigitalCommons@URI. For more information, please contact digitalcommons-group@uri.edu. For permission to reuse copyrighted content, contact the author directly.

EFFECTS OF HIGH TEMPERATURE EXPOSURE ON THE TENSILE
DUCTILITY OF AN AGED METASTABLE BETA TITANIUM ALLOY

BY

MOHAMMED ALMESALLMY

A THESIS SUBMITTED IN PARTIAL FULFILLMENT OF THE
REQUIREMENTS FOR THE DEGREE OF
MASTER OF SCIENCE
IN
OCEAN ENGINEERING

UNIVERSITY OF RHODE ISLAND

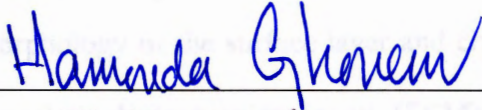
2001

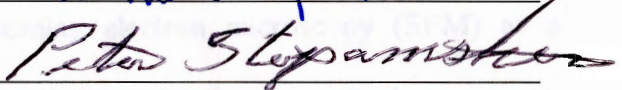
MASTER OF SCIENCE THESIS
OF
MOHAMMED ALMESALLMY

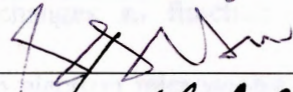
APPROVED:

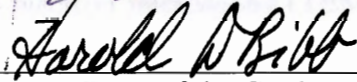
Thesis Committee

Major Professor









Dean of the Graduate School

UNIVERSITY OF RHODE ISLAND

2001

ABSTRACT

The recommended continuous operating temperature for Timetal 21S is below 540 °C. Application temperature for this alloy can, however exceed this level, with attendant embrittlement due to oxidation. The present study examines the effects of exposures in air on the tensile ductility of fully aged Timetal 21S sheet specimens in temperature range 482 – 693 °C. In this thesis, the kinetics of the loss of tensile ductility is investigated as a function of exposure temperature and sheet thickness. The experimental embrittlement activation energies are estimated by determining exposure times at various temperatures to reach close to zero ductility at room temperature. The embrittlement kinetics is investigated for three different sheet thickness; 0.12, 0.39, and 1.0 mm. The morphology of the surface layer and changes in microstructure are examined using scanning electron microscopy (SEM) as a function of exposure conditions. Phase changes as function of the exposure parameters are investigated using transmission electron microscopy (TEM). Kinetics of weight gain during exposure is also investigated. Results of this study show that two distinct embrittlement mechanisms exist within the temperature range mentioned above. At higher temperatures, >550 °C, the activation energy is 57 kcal/mole indicating that the embrittlement process is controlled by diffusion of oxygen. Below 550 °C, the embrittlement activation energy approaches zero, a characteristic of a diffusionless athermal transformation. Furthermore, the SEM examinations reveal that a protective oxide layer is present only at temperatures higher than 550 °C. There is also an indication of increased volume fraction of α phase in the vicinity of the

surface. TEM examinations reveal an increase of the isothermal ω phase as function of the exposure time increase. The general trend of these results lead to the conclusion that embrittlement at higher temperature is caused by enhanced diffusion of oxygen, which increases both the volume fraction of α phase and dissolved oxygen. At lower temperature, below 550 °C, embrittlement is probably caused by an athermal transformation of β to ω phase resulting from oxidation of molybdenum, which is a β stabilizer.

ACKNOWLEDGEMENT

I would like to express my appreciation to Professor Hamouda Ghonem from the bottom of my heart for his patience, guidance, and the opportunity to complete this course of my research at the Mechanics of Materials Laboratory, URI.

I am indebted to my friends and colleagues in both of Ocean Engineering, and Mechanical Engineering and applied mechanics departments. Thank you to Deborah Osborne for her unlimited support and guidance during all my thesis work. I am very thankful to Mostafa Shazly for his unlimited time and great discussion ideas in the editing procedures during the final stage of the thesis work. I am especially so thankful to Frederic Sansoz for these outstanding efforts and insight ideas in Scanning Electron Microscopy work in this thesis. Thank you Suppayya Sankaranarayanan, and Irsan Prodjonogoro for the unforgettable guidance in the beginning of my graduate study.

I would like to acknowledge the advice from Kevin Donovan on design and fabrication of specimen, and fixtures. I am very thankful to Ray McLaughlin on his electrical and electronic circuitry. Thank you so much Jim Byrnes I have indeed learned a great deal from these great individuals, and will always appreciate the time and interest they have given to me.

The assistance and inspiration I received from Dolores Provest, Goloria Anzevino and Dorothy Deck is greatly acknowledged.

I extend great gratitude to the faculty at URI with which I have interacted through the years.

To Mom and Dad, no words will reward your love, care and prayer for me.

Lovely wife, children Ahmed, Shrief, and Mustafa my thanks and love to you.

**EFFECTS OF HIGH TEMPERATURE ON THE TENSILE DUCTILITY OF
AN AGED BETA TITANIUM ALLOY**

TABLE OF CONTENTS

| | |
|--|------|
| ABSTRACT..... | ii |
| ACKNOWLEDGMENTS..... | iv |
| TABLE OF CONTENTS..... | v |
| LIST OF TABLES..... | viii |
| LIST OF FIGURES..... | xi |
| APPENDICES..... | v |
| A. 1 - Free – Energy..... | 183 |
| A. 2 - Moly Equation..... | 184 |
| A. 3- Random Walk..... | 185 |
| A. 4- Homogenous Point Defect..... | 188 |
| A. 5- Diffusion in Nonhomogenous Concentration Crystal..... | 194 |
| A. 6 - Example of Oxides Resistance..... | 197 |
| A. 7 - Mixing Entropy..... | 199 |
| A. 8 - Equilibrium between Two Phases..... | 202 |
| A. 9 – Definitions..... | 204 |
| A. 10 - A Matlab code to plot the theoretical concentration of a diffused element in a material..... | 206 |

| | |
|---|-----|
| CHAPTER I: INTRODUCTION..... | 1 |
| I.1 INTRODUCTION..... | 1 |
| CHAPTER II: REVIEW OF BETA TITANIUM ALLOYS..... | 7 |
| II.1 Role of Composition..... | 7 |
| II.2 Heat treatment of metastable beta titanium alloys..... | 9 |
| II.3 Diffusion and oxygen in metal alloys..... | 12 |
| II.4 Review of Timetal 21S..... | 15 |
| CHAPTER III: EXPERIMENTAL PROCEDURES AND RESULTS..... | 57 |
| III.1 Introduction..... | 57 |
| III.2 Test Specimen..... | 57 |
| III.3 Heat treatment..... | 59 |
| III.4 Thermal Exposure Tests – Procedure and Results..... | 62 |
| III.5 Monotonic Tensile Tests – procedure and results..... | 63 |
| III.6 Fatigue Experiments..... | 65 |
| CHAPTER IV: ANALYSIS AND DISCUSSION..... | 103 |
| IV.1 Objective..... | 103 |
| IV.2 Exposure and Thickness effects on the embrittlement rate..... | 103 |
| IV.3 Activation energy involved in the embrittlement of β -21S..... | 104 |

| | | |
|--|---|-----|
| IV.4 | Oxygen role in the embrittlement of β -21S..... | 110 |
| IV.5 | Oxygen in the bulk of β -21S..... | 112 |
| IV.6 | Embrittlement Mechanism..... | 119 |
| IV.7 | Influence of thermal exposure on fatigue crack growth and ΔK_{th} | 122 |
| IV.7.1 | Crack growth rate and thermal exposure in air..... | 123 |
| IV.7.2 | Threshold stress intensity range ΔK_{th} and the bulk changes..... | 125 |
| CHAPTER V: CONCLUSION AND RECOMMENDATIONS..... | | 178 |
| V.1 | Conclusions..... | 178 |
| VI.2 | Future work..... | 182 |
| REFERENCES..... | | 207 |
| BIBLIOGRAPHY..... | | 211 |

LIST OF TABLES

| | |
|---|----|
| Table 2.1 – The periodic table of elements [10]..... | 21 |
| Table 2.2 – Beta Stabilizing Elements [11]..... | 22 |
| Table 2.3 – Diffusion parameters for air elements in α -Ti and β -Ti..... | 24 |
| Table 3. 1– The weight gain in 1.0 mm tensile specimens as function of the exposure parameters. (t: exposure time, W_b : specimen’s weight before exposure, W_a : specimen’s weight after exposure, A: exposed surface area each specimen, W: weight gain due to exposure)..... | 66 |
| Table 3.2– The weight gain in the 0.39 mm tensile specimens as function of exposure parameters. (t: exposure time, W_b : specimen’s weight before exposure, W_a : specimen’s weight after exposure, A: exposed surface area each specimen, W: weight gain due to exposure)..... | 67 |
| Table 3.3– Ductility as read from the Stress-Elongation curves of 1.0 mm thickness at different aging parameters. (T: exposure temperature, t: exposure time, d: remaining elongation, σ : yield strength)..... | 68 |
| Table 3.4– Ductility as read from the stress-elongation curves of 0.39 mm sheet thickness at different aging parameters..... | 69 |
| Table 3.5– Ductility as read from the stress-elongation curves for sheet thickness 0.12 mm at different aging parameters..... | 70 |
| Table 3.6– Exposure Conditions of fatigue crack growth Specimens..... | 71 |

| | |
|---|-----|
| Table 3.7– α and β two constants of the power equation $W = \alpha t^b$ to fit the weight gain – time data in Fig. 3.13..... | 84 |
| Table 3.8– α and β two constants of the power equation $W = \alpha t^b$ to fit the weight gain–time data in Fig. 3.14..... | 85 |
| Table 3.9– α and β two constants of the power equation $W = \alpha t^b$ to fit the weight gain – time data in Fig. 3.15..... | 86 |
| | |
| Table 4.1 – Elongation d obtained from the Stress-Elongation curves of 1.0 mm thickness at different aging parameters..... | 126 |
| Table 4.2 – Elongation d obtained from the stress-elongation curves of 0.39 mm sheet thickness at different aging parameters..... | 127 |
| Table 4.3 – Elongation obtained from the stress-elongation curves for sheet thickness 0.12 mm at different aging parameters..... | 128 |
| Table 4.4 – The natural logarithm of the exposure times, which were extracted from the d-t curves Fig. V.1 for the four arbitrary elongation values which were used to plot the t –T relationship for that sheet thickness of 0.12 mm which is shown in Fig. V.8..... | 129 |
| Table 4.5 – The natural logarithm of the exposure times, which were extracted from the d-t curves Fig. V.1 for the four arbitrary elongation values which were used to plot the t –T relationship for that sheet thickness of 0.39 mm which is shown in Fig. V.9..... | 130 |

| | |
|--|-----|
| Table 4.6 – The natural logarithm of the exposure times, which were extracted from the d-t curves Fig. V.1 for the four arbitrary elongation values which were used to plot the t –T relationship for that sheet thickness of 1.0 mm which is shown in Fig. V.10. | 131 |
| Table 4.7 – The activation energy as function of constants (b), and m for the three sheet thickness under research..... | 132 |
| Table 4.8 – Transition temperatures (T_1) due to the thermal exposure of Timetal 21S sheets..... | 133 |
| Table 4.9 – The mechanical properties of two sets of specimens with two different heat treatments as function of the exposure in air..... | 134 |

LIST OF FIGURES

| | |
|---|----|
| Fig. 1.1 - Nozzle is one of the applications Timetal 21S alloy is used for..... | 6 |
| Fig.2.1 – The two basic forms of solid solution [12]..... | 25 |
| Fig.2.2 – HCP and BCC are the two microstructures forming α -phase and β -phase respectively in titanium alloys | 26 |
| Fig.2. 3 - The average number of valence electron per atom ratio (e/a) versus the elastic shear modulus as function of the additions of TM [12]..... | 27 |
| Fig.2.4 – Principal feature of (4-a) the β – isomorphous, and (4-b) the β – eutectoid classes of β – stabilized equilibrium Ti – base transition – metal alloy (Ti – TM) equilibrium phase diagram. An intermetallic compound is represented by γ [12].... | 28 |
| Fig.2.5 – Phase diagram of titanium and a beta stabilizer..... | 29 |
| Fig.2.6 – Moly Equivalent values for various commercial alloys [11]..... | 30 |
| Fig.2.7 – Influence of oxygen on the $\beta \rightarrow \alpha + \beta$ transformation kinetics of B isomorphous alloy Ti – 11 Mo ; (a) transformation start, (b) transformation finish [13]..... | 31 |
| Fig.2.8 – Tracer diffusion coefficients for the 3d solutes V, Cr, Mn,..... | 32 |
| Fig.2.9 – Schematic representation of the occurrences of the martensitic α' – and α'' – phases (i.e., α^m , collectively) and the ω - phase in Ti- TM alloys [13]..... | 33 |
| Fig.2.10 – Development of the w – structure through the application of 2/3 (111) longitudinal displacement wave to the bcc lattice [13]..... | 34 |

| | |
|---|----|
| Fig.2. 11 – Schematic representation of the locations of the two metastable phases $\omega+\beta$ and $\beta'+\beta$, within the equilibrium $\alpha+\beta$ -phase field in a typical Ti-TM alloy [13]..... | 35 |
| Fig.2. 12 - Deformation cell growth as a function of (a) time and (b) temperature [13]..... | 36 |
| Fig.2.13 - Double – logarithmic plot ($\log x$ versus $\log t$) of parabolic and logarithmic oxidation. If such processes take place simultaneously, the overall oxidation may obey an approximate cubic rate ($x^3 \propto t$) [14]..... | 37 |
| Fig.2. 14 – Scale composition for one of the titanium alloys showing the kinetics of the oxides formation as function of time at 900 °C..... | 38 |
| Fig.2.15 - The titanium – oxygen phase diagram [14]..... | 39 |
| Fig.2.16 – Ellingham/Richardson diagram for some oxides of importance in the high temperature oxidation of metals and alloys [14]..... | 40 |
| Fig.2. 17 - Illustration of the internal oxidation of dilute A –B alloys. It is assumed that A is a noble metal, B atoms to be immobile in the alloy and to have been oxidized to BO_v particles in the internally oxidized zone [14]..... | 41 |
| Fig.2.18 – Schematic illustration of the growth of internal oxide in the form of rods normal to the surface [14]..... | 41 |
| Fig.2.20 – Diffusion by vacancy mechanism [15]. Fig.2.21 – Diffusion by interstitial mechanism [15]..... | 43 |
| Fig.2.22 – Energy of an impurity atom as it moves from an initial position A in one cage to a final position C in an adjacent cage in a simple cubic structure [15]..... | 44 |

Fig.2.23 - Diffusion by an interstitialcy mechanism: (a) initial state, (b) activation state, (c) final state [14].....45

Fig.2. 25 - Comparison of the oxidation of the three different alloys shown above [15].....47

Fig.2.27 – Schematic β -isomorphous phase diagram showing the principal feature of Timetal 21S as function of the temperature.....49

Fig.2.28 – Relative oxidation resistance of beta Titanium alloys in air at 650 °C [1].50

Fig.2.29 – DTA thermogram showing the β transus temperature, T_{β} , and silicide solvus, T_s , of the Timetal 21S alloy [18].....51

Fig.2.30 – Influence of Hydrogen content on the ductility-to-brittle transition temperature of Timetal 21S.....52

Fig.2.31 – Ductility of brittle behavior of Timetal 21S for 0.39 wt. % Hydrogen.....53

Fig.2.32 – Room-temperature mechanical property data for Timetal 21S after 12 hrs exposure to air at the indicated temperatures. The vacuum data shows the effect of thermal exposure, and the difference between air and vacuum shows the effect of the air environment [1].....54

Fig.2. 33 – Stress-Elongation behavior of Timetal 21S as function of the test temperature [27].....55

Fig. 3.1 - The tensile specimen and the center cracked tension fatigue specimen(CCT). 72

Fig. 3.2– Stress–elongation curve of the as received Timetal–21S material 73

Fig. 3.3 – Morphology of the as received Timetal – 21S microstructure (β phase)..... 74

Fig. 3.4 – Ductile surface of the as received Timetal – 21S tensile – fractured specimen.....75

Fig. 3.5 – Dimples of the ductile surface of the as received Timetal – 21S tensile – fractured specimen.....76

Fig. 3.6 – Heat treatment cycles.....77

Fig. 3.7 – The stress – elongation curves of Timetal – 21S as function of different heat treatment cycles in air.....78

Fig. 3.8 – The stress – elongation curves of Timetal – 21S as function of different heat treatment cycles in vacuum.....79

Fig. 3.9 – The microstructure of Timetal 21S close to surface of the heat – treatedspecimen, where alpha phase is the dark black color, and beta phase is the rest.....80

Fig. 3.10 – The microstructure of Timetal 21S in the bulk of heat – treated specimen, where alpha phase is the dark black color, and beta phase is the rest.....81

Fig. 3.11 – The microstructure of Timetal 21S in the bulk of heat–treated specimen, where alpha phase is the dark black color, and beta phase is the rest.....82

Fig. 3.12 – Shows the microstructure with a magnification of X 10,000 in the bulk of Timetal 21S heat – treated specimen, where alpha phase is the dark black color, and beta phase is the rest.....83

Fig. 3.13– The weight gain in the 1.0 mm specimens as function of the exposure temperature and time.....84

Fig. 3.14 – The weight gain in the 0.39 mm specimens as function of the exposure time and temperature.....85

| | |
|---|----|
| Fig. 3.15– The weight gain in the 0.12 mm specimens as function of the exposure time and temperature..... | 86 |
| Fig. 3.16 – Shows the stress – elongation curves as function of the loading rate for 0.12 mm thickness of Timetal 21S sheets..... | 87 |
| Fig. 3.17 – Shows the stress – elongation curves as function of the loading rate for 0.39 mm thickness of Timetal 21S sheets..... | 88 |
| Fig. 3.18 – Stress – elongation curves for Timetal 21S – 1.0 mm thickness specimens with over – aging heat treatment then exposure in air at temperature 538 °C..... | 89 |
| Fig. 3.19 – Stress – elongation curves for Timetal 21S – 1.0 mm thickness specimens with over – aging heat treatment then exposure in air at temperature 600 °C..... | 90 |
| Fig. 3.20 – Stress – elongation curves for Timetal 21S – 1.0 mm thickness specimens with over-aging heat treatment then exposure in air at temperature 650 °C..... | 91 |
| Fig. 3.21 – Stress – elongation curves for Timetal 21S – 1.0 mm thickness specimens with over–aging heat treatment then exposure in air at temperature 693 °C..... | 92 |
| Fig. 3.22– Stress – Elongation curves for Timetal 21S – 0.39 mm thickness specimens with over – aging heat treatment then exposure in air at temperature 482 °C..... | 93 |
| Fig. 3.23 – Stress – Elongation curves for Timetal 21S – 0.39 mm thickness specimens with over – aging heat treatment then exposure in air at temperature 538 °C..... | 94 |
| Fig. 3.24 – Stress – Elongation curves for Timetal 21S – 0.39 mm thickness specimens with over–aging heat treatment then exposure in air at temperature 650 °C..... | 95 |
| Fig. 3.25 – Stress – Elongation curves for Timetal 21S – 0.39 mm thickness specimens with over – aging heat treatment then exposure in air at temperature 693 °C..... | 96 |

Fig. 3.26 – Stress – Elongation curves for Timetal 21S – 0.12 mm thickness specimens with over – aging heat treatment then exposure in air at temperature 482 °C.....97

Fig. 3.27 – Stress – Elongation curves for Timetal 21S – 0.12 mm thickness specimens with over – aging heat treatment then exposure in air at temperature 538 °C.....98

Fig. 3.28 – Stress–Elongation curves for Timetal 21S – 0.12 mm thickness specimens with over – aging heat treatment then exposure in air at temperature 594 °C.....99

Fig. 3.29 – Stress – Elongation curves for Timetal 21S – 0.12 mm thickness specimens with over – aging heat treatment then exposure in air at temperature 650 °C..... 100

Fig. 3.30 – Stress – Elongation curves for Timetal 21S – 0.12 mm thickness specimens with over – aging heat treatment then exposure in air at temperature 693 °C.....101

Fig. 3.31– Crack growth rate versus stress intensity factor range for Timetal 21S – 0.39 mm specimen’s thickness with over – aging heat treatment in vacuum then exposed in air.....102

Fig. 4.1– The available elongation (d) of sheet specimens with 1.0 mm thickness after exposure time (t).....135

Fig. 4.2– The available elongation (d) of sheet specimens with 0.39 mm thickness after exposure time (t).....136

Fig. 4.3– The available elongation (d) of sheet specimens with 0.12 mm thickness after exposure time (t).....137

Fig. 4.4 – Time range of the fast rate of the loss of ductility as function of the specimen’s thickness.....138

Fig. 4.5 – Stress strain relationship of 1.0 mm exposed β -21S specimen in vacuum for 120 hrs at 650 °C.....139

Fig. 4.6 – Shows the relationship between erf function (y-axis) and $1/\sqrt{t}$ where t is the time in sec., for the assumed value of the diffusion coefficient $D = 10^{-10}$ cm² / sec and plate thickness of 0.1cm during the first 100 hrs of exposure.....140

Fig. 4.7 – Shows the relationship between erf function (y-axis) and $1/\sqrt{t}$ where t is the time in sec., for the assumed value of the diffusion coefficient $D = 10^{-10}$ cm² / sec and plate thickness of 0.039 cm during the first 5 hrs of exposure.....141

Fig. 4.8 – Shows the relationship between erf function (y-axis) and $1/\sqrt{t}$ where t is the time in sec., for the assumed value of the diffusion coefficient $D = 10^{-10}$ cm² / sec and plate thickness of 0.012 cm during the first 100 hrs of exposure.....142

Fig. 4.9 – The exposure time – temperature relationship of 0.12 mm specimen for certain elongation (d) (d : the remaining elongation after exposure).....143

Fig. 4.10 – The exposure time – temperature relationship of 0.39 mm specimen for certain elongation (d) (d : the remaining elongation after exposure).....144

Fig. 4.11– The exposure time – temperature relationship of 1.0 mm specimen for certain elongation (d) (d : the remaining elongation after exposure).....145

Fig. 4.12– Alpha phase to beta phase volume fraction ratio, where the red and black colors represent alpha-phase and beta-phase respectively.....146

Fig. 4.13 – The fracture surface of 1.0 mm, tensile, and exposed specimen of Timetal – 21S with exposure parameters 538 °C, and 40 hrs.....147

Fig. 4.14 – The fracture surface of 1.0 mm, tensile, and exposed specimen of Timetal – 21S with exposure parameters 538 °C, and 862 hrs.....148

| | |
|--|-----|
| Fig. 4.15 – The fracture surface of 1.0 mm, tensile, and exposed specimen of Timetal – 21S with exposure parameters 650 °C, and 40 hrs..... | 149 |
| Fig. 4.16 – The fracture surface of 1.0 mm, tensile, and exposed specimen of Timetal – 21S with exposure parameters 650 °C, and 118 hrs..... | 150 |
| Fig. 4.17 – The fracture surface of 1.0 mm, tensile, and exposed specimen of Timetal – 21S with exposure parameters 693 °C, and 40 hrs..... | 151 |
| Fig. 4.18 – The fracture surface of 1.0 mm, tensile, and exposed specimen of Timetal – 21S with exposure parameters 693 °C, and 80 hrs..... | 152 |
| Fig. 4.19 – The effect of exposure parameters on the formation of alpha – case..... | 153 |
| Fig. 4.20 – Specimen surface after the alpha - case layer is removed by the mechanical pickling of an exposed specimen with 118 hrs and 650 °C..... | 154 |
| Fig. 4.21 - σ - ϵ relationship of 1.0 mm exposed specimen at 650 °C for 118 hrs after removing the oxide layer..... | 155 |
| Fig. 4.22 – The distribution of the oxygen concentration (C) as function of the distance (x) measured from the surface of the test specimen and the maximum depth of oxygen penetration in the bulk of the specimen. Also, it shows the measured values of the alpha case in different specimens' thickness (0.12 and 0.39 mm) are in good agreement with 1.0 mm specimen thickness..... | 156 |
| Fig. 4.23 – 1: total weight of oxygen diffused in the specimen, 2: weight of oxygen diffused in the specimen's bulk where the equivalent oxygen concentration in titanium is C=0.5 %, 3: weight of oxygen diffused in α -case where the equivalent oxygen concentration in titanium is C=0.5 %..... | 157 |

| | |
|---|-----|
| Fig. 4.24 – The weight gain in the bulk of the specimen at three cases of the surface layer; first, no oxide layer, second, oxide layer is TiO_2 , and third, oxide layer is titanium oxides. 1: total weight of oxygen diffused in the specimen. 2, 3: weight of oxygen diffused in oxide layer and in the bulk respectively where the equivalent oxygen concentration in titanium is $C=2\%$. 4, 5: weight of oxygen diffused in oxide layer and in the bulk respectively where the equivalent oxygen concentration in titanium is $C=0.5\%$ | 158 |
| Fig. 4.25 – The microstructure at the surface of 1.0 mm heat treated specimen of Timetal 21S alloy..... | 159 |
| Fig. 4.26 – The microstructure at the surface of 1.0 mm Timetal – 21S exposed specimen with exposure parameters of 538 °C, and 100 hrs and magnification X 2,000..... | 160 |
| Fig. 4.27 – The microstructure at the surface of 1.0 mm Timetal – 21S expose specimen with exposure parameters of 650 °C, and 100 hrs..... | 161 |
| Fig. 4.28 – The microstructure in bulk of 1.0 mm heat treated specimen of Timetal – 21S alloy..... | 162 |
| Fig. 4.29 – The microstructure in the bulk of 1.0 mm Timetal – 21S exposed specimen with exposure parameters of 538 °C, and 100 hrs..... | 163 |
| Fig. 4.30 – The microstructure in the bulk of 1.0 mm Timetal – 21S exposed specimen with exposure parameters of 650 °C, and 100 hrs..... | 164 |
| Fig. 4.31 – The microstructure in the bulk of 1.0 mm heat treated specimen with a magnification of X10,000..... | 165 |

Fig. 4.32 – The microstructure in the bulk of 1.0 mm exposed specimen with exposure parameters of 650 °C, and 100 hrs, and a magnification of X10,000.....166

Fig. 4.33 - Vertical arrow from the beginning of the substantial loss of ductility to the horizontal arrow, which in turn pointing at the corresponding weight percentage of the diffused oxygen into the bulk of Timetal 21S. 1: total weight gain after exposure 650 °C /100 hrs. 2, 3: oxygen weight in the bulk and oxide layer (TiO₂) respectively after the same exposure.....167

Fig. 4.34 – Ductility loss as function of temperature after exposure of 1000 hrs for β-21S sheet thickness of 0.12, 0.39, 0.58, 1.0, and 1.32 mm.....168

Fig. 4.35 – Stress-strain relationship of two exposed specimens at 650 °C and 118 hrs. 1: specimen before pickling, 2: Specimen after pickling.....169

Fig. 4.36 – Theoretical Distribution of O₂ across the specimen’s cross-section after exposure at 538, 600 , and 693 °C for 1000 hrs.....170

Fig. 4.37 – The distribution of Alpha phase before the decoration process in the exposed Timetal 21S specimen (with exposure parameters 650 °C, and 40 hrs).....171

Fig. 4.38 – The distribution of Alpha phase after the decoration process in the exposed Timetal 21S specimen (with exposure parameters 650 °C, and 40 hrs) where the alpha phase distribution in the bulk disappeared.....172

Fig. 4.39– The brittle tensile fracture surface to be compared with the alpha – case thickness in the following Fig. V.31 for the same exposure parameters.....172

Fig. 4.40– The Alpha – case thickness layer to be compared with brittle tensile fracture surface in the previous Fig. V.30 for the same exposure parameters.....173

Fig. 4.41– The brittle tensile fracture surface to be compared with the Alpha – case thickness in the following Fig. V.33 for the same exposure parameters.....173

Fig. 4.42 – Shows the Alpha – case thickness layer to be compared with brittle tensile fracture surface in the previous Fig. V.32 for the same exposure parameters.....174

Fig. 4.43 - Characterization of ω phase in β -21S changes in (113) diffraction pattern with aging and exposure: a) 600 °C / 80 hrs; b) 650 °C / 500 hrs; c) dark field image for exposure 650 °C / 500 hrs.....175

Fig. 4.44 – Shows the crack front of a center crack tension, 0.39 mm thickness, and heat-treated specimen due to a room temperature fatigue loading with rate of 20 hz.....176

Fig. 4.45 – Shows the crack front of a center crack tension specimen with 0.39 mm thickness, and exposure of 538 °C and 40 hrs due to a fatigue loading with rate of 20 hz. X200.....177

CHAPTER I: INTRODUCTION

I.1 INTRODUCTION

The fundamental contribution of titanium alloys in aerospace applications stems from the combination of their fatigue and time-dependent mechanical properties as well as their relative low density and their high resistance to aggressive environment and impact loads. These considerations have led to an extensive use of titanium attaining contents as high as 30% and 40% of the total mass in commercial and military engines, respectively.

Titanium can take two microstructure configurations; α and β . Below about 885 °C pure titanium atoms arrange themselves in a hexagonal close-packed array called α phase. Above this transition temperature, the atoms arrange themselves into a body-centered cubic structure called β phase. Titanium alloys that contain substantial amounts of both phases are called α / β types. The additions of other metallic alloying elements favor one of these two crystallographic forms. For example, vanadium, molybdenum, and iron are β -phase stabilizers while aluminum, is an α -phase stabilizer. β alloys have higher strength than α / β alloys and can be rolled into sheets and foils without introducing texture effects.

One of the possible applications of the β titanium alloys is the engine's plug and nozzle, which is shown in Fig. 1.1. This structure, which requires the use of thin sheets to manufacture its honeycomb design, is located at the exit end of the engine and is exposed to turbine gases with temperatures reaching up to 621 °C. As such,

considerable efforts were made to examine the viability of Timetal-21S as a candidate for this type of applications. The ductility response of this alloy to thermal exposure parameters (temperature and time) and related embrittlement mechanisms are the focus of this thesis.

Several studies in literature pertaining to Timetal-21S have examined effects of temperature on the alloy's properties. Schutz [1], for example, showed that the upper temperature limit for practical use of Timetal-21S is 540–600 °C. At this temperature range, extensive ductility loss occurs. Wallace et al [2] showed that ductility is sensitive to a small weight gain during thermal exposure in air while Bird et al [3] and Paris [4] studied effects of the thermal exposure in the laboratory air and in vacuum, respectively. Their results showed that the diffusion of air elements has an aggressive effect on the ductility limit. Wallace et al [5] calculated the activation energy (Q) of embrittlement on the basis of the weight gain due to thermal exposure at 600–800 °C. In this work the value of Q was related to oxygen diffusion in titanium. Ignatov et al [6] showed that the possible activation energy for oxygen diffusion in α -titanium ranges from 16–75 kcal / mole while for β -titanium phase, Q ranges from 30–75 kcal / mole. William et al [7] showed that Q in α -titanium phase is 33.5 kcal/mole, and in β -titanium is 68.7 kcal/mole. The two previous studies showed that the microstructure constituent of the alloy (α and β phases) affects the diffusion parameter.

Paris [8] tested the oxygen concentration limit that Timetal-21S can bear without a substantial effect on the material's ductility. This limit, which is estimated as 0.25 wt% of the material, was calculated by measuring the elongation after exposing the material to temperatures ranging from 482 °C to 593 °C for duration of 4

- 24 hours. Paris [8] also investigated the surface effects where heat-treated specimens at 691 °C / 8 hrs followed with an air cooling (AC), and 649 °C / 8 hrs / AC were exposed to the laboratory air at 510 – 616 °C for 1000 hours. Ductility was regained completely after removing the surface layer. Wallace [5] showed that the surface oxide of a specimen exposed at 800 °C for 100 hours consists of two regions: a porous surface layer, and a relatively thick compact layer. Energy dispersive X-ray spectroscopy (EDS) analysis of the surface layer showed the presence of Ti, Al, and O, while analysis of the middle layer showed the presence of Ti, O and a small amount of Nb. EDS analysis combined with X-ray diffraction (XRD) analysis showed that the surface and middle layers oxides are primary TiO₂, with a mixture of Al₂O₃ and TiO₂ at the surface layer.

Limited studies were carried out to investigate the embrittlement mechanisms in Timetal-21S. Huang [9] investigated the mechanisms occurring in relation to specific heat treatment and aged conditions, such as received and aging at 400 – 677 °C / 8 hours. At low aging temperature (400 °C), it was shown that in α/β systems, embrittlement occurs due to precipitation of α phase which takes place at vacancies. Solution treatment and fast air-cooling rate produce an excess vacancy concentration. At the same time, vacancies move toward vacancy sink (grain boundary in this case) during aging. Therefore, areas near the grain boundaries have a lower vacancy density than the center of the grain, which causes a precipitation depletion zone when aging at high temperature (677 °C). The excess vacancy concentration is reduced by annihilation at vacancy sinks. This lessens the importance of vacancies on precipitate

distribution and causes grain boundaries to become a more dominant site for α precipitation during the initial stage of aging.

The objective of this thesis is to examine the ductility exhaustion of Timetal 21S alloy as a function of temperature and time. The current study will be carried out using different gage thickness 120, 390, and 1000 μm . The temperature range of interest here is 482, 538, 600, 650, and 693 $^{\circ}\text{C}$. The current study will analyze the weight gain in the material due to the exposure processes. This will serve in defining both of the activation energy (Q) of the embrittlement and the critical value of oxygen weight concentration. In order to calculate Q, this study will examine the heat treatment process with the aim of determining a stable microstructure during the exposure process and optimum tensile mechanical properties. The study of Q will serve in defining the diffused element leading to the alloy embrittlement. This will be achieved by correlating the activation energy of the embrittlement process of Timetal-21S with the activation energy required to diffuse each of the air elements into the material during the thermal exposure. Furthermore, extensive scanning electron microscopy as well as transmission microscopy will be carried out to determine the microstructure variations due to thermal exposures. The combined components of this study will attempt to define the embrittlement mechanisms in Timetal-21S as a function of temperature and exposure time.

This thesis is arranged in the following manner. Chapter 2 is a review of the beta titanium alloys with focus on the role of the composition, heat treatment processes, and oxygen diffusion. This chapter will also review β -21S alloy and explain its composition, heat treatment, and effects of hydrogen and oxygen diffusion

on ductility. Appendix 9 shows definitions to some expressions used in this chapter. Chapter 3 describes the experimental procedure carried out in this research and its detailed results. Chapter 4 describes the analysis of the experimental results and shows the mechanism responsible for ductility exhaustion. The final chapter lists the conclusion of this study and suggestion for future research work.

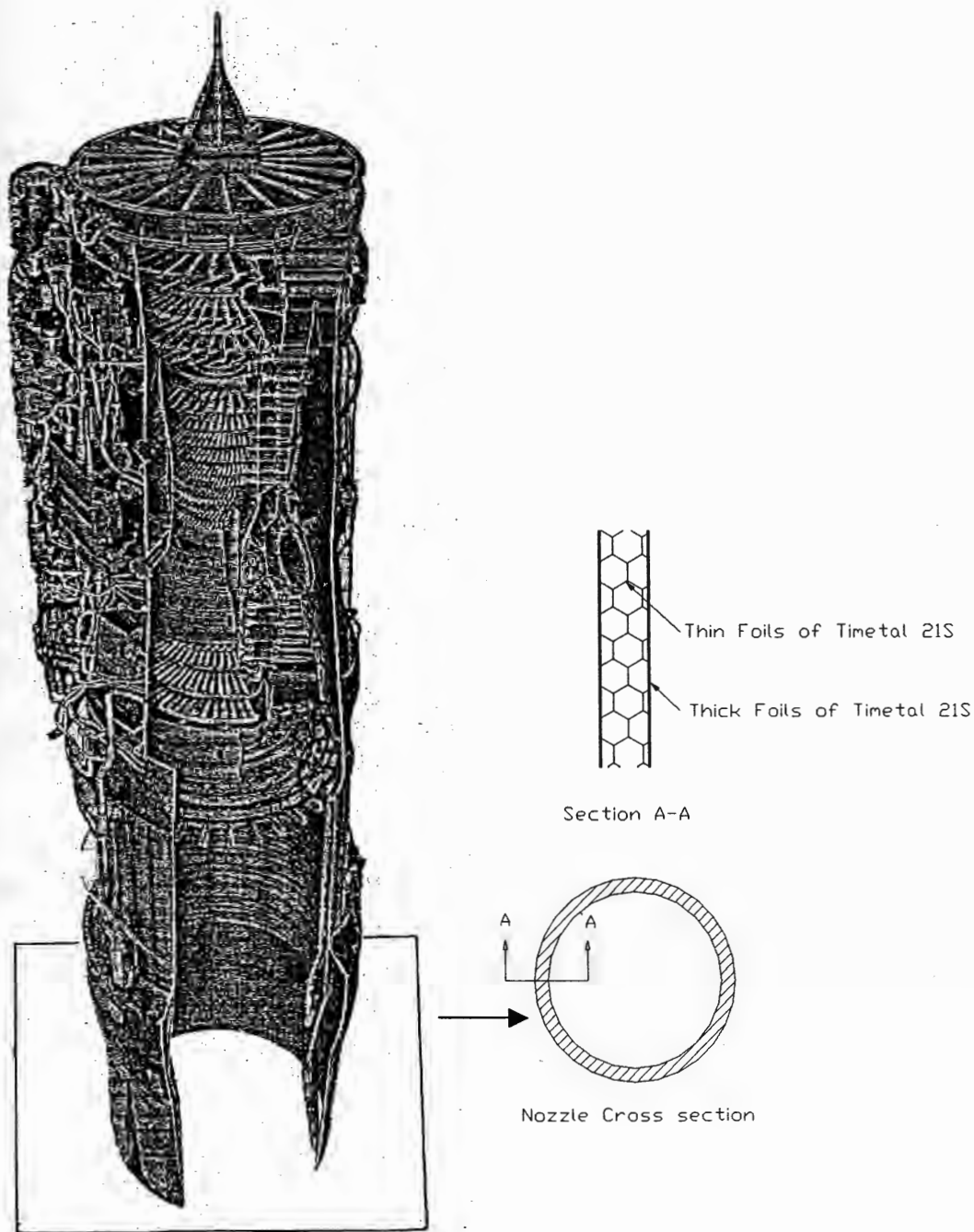


Fig. 1.1 - Nozzle is one of the applications Timal 21S alloy is used for.

CHAPTER II: REVIEW OF BETA TITANIUM ALLOYS

This chapter will show the composition of α -Ti alloys and present, the role of heat treatments in optimizing the mechanical properties. This chapter will also review the diffusion mechanisms in the α -Ti alloys. This review will be used to describe the Timetal 21S alloy, which is the foundation of this thesis.

II.1 Role of Composition

Table 2.1 shows that titanium is a transition metal where the shell inside the valence shell is electronically incomplete. This gives titanium the ability to dissolve interstitial atoms, as shown in Fig. 2.1. Also in titanium, as in other transition metals (TM), the increase in the average number of valence electron per atom ratio (e/a) in a subenergy levels 's + d' from 4 to 6 in the transition metals (TM) leads to a microstructure transformation from hcp to bcc Fig. 2.2. The increase in valence number can be achieved by increasing the amplitude of the lattice vibration by raising the temperature and /or adding TM to the element under consideration, which is shown in Fig. 2.3.

Different additions of TM to titanium would produce two different phase systems, isomorphous and eutectoid. Two main differences exist between the two systems. The first difference is the narrower freezing range in the isomorphous system, Fig. 2.4-a, when compared with that in the eutectoid system, Fig. 2.4-b. Therefore, isomorphous system produces lower element segregation upon cooling than eutectoid. The second difference is the additions of TM lead to the isomorphous type,

decreased β transus temperature less than those additions leading to the eutectoid system which is shown in Table 2. The two previous differences make the selection of TM which could lead to an isomorphous system preferable as titanium beta stabilizers (retaining β -phase upon quenching). The privilege of minimizing the chance of segregation during the alloy's cooling process, which will have a lower transus than the bulk is to have the ability of controlling the alloy's mechanical properties through controlling the amount of precipitates under different heat treatment conditions.

Fig. 2.5 shows the isomorphous equilibrium phase diagram of Ti base TM divided to three different regions, metastable, stable, and martensitic regions. The metastable range at the room temperature is bounded by a martensite M_s and β -transus temperature curves. Alloys falling in the metastable beta region can be formed into sheets while avoiding the presence of texture effect (loss of the isotropic property) and good hardenability. Good hardenability is due to the ability of manipulating the alpha precipitate process (volume fraction, distribution and α -grains' size) during the aging process of the heat treatments. Second region is the martensitic transformation range. It is a range in which cooling the bcc structure of titanium alloys begins an instantaneous allotropic transformation via a complicated shearing process to a martensite structure which is designated α' or α'' depending on whether the transformation product is hcp or orthorhombic. The third region is the stable beta titanium alloy range, which does not provide hardenability upon aging.

The additional quantity of TM to titanium which assure that the alloy will retain 100 % β -phase from above β -transus temperature and not transform to martensite upon quenching is stabilized using the 10 Moly Equivalent, Mo. Eq., see

App. 2. The Mo. Eq. is a convenient way to determine the overall beta stability of an alloy. Fig. 2.6 shows an example of the moly equivalent values for different beta alloys.

Within the metastable region, the phase change of the retained beta-phase is affected by several factors. First factor is the heat treatments (solution treatment or annealing, quenching rates, aging), that could lead to stable and metastable reversible and nonreversible phases. Other factors which mainly accelerate the phases change rates are related to loading (stress or elongation in elastic region, heavy elongation), and environment (adding substitution elements i.e. O₂, N, C, etc.). Fig. 2.7 shows an example of the effect of increasing the dissolved oxygen on accelerating the phase changes.

The following section will define the possible phases that can be produced through the heat treatments processes of titanium beta alloys.

II.2 Heat treatment of metastable beta titanium alloys

Heat treatment is the most crucial process after building the material composition, it manipulates the mechanical properties of the alloy. One can either treat a material for “stress relieving” or to manipulate its microstructure in order to achieve desired thermal stable alloys.

The heat treatment may include all or at least two of the following three procedures, solution treatment or annealing, quenching, aging, with or without different repeatable order in a selected environment.

Solution treatment: Solution treatment is to increase the solubility of the alloy components (TM as solutes) in titanium (as a solvent), this procedure is a diffusion process. For rich beta alloys, the temperature for solution treatment is mostly above the beta transus temperature, with the minimum of 20 to 30 min./in as a soaking time. Here one must be aware of the fast grain growth since β -phase is the only phase that exists at that temperature. For lean beta alloys, the temperature for solution treatment is lower than the transus (α - β anneal). Such solution treatment will produce alpha phase (globular morphology of alpha) and retained β -phase. Here one must expect a bimodal of alpha upon aging (primary alpha plus the precipitated alpha from the retained β -phase). Commercial beta alloys are generally supplied in the solution-treated condition.

Quenching: Quenching can be a diffusional or a diffusionless process depending on the diffusion coefficient of the alloy components, which are shown in Fig. 2.8 with respect to the applied quenching rate. Quenching process also depends on the alloy composition. For example, if it is located within the martensitic domain a diffusionless transformation could occur. Therefore the element's diffusion coefficients into titanium and the martensitic temperature boundary are the two important parameters, which define the proper selection of the quenching rate for beta titanium alloys. This is explained as follows.

Down quenching or up quenching, is to cool or heat an equilibrium alloy (the alloy has minimum free energy) with a suitable rate that leads to a supersaturated solid solution without segregation. Therefore in order to preserve (avoid segregation) the alloy's homogeneity during the quenching process, the suitable quenching rate is

important. For example, applying the same quenching rate for a TM with faster diffusion coefficients as Fe, Co, and Ni, instead of a TM with slower diffusion coefficients such as Nb will lead to structure segregation.

Furthermore, the optimum quenching process for titanium alloys in the vicinity of the martensite boundary (M_s) is influenced by both of the quenching rate and martensite temperatures as shown in the schematic diagram Fig. 2.9. The martensite boundary (M_s) itself will decrease as the quenching rate increases, but it will become independent of the quenching rate at 30 °C/sec (critical cooling rate). Different types of martensite (α' , α'' , athermal- ω phases) could be formed upon quenching, depend on the alloy composition and the quenching temperature.

Martensitic reactions from β -phase (not β -alloy) are fast. Diffusionless (no composition change such as Ti_3Al for example) transformation in crystal structure will lead to unstable microstructure such as α' , α'' , and ω phases i.e. from bcc to one or more of the hcp, orthorhombic, ω microstructures, see Fig. 2.10.

Up quenching as shown in Fig. 2.11, it is taking an aged alloy in $\omega+\beta$ field and by raising the temperature, would place it in the $\beta'+\beta$ field, where the isothermal (not athermal) ω -phase reverts to β' -phase (leaner in solute content than the matrix β -phase). That reaction is not reversible, where β' -phase remains as the alloy is returned back to the room temperature. It should be noted here, that β' -phase provides higher strength with better ductility than ω -phase plus sites for α -phase nucleation upon next aging for better distribution hence higher strength.

Aging: In general aging is the final step in the heat treatment and it can be considered as the first and only step of the heat treatment for beta titanium alloys' to achieve the optimum tensile and fatigue properties for a certain service, conditions.

From the schematic diagram Fig. 2.11, the initial phases upon aging of an alloy can be predicted. The important factor in this process is whether the time-temperature transformation (TTT) diagram that shows the kinetic of the phases exists, for the alloy under consideration.

Over aging is a more aging time than that required to transform to nonequilibrium phases which leads to a precipitation of α -phase on the interfaces of the transition phases ω and β' with β -phase, and a direct transformation of the retained β -phase to α -phase.

Also, in some of the titanium alloys a trend of cell growth could occur depending on the applied aging parameters (time and temperature), see Fig. 2.12.

Usually, beta titanium alloys' heat treatment are completed in vacuum in order to avoid embrittlement resulting from chemical reactivity of titanium alloys with O_2 , H, CO, CO_2 , and N from air at the elevated temperature. Also vacuum heat treatment eases the stress corrosion cracking at temperature above $315^\circ C$ due to the chlorides that may exist in some degreasing solutions.

II.3 Diffusion and oxygen in metal alloys

Diffusion: A diffusion process is defined as the trajectory of an atom inside the solid phases. This process represents a dynamic system with a reaction rate that could be mathematically expressed as logarithmic, quadratic as shown in Fig. 2.13.

Furthermore, diffusion process could lead to metastable phases, which may form during and disappear at the end of the reaction process. For example, Fig. 2.14, which shows the relative rates of phase formation (reaction products) for Ti – 7Al – 4Mo alloy at 900 °C.

Diffusion takes place due to the presence of defects in solids. Defects are classified into two categories: (1) Point defects that are caused by vacancy (as self-diffusion, substitutional impurity diffusion, diffusion couples and the Kirkendall effect), and interstitial (as O₂, C, N etc. in alloys). (2) Line and surface defects (short-circuit diffusion) such as the grain boundaries, dislocations, inner and outer surfaces etc.

Further, the different diffusion mechanisms depend on the crystal types under consideration these types are classified as homogenous and nonhomogenous systems. In the homogenous crystal system, atoms have a random motion with a resulting zero net movement. In the nonhomogenous crystal system, the impurity atoms diffused through a random walk process see App. 3 will eventually disperse and spread throughout the crystal.

Related description of diffusion in homogenous and nonhomogenous point defect is presented in Apps. 4 and 5.

Oxidation: Under certain conditions atoms diffuse and transport, also could react with the alloy components to form a new chemical composition, which produce phase changes i.e. β to α as in titanium.

It is found that the ‘over all oxidation’ reaction rate of titanium (simultaneous oxide scale formation and oxygen diffusion) is parabolic, where the oxide scale

formation rate is parabolic and the oxygen dissolution (transport) takes place by a point diffusion mechanism. Through a closer look in the titanium scale see Fig. 2.15 one can see different layers of oxides. The formation of one oxide rather than others (Ti_2O_3 , Ti_nO_{2n-1} , etc.) is due to the 'stability' of that oxide. This stability in turn is a function of the oxygen partial pressure (P_{O_2}) in the ambient where the reaction occurs. This partial pressure can be extracted from Ellington/Richardson diagram, which is shown in Fig. 2.16. For example, if the dissociation pressure (partial pressure of oxygen) to form TiO_2 is 10^{-20} atm at about 1400 °C, the titanium will consequently not be oxidized to TiO_2 in environment lower partial pressure. This Ellington/Richardson diagram Fig. 2.16 shows a great deal of understanding the internal oxidation phenomena, especially in the alloys where one will be able to expect which component will be oxidized first (of course based on the oxygen partial pressure at the reaction temperature).

Further, alloy's oxidation can be divided into two types. First type is the internal oxide (subscale formation), which occur when oxygen dissolves in the alloy phase and react with the least noble component and/or components under the suitable

oxide conditions ($p_{O_2} \geq \left(\frac{a_{MaO_b}}{a_M} \right)^{2/b} \exp \left\{ -\frac{2\Delta G_{MaO_b}}{bRT} \right\}$). Second type is the external

oxide (front scale), which occurs at the oxygen/metal interface under the same previous conditions. Manipulating the interaction between the alloy's components and its oxide rates can control the oxidation directionality, distribution, and the penetration rates see Figs. 2.17 and 2.18 and the example in the App. 6.

From this previous presentation it is clear that the ability of understanding the interaction of the alloy's elements to resist oxidation will provide a better alloys to resist the environment attack upon exposure. One of These alloys is the Timetal-21S, which will be presented, in the next chapter.

II.4 Review of Timetal 21S

Timetal-21S is developed in 1989 by Timet to provide an oxidation resistance foil product for the use by McDonnell Douglas as a matrix in titanium metal matrix composites as a part of the National Aerospace Plane program. The chemical composition of Timetal 21S in weight percent is Ti-15Mo-2.7Nb-3Al-0.2Si. This alloy is designated β -21S, which means that β alloy contain 21 % alloying additions and S for silicon. In this thesis Timetal 21S alloy will be referred to as β -21S alloy.

β -21S is a metastable β -titanium alloy that has the ability to maintain almost all its mechanical properties, such as strength and creep resistance at elevated temperatures. The good formability due to its bcc microstructure provides the ability to roll the alloy into thin sheets without encountering cracking neither pre-cracking due to texture effects. β -21S also provides high specific weight ratio (strength/density ratio) as compared to superalloys [10], and has a good corrosion resistance. These advantages make the Timetal-21S a good candidate for aerospace applications. One of these applications is hot air ducting structures see Fig. 1.1, where the alloy. In these applications, the alloy is exposed to two main environments that could degrade its mechanical. The first environment is the engine exhaust (hot) gas that can effect the mechanical properties and the second environment is the decomposed fluid products

such as organophosphoric acid, which represent a corrosion environment. This thesis will concentrate on the influence of hot gases environment on the mechanical properties of β -21S. Under this condition, the alloying components of the material can respond to these hot gases as follows by either permit the diffusion or adsorption of the gas or gases into the alloy and form various phases and / or altering the chemical composition if the gases found a suitable temperature and partial pressure on either the surface (scales) and / or inside the alloy. These responses are the main causes of changing the mechanical properties of the alloy in the applications described above. In order to understand this phenomenon, this chapter will review aspects dealing with the interaction of alloying elements, heat treatments and the air effects at elevated temperature on β -21S.

Composition: The chemical composition of Timetal-21S is Ti-15Mo-2.7Nb-3Al-0.2Si in weight percentage. Mo, Nb, and Si are beta phase (bcc) stabilizers while Al is an alpha phase (hcp) stabilizer, see Fig. 2.26. This alpha phase has two major roles; it increases alloy's strength, and maintains the phase distribution through the alloy microstructure during the possible exposure to different environments. The maintained phase distribution is the reason of the good thermal stability condition of this alloy within certain temperature range. The alloying elements Mo, Nb, Si, Al significantly enhance the oxidation resistance of B-21S. They also give a moly equivalent of about 12.8 (see App. 2) which indicates that β -21S is within the metastable region, see Fig. 2.27. "The Metastable" phrase means that the retained beta phase alloy upon quenching will precipitate a second phase (usually alpha) upon aging. Fig. 2.27 shows that the metastable beta alloys starts with a moly value of 10

(β_c). It shows also that the one phase region (beta phase) for β -21S will start at a temperature of 815 °C (beta transus temperature). Furthermore, this figure shows that a combination of one or more of ω , β' , α , and β phases will be expected in the microstructure of β -21S when increasing the temperature in vacuum.

In air at elevated temperatures, the resistance of Timetal 21S to oxidation is very high when it is compared with other titanium alloys. Fig 3.28 shows the oxidation comparison of β -21S at 650 °C in air with the pure commercial titanium and Ti 15-3-3-3. This feature is attributed to the presence of Mo., which also has a great effect of increasing the alloy's tolerance to hydrogen embrittlement.

Heat Treatment: As all beta titanium alloys, Timetal 21S must be heat-treated to achieve stable metallurgical condition at the exposure conditions of choice. This stability is usually achieved after the aging step. Once the aging is done, it will require a long exposure time to get phase changes based on the time temperature transformation curve (T-T-T curve) which is not established yet for the β -21S. However, using PERKIN ELMER Differential Thermal Analysis SYSTEM 1700 showed that the beta transus is about 815 °C [6 - 8], while the theoretical one is 835 °C. The later value was calculated using the following equation

$$\beta \text{ transus} = T_o + b_j x_j \text{ [9, 10]}$$

where T_o is 882 °C for pure titanium, x_j is the amount of alloying element in at. pct., and b_j is coefficient in °C / at. pct. Also, Fig. 2.29 shows that the silicide solvus temperature T_s is about 1025 °C. Furthermore, quenching the β -21S leads to the

formation of athermal ω phase, which is also formed when aging the alloy at 350 °C [18, 22].

Effect of Thermal Exposure: Exposing the alloy at elevated temperature in air leads to an interaction between the alloying elements and air components. This interaction is controlled the environment conditions, such as temperature, pressure which represent the thermodynamic conditions, to initiate a chemical reactions. It is also controlled by microstructure conditions, such as the alloying atoms size with respect to air element atoms size, alloying element location in the periodic table (i.e. transition metals (TM) which have the ability to dissolve interstitial atoms due to their incomplete electronic structure in the shell inside the valance one), and the fraction volume of phases (bcc, hcp etc.) in the alloy where the air elements' diffusion coefficients are higher in one phase than the other as shown in Table 2.3. This interaction can be interpreted generally as diffusion process which can cause either or both of the phase changes and / or chemical composition changes. Some of those diffusion parameters for the interstitial elements (air elements) in beta and alpha titanium are shown in Table 2.3.

Hydrogen Effect on β -21S Ductility: Hydrogen embrittlement occurs generally due to the lowering of the hydrogen solubility in the alloy bulk. This solubility can be affected (decreased) by two factors. The first factor is due to the fact that the transition temperature of embrittlement increases as the hydrogen content increases, see Fig. 2.30 [1]. For example, if the hydrogen contents in the Timetal 21S is 0.39 wt. % the temperature must be maintained higher than the room temperature otherwise the

loss of ductility will occur as shown in Fig 2.31. The second factor is the increase of the alpha phase volume fraction due to either aging or exposure which in turn could form a brittle titanium hydride phase for the order of several hundred ppm hydrogen [1, 23, 24].

Oxygen Effects: Generally, the upper temperature limit for practical use of titanium alloys in atmospheric exposure is identified by the onset of excessive surface oxidation and absorbed oxygen embrittlement. T.A.Wallace et al [3] and W.M.Paris [4] show in Fig. 2.32 that the room temperature elongation, yield strength, and the ultimate tensile strength were degraded due to the exposure of Timetal 21S in air.

Paris and Bania [8] found that oxygen percentage content in the bulk of fully aged sheet specimens within a temperature range 481 to 593 °C of Timetal-21S effects the strength – ductility relationship. It was shown that, if the oxygen range is 0.12 to 0.25 % in the bulk, there will be no effects on either the strength or the ductility. If the oxygen content is less than 0.12 % in the bulk the strength decrease would be significant. Also if oxygen level is higher than 0.25 % in the bulk this will cause degradation in the ductility. Furthermore, it was concluded [8] found that the depth of the contaminated surface layers for the over-aged specimen due to exposure at 482 and 566 °C are 0.13 and 0.25 mm respectively.

Concluding Remarks

It is useful to locate Timetal 21S on the schematic phase diagram as shown in Fig. 2.27. This gives a clear understanding of what phases should be expected upon choosing a certain heat treatment for Timetal 21S.

It will be expected from Fig. 2.32 that the activation energy of Timetal 21S alloy is within the range of 30 to 68 kcal / mol. However, the activation energy is function of the diffusion coefficient (D), which in turn is function of the volume fraction of the β -21S phases (alpha and beta), and the temperature, which ranges for this alloy within (600 to 1570 °C).

Fig. 2.32 shows that the most affected tensile property is the ductility as function of the exposure. Table 2.3 shows that the weight gain due to exposure is function of the phase. Therefore it will be required to eliminate the phase factor in order to investigate the effects of exposure parameters (temperature and time) on Timetal 21S.

Fig. 2.33 shows that the worst condition for the ductility is the room temperature. Therefore, the current work will have to focus on the exposure effect on room temperature ductility.

THE PERIODIC TABLE OF ELEMENTS (Long Form)

The number of electrons in filled shells is shown in the column at the extreme left; the remaining electrons for each element are shown immediately below the symbol for each element. Atomic numbers are enclosed in brackets. Atomic weights (rounded, based on Carbon-12) are shown above the symbols. Atomic weight values in parentheses are those of the isotopes of longest half-life for certain radioactive elements whose atomic weights cannot be precisely quoted without knowledge of origin of the element.

| METALS | | | | | | | | | | | | | NON-METALS | | | | | | | | | |
|---------|-------------------------------|-------------------------------|--------------------------|-------------------------------|--------------------------------|------------------------------|--------------------------------|------------------------------|-------------------------------|--------------------------|--------------------------------|-------------------------------|-------------------------------|-------------------------------|------------------------------|--------------------------------|------------------------------|------------------------------|------------------------------|---------------------|-----------------------|-----------------------|
| periods | I A | | | | | | | | | | | VII A O | | | | | | | | | | |
| 0 | 1 | II A | | | | | | | | | | TRANSITION METALS | | | | | | 1 | 2 | | | |
| 2 | 1 | 2 | III A | | | | | | | | | | 3 | 4 | 5 | 6 | 7 | 8 | | | | |
| 3 | 1 | 2 | VIII | | | | | | | | | | 3 | 4 | 5 | 6 | 7 | 8 | | | | |
| 4 | 1 | 2 | 3 | 4 | 5 | 6 | 7 | 8 | 9 | 10 | 11 | 12 | 13 | 14 | 15 | 16 | 17 | 18 | | | | |
| 1 | 1.0079 H[1] 1 | | | | | | | | | | | | | | | | 1.0079 H[1] 1 | 4.0026 He[2] 2 | | | | |
| 2 | 6.941 Li[3] 1 | 9.0122 Be[4] 2 | | | | | | | | | | | | | | | 10.81 B[5] 3 | 12.011 C[6] 4 | 14.007 N[7] 5 | 16.000 O[8] 6 | 19.000 F[9] 7 | 21.179 Ne[10] 8 |
| 3 | 22.99 Na[11] 1 | 24.305 Mg[12] 2 | | | | | | | | | | | | | | | 26.982 Al[13] 3 | 28.086 Si[14] 4 | 30.974 P[15] 5 | 32.06 S[16] 6 | 35.453 Cl[17] 7 | 39.948 Ar[18] 8 |
| 4 | 39.098 K[19] 8, 1 | 40.08 Ca[20] 8, 2 | 44.956 Sc[21] 9, 2 | 47.90 Ti[22] 10, 2 | 50.941 V[23] 11, 2 | 51.996 Cr[24] 13; 1 | 54.938 Mn[25] 13, 2 | 55.847 Fe[26] 14, 2 | 58.933 Co[27] 15, 2 | 58.70 Ni[28] 16, 2 | 63.546 Cu[29] 18, 1 | 65.38 Zn[30] 18, 2 | 69.72 Ga[31] 18, 3 | 72.59 Ge[32] 18, 4 | 74.922 As[33] 18, 5 | 78.96 Se[34] 18, 6 | 79.904 Br[35] 18, 7 | 83.80 Kr[36] 18, 8 | | | | |
| 5 | 85.468 Rb[37] 8, 1 | 87.62 Sr[38] 8, 2 | 88.906 Y[39] 9, 2 | 91.22 Zr[40] 10, 2 | 92.906 Nb[41] 12, 1 | 95.94 Mo[42] 13, 1 | (97) Tc[43] 14, 1 | 101.07 Ru[44] 15, 1 | 102.906 Rh[45] 16, 1 | 106.4 Pd[46] 18 | 107.868 Ag[47] 18, 1 | 112.41 Cd[48] 18, 2 | 114.82 In[49] 18, 3 | 118.69 Sn[50] 18, 4 | 121.75 Sb[51] 18, 5 | 127.60 Te[52] 18, 6 | 126.905 I[53] 18, 7 | 131.30 Xe[54] 18, 8 | | | | |
| 6 | 132.905 Cs[55] 18, 8, 1 | 137.33 Ba[56] 18, 8, 2 | * [57-71] | 178.49 Hf[72] 32, 10, 2 | 180.948 Ta[73] 32, 11, 2 | 183.85 W[74] 32, 12, 2 | 186.207 Re[75] 32, 13, 2 | 190.2 Os[76] 32, 14, 2 | 192.22 Ir[77] 32, 16, 2 | | 196.967 Pt[78] 32, 17, 1 | 200.59 Au[79] 32, 18, 1 | 200.59 Hg[80] 32, 18, 2 | 204.37 Tl[81] 32, 18, 3 | 207.2 Pb[82] 32, 18, 4 | 208.980 Bi[83] 32, 18, 5 | (209) Po[84] 32, 18, 6 | (210) At[85] 32, 18, 7 | (222) Rn[86] 32, 18, 8 | | | |
| 7 | (223) Fr[87] 18, 8, 1 | 226.025 Ra[88] 18, 8, 2 | † [89-103] | Rf[104] 32, 10, 2 | Ha[105] 32, 11, 2 | [106] 32, 12, 2 | [107] | [108] | | | | | | | | | | | | | | |

Table 2.1 – The periodic table of elements [10].

Table 2.2 – Beta Stabilizing Elements [11].*

| β - Stabilizer | Type | β_c (Wt %) ¹ | β_t Suppression (°F) ² |
|----------------------|-------------|----------------------------------|--|
| Mo | Isomorphous | 10.0 | 17 |
| V | Isomorphous | 15.0 | 22 |
| W | Isomorphous | 22.5 | 7 |
| Cb | Isomorphous | 36.0 | 13 |
| Ta | Isomorphous | 45.0 | 4 |
| Fe | Eutectoid | 3.5 | 32 |
| Cr | Eutectoid | 6.5 | 27 |
| Cu | Eutectoid | 13.0 | 22 |
| Ni | Eutectoid | 9.0 | 40 |
| Co | Eutectoid | 7.0 | 38 |
| Mn | Eutectoid | 6.5 | 40 |
| Si | Eutectoid | - | 70 |

¹Approximate wt. % needed to retain 100 % β phase upon quenching.

²Approximate amount of β transus reduction per wt. % of addition.

| Diffused Element | Solvent | Temperature Range (°C) | Frequency factor, D_0 (cm^2s^{-1}) | Atomic Activation Energy (kcal / mol) | Diffusivity at [ToC] D (cm^2s^{-1}) | Comments | Reference | |
|------------------|--------------------|------------------------|--|---------------------------------------|---|--|---|------|
| C | α - Ti | 600 – 800 | | 30.5 | | | [22] | |
| | β - Ti | 950 – 1150 | 108 | 48.3 | | | [23] | |
| H | α - Ti | RT | | | 10^{-10} [RT] | hydrogen diffusion in β phase is 1000 times greater than in α phase | [1] | |
| | β - Ti | | | | 5×10^{-7} [RT] | | | |
| N | β - Ti | 900 – 1570 | 3.5×10^{-2} | 37.95 | 1.8×10^{-14} [380] | | [23] | |
| O | α - Ti | 538 | | | 1.5×10^{-16} [538] | Oxygen diffusion in β phase is 15 times greater than in α phase | [1] | |
| | | | | | 10^{-17} [538] | | | |
| | | | | | | | | |
| | | | | | 47.5 | | The average variation of the activation energies in Ti α -phase is 55.6 kcal / mol | [20] |
| | 700-850 | 5.08×10^{-1} | 33.45 | | | | [21] | |
| | 850-1000 | 3.2×10^4 | 61.89 | | | | | |
| | 900-1300 | 8.9×10^2 | 52.57 | | | | | |
| | 932-1142 | 77.8 | 48.51 | | | | | |
| | 750-850 | 1.7×10^3 | 52.33 | | | | | |
| | 650-875 | 40.8 | 47.07 | | | | | |
| 700-950 | 45 | 48.03 | | | | | | |
| 750-900 | 2.15×10^6 | 71.21 | | | | | | |

| | | | | | | | | | |
|----------|-------------------|--------------|-----------------------|----------------------|---------------------------|---|-----------------------------|---|------|
| | | 815-1149 | 20.3×10^6 | 75.27 | | [23] | | | |
| | | 750-1048 | 9.4×10^4 | 68.58 | | | | | |
| | | 250-900 | 45 | 51.37 | | | | | |
| | | 750-870 | 1.6×10^3 | 52.09 | | | | | |
| | | 930 - 1150 | 3.14×10^4 | 68.7 | 5×10^{-8} [1000] | | | | |
| | | β - Ti | 932 - 1142 | 3.3×10^2 | 58 | | 3.6×10^{-8} [1000] | The average variation of the activation energies in Ti β -phase is 52.45 kcal / mol | [21] |
| | | | 950 - 1415 | 1.6 | 48.2 | | 8.4×10^{-9} [1000] | | |
| | | | 1135 - 1355 | 8.3×10^{-2} | 31.2 | | 3.6×10^{-7} [1000] | | |
| | | | 900-1150 | 3.14×10^6 | 68.82 | | | | |
| | | | 950-1414 | 1.6×10^2 | 49.70 | | | | |
| 932-1142 | 3.3×10^4 | 58.78 | | | | | | | |
| Mo | β -Ti | 900-1650 | | 65 | | Two values because of curvature in the Arrhenius plot | [22] | | |
| | | | | 36.9 | | | | | |
| Nb | β -Ti | 1000-1650 | | 69.5 | | Two values because of curvature in the Arrhenius plot | [22] | | |
| | | | | 34.9 | | | | | |
| Al | α -Ti | 560-648 | 9.59×10^{-4} | 22.1 | | [21] | | | |
| | β -Ti | 900-1000 | 3.1×10^{-2} | 32.26 | | | | | |
| | | | 5.89×10^{-2} | 40.62 | | | | | |
| | | | 0.331 | 37.5 | | | | | |
| | | | 3.55×10^{-2} | 38.47 | | | | | |

Table 2.3 – Shows the frequency factor, the diffusivity, and the atomic activation energy of different element's diffusion into the titanium.

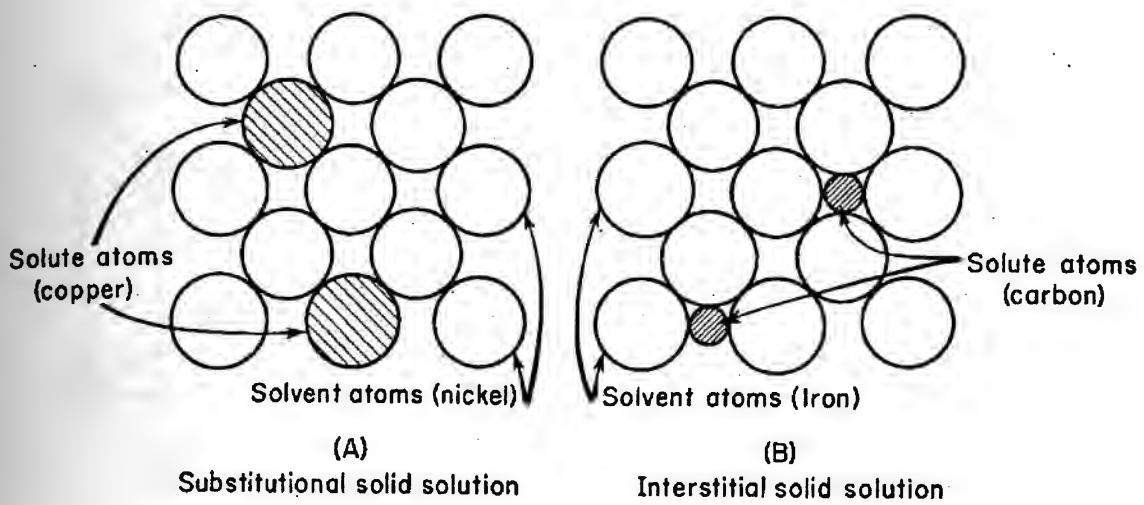
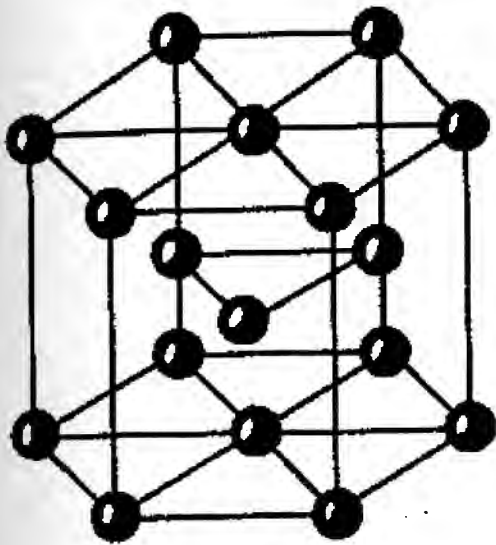
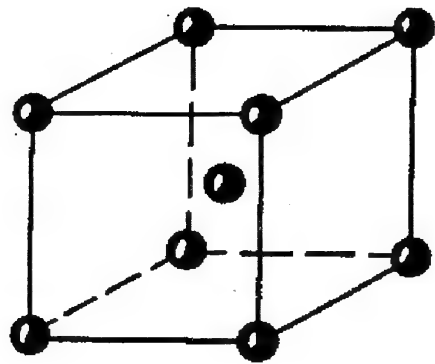


Fig.2.1 – The two basic forms of solid solution [12].*

* Extracted from "Physical Metallurgy principles," edited by Robert E. Reed – Hill, pp. 220, 1964.



Hexagonal close - packed (HCP)



Body - centered cubic (BCC)

Fig.2.2 – HCP and BCC are the two microstructures forming α -phase and β -phase respectively in titanium alloys

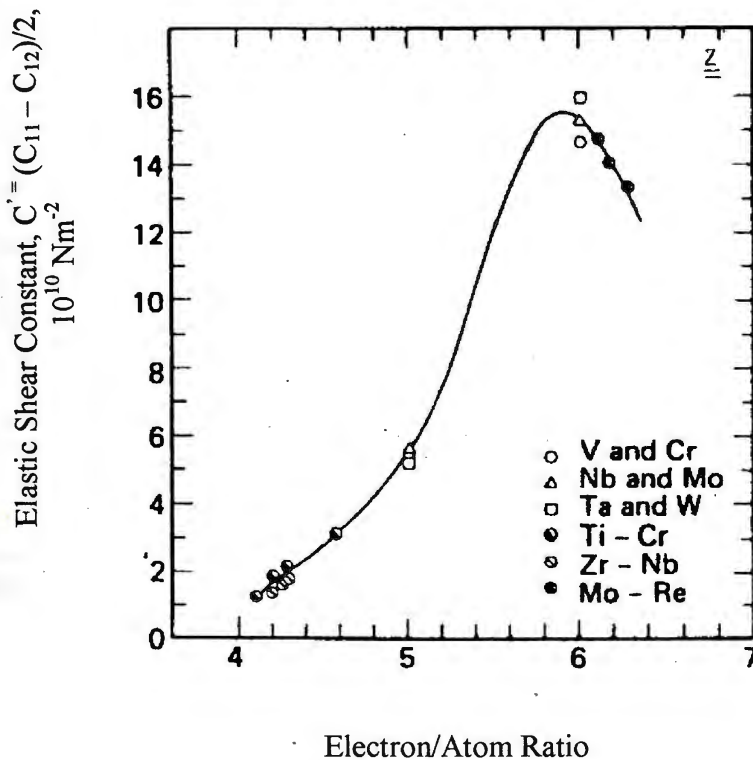
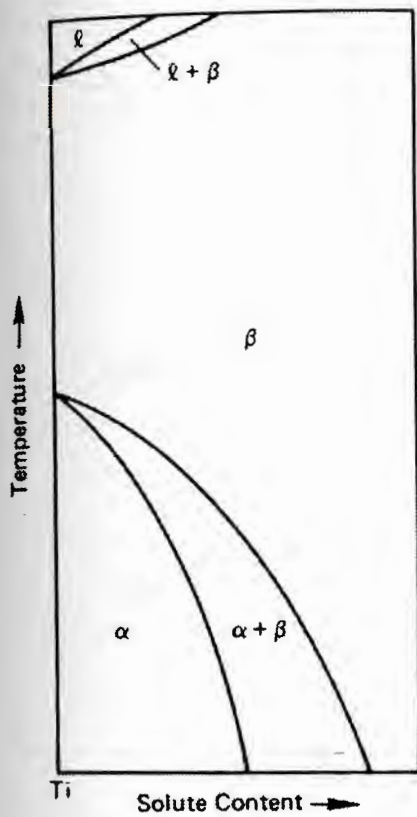
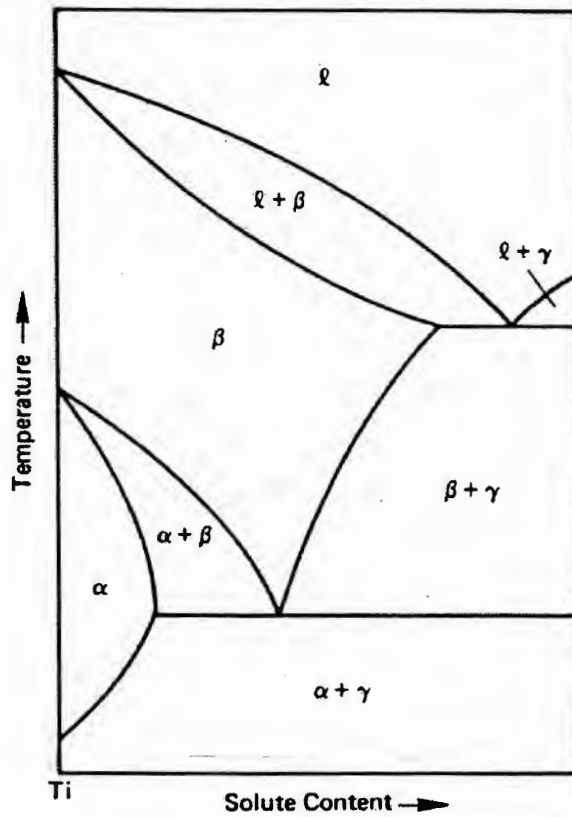


Fig.2. 3 - The average number of valence electron per atom ratio (e/a) versus the elastic shear modulus as function of the additions of TM [12].*

* Extracted from "Applied Superconductivity, Metallurgy, and Physics of Titanium Alloys," edited by E.W.Collings, V.1, pp. 6, 1985.



(4-a)



(4-b)

Fig.2.4 – Principal feature of (4-a) the β – isomorphous, and (4-b) the β – eutectoid classes of β – stabilized equilibrium Ti – base transition – metal alloy (Ti – TM) equilibrium phase diagram. An intermetallic compound is represented by γ [12].

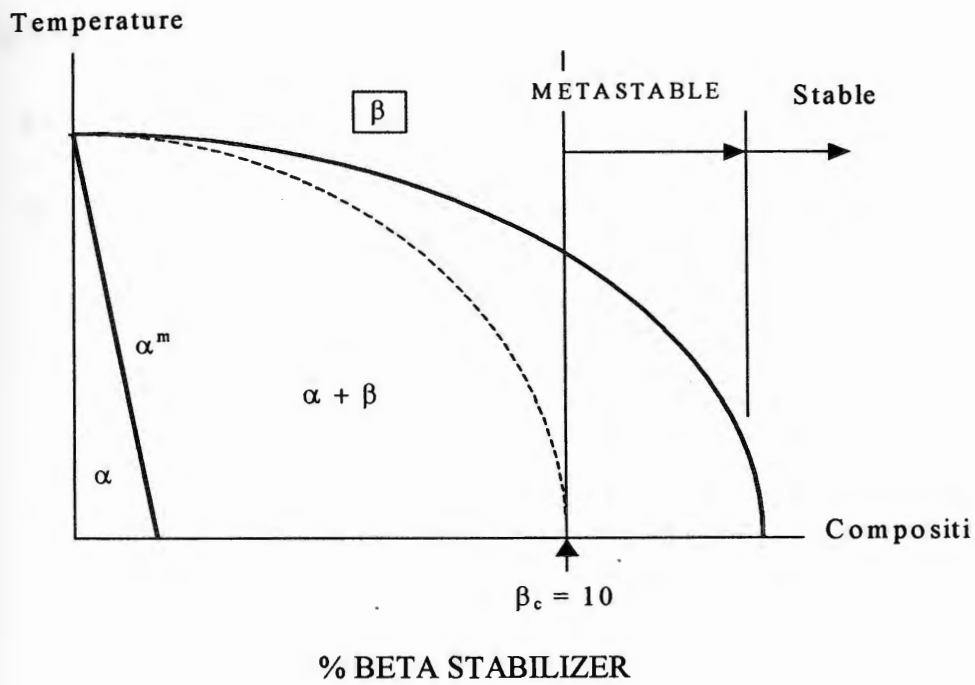


Fig.2.5 – Phase diagram of titanium and a beta stabilizer.*

* Extracted from "Applied Superconductivity, Metallurgy, and Physics of Titanium Alloys," edited by E.W.Collings, V.1, pp. 54, 1985.

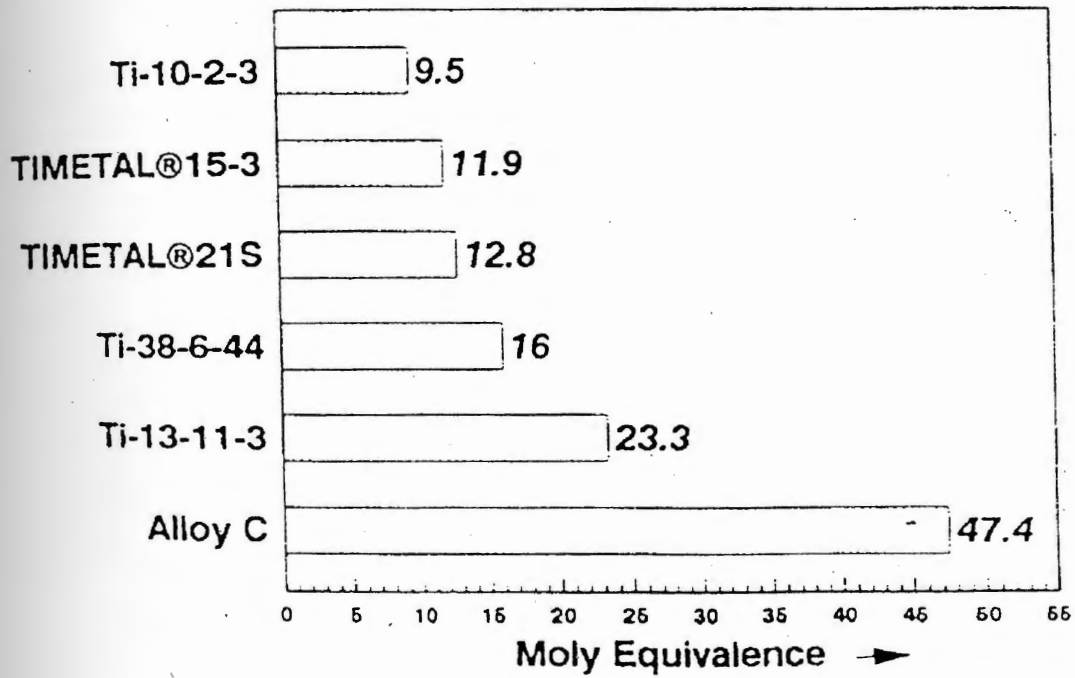


Fig.2.6 – Moly Equivalent values for various commercial alloys [11].

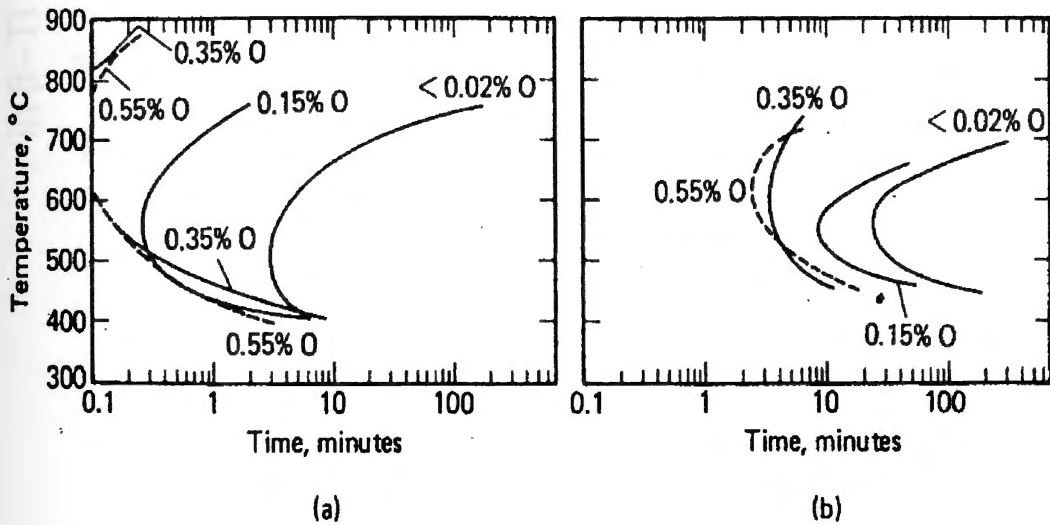


Fig.2.7 – Influence of oxygen on the $\beta \rightarrow \alpha + \beta$ transformation kinetics of B isomorphous alloy Ti – 11 Mo ; (a) transformation start, (b) transformation finish [13].

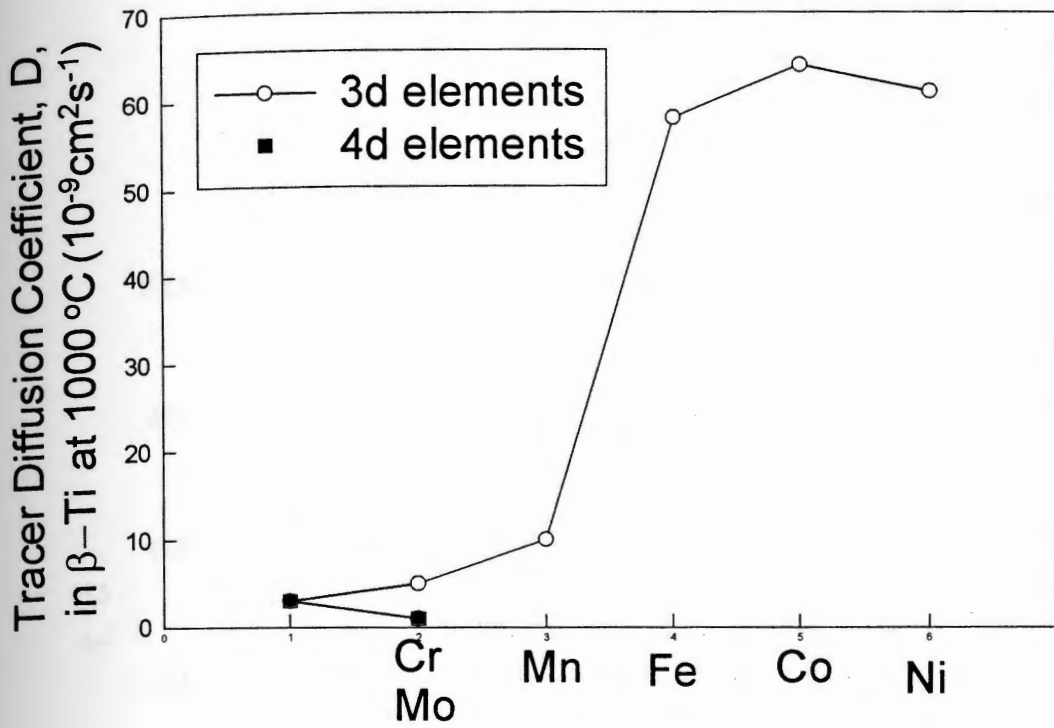


Fig.2.8 – Tracer diffusion coefficients for the 3d solutes V, Cr, Mn, Fe, Co, and the 4d solutes Nb and Mo in B-Ti at 1000 oC [13].*

* Extracted from "Applied Superconductivity, Metallurgy, and Physics of Titanium Alloys," edited by E.W.Collings, V.1, pp. 23, 1985.

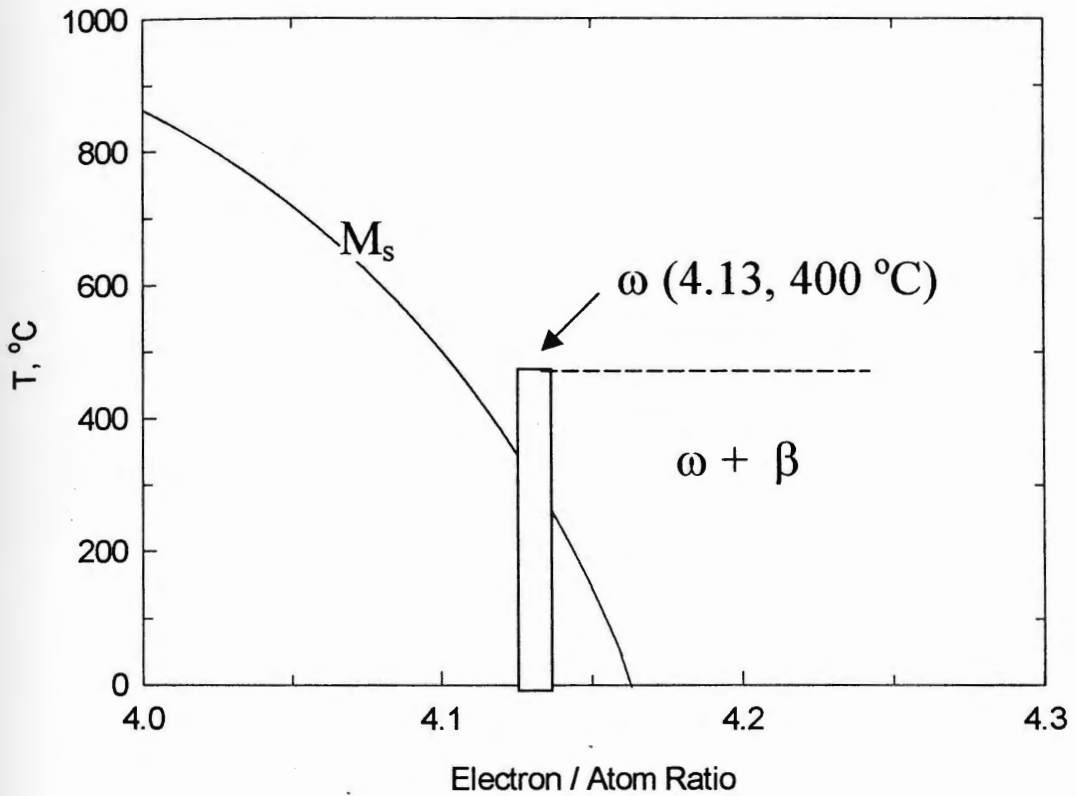


Fig.2.9 – Schematic representation of the occurrences of the martensitic α' – and α'' – phases (i.e., α^m , collectively) and the ω - phase in Ti- TM alloys [13].*

* Extracted from “Applied Superconductivity, Metallurgy, and Physics of Titanium Alloys,” edited by E.W.Collings, V.1, pp. 22, 1985.

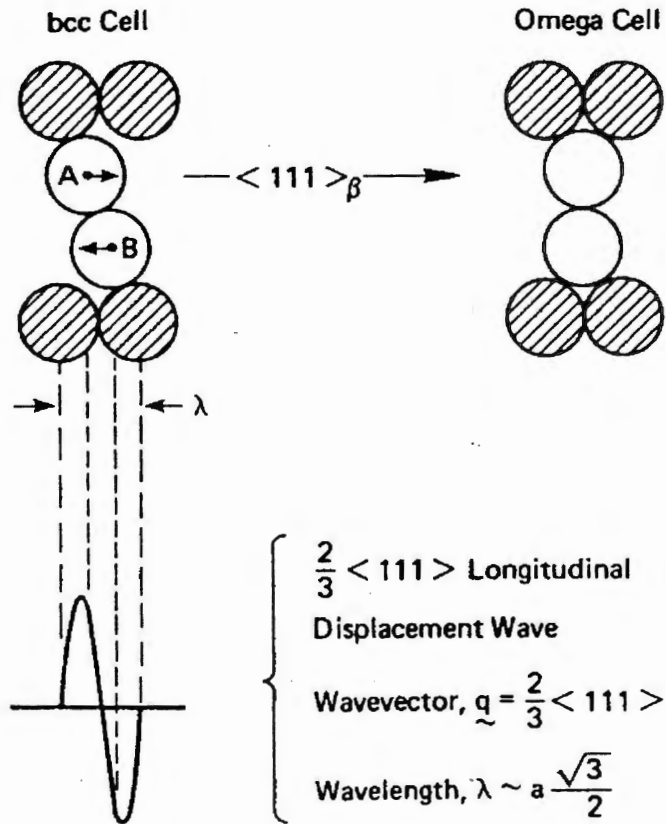


Fig.2.10 – Development of the w – structure through the application of $\frac{2}{3} \langle 111 \rangle$ longitudinal displacement wave to the bcc lattice [13].

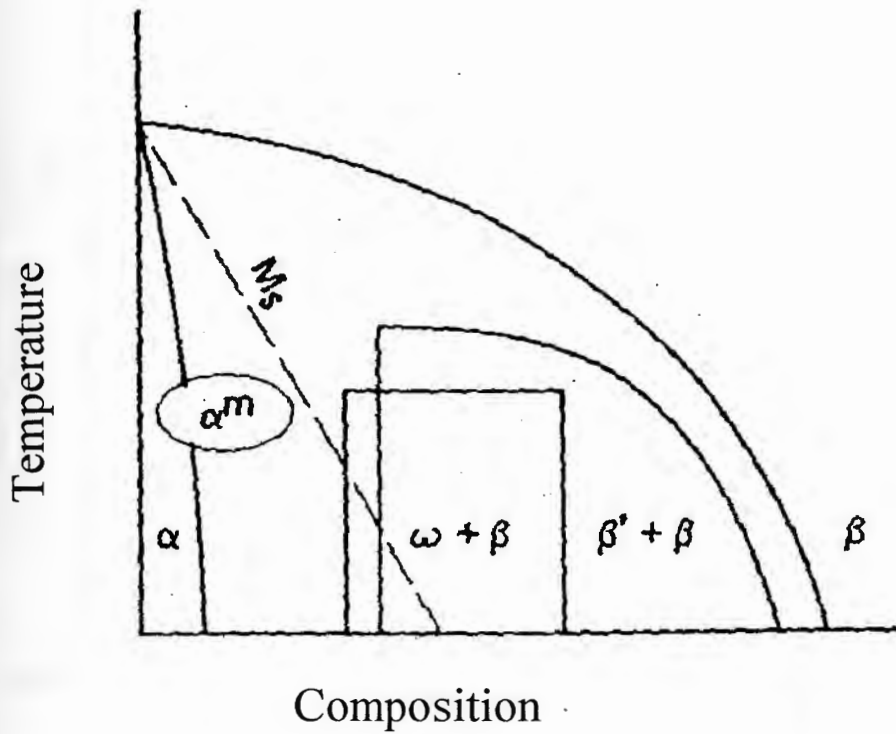


Fig.2. 11 – Schematic representation of the locations of the two metastable phases $\omega + \beta$ and $\beta' + \beta$, within the equilibrium $\alpha + \beta$ -phase field in a typical Ti-TM alloy [13].

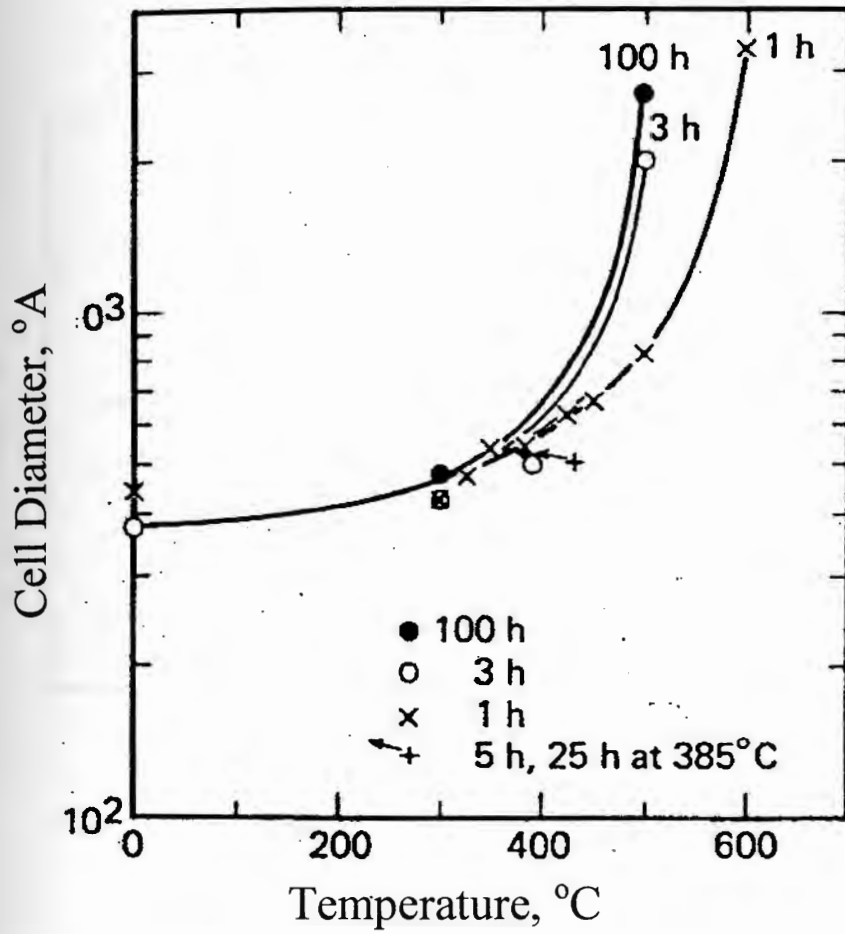


Fig.2. 12 - Deformation cell growth as a function of (a) time and (b) temperature [13].

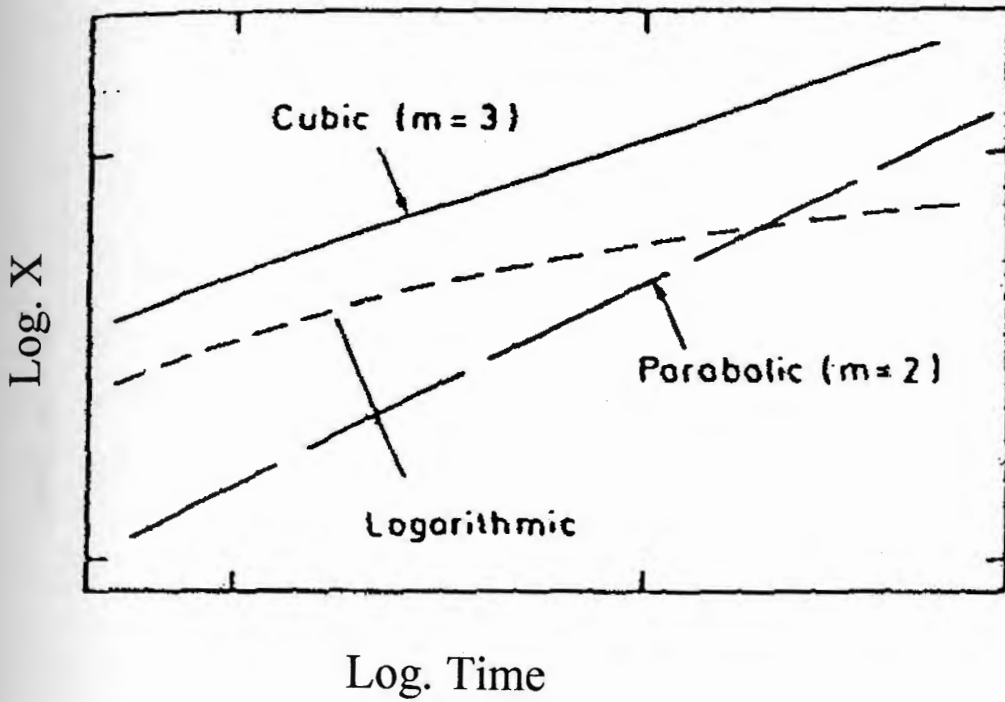


Fig.2.13 - Double - logarithmic plot (log x versus log t) of parabolic and logarithmic oxidation. If such processes take place simultaneously, the overall oxidation may obey an approximate cubic rate ($x^3 \propto t$) [14].*

* Extracted from "High Temperature Corrosion," edited by Per Kofstad, pp. 20, 1988.

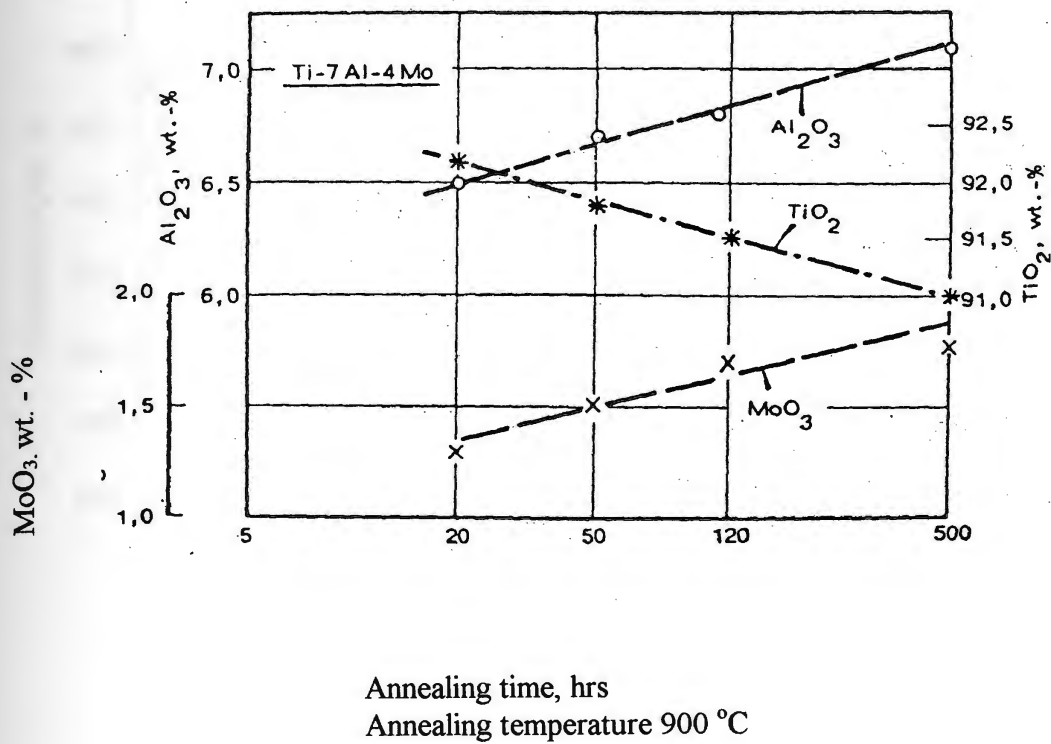


Fig. 2. 14 – Scale composition for one of the titanium alloys showing the kinetics of the oxides formation as function of time at 900 °C.

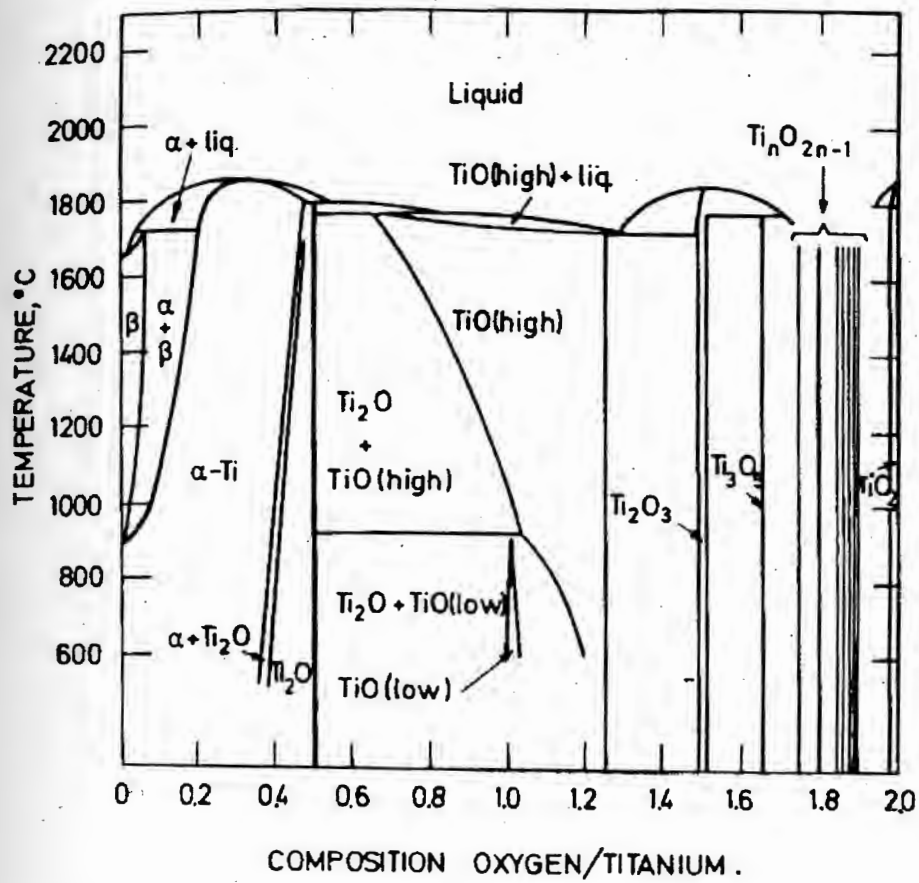


Fig.2.15 - The titanium – oxygen phase diagram [14].

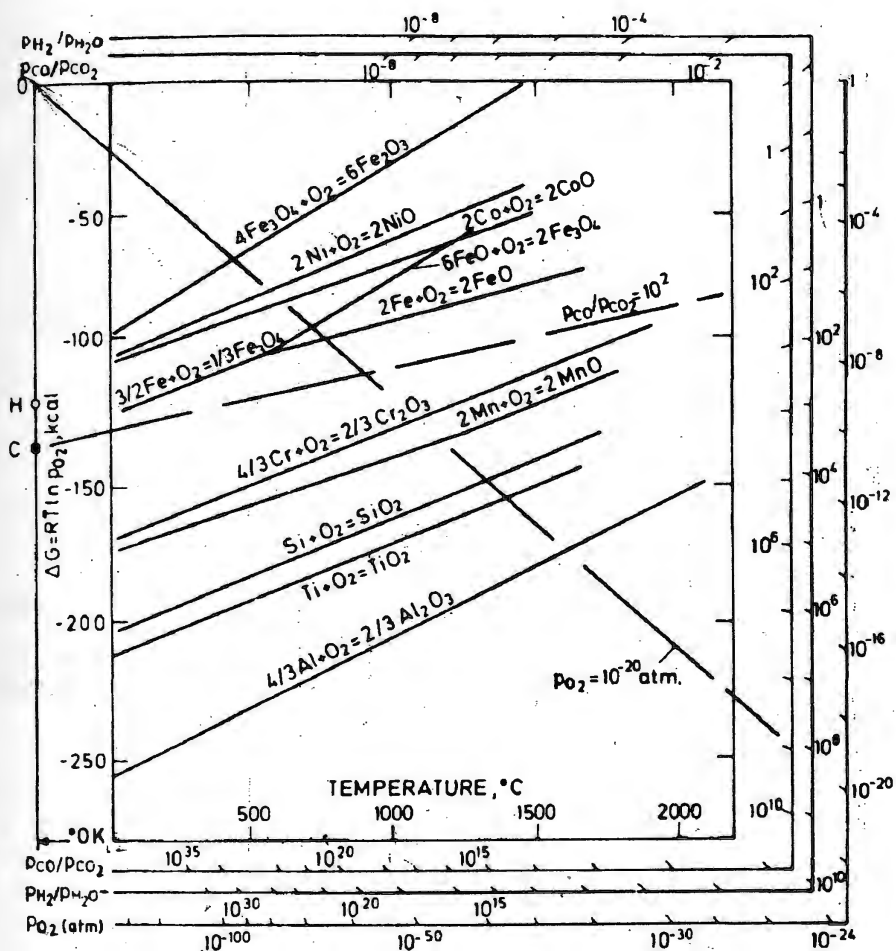


Fig.2.16 – Ellingham/Richardson diagram for some oxides of importance in the high temperature oxidation of metals and alloys [14].

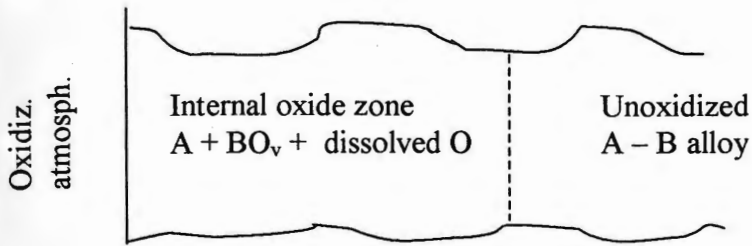


Fig.2. 17 - Illustration of the internal oxidation of dilute A -B alloys. It is assumed that A is a noble metal, B atoms to be immobile in the alloy and to have been oxidized to BO_v particles in the internally oxidized zone [14].*

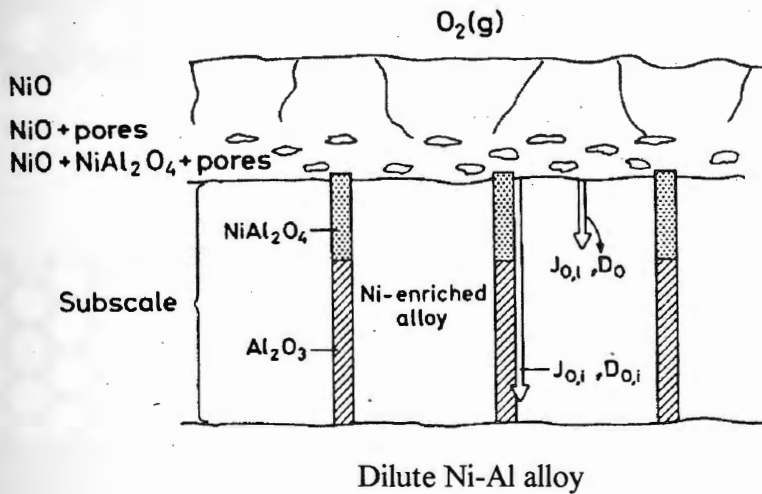
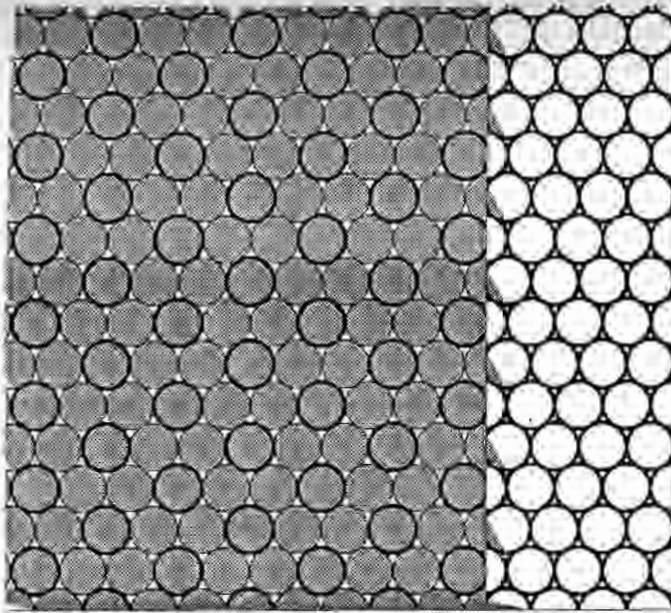
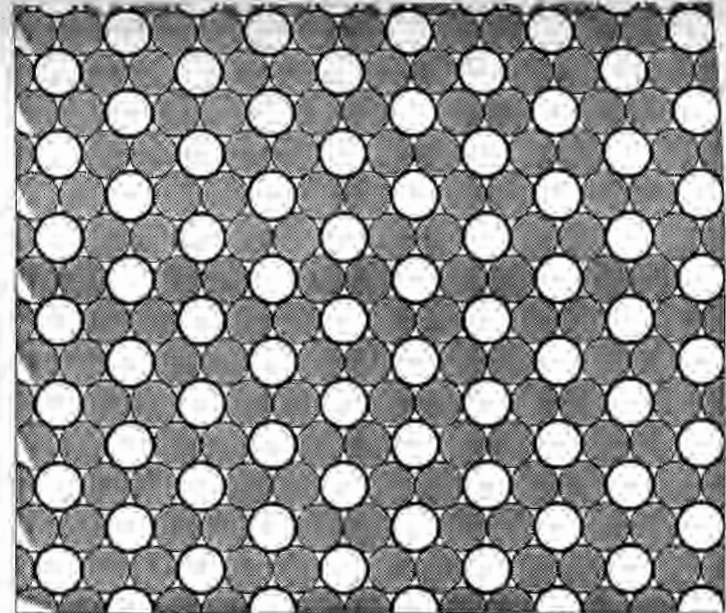


Fig.2.18 - Schematic illustration of the growth of internal oxide in the form of rods normal to the surface [14].

* Extracted from "High Temperature Corrosion," edited by Per Kofstad, pp. 327, 1988.



(A)



(B)

Fig.2.19 – The box analogy of a crystal. (A) Vacancies and atoms in the segregated state. Atoms to the left, vacancies to the right. (B) The mixed state [11].*

Extracted from "Physical Metallurgy Principles," edited by Per Reed - Hill, pp. 167, 1968.

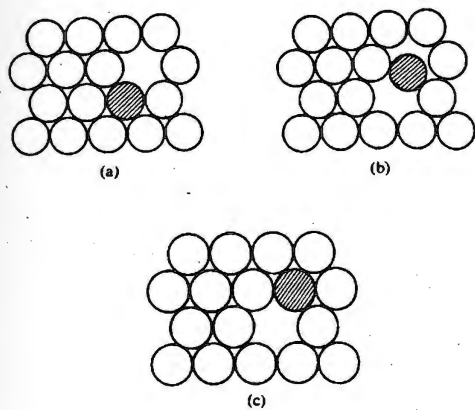


Fig.2.20 – Diffusion by vacancy mechanism [15].

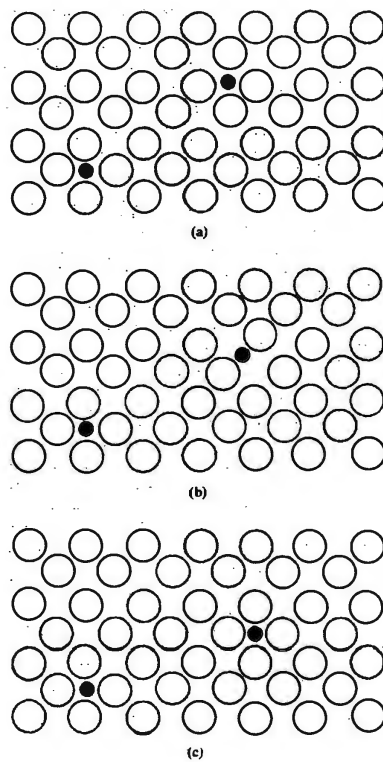


Fig.2.21 – Diffusion by interstitial mechanism [15].*

* Extracted from "Atomic Migration in Crystals," edited by L. A. Girifalco, pp. 30, 1964.

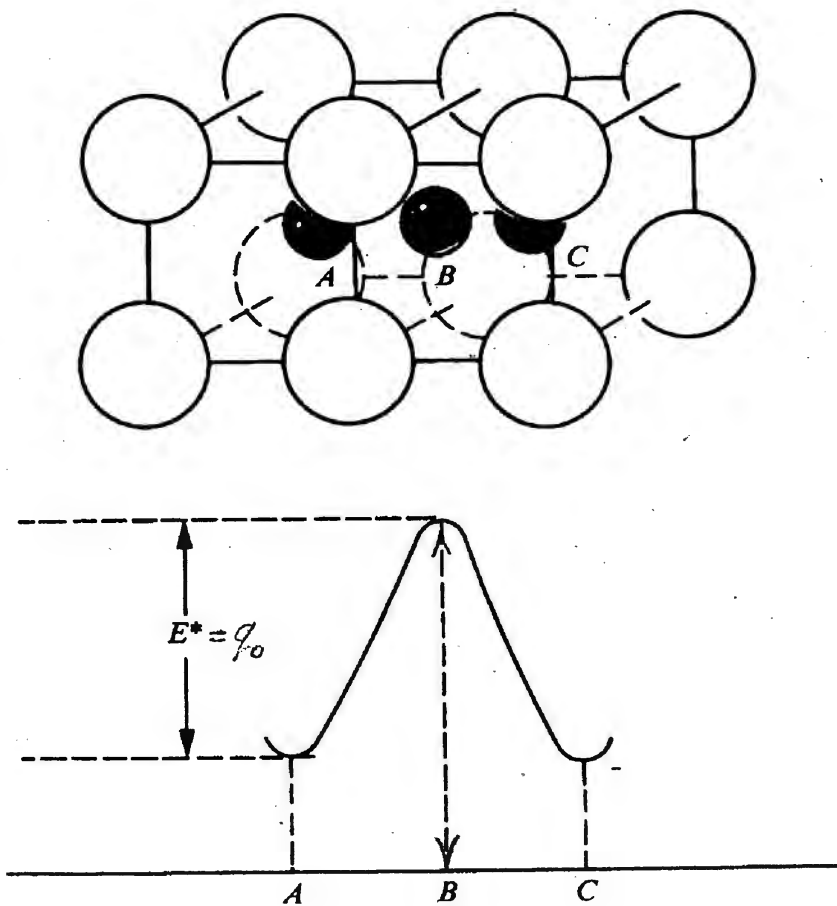


Fig.2.22 – Energy of an impurity atom as it moves from an initial position A in one cage to a final position C in an adjacent cage in a simple cubic structure [15].*

* Extracted from "Atomic Migration in Crystals," edited by L. A. Girifalco, pp. 39, 1964.

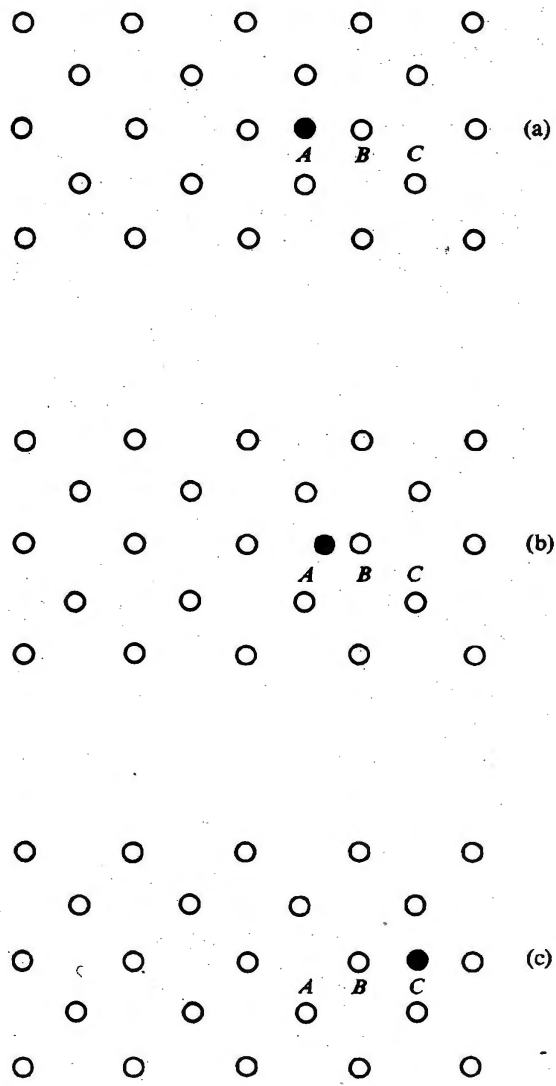


Fig.2.23 - Diffusion by an interstitialcy mechanism: (a) initial state, (b) activation state, (c) final state [14].*

* Extracted from "Atomic Migration in Crystals," edited by L. A. Girifalco, pp. 31, 1964.

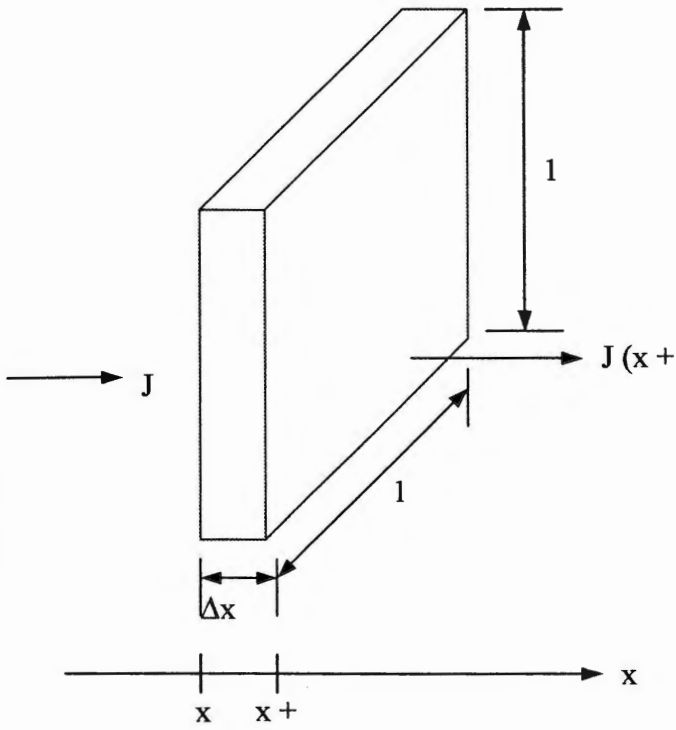


Fig.2.24 – Rectangular parallelepiped in a crystal with dimensions $1 \times 1 \times dx$ cm.

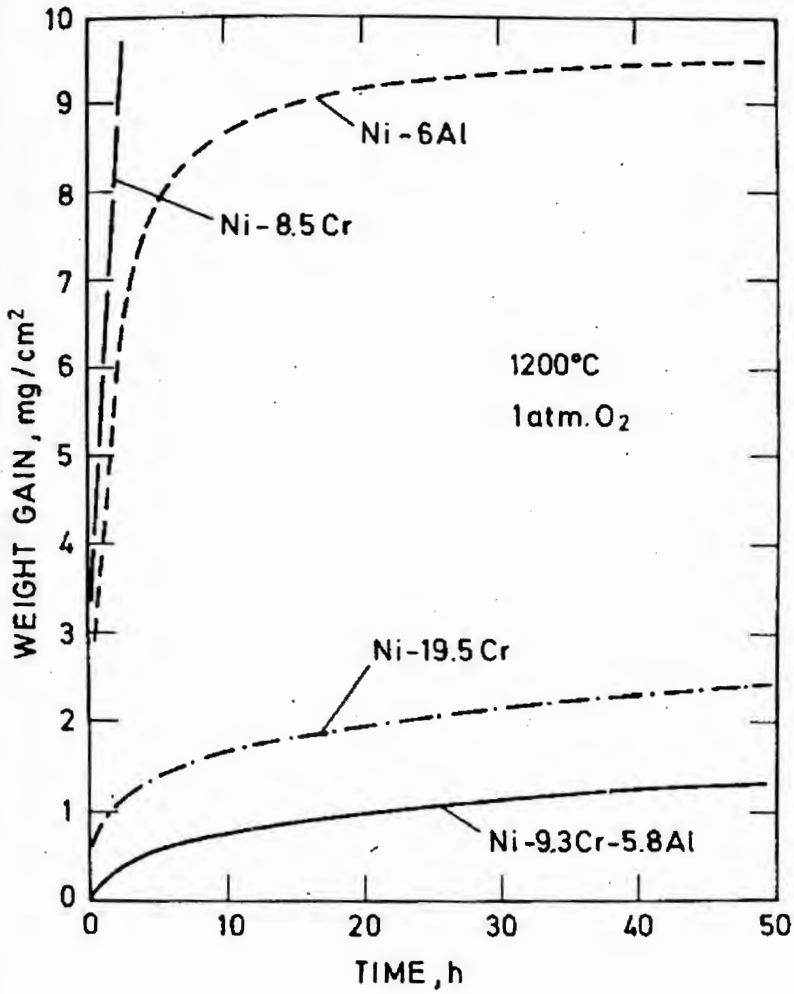


Fig.2. 25 - Comparison of the oxidation of the three different alloys shown above [15].

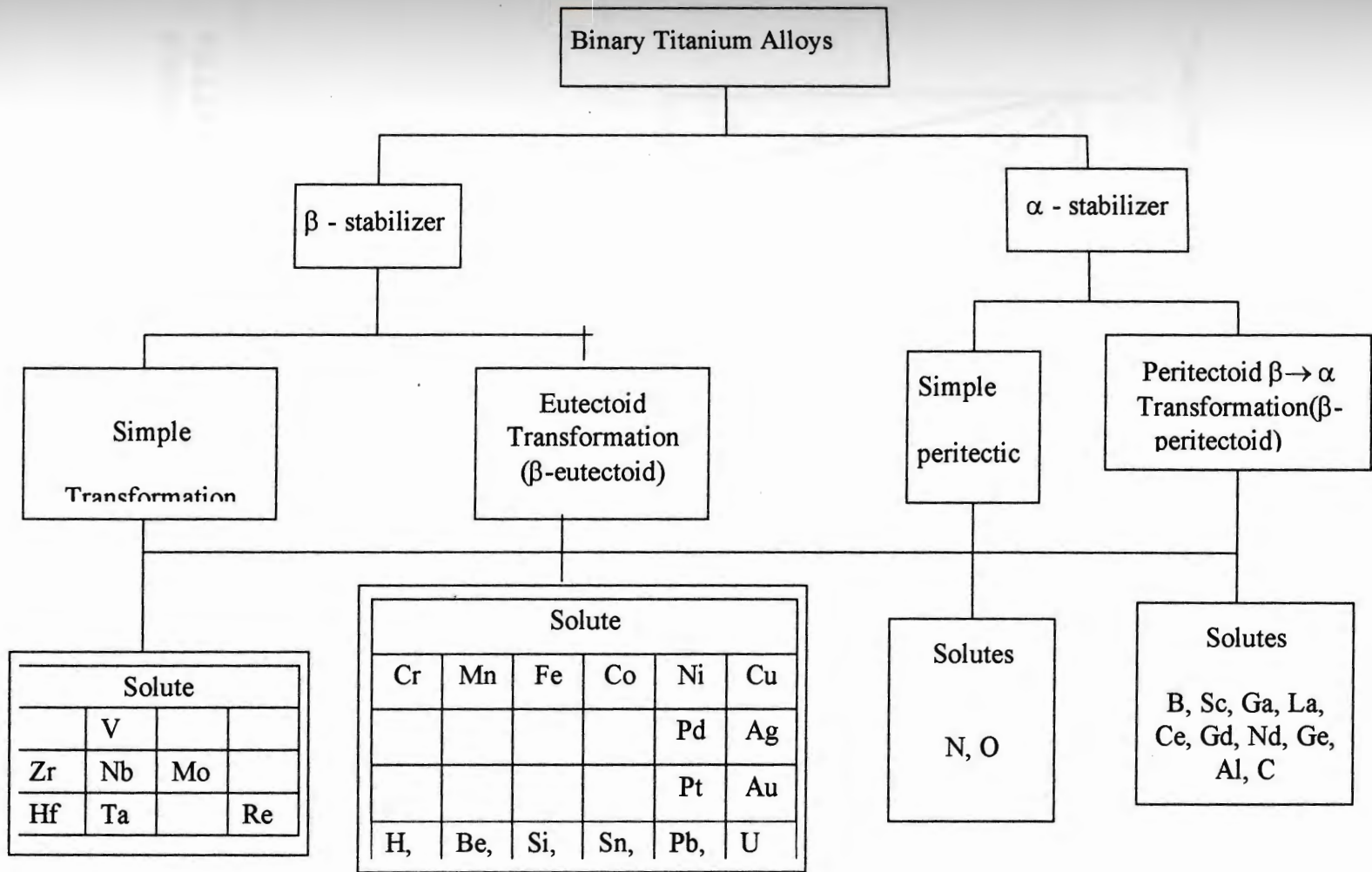


Fig.2.26 – Classification scheme for binary alloys of Titanium [13].

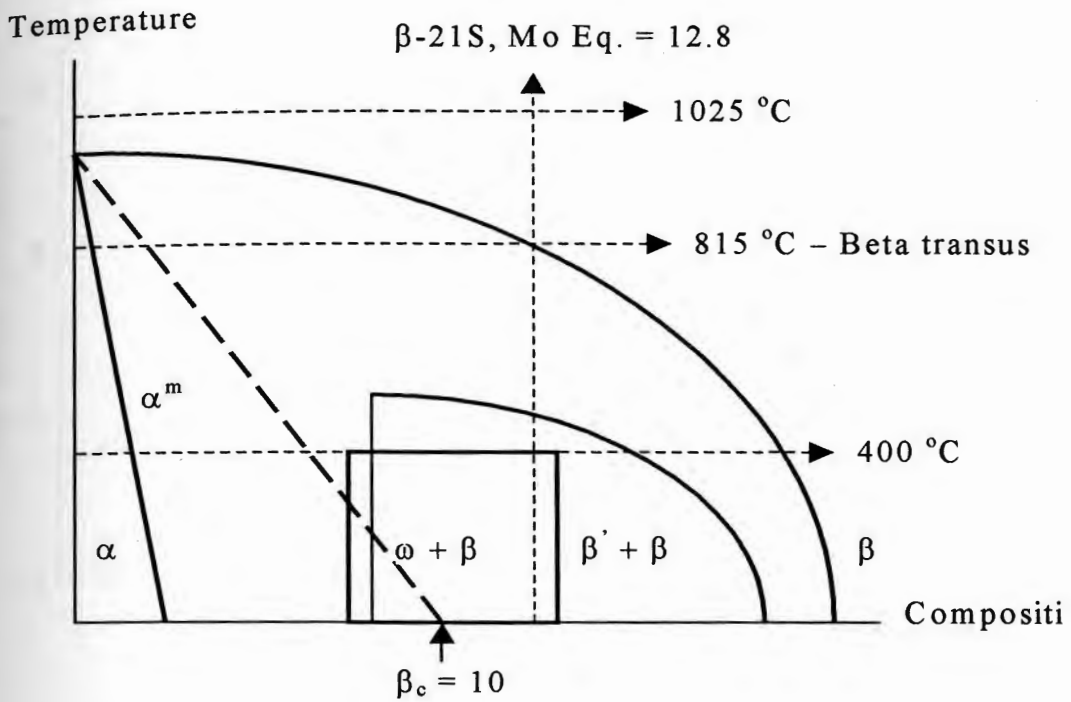


Fig.2.27 – Schematic β -isomorphous phase diagram showing the principal feature of Timetal 21S as function of the temperature.*

* Extracted from "Applied superconductivity, Metallurgy, and Physics of Titanium alloy", edited by E.W.Collings, pp. 54, 1986.

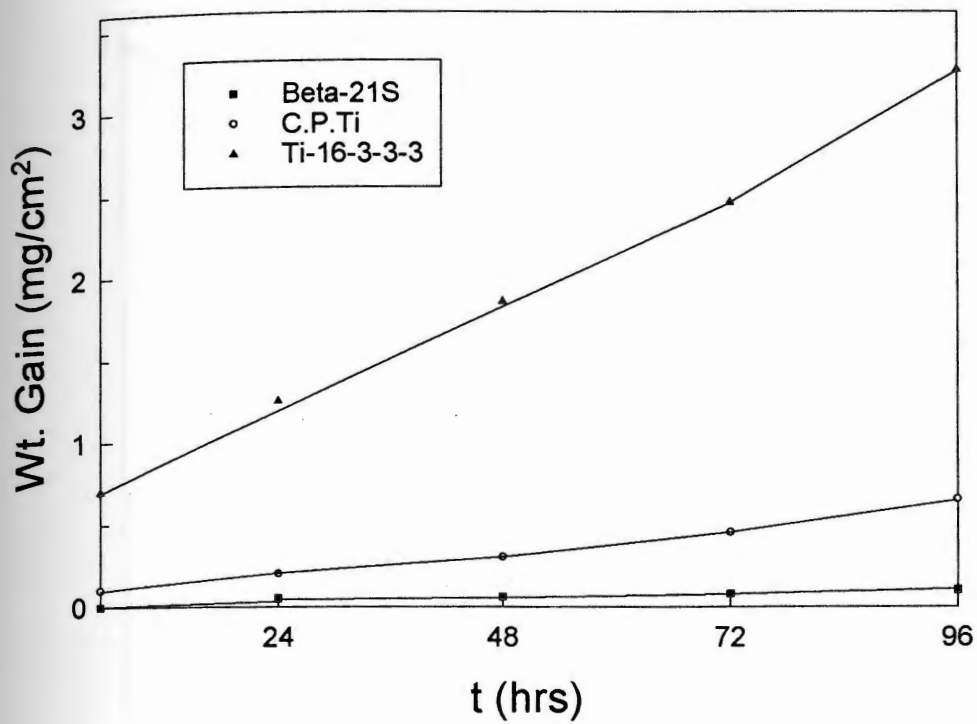


Fig.2.28 – Relative oxidation resistance of beta Titanium alloys in air at 650 °C [1].*

*Extracted from "An Overview of Beta Titanium Alloy Environment Behavior," edited by R. W. Schutz, 1993.

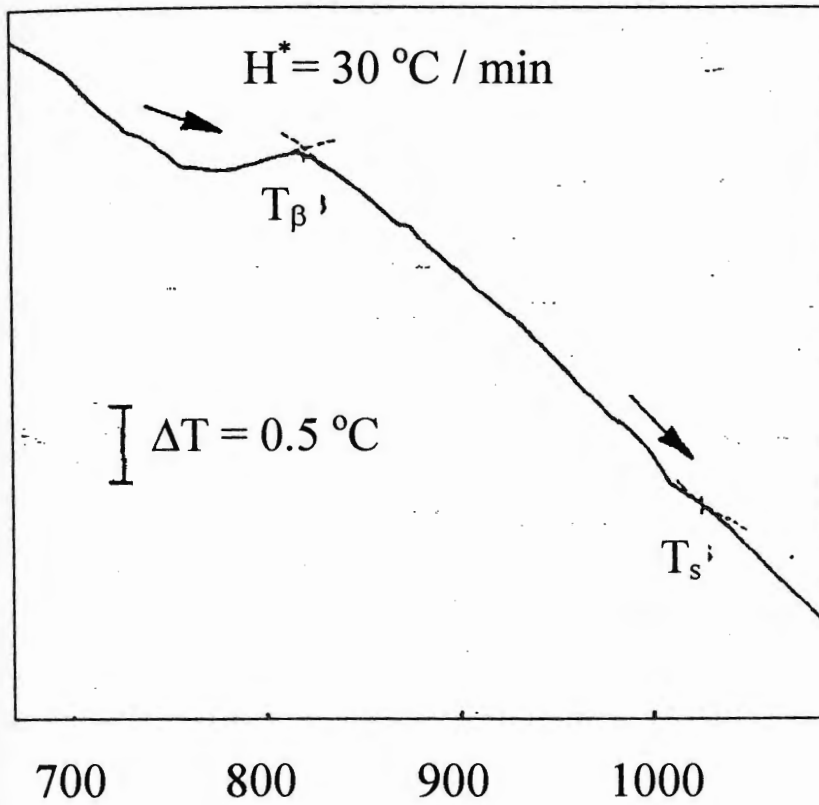


Fig.2.29 – DTA thermogram showing the β transus temperature, T_β , and silicide solvus, T_s , of the Timetal 21S alloy [18].

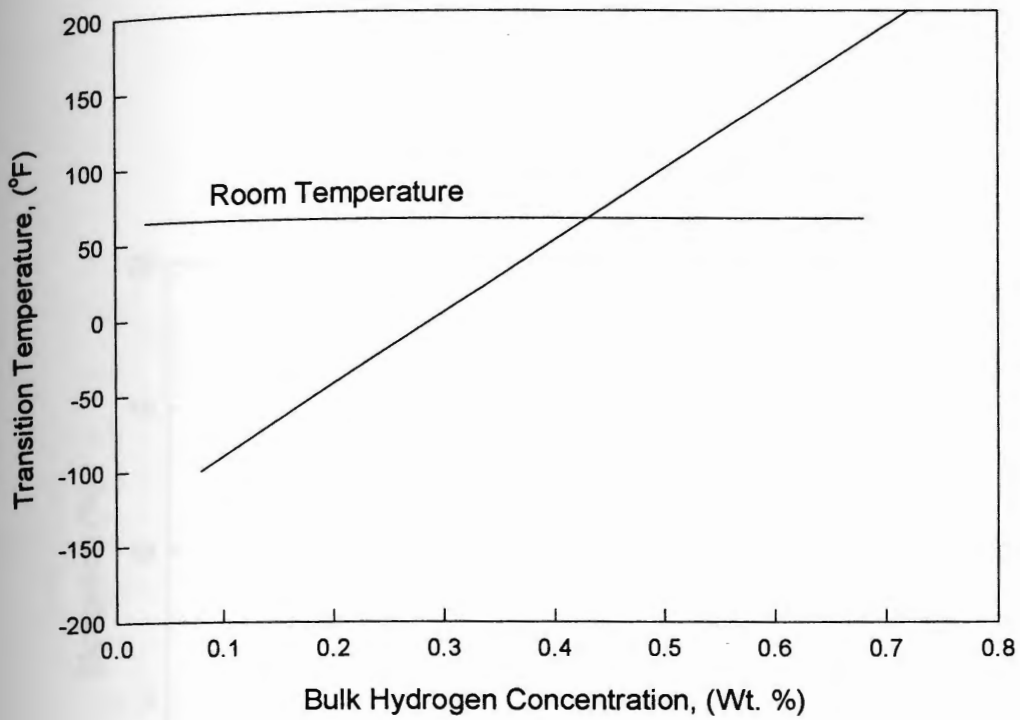


Fig.2.30 – Influence of Hydrogen content on the ductility-to-brittle transition temperature of Timetal 21S.*

* Extracted from "An Overview of Beta Titanium alloy Environment Behavior", Edited by R. W. Schutz, 1993 [1]

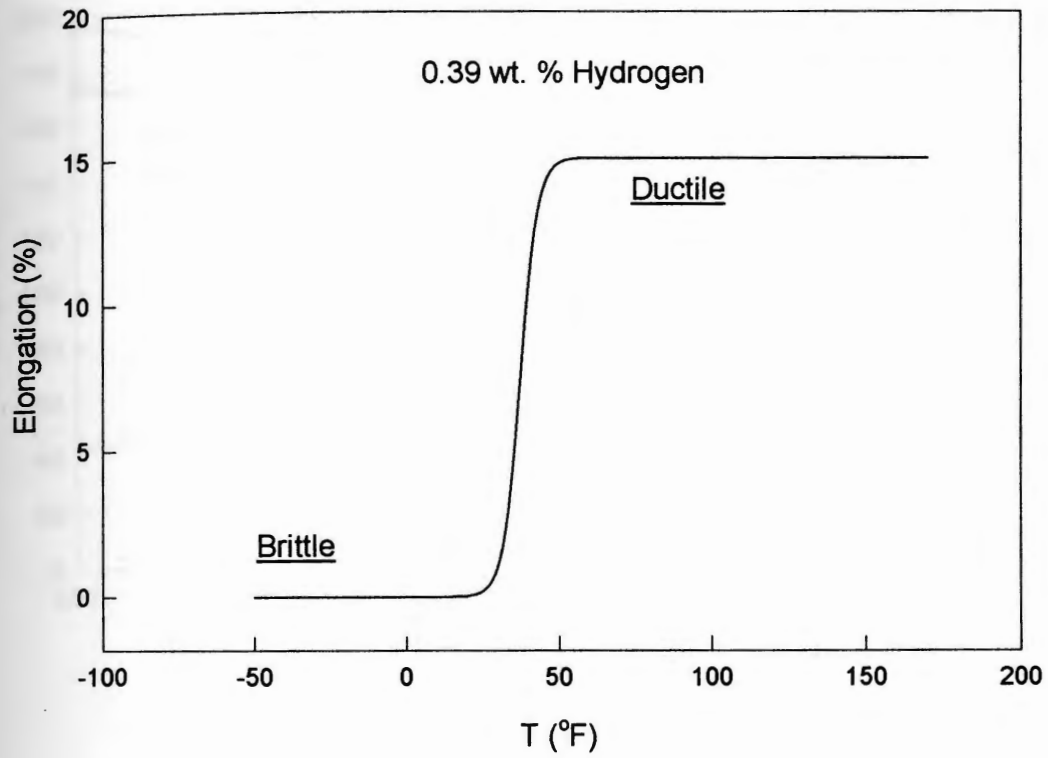


Fig.2.31 – Ductility of brittle behavior of Timetal 21S for 0.39 wt. % Hydrogen.

* Extracted from "An Overview of Beta Titanium alloy Environment Behavior", Edited by R. W. Schutz, 1993 [1]

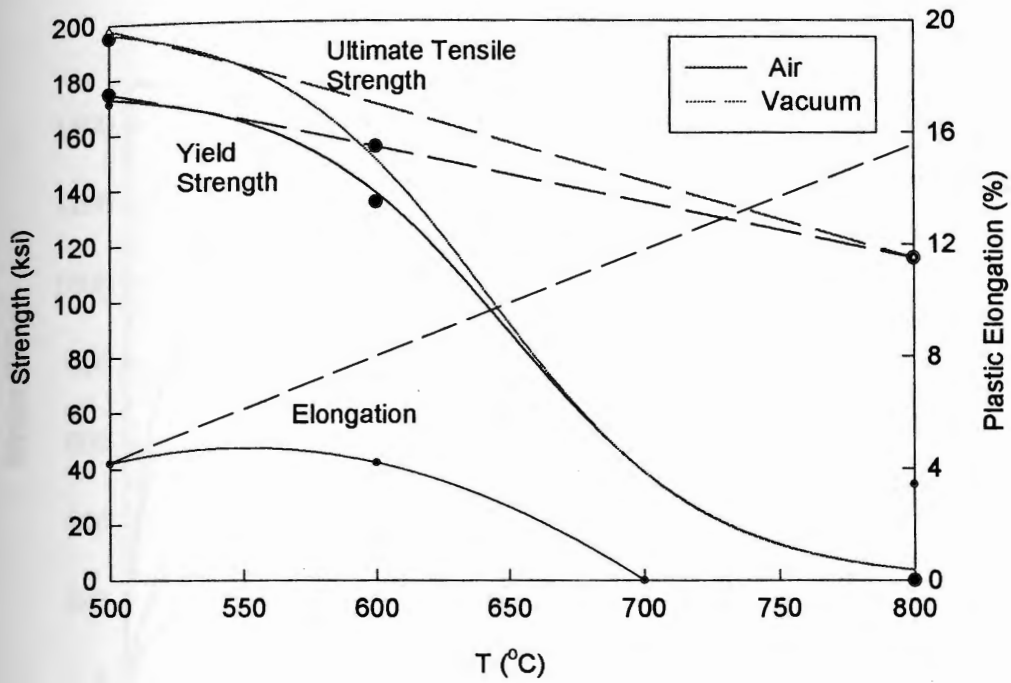


Fig.2.32 – Room-temperature mechanical property data for Timetal 21S after 12 hrs exposure to air at the indicated temperatures. The vacuum data shows the effect of thermal exposure, and the difference between air and vacuum shows the effect of the air environment [1].*

* Extracted from "An Overview of Beta Titanium alloy Environment Behavior", Edited by R. W. Schutz, 1993 [1]

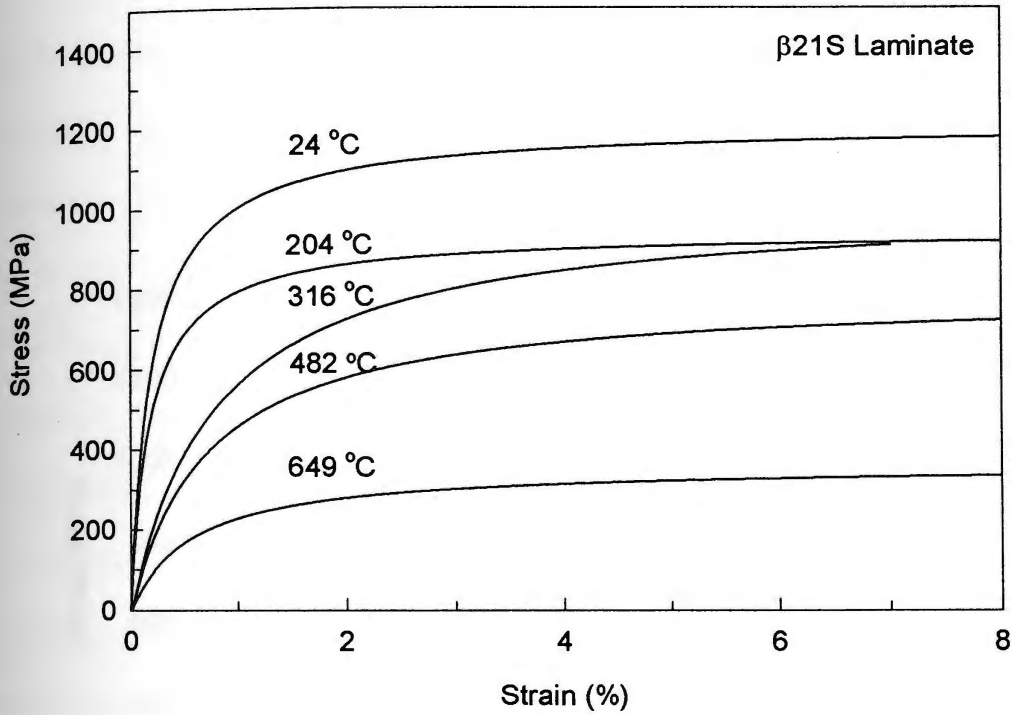


Fig.2. 33 – Stress-Elongation behavior of Timetal 21S as function of the test temperature [27].*

* Extracted from "Effect of Temperature and Frequency on Fatigue Crack Growth in Titanium Beta monolithic Laminate", Edited by Ghonem et al., 1992.

the effect of thermal exposure, and the difference between air and vacuum shows the effect of the air environment [1].*

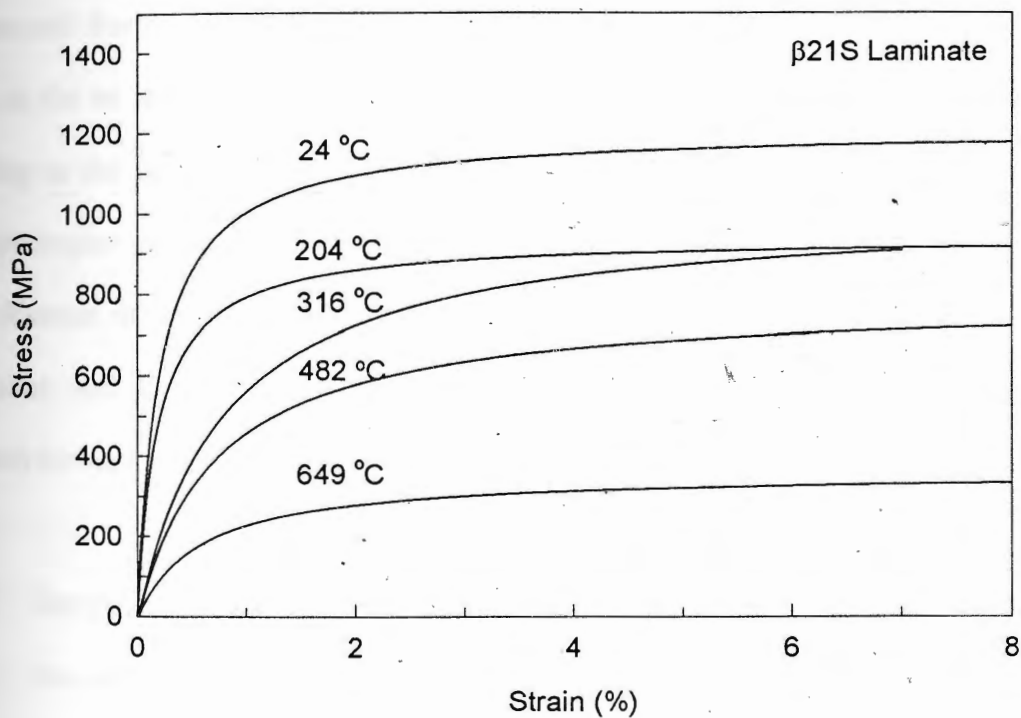


Fig.2. 33 – Stress-Elongation behavior of Timetal 21S as function of the test temperature [27].*

* Extracted from "An Overview of Beta Titanium alloy Environment Behavior", Edited by R. W. Schutz, 1993 [1]

CHAPTER III: EXPERIMENTAL PROCEDURES AND RESULTS

III.1 Introduction

A series of monotonic tensile and fatigue crack growth experiments are carried out on specimens made of β -21S. The important variables in these experiments are the exposure temperature and the time of the exposure. These variables were examined in relation to changes in the specimens' weight gain and ductility measured in terms of the magnitude of the plastic elongation reached prior to the specimen monotonic fracture. This chapter describes the mechanical properties of the Timetal-21S in the as received condition and outlines in details the heat treatment attempts leading to the optimum heat treatment cycle which is applied to the test specimens. Morphologies of microstructures corresponding to each thermal exposure condition and features of fracture surfaces will be detailed in this chapter. The main results, however, will focus on the weight gain, and ductility response and fatigue crack growth for each thermal exposure condition.

III.2 Test Specimen

As mentioned before, the concern of this study is to investigate the effect of thermal exposure on thin specimens of Timetal-21S. Under the exposure conditions that will be studied in this work, the possibility of variations in the specimen's thickness could affect the local size of the alloy microstructure under investigation. In order to account for these effects, specimens with three different thickness are examined here; 0.12, 0.39, and 1.0 mm. This thickness range while covers those used

in the manufacturing of jet duct systems and the engine nacelles structure, is the minimum required for the use in data interpolation.

Fig. 3.1(a) shows the dimensions of the tensile specimens with a gage width of 6.3 mm and a gage length of 30 mm. The corresponding dimensions of the center-notch fatigue crack growth (FCG) specimens, shown in Fig. 3.1(b), are 25 × 30 mm. In both these configurations the longer dimension is taken parallel to the rolling direction of the sheet. All the specimens were cut using both conventional and electro-discharge machining.

All monotonic tests and fatigue crack growth tests were carried out using an automated servo hydraulic testing machine. Details of each of these tests will be described in its corresponding section in this chapter. The procedure for mounting the sheet specimens in the testing machine was the same for the tensile and fatigue crack growth specimens. The same loading grips were used in these mounting procedures. The loading grips consist of a grip frame, two wedges, and a plunger. Two loading grips, lower and upper parts, were required to mount a specimen. The idea of utilizing these loading grips is to transform a hydraulic pressure, which causes a vertical force on the wedges through the plungers to a transverse force, which in turn holds the specimen in a fixed position in the testing machine. This fixed position was based on aligning the loading direction with centerline of the specimen's length. All test specimens were polished with a 600 grit sand paper and checked with optical microscopy for the presence of deep surface scratches, which may cause an early fracture or contribute to the surface contamination during thermal exposure tests.

Monotonic tension tests were carried out on specimens made of the as received material in order to identify the base mechanical properties. Results in terms of the stress-elongation relationship are shown in Fig. 3.2. They indicated a softening behavior, where the stress were decreases as the elongation increases. This ductile response is supported by the morphology of the fracture surface as obtained using scanning electron microscopy; Figs. 3. 4 and 3.5 show ductile dimples across the entire fracture surface. Furthermore, the microstructure of the as received material as shown in Fig. 3.3 indicates the presence of a single beta phase. In order to avoid the occurrence of the softening behavior, a process of heat treatment was carried out. The purpose of the heat treatment is to generate a complex microstructure with the presence of precipitates that could result in both hardening the material and in providing a stable microstructure that exhibit little or no changes during the thermal exposure testing. Details of the efforts carried out to obtain an optimum heat treatment procedure are described in the following section.

III.3 Heat treatment

The approach in selecting a heat treatment (HT) procedure is based on optimizing the corresponding mechanical properties particularly the yield strength and ductility. To achieve this goal, a series of heat treatment cycles were examined. For simplicity, this was done, first, in air environment. The heat treatment cycle was selected on the basis of the corresponding stress-elongation relationship. This was then applied to all test specimens but under vacuum condition. This HT in vacuum was made in order to avoid surface contamination that could occur during heat

treatment and could possibly contribute to errors in the results of the preceding thermal exposure tests.

Fig. 3.6 shows six different heat treatment cycles (A to F) identifying the heating, hold time and cooling segments of each cycle. Fig. 3.7 shows the stress-elongation curves corresponding to each of these cycles. Cycle A in Fig. 3.6 consists of a solution treatment at a 925 °C (the β transus temperature is 815 °C) for one hour followed by a quenching to the room temperature (RT) then aging at 650 °C for 8 hrs followed by another quenching. This heat treatment produces curve 1 in Fig. 3.7, which shows a complete embrittlement (zero ductility). Cycle B consists of a solution treatment at 925 °C for one hour followed by quenching in air to RT. This heat treatment produces curve 2 in Fig. 3.7, which shows a ductility of about 20 % with a slight reduction in the yield stress. Cycles A and B were then modified to cycles D and C, respectively. In cycle C the solution heat treatment was increased to 8 hours. This cycle causes a reduction in the ductility to about 8% and noticeable hardening effects see curve 3 of Figs. 3.7. Cycle D includes an aging treatment without prior quenching to RT after the solutioning part of the cycle. The result of this cycle, curve 4 in Fig. 3.7, shows, that aging causes more loss of ductility than curve C without change in the yield stress. Results of this heat treatment exercise show that quenching after the solution treatment has no effect on the material stress-elongation response. Also, they show that the magnitude of ductility is inversely proportional to the time duration of the solution treatment. Consequently, two additional heat treatment cycles were examined, cycles E and F Fig. 3.6, both of which were carried out in vacuum environment. The variable in these two cycles is the temperature level of the solution

treatment, which was set at or lower than the β transus. This insures that the resulting microstructure would consist of more than one phase. In cycle E, the solution temperature was selected as 833 °C, a little higher than the beta transus, for one hour followed by aging at 650 °C for eight hours. This cycle produced a ductility of 7% and a yield stress of 875 MPa, see curve 5 in Fig. 3.8. Cycle F in Fig. 3.6 consists of a sequence of two aging treatments. The first aging is at 693 °C for 8 hours followed by another aging at 650 °C for eight hours. As shown in curve 6 of Fig. 3.8, this over-aging heat treatment gave a ductility of 11 % along with a yield stress of 980 MPa and a moderate improvement in the hardening coefficient. The improvement in the strength and hardening characteristics are possibly due to the alpha phase precipitation occurring during the aging part in the heat treatment, see the phase diagram in Fig. 3.3. This duplex heat treatment is seen as an optimum cycle and was selected as the one to be applied to all test specimens in this study. The microstructure corresponding to this cycle is shown in Figs. 3.9 – 3.11. In these micrographs, the dark black color represents the alpha phase while the white color represents the beta phase. Fig. 3.9 shows the increase in α phase along the surface of the specimen which probably due to oxygen contamination during the heat treatment. The grain size of this treated material has an average of 18 μm . Figs. 3.10 and 3.11 indicate the uniform distribution of α phase within the microstructure. However the grain boundaries consist of a continuous alpha phase. Fig. 3.12 shows in more detail the microstructure shown in Figs. 3.10 and 3.11.

III.4 Thermal Exposure Tests – Procedure and Results

The program of thermal exposure was carried out in air environment on specimens that have been heat treated with the duplex aging cycle as discussed in the previous section. Five temperatures were selected for these tests; 693, 650, 600, 538 and 482 °C. The first three temperatures represent an upper limit for the use of thin sheets of this alloy while the latter two temperatures represent the application temperature range intended for β -21S. The time duration for exposure at each of these temperatures extended from 0.5 hours to over 150 hours, see Tables 3.1, and 3.2. Prior to the start of the heat treatment, all test specimens were cleaned using fine polishing papers followed by ultrasonic washing. Once the heat treatment is completed, each test specimen was weighed using a digital weight scale with a resolution of 0.1 mg. The furnace temperature was elevated to the required exposure temperature. Once the temperature in the furnace was stabilized, the specimens were put in the furnace for the thermal exposure. This exposure technique was applied to avoid the possible effects of ω phase, as it was shown in the previous chapter 1 that ω phase could be precipitated at temperatures less than 450 °C.

Once a thermal exposure test is completed for a specimen, it was weighed again in order to determine the weight gain due to exposure. This gain was then divided by the specimen's cross-section area to obtain the weight gain as mg/cm^2 . Tables 3.1, 3.2 and 3.3 list the weight gain/area for each of the specimen thickness 1000, 390, and 120 μm respectively. The relationships between the weight gain and exposure time for all temperatures are shown in Figs. 3.13, 3.14 and 3.15 for the 1.0, 0.39 and 0.120 mm specimens, respectively. These curves show that the weight gain

is proportional to exposure temperature and time with the highest gain occurring at the 693 °C. In order to quantify the trends of these curves, they were fitted into a two parameters power equation in the form $W = \alpha t^b$, where, W represents the weight gain due to exposure, t is the exposure time. α and b are two temperature-dependent variables, their values are listed in Tables 3.3, 3.4, and 3.5. It should be noted here, that the regression coefficients of all these fitted curves in Figs. 3.13 – 3.15 ranged from 0.97 to 0.99, which indicate a high accuracy of achieving the fitting constants α and

III.5 Monotonic Tensile Tests – procedure and results

As mentioned before, the main goal of this research is to examine the effects of the thermal exposure on the tensile ductility of the Timetal-21S alloy. To achieve this, each thermally exposed specimen, was subjected to a monotonic tensile test, which provides a stress-elongation relationship for this specific specimen. All the monotonic tests were carried out at room temperature and were continued until the test specimen fractures. In preparation for these tests and in order to determine an appropriate loading rate, which would not induce elongation rate effects, two different loading rates 4.2×10^{-3} mm/sec and 4.2×10^{-2} mm/sec were examined. Figs. 3.16 and 3.17 show the stress–elongation curves of four test specimens tested with these two loading rates. These figures show the effects of these two different loading rates on the yield stress and the elastic modulus. For the case of the 0.120 mm thickness, the high loading rate affects the ductility as shown in Fig. 3.16. As shown in Fig. 3.17, no apparent effects

on the 0.390 mm gage thickness. It was decided to adopt the lower loading rate 4.2×10^{-3} mm/sec in the work performed in this thesis.

All monotonic tensile tests were carried out in air environment at room temperature, using an automated servo-hydraulic material testing machine. This system has a load error of ± 1.3 % and a displacement error of ± 0.02 %. Results of each test were obtained in the form of load versus gage-length displacement. The displacement data were collected using the LVDT attached to the actuator. This procedure was adopted by examining the differences in displacements collected using the LVDT and an elongation transducer attached to a test specimen. As no plastic deformation could occur in any of the specimen grip components within the load level required to fracture any of the test specimen, the ductility data obtained from these two different approaches were considered identical. The LVDT was then selected as an approach to collect the displacement data for all test specimens. The simplicity of this choice, while does not affect the accuracy of the results, permits the completion of a large number of monotonic experiments tests in a reasonable amount of time. Each test was repeated two or three times and results were averaged. The load and the displacement data were used to calculate the stress and the elongation receptively, by using the initial specimen's cross-section. The stress – elongation curves for all the tests carried on the previous thermally exposed specimens are shown in Figs. 3.18 to 3.30. These figures are arranged in terms of the specimen's thickness and exposure temperature. Tables 3.6 – 3.8, list the yield stress and ductility for each of these tests.

III.6 Fatigue Experiments

Specimens were also tested for determining threshold stress intensity factor. The configurations of these specimens are shown in Fig. 3.1. After the specimens were machined, heat-treated, and thermally exposed at temperatures described as shown in Fig. 3.9, they were pre-cracked to a crack length of 50 μm . The threshold was determined using the load shedding technique. These experiments were carried out under loading control conditions using a digitally automated material testing system. All the software and parameters manipulation for these tests are developed in the mechanics of materials laboratory. Once ΔK_{th} is achieved, the same specimen was used to determine the subcritical crack growth rate (da / dN) versus ΔK . Results of crack growth experiments are shown in Fig. 3.31

Table 3. 1- The weight gain in 1.0 mm tensile specimens as function of the exposure parameters. (t: exposure time, W_b: specimen's weight before exposure, W_a: specimen's weight after exposure, A: exposed surface area each specimen, W: weight gain due to exposure.

| Spec. # | T (°C) | t (hrs) | W _b (g) | W _a (g) | W=W _a -W _b (g) | A (cm ²) | W (mg/cm ²) |
|---------|--------|---------|--------------------|--------------------|---|----------------------|-------------------------|
| 1 | 482 | 45.5 | 6.0566 | 6.0581 | 0.0015 | 27 | 0.06 |
| 2 | | 111.5 | 7.0176 | 7.0204 | 0.0028 | 31 | 0.09 |
| 3 | | 156.5 | 6.8538 | 6.8570 | 0.0032 | 31 | 0.1 |
| 4 | 538 | 40 | 6.0878 | 6.0907 | 0.0029 | 27 | 0.11 |
| 5 | | 40 | 6.1549 | 6.1575 | 0.0026 | 27 | 0.096 |
| 6 | | 100 | 6.9567 | 6.9600 | 0.0033 | 31 | 0.107 |
| 7 | | 100 | 6.0242 | 6.0272 | 0.0030 | 31 | 0.097 |
| 8 | | 163 | 6.1670 | 6.1703 | 0.0033 | 27 | 0.12 |
| 9 | 600 | 80 | 6.1597 | 6.1644 | 0.0047 | 27 | 0.17 |
| 10 | | 80 | 6.1625 | 6.1674 | 0.0049 | 27 | 0.18 |
| 11 | | 40 | 6.1696 | 6.1729 | 0.0033 | 27 | 0.12 |
| 12 | | 40 | 6.1560 | 6.1593 | 0.0033 | 27 | 0.12 |
| 13 | | 151.5 | 6.1549 | 6.1604 | 0.0055 | 27 | 0.20 |
| 14 | | 151.5 | 6.1547 | 6.1602 | 0.0055 | 27 | 0.204 |
| 15 | 650 | 40 | 6.1595 | 6.1658 | 0.0063 | 27 | 0.23 |
| 16 | | 40 | 6.1637 | 6.1699 | 0.0062 | 27 | 0.23 |
| 17 | | 85.5 | 6.1503 | 6.1588 | 0.0085 | 27 | 0.32 |
| 18 | | 85.5 | 6.1668 | 6.1752 | 0.0084 | 27 | 0.31 |
| 19 | | 118 | 6.1608 | 6.1704 | 0.0096 | 27 | 0.36 |
| 20 | | 118 | 6.1555 | 6.1649 | 0.0094 | 27 | 0.35 |
| 21 | 693 | 40 | 6.8841 | 6.8954 | 0.0113 | 31 | 0.37 |
| 22 | | 80 | 6.9671 | 6.9918 | 0.0247 | 31 | 0.77 |
| 23 | | 53 | 6.8499 | 6.8623 | 0.0124 | 31 | 0.4 |

Table 3.2- The weight gain in the 0.39 mm tensile specimens as function of exposure parameters. (t: exposure time, W_b : specimen's weight before exposure, W_a : specimen's weight after exposure, A: exposed surface area each specimen, W: weight gain due to exposure).

| Spec. # | T (°C) | t (hrs) | W_b (g) | W_a (g) | W_{gain} (mg.) | W_{gain} (mg/cm ²) |
|---------|--------|---------|-----------|-----------|------------------|----------------------------------|
| 1 | 482 | 100 | 2.386 | 2.3885 | 2.5 | 0.09 |
| 2 | | 20.0 | 2.3885 | 2.3897 | 1.2 | 0.04 |
| 3 | 538 | 5.00 | 2.3907 | 2.3918 | 1.1 | 0.041 |
| 4 | | 20.0 | 2.3744 | 2.3763 | 1.9 | 0.07 |
| 5 | | 100 | 2.4479 | 2.4502 | 2.3 | 0.09 |
| 6 | 600 | 40.0 | 2.3871 | 2.3898 | 2.7 | 0.1 |
| 7 | | 20.0 | 2.4456 | 2.4479 | 2.3 | 0.09 |
| 8 | | 100 | 2.3836 | 2.3882 | 4.6 | 0.7 |
| 9 | 650 | 2.00 | 2.3886 | 2.3906 | 2.0 | 0.074 |
| 10 | | 5.00 | 2.384 | 2.3867 | 2.7 | 0.1 |
| 11 | | 20.0 | 2.3857 | 2.3902 | 4.5 | 0.17 |
| 12 | | 80.0 | 2.395 | 2.4028 | 7.8 | 0.29 |
| 13 | 693 | 00.5 | 2.3858 | 2.3878 | 2.0 | 0.07 |
| 14 | | 5.00 | 2.44 | 2.4449 | 4.9 | 0.18 |
| 15 | | 5.00 | 2.3854 | 2.39 | 4.6 | 0.17 |

Table 3.3– Ductility as read from the Stress-Elongation curves of 1.0 mm thickness at different aging parameters. (T: exposure temperature, t: exposure time, d: remaining elongation, σ : yield strength)

| T (°C) | t (hrs) | d (%) | σ (MPa) |
|--------|---------|-------|----------------|
| 538 | 40 | 12.2 | 1030 |
| | 100 | 11 | 1030 |
| | 163 | 9.8 | 1070 |
| | 862 | 8.5 | 1015 |
| 600 | 40 | 11.1 | 1030 |
| | 80 | 9.9 | 1030 |
| | 150 | 8 | 1030 |
| | 700 | 3 | 1030 |
| 650 | 40 | 6.3 | 1010 |
| | 85.5 | 3.6 | 980 |
| | 118 | 2.7 | 980 |
| | 500 | 0.0 | 810 |
| 693 | 40 | 1 | 920 |
| | 80 | 0.3 | 910 |
| | 186 | 0.0 | |

Table 3.4– Ductility as read from the stress-elongation curves of 0.39 mm sheet thickness at different aging parameters

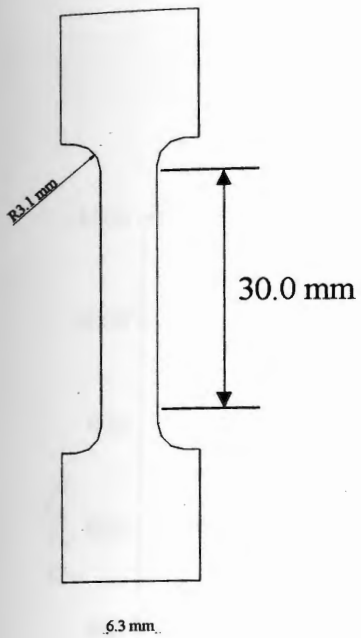
| T (°C) | t (hrs) | σ (MPa) | d (%) |
|--------|---------|-------------------|-------|
| 482 | 24 | 930 | 5.8 |
| | 111.5 | 920 | 5.25 |
| 538 | 20 | 1010 | 5.9 |
| | 41.5 | 1010 | 5 |
| | 116 | 1010 | 4.6 |
| 650 | 5 | 950 | 4 |
| | 20 | 950 | 2.8 |
| | 80 | 950 | 2.2 |
| 693 | 12 | 900 | 1.5 |

Table 3.5– Ductility as read from the stress-elongation curves for sheet thickness 0.12 mm at different aging parameters

| T (°C) | t (hrs) | σ (MPa) | d (%) |
|--------|---------|----------------|-------|
| 482 | 20 | 900 | 0.9 |
| | 39 | | 0.65 |
| | 50 | | 0.42 |
| | 100 | | 0.36 |
| 538 | 5 | 900 | 0.8 |
| | 52 | | 0.35 |
| | 100 | | 0.2 |
| 594 | 5 | 930 | 0.5 |
| | 15 | | 0.4 |
| | 34 | | 0.15 |
| 650 | 5 | 940 | 0.45 |
| | 10 | | 0.12 |
| | 20 | | 0 |
| 693 | 1 | 900 | 0.6 |
| | 2 | | 0.13 |
| | 3 | | 0 |

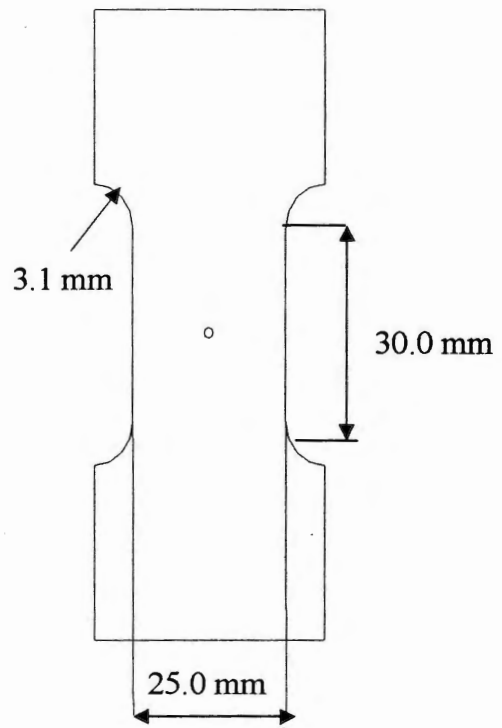
Table 3.6– Exposure Conditions of fatigue crack growth Specimens.

| Test Temp. C | Spec. thickness (mm) | T (°C) | t (hrs) | 0.12 (mm). | 0.4 (mm) | 1 mm | Spec. # | |
|---|-------------------------|--------|--------------|------------|----------|------|----------|----------|
| RT | 0.12 | 0 | 0 | 1 | | | | |
| | | 538 | 22,41,5,81 | 3 | | | 46,47,48 | |
| | | 650 | 3,11,24 | 3 | | | 34,36,38 | |
| | | 693 | 1,3,25,7 | 3 | | | 40,42,44 | |
| | 0.4 | 0 | 0 | | | 1 | | |
| | | 538 | 20,40,80 | | | 3 | | 10,11,12 |
| | | 650 | 5,20,50 | | | 3 | | 1,3,5 |
| | | 693 | 3,11,19 | | | 3 | | 20,18,16 |
| | 1 | 0 | 0 | | | | 1 | |
| | | 538 | 40,100,200 | | | | 3 | 13,14,15 |
| | | 650 | 46.5,107,146 | | | | 3 | 28,30,32 |
| | | 693 | 19,40,115 | | | | 3 | 22,24,26 |
| 538 | 0.12 | 650 | 3,11,24 | 3 | | | 35,37,39 | |
| | | 693 | 1,3,25,7 | 3 | | | 41,43,45 | |
| | 0.4 | 650 | 5,20,50 | | | 3 | | 2,4,6 |
| | | 693 | 3,11,19 | | | 3 | | 21,19,17 |
| | 1 | 650 | 46.5,107,146 | | | | 3 | 29,31,33 |
| | | 693 | 19,40,115 | | | | 3 | 23,25,27 |
| Total Spec. for each gage | | | | 16 | 16 | 16 | | |
| Note 1) Specimen number in order with its aging time. 2) Specimen thickness 0.12mm is a mechanical conventional not EDM cut | | | | | | | | |



Tensile Specimen

(a)



Fatigue Specimen

(b)

Fig. 3.1 - The tensile specimen and the center cracked tension fatigue specimen (CCT).

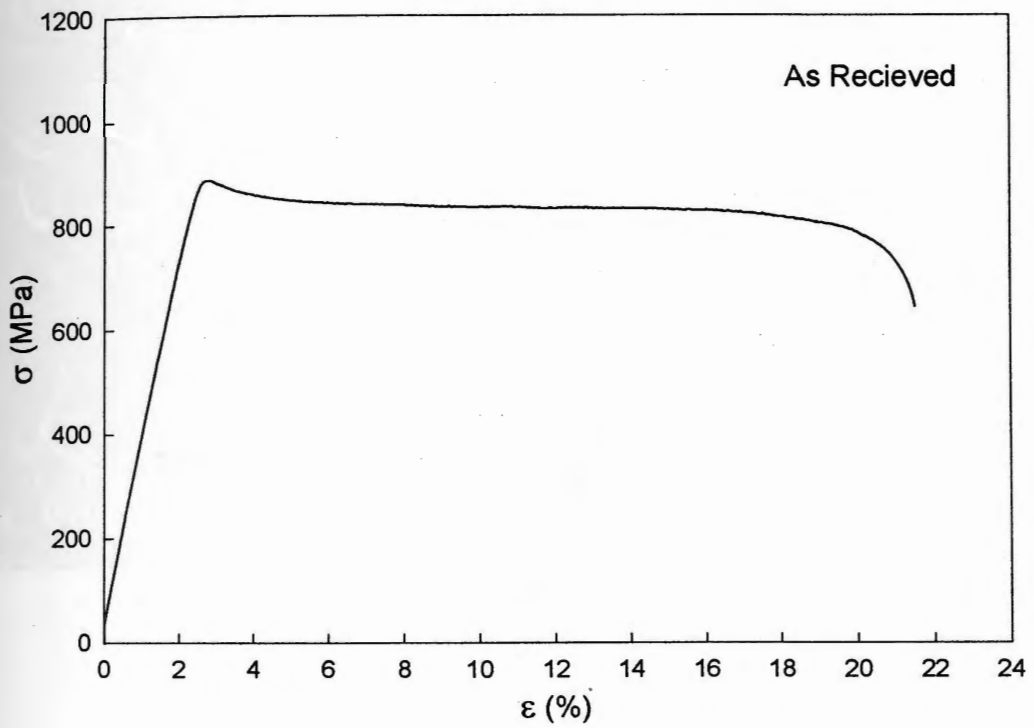


Fig. 3.2- Stress-elongation curve of the as received Timetal-21S material

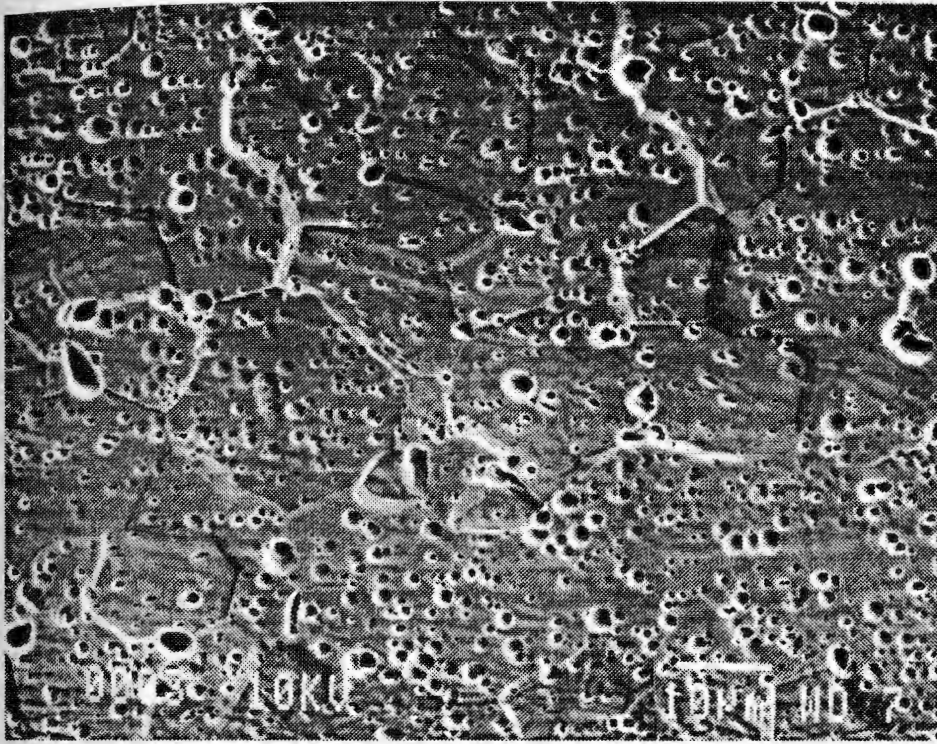


Fig. 3.3 – Morphology of the as received Timetal – 21S microstructure (β phase)

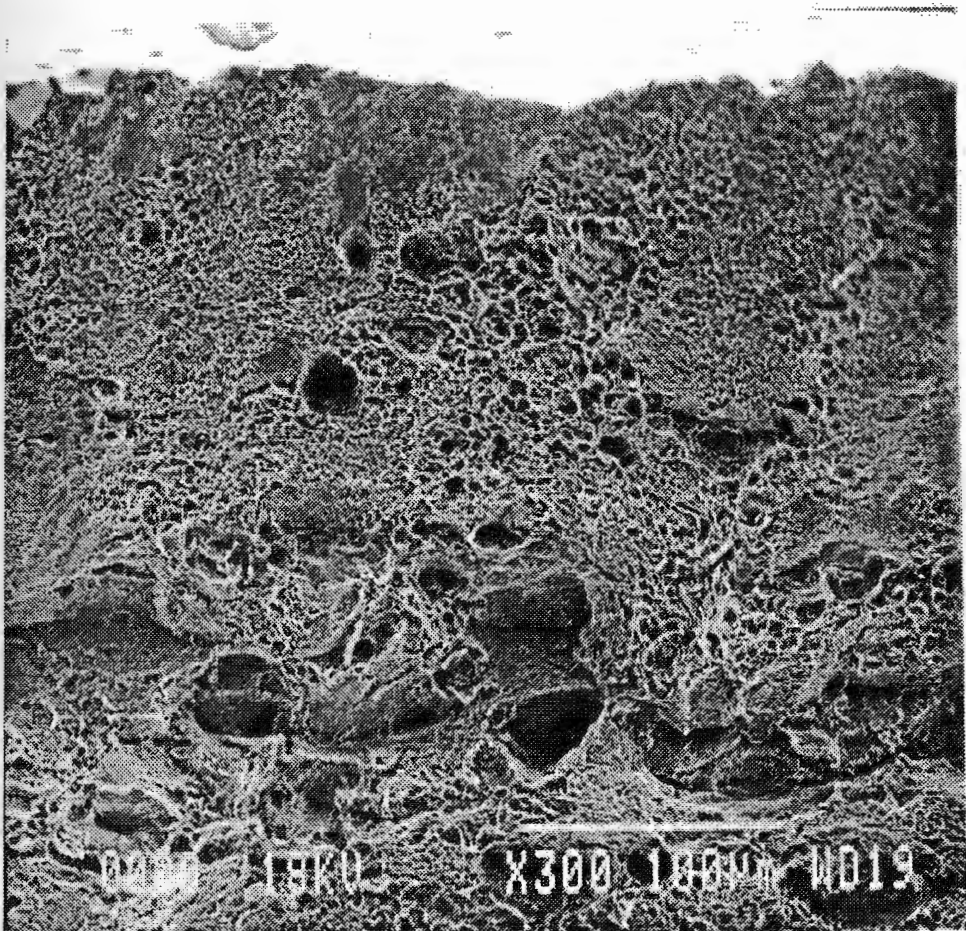


Fig. 3.4 – Ductile surface of the as received Timetal – 21S tensile – fractured specimen.

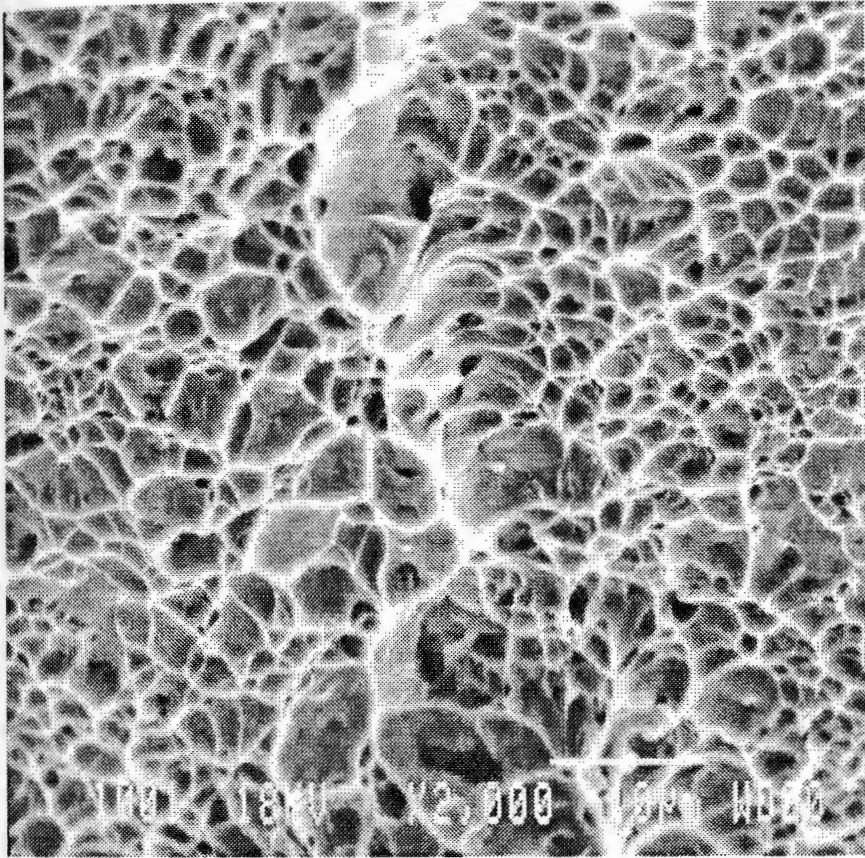


Fig. 3.5 – Dimples of the ductile surface of the as received Timetal – 21S tensile – fractured specimen

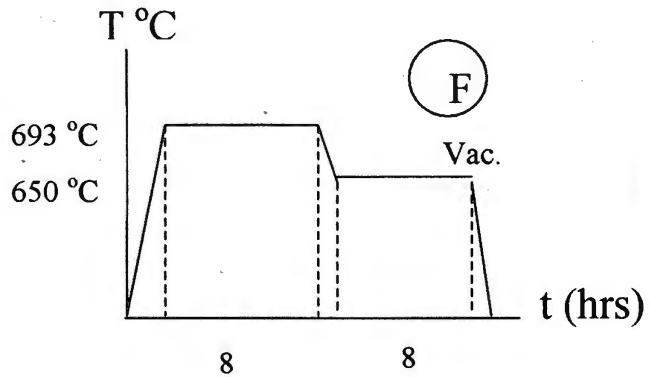
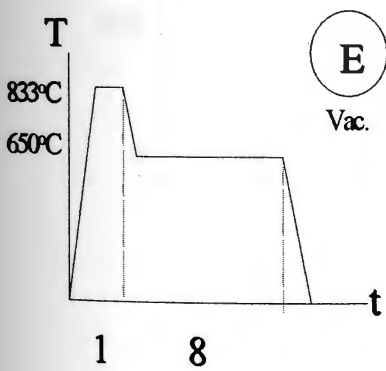
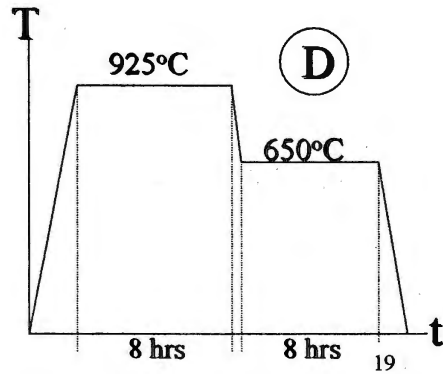
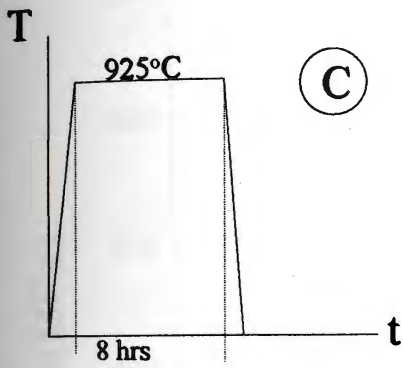
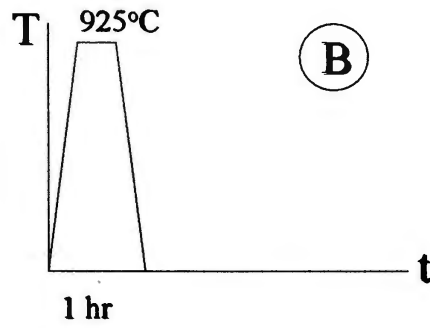
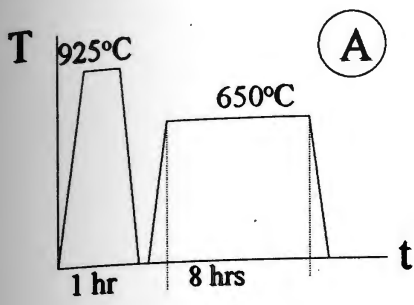


Fig. 3.6 – Heat treatment cycles

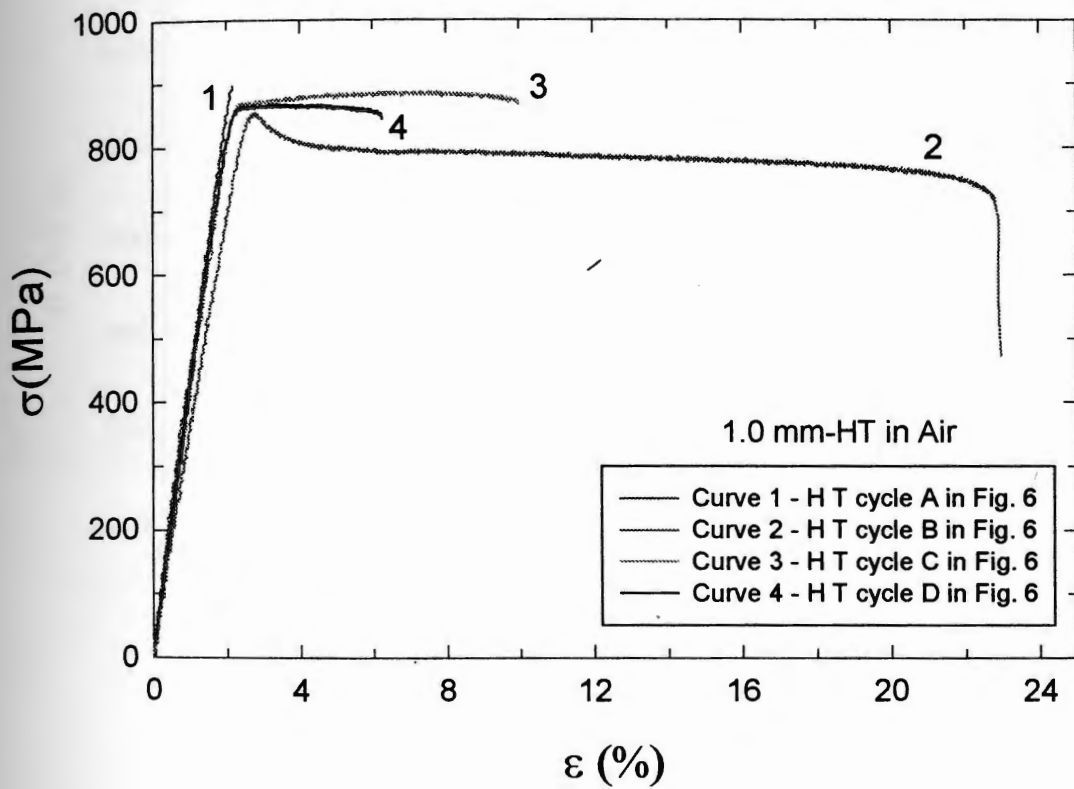


Fig. 3.7 – The stress – elongation curves of Timetal – 21S as function of different heat treatment cycles in air.

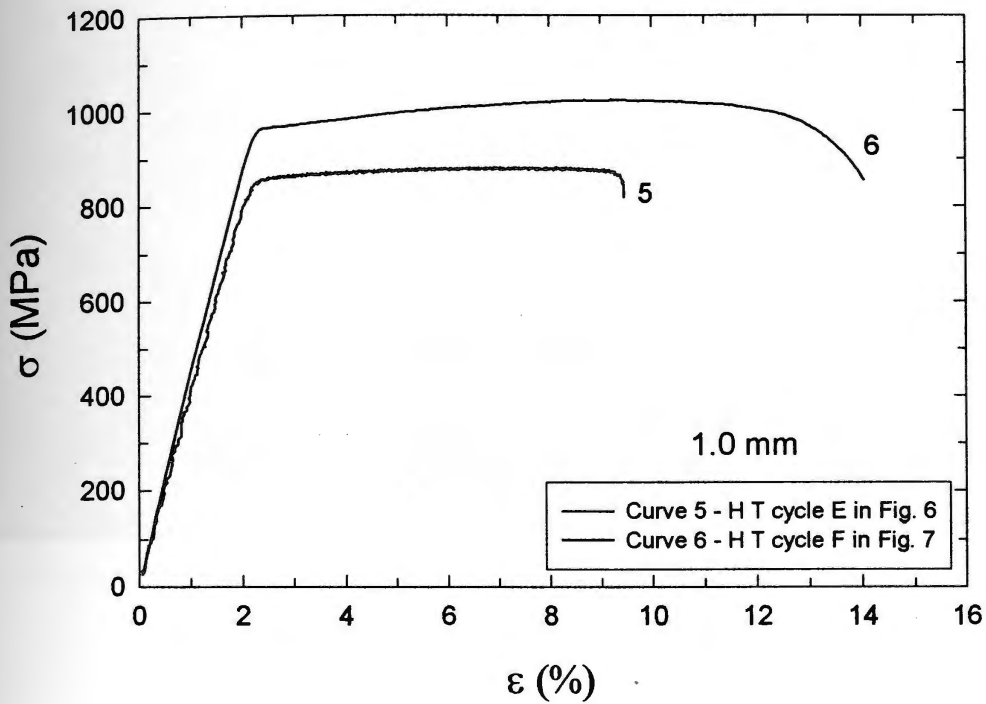


Fig. 3.8 – The stress – elongation curves of Timetal – 21S as function of different heat treatment cycles in vacuum.

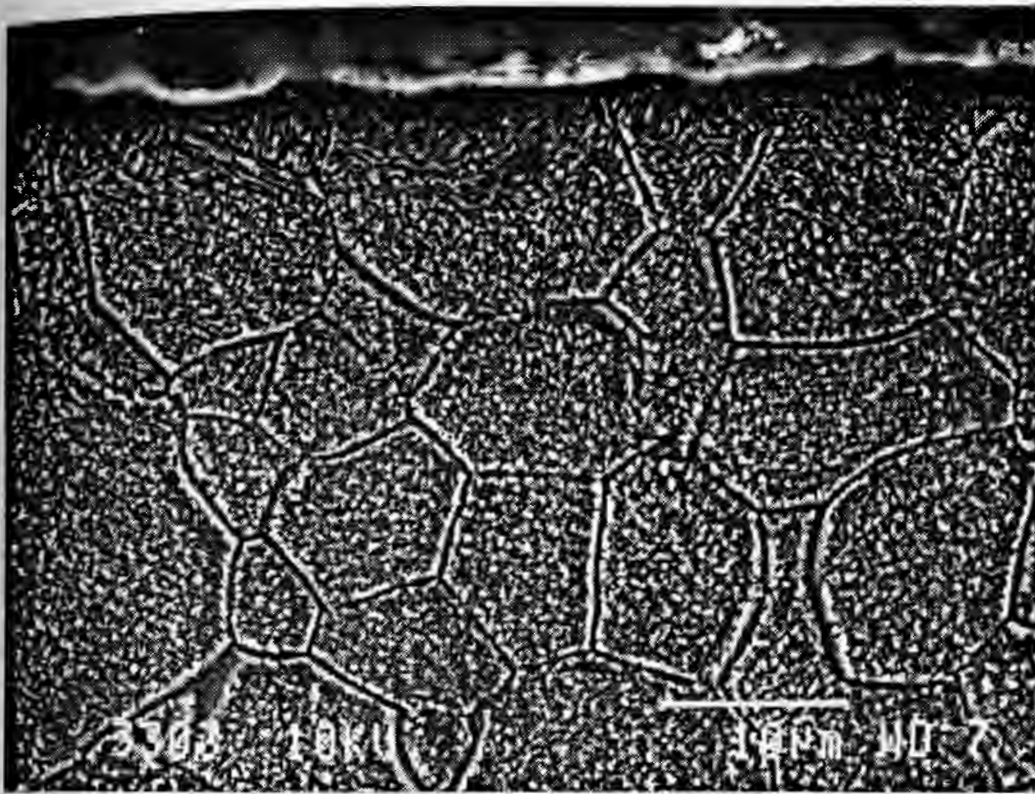


Fig. 3.9 – The microstructure of Timetal 21S close to surface of the heat – treated specimen, where alpha phase is the dark black color, and beta phase is the rest.

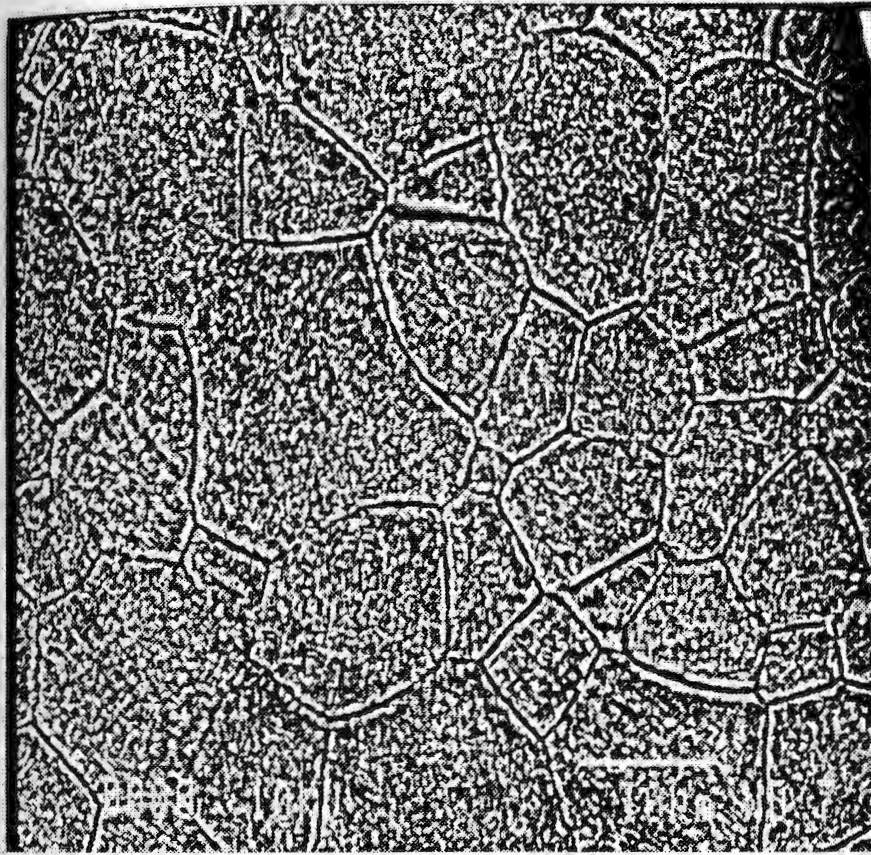


Fig. 3.10 – The microstructure of Timetal 21S in the bulk of heat – treated specimen, where alpha phase is the dark black color, and beta phase is the rest.

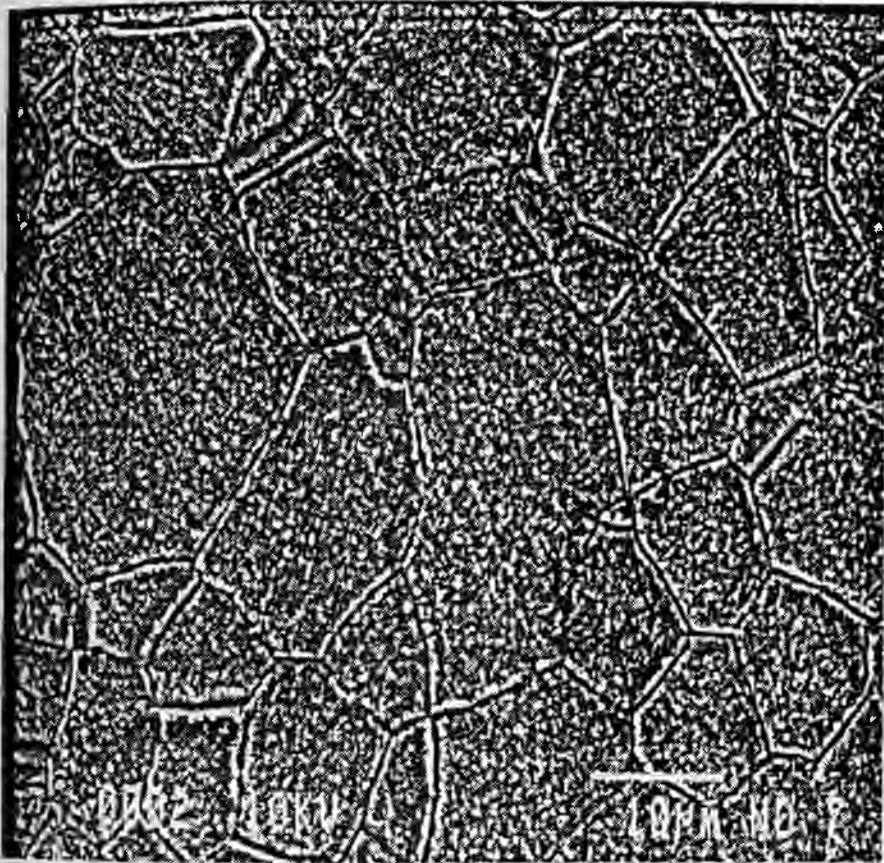


Fig. 3.11 – The microstructure of Timetal 21S in the bulk of heat-treated specimen, where alpha phase is the dark black color, and beta phase is the rest.

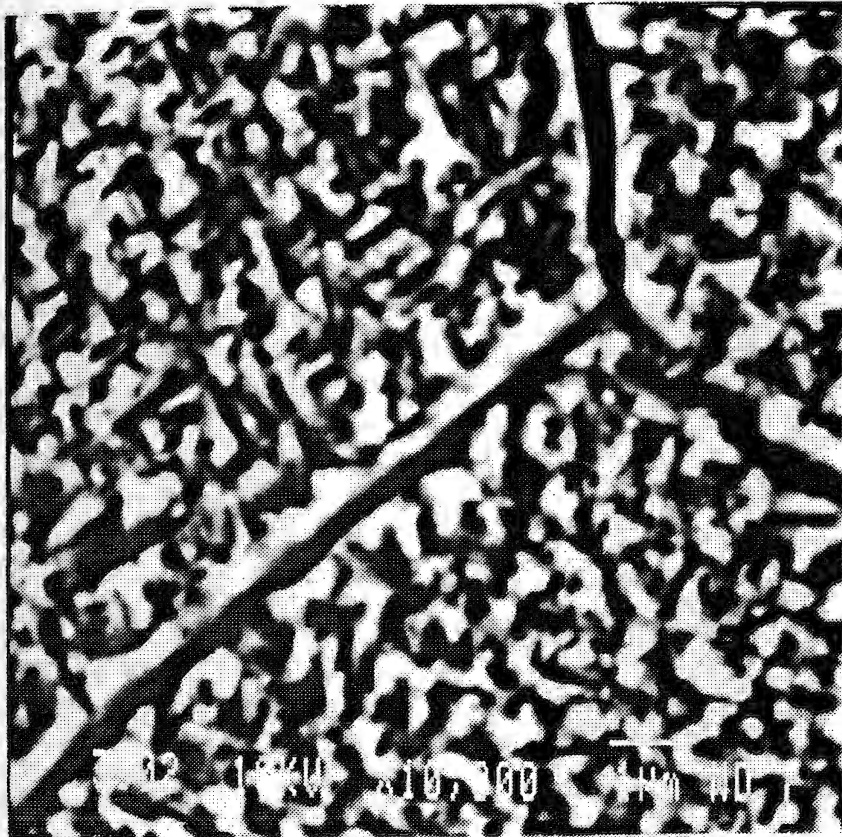


Fig. 3.12 – Shows the microstructure with a magnification of X 10,000 in the bulk of Timetal 21S heat – treated specimen, where alpha phase is the dark black color, and beta phase is the rest.

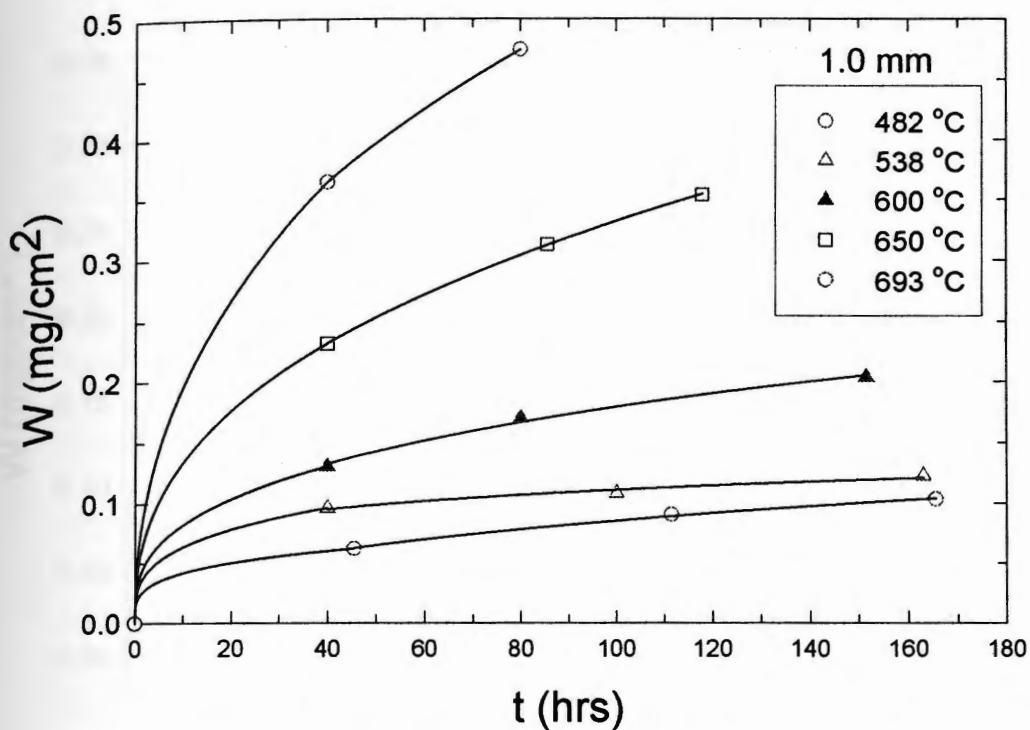


Fig. 3.13– The weight gain in the 1.0 mm specimens as function of the exposure temperature and time.

Table 3.7– α and β two constants of the power equation $W = \alpha t^b$ to fit the weight gain – time data in Fig. 3.13

| T | α | b |
|-----|----------|--------|
| 482 | 0.0139 | 0.3934 |
| 538 | 0.0505 | 0.1705 |
| 600 | 0.0392 | 0.33 |
| 650 | 0.0545 | 0.3926 |
| 693 | 0.0899 | 0.3794 |

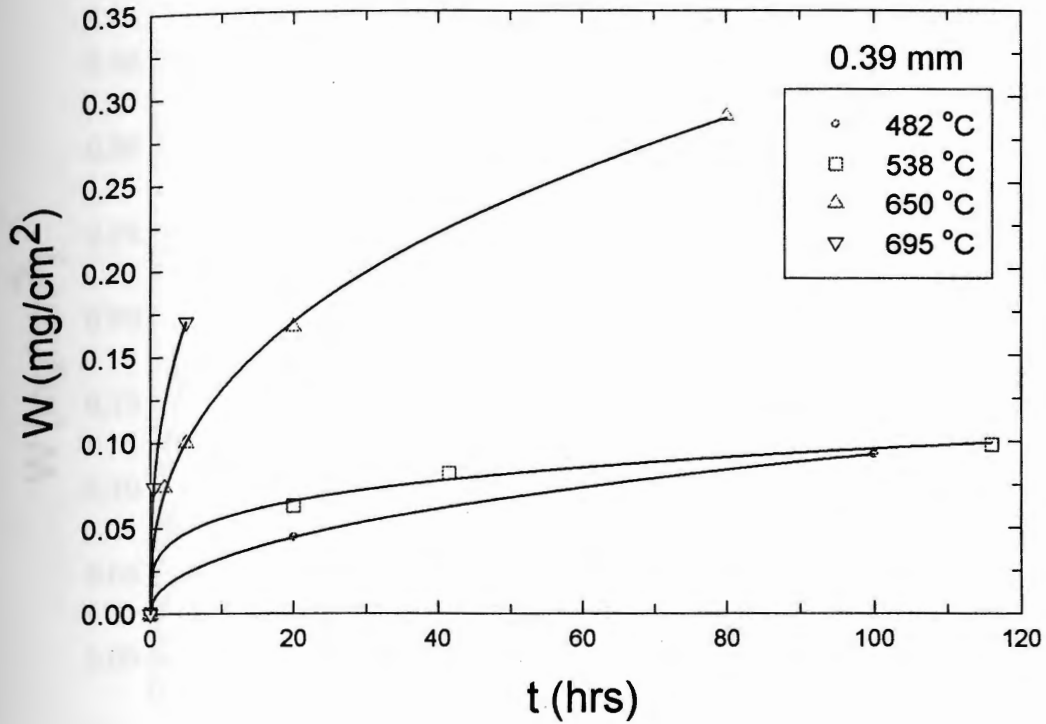


Fig. 3.14 – The weight gain in the 0.39 mm specimens as function of the exposure time and temperature.

Table 3.8– α and β two constants of the power equation $W = \alpha t^b$ to fit the weight gain–time data in Fig. 3.14

| T | α | b |
|-----|----------|--------|
| 482 | 0.0139 | 0.3934 |
| 538 | 0.0505 | 0.1705 |
| 650 | 0.0545 | 0.3926 |
| 693 | 0.0899 | 0.3794 |

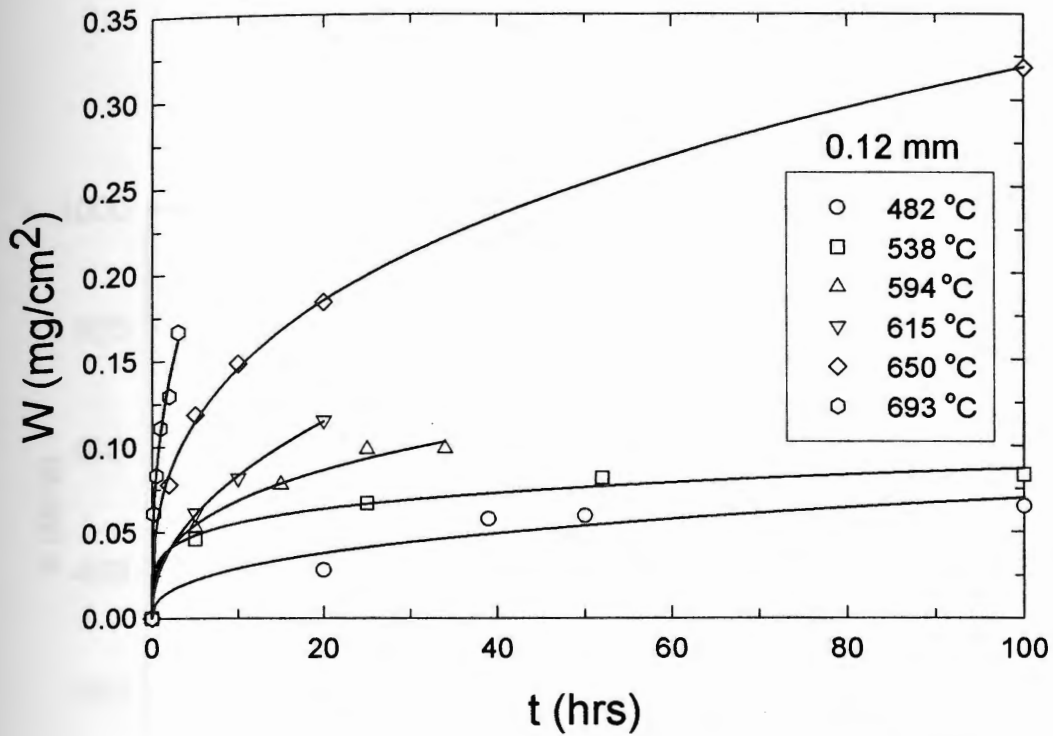


Fig. 3.15– The weight gain in the 0.12 mm specimens as function of the exposure time and temperature.

Table 3.9– α and β two constants of the power equation $W = \alpha t^b$ to fit the weight gain – time data in Fig. 3.15

| T | α | b |
|-----|----------|--------|
| 482 | 0.0124 | 0.3772 |
| 538 | 0.0354 | 0.1957 |
| 600 | 0.0319 | 0.3315 |
| 650 | 0.0668 | 0.34 |
| 693 | 0.1075 | 0.3666 |

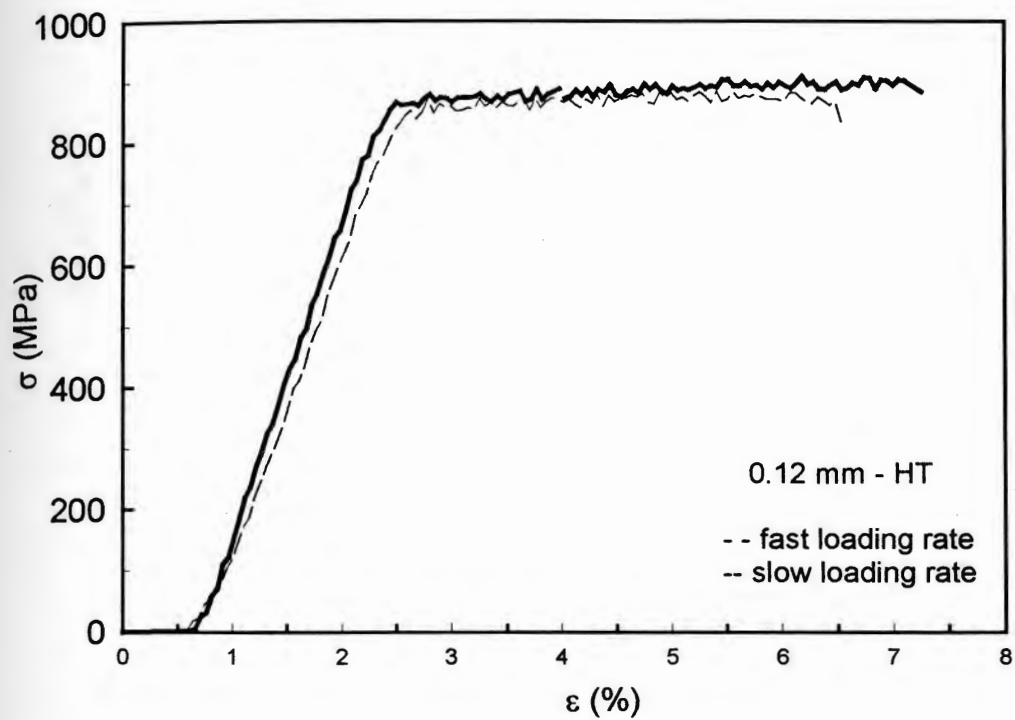


Fig. 3.16 – Shows the stress – elongation curves as function of the loading rate for 0.12 mm thickness of Timetal 21S sheets

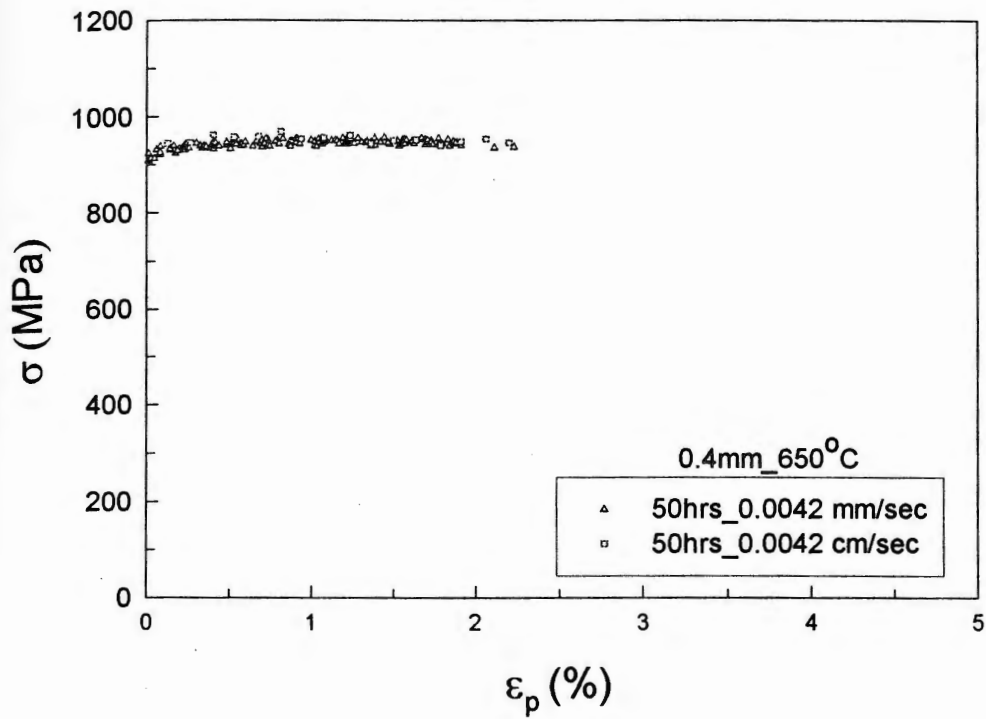


Fig. 3.17 – Shows the stress – elongation curves as function of the loading rate for 0.39 mm thickness of Timetal 21S sheets

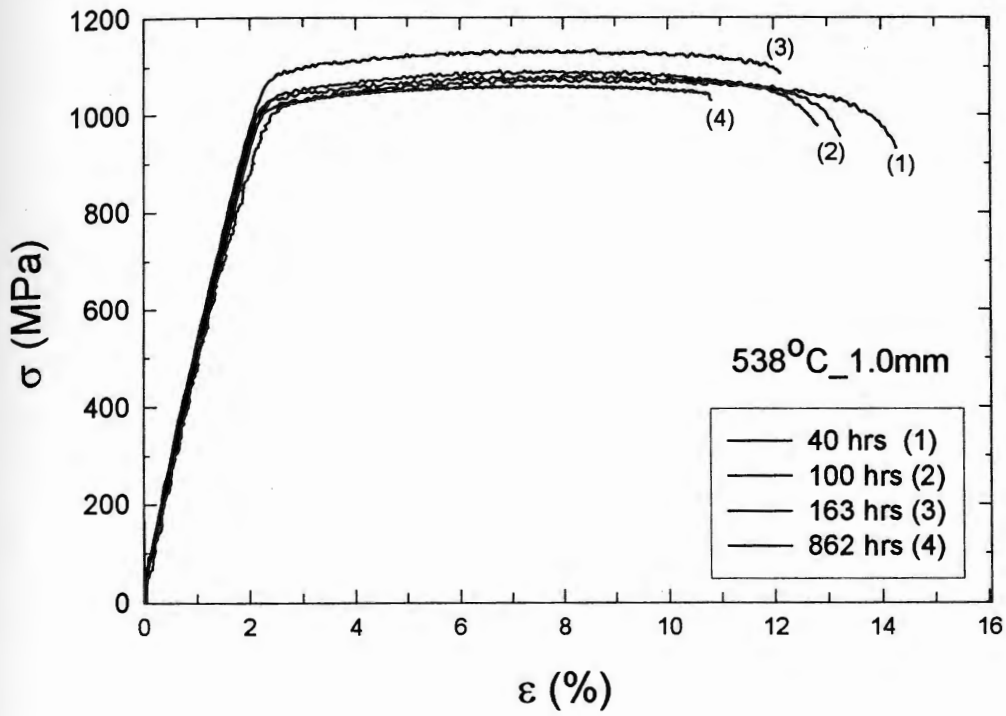


Fig. 3.18 – Stress – elongation curves for Timetal 21S – 1.0 mm thickness specimens with over – aging heat treatment then exposure in air at temperature 538 °C.

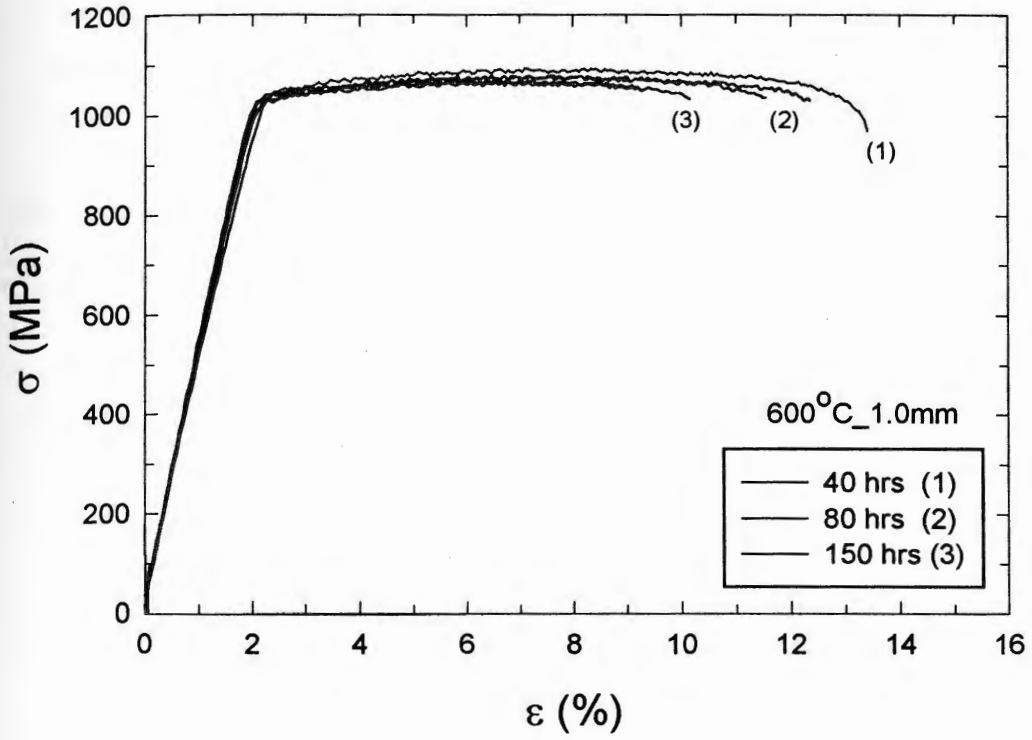


Fig. 3.19 – Stress – elongation curves for Timetal 21S – 1.0 mm thickness specimens with over – aging heat treatment then exposure in air at temperature 600 °C.

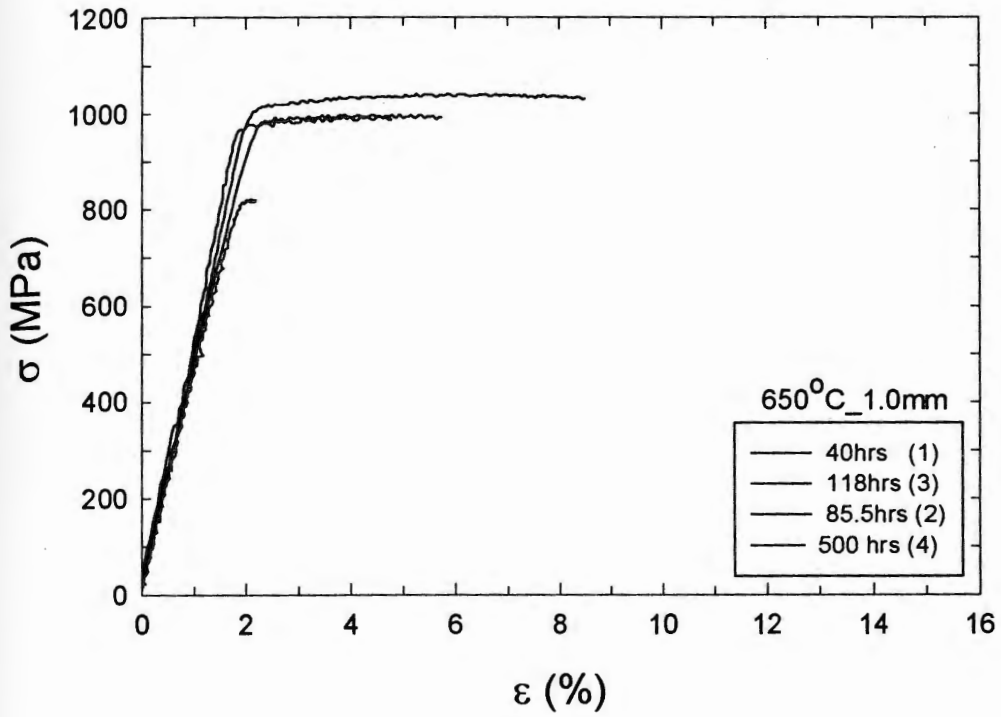


Fig. 3.20 – Stress – elongation curves for Timetal 21S – 1.0 mm thickness specimens with over-aging heat treatment then exposure in air at temperature 650 °C.

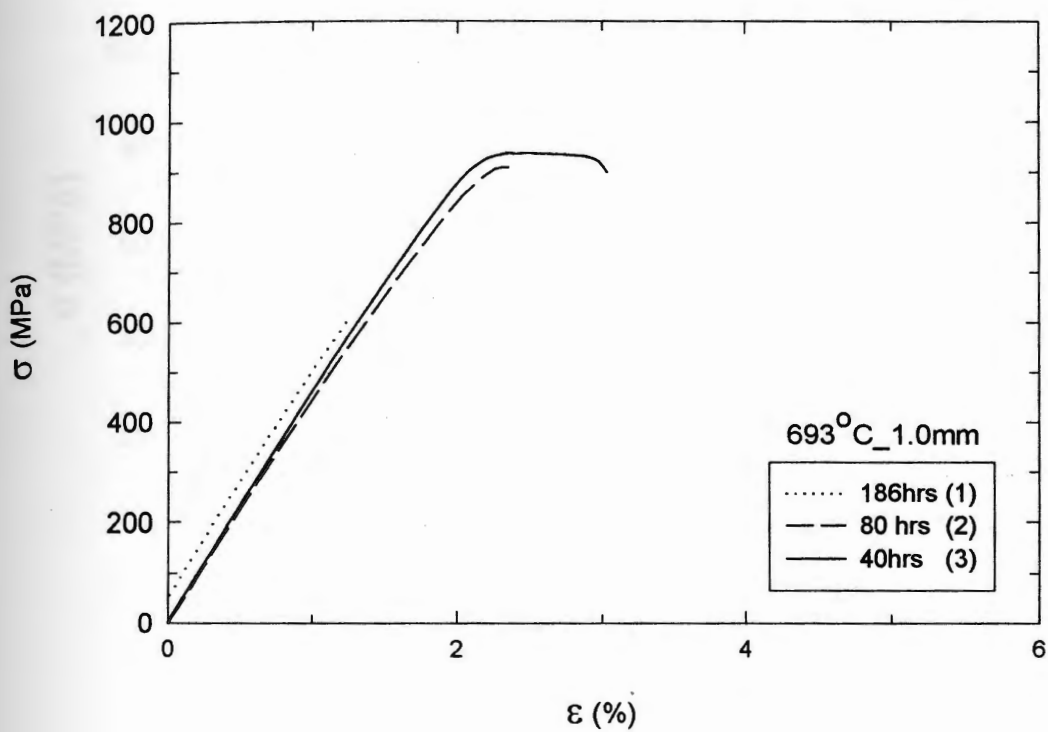


Fig. 3.21 – Stress – elongation curves for Timetal 21S – 1.0 mm thickness specimens with over-aging heat treatment then exposure in air at temperature 693 °C.

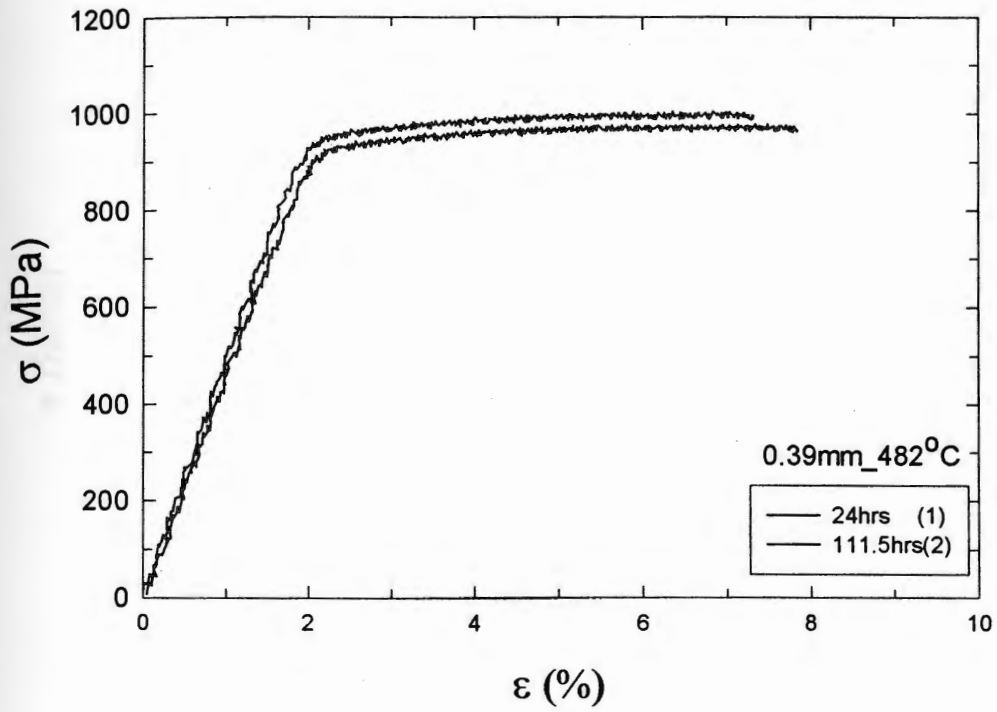


Fig. 3.22- Stress - Elongation curves for Timetal 21S - 0.39 mm thickness specimens with over - aging heat treatment then exposure in air at temperature 482 °C.

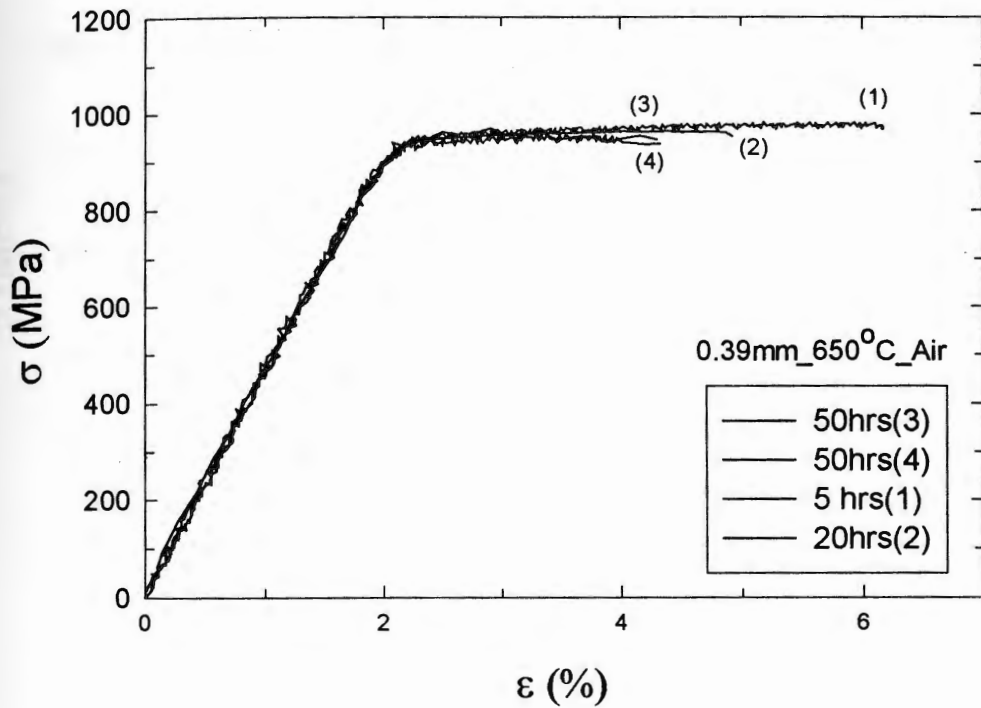


Fig. 3.23 – Stress – Elongation curves for Timetal 21S – 0.39 mm thickness specimens with over – aging heat treatment then exposure in air at temperature 538 °C.

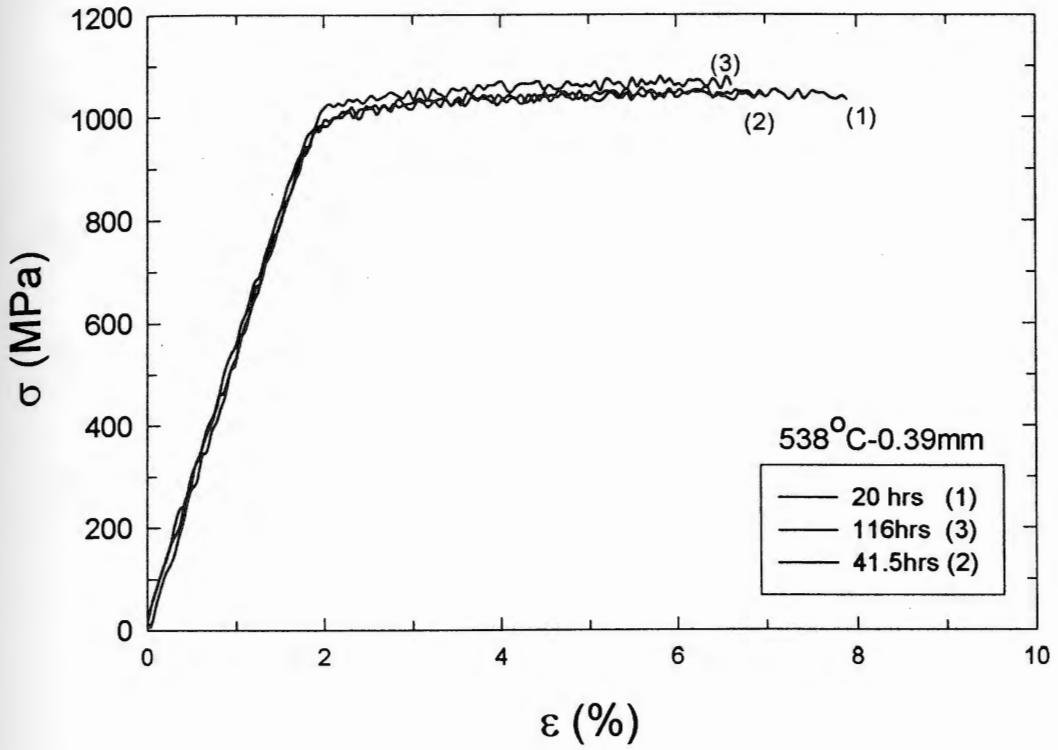


Fig. 3.24 – Stress – Elongation curves for Timetal 21S – 0.39 mm thickness specimens with over-aging heat treatment then exposure in air at temperature 650 °C.

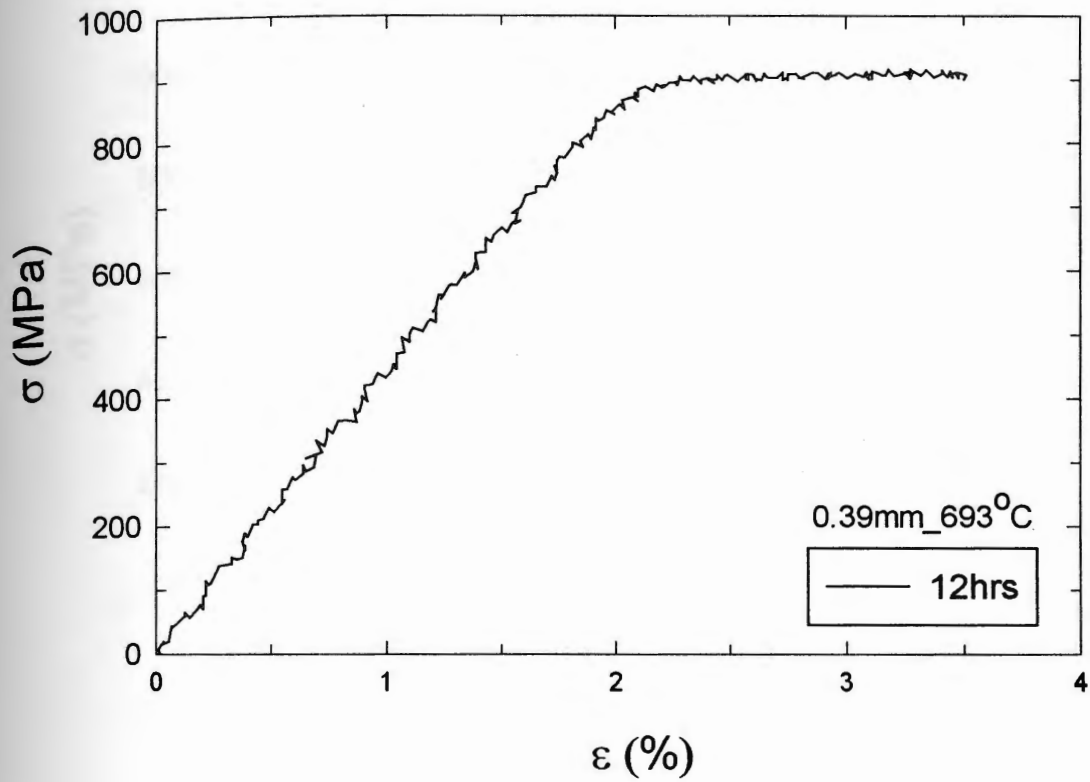


Fig. 3.25 – Stress – Elongation curves for Timetal 21S – 0.39 mm thickness specimens with over – aging heat treatment then exposure in air at temperature 693 °C.

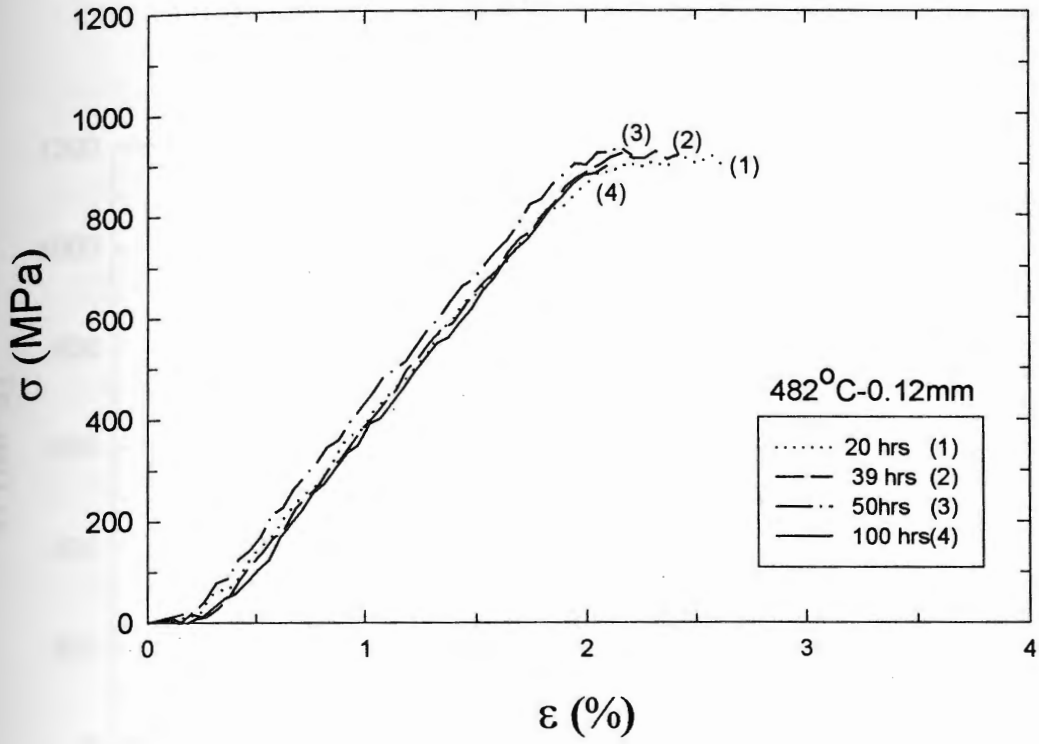


Fig. 3.26 – Stress – Elongation curves for Timetal 21S – 0.12 mm thickness specimens with over – aging heat treatment then exposure in air at temperature 482 °C.

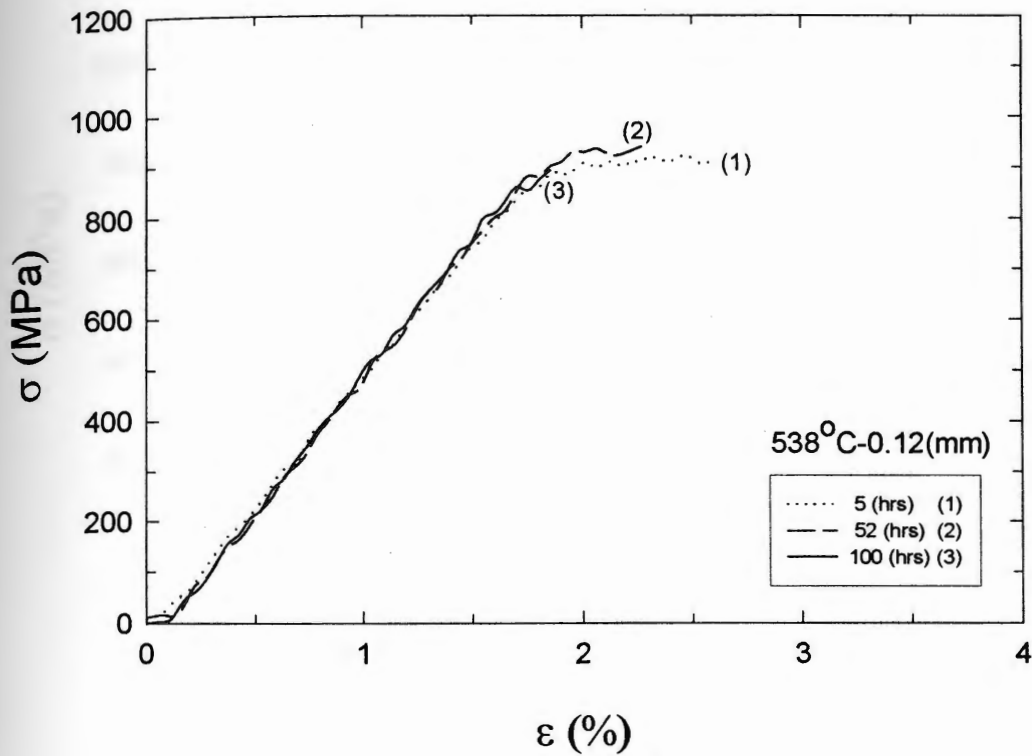


Fig. 3.27 – Stress – Elongation curves for Timetal 21S – 0.12 mm thickness specimens with over – aging heat treatment then exposure in air at temperature 538 °C.

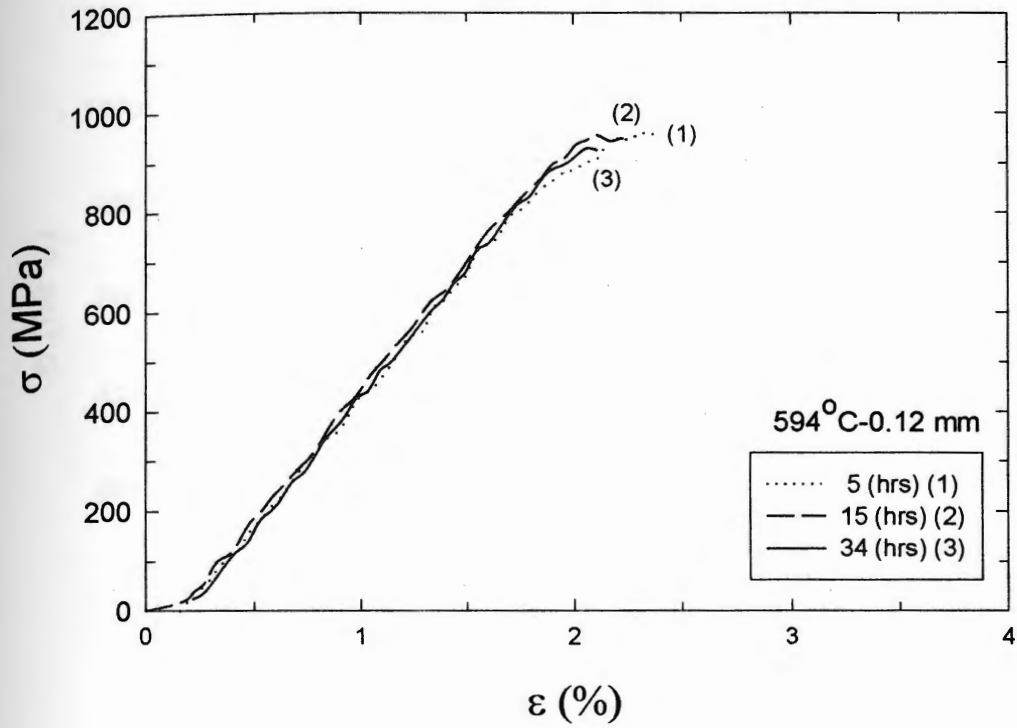


Fig. 3.28 – Stress–Elongation curves for Timetal 21S – 0.12 mm thickness specimens with over – aging heat treatment then exposure in air at temperature 594 °C.

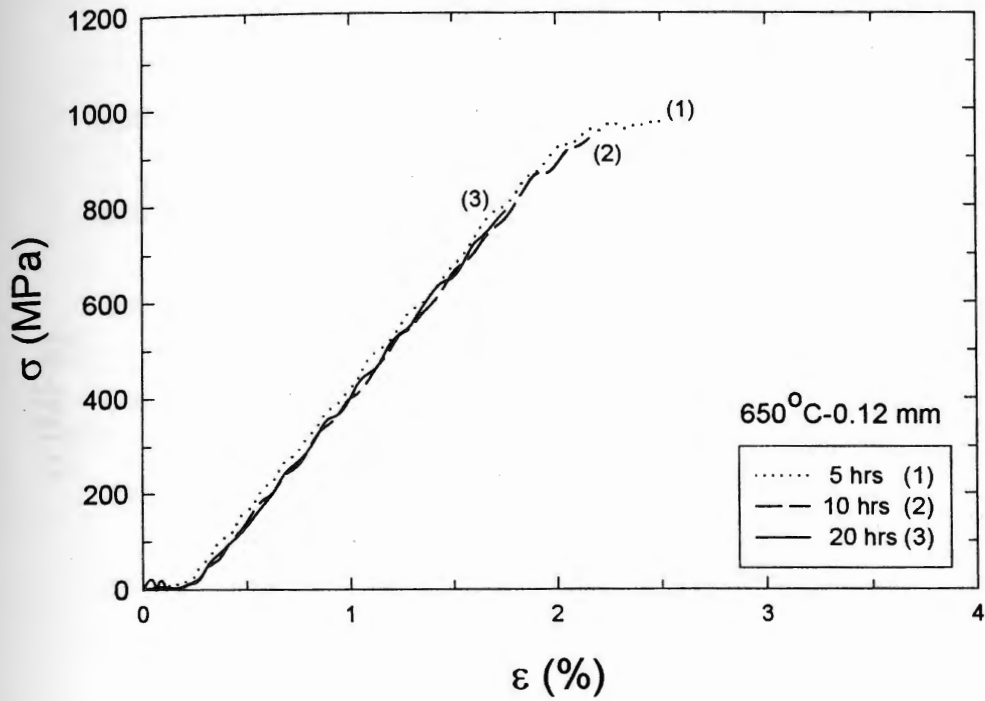


Fig. 3.29 – Stress – Elongation curves for Timetal 21S – 0.12 mm thickness specimens with over – aging heat treatment then exposure in air at temperature 650 °C.

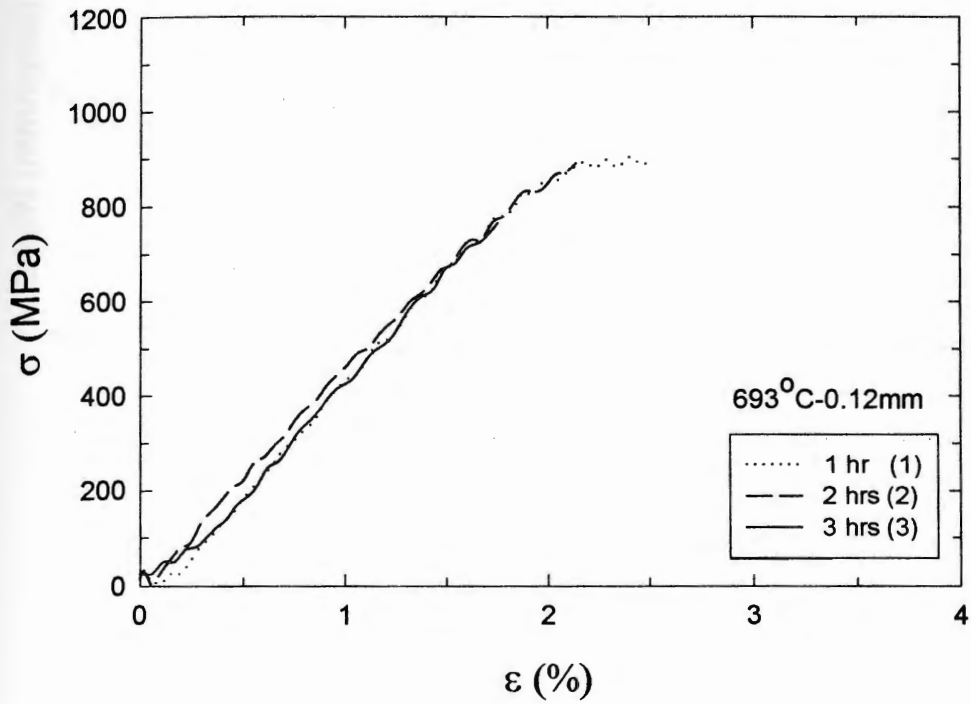


Fig. 3.30 – Stress – Elongation curves for Timetal 21S – 0.12 mm thickness specimens with over – aging heat treatment then exposure in air at temperature 693 °C.

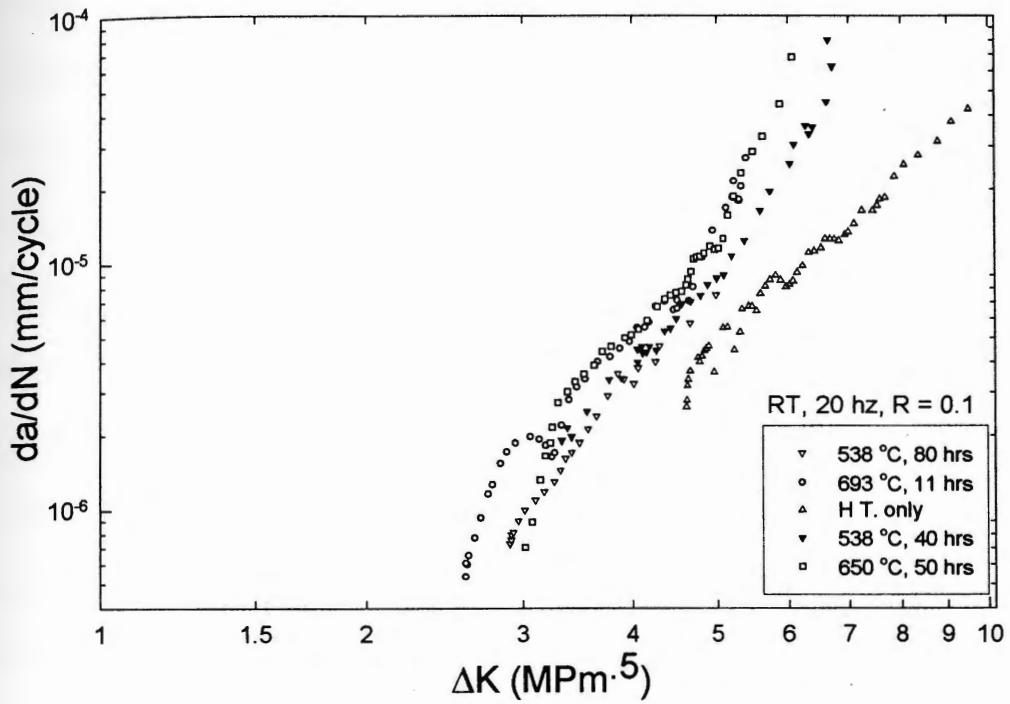


Fig. 3.31– Crack growth rate versus stress intensity factor range for Timetal 21S – 0.39 mm specimen's thickness with over – aging heat treatment in vacuum then exposed in air.

CHAPTER IV: ANALYSIS AND DISCUSSION

IV.1 Objective

In this chapter, two sets of results will be analyzed and discussed. The first set deals with the effect of the specimens' thickness and the exposure parameters on the embrittlement of the β -21S. The role of air oxygen in the embrittlement of this alloy will be discussed. Oxide layer is oxygen enriched surface layer that results from the diffusion of oxygen at the surface with sufficient concentration to form titanium oxides. The continuous diffusion of oxygen within the bulk would increase the α -phase precipitation especially at the grain boundaries without forming oxides. Extensive scanning electron microscopy is conducted to examine these effects. The second set of results deals with the crack growth behavior of thermally exposed specimens. The analysis will focus on the effect of exposure on the threshold stress intensity range, which is treated in this thesis as an intrinsic property of β -21S.

IV.2 Exposure and Thickness effects on the embrittlement rate

The effect of thermal exposure in air on the elongation of the β -21S sheets (thickness 0.12, 0.39, 1.0 mm), are plotted in Figs. 3.18 – 3.30, which show the total elongation versus the exposure time. These data are listed in Tables 4.1 – 4.3 and are plotted in Figs. 4.1 – 4.3 in term of available plastic elongation, d , as a function of the exposure time, t , for the three sheets thickness; 1.0, 0.39, and 0.12 mm. These d - t curves show that there are two different rates for the reduction of ductility; a fast rate followed by a slow rate or a steady state condition. These rates are approximately

separated with vertical lines on the x - axis (time axis) as shown in Figs. 4.1 - 4.3. Fig. 4.4 shows the relationship between the time to reach the steady state condition, t , and the specimen's thickness, h . It indicates that the loss of ductility slower as the specimen's thickness increases.

Furthermore, in order to distinguish the role of the thermal effects in air versus in vacuum on the embrittlement, a test specimen (heat-treated specimen) was exposed at 650 °C for 120 hrs in vacuum. Fig. 4.5 shows that the measured tensile elongation of this specimen is similar to that of the non-exposed one. This indicates that the thermal exposure effects are related to the air conditions

The second step in this analysis is to evaluate the kinetics of the ductility loss by calculating the activation energy involved in this process on the basis of the tensile experimental data in Figs. 4.1 - 4.3. This was then compared with the activation energy of the different air elements in order to identify the cause of the embrittlement mechanism.

IV.3 Activation energy involved in the embrittlement of β -21S

The objective of this calculation is to correlate the exposure parameters with the activation energy for a semi-infinite solid metal (assuming that specimen has infinite extension in the diffusion direction). It will be assumed that the specimen during the time of exposure maintains a constant surface composition so the diffusion coefficient can be assumed constant. Making use of Fick's second law, the diffusion rate can be written as:

$$\frac{\partial c}{\partial t} = D \frac{\partial^2 c}{\partial x^2} \quad (1)$$

where c is the concentration of the solute (number of diffused atoms per unit volume) at position x within the bulk and at time t , c_s is the concentration of the solute at the specimen's surface and D is the diffusion coefficient which is a composition independent and therefore can be assumed constant during the diffusion process.

Applying the conditions: $c(0,t) = c_s$, and $c(x,t) = 0$

the solution of Eq. 1 becomes

$$c = c_s(1 - \text{erf}(y)) \quad (2)$$

where:

$$\text{erf}(y) = \frac{2}{\sqrt{\pi}} \int_0^y e^{-y^2} dy \quad (3)$$

$$y = \frac{x}{2\sqrt{Dt}} \quad (4)$$

Furthermore, the weight gain of the diffused oxygen is calculated as:

$$W = \omega \int_0^t J dt \quad (5)$$

where W is the weight gain per unit area of the diffusion element, ω is atomic weight of the diffused element, and J is the flux (number of oxygen atoms per second passing through a unit area) which is given by Fick's first law as:

$$J = -D \frac{dc}{dx} \quad (6)$$

Substituting Eq. 2 into Eq. 6 yields:

$$J = -D c_s \frac{d}{dx} (1 - \text{erf}(y)) \quad (7)$$

Combining Eqs. 7, 3, and 4 yields:

$$J = c_s \sqrt{\frac{D}{\pi}} \left(\int_0^y e^{-y^2} d\frac{1}{\sqrt{t}} \right) \quad (8)$$

Substituting Eq. 8 in Eq. 5 gives:

$$W = \omega c_s \sqrt{\frac{D}{\pi}} \int_0^t \left(\int_0^y e^{-y^2} d\frac{1}{\sqrt{t}} \right) dt \quad (9)$$

In order to estimate the error function (erf) integral $\left(\int_0^y e^{-y^2} d\frac{1}{\sqrt{t}} \right)$ in the above equation, the diffusion coefficient D in the expression y (Eq. 4) is taken as 10^{-10} cm²/sec for the β -21S, see Table 2.3. x is given the value of the specimen's thickness, and t is the diffusion time. The selection is made for t equals 100, 5, 1 hrs for the three thickness of 1, 0.39, 0.12 mm; respectively. These values represent the time duration to reach a steady state condition. The solution of erf as function of $1/\sqrt{t}$ for the exposure time are shown in Figs. 4.6, 4.7, and 4.8. They indicate that the integral is a constant value expressed here as r now Eq. 9 can be simplified into:

$$W = \omega c_s \sqrt{\frac{D}{\pi}} \int_0^t r dt \quad (10)$$

$$W = r \omega c_s \sqrt{\frac{D}{\pi}} t \quad (11)$$

Eq. 11 represents the theoretical weight gain, W , of the diffused element in β -21S. This weight gain can now be compared with that obtained experimentally on the bases of Figs. 3.13 – 3.15 as a function of the exposure time. This experimental weight gain is expressed as:

$$W = k t^b \quad (12)$$

By equating Eqs. 10 and 11 and eliminating, W, one obtains:

$$r \omega c_s \sqrt{\frac{D}{\pi}} t = k t^b$$

$$D = \left(\frac{k}{r \omega c_s} \right)^2 \pi t^{2(b-1)} \quad (13)$$

Since D could also be described in an Arrhenius form:

$$D = D_o e^{-\frac{Q}{RT}}$$

Equation (13) could then be rewritten as:

$$\left(\frac{k}{r \omega c_s} \right)^2 \pi t^{2(b-1)} = D_o e^{-\frac{Q}{kT}}$$

By rearranging the terms of the above equation the exposure time could then be expressed as:

$$t = \left[\left(\frac{r \omega c_s}{k} \right)^{\frac{1}{(b-1)}} \left(\frac{D_o}{\pi} \right)^{\frac{1}{2(b-1)}} \right] e^{\frac{Q}{2(b-1)RT}} \quad (14)$$

taking the natural logarithmic of both sides of this equation yields:

$$\ln t = \ln \left[\left(\frac{r \omega c_s}{k} \right)^{\frac{1}{(b-1)}} \left(\frac{D_o}{\pi} \right)^{\frac{1}{2(b-1)}} \right] - \frac{Q}{2R(b-1)T} \quad (15)$$

This is a relationship describing the time to reach a particular ductility as a function of the various diffusion parameters for a selected temperature.

With the aid of Figs.4.1 – 4.3, four different ductility levels were selected for all exposure temperature. These ductility levels are shown in Tables 4.4, 4.5, and 4.6.

The relationship is plotted in the form $\ln (t = \text{particular ductility})$ versus $1000/T$ where

T is temperature in Kelvin. Results are shown in Figs. 4.9 – 4.11. These results indicate that the embrittlement process in the range 482 – 693 °C follows two distinctive mechanisms. The first is athermal mechanism indicated by a linear relationship between the time t and 1000/T, in this regime the time to reach a particular ductility decrease as the temperature increases. The second important embrittlement mechanism is athermal process where the ductility changing rate is so fast. This mechanism is defined by a transition temperature, approximate values of which are shown in Table 4.7. The mechanism in this particular regime will be discussed later in the embrittlement mechanism section. The following analysis will focus on the embrittlement mechanism in the temperature dependent region. However, Eq. 15 is a linear relationship in the form $y = k + m x$ where the slope m is equal to:

$$m = Q / 2 R (1 - b)$$

thus

$$Q = 2 R (1 - b) m.$$

the constant R is the universal gas constant which equal 1.986 cal / mol.K. This equation indicates that Q could be calculated from the knowledge of b and m, which are evaluated experimentally as follows. The constant b is calculated by fitting the time-weight gain relationships Figs. 3.13 – 3.15 with a power equation of two parameter, where b will be the exponent of this equation. Tables 3.7 – 3.9 show the values of the constant b as a result of this fitting procedure. Furthermore, the constant m is calculated from slope of the plot t-T in Figs. 4.9 - 4.11. Table 4.7 shows the three values of m, b, and k which, used to define the activation energy of the embrittlement

process. The average calculated activation energy is found to be 57.75 kcal / mol. Also, Table 4.8 represents the transition temperatures, which divides the two embrittlement mechanisms of β -21S.

The second step in determining the kinetics of the embrittlement process is to calculate the activation energy of the diffused air element in β -21S. This was made based on the observation that air elements cause the embrittlement of β -21S. The first step in this process is to calculate the different phases in the β -21S material for this purpose; three specimens with different exposure conditions of the over-aged β -21S were analyzed to estimate the volume fraction of both α and β phases in β -21S. The first specimen was a heat treated specimen (without exposure), while the second and third were specimens that have been exposed at 650 and 538 °C for 118 and 40 hours, respectively. Microstructures of these specimens were obtained using a scanning electron microscopy (SEM) and scanned using an image analysis procedure. Estimates were then made statistically to determine the α/β ratio Fig. 4.12 shows an analyzed micrograph, where the red and black colors represent α phase and β phase; respectively. Results of these analyses have shown that α phase has a percentage of 33.6 to 34.7 % while the rest is for β phase. However, it was noticed that further exposure in air for different exposure parameters did not change the fraction volume of α phase, where Huang [9] shows a value of 33 % of α phase for an aged specimen with 538 °C for 8 hrs. Therefore, 34 % considered being the highest volume fraction of α phase in β -21S.

A simple equation was used to calculate the activation energy of a diffused mater in β -21S $(Q_m)_{\beta-21S}$ based on the knowledge of the activation energy in the constituents of β -21S. This equation is:

$$(Q_m)_{\beta-21S} = \alpha \% \times (Q_m)_{\alpha} + \beta \% \times (Q_m)_{\beta}$$

where α % and β % are the volume fraction of alpha and beta phase percentages in the exposed specimen respectively. $(Q_m)_{\alpha}$ and $(Q_m)_{\beta}$ are the average activation energy of a mater in α and β phases respectively. for the average activation energy of the mater in β phase) / Total phase ratio. With the aid of Table 2.3, the activation energies of O_2 and C in β -21S are calculated as 57.4623 and 42.248 kcal / mol respectively. From this exercise it is apparent that the activation energy of embrittlement is equal to that of oxygen diffusion in β -21S and one could conclude that oxygen is the air element responsible for the loss of ductility during the thermal exposure experiments. The important aspect of this, however, is to determine the role of O_2 in the embrittlement process. This is explained in the following section.

IV.4 Oxygen role in the embrittlement of β -21S

To find out how the oxygen is affecting the elongation of the β -21S, the fracture surface of the exposed tensile test specimens were investigated using a scanning electron microscopy. Figs 4.13 – 4.18 show examples of the fracture surfaces, where the exposure parameters for each fractography are indicted in the caption of the corresponding figure. Each of these figures shows two fracture regions; a brittle fracture region, which is close to the specimens' surfaces, hereafter called

oxide layer, and a ductile fracture region, which corresponds with the specimens' bulks. The trend of oxide layer shows that its thickness increases as the exposure time increases. Also, the increase in the oxide layer reaches a saturation level. This trend is shown clearly in Figs. 4.13 and 4.14, where the measured thickness of oxide layer after 40 hrs of exposure was 14.3 μm while its measured thickness after 800 hours has reached 19.5 μm . Table 4.9 shows all the measured thickness of the oxide layer for the different exposed specimens. Results are plotted in Fig. 4.19, showing the trend of oxide layer formation as function of the exposure time.

Analyzing the saturation behavior of oxide layer versus the loss of the elongation shows that a loss of the elongation is not fully dependent on the formation of this layer. For example, comparing the two curves of the 600 °C in Fig. 4.1 and Fig. 4.19 shows that the oxide layer thickness has reached a saturation level after 150 hrs, the loss of the elongation, however, did not stop and continued to decrease with the increase of the exposure time beyond 150 hours. This observation suggests that the continuation of the ductility loss of β -21S beyond the saturation of oxide layer could be due to changes occurring in the interior of β -21S or by to a further embrittlement in the saturated oxide layer.

To investigate these possibilities the elongation of two different specimens exposed with the same number of hours was compared. The first specimen was subjected to the removal of the oxide layer using mechanical grinding. While, in the second specimen was left with the oxide layer. This comparison was carried out on two sets of specimens, which were exposed at 650 °C for 46 and 118 hrs. The thickness of the oxide layer to be removed from the surface of two of these specimens

was established from Fig. 4.19 and Table 4.9 respectively. To make sure that the required oxide layer was fully removed, one side of each specimen was polished with 600 grit grinding papers and measured with a micrometer along the length of the specimen. The same procedure was repeated on the other side of the surface of the specimen. The two specimens without the oxide layer were then tested to determine their plastic elongation, this was followed by an SEM examination of their fracture surfaces were checked with SEM. Results are shown in Fig. 4.20, which assured that the oxide layer layers were removed completely. The ductility of the exposed specimen at 650 °C for 118 hours with the surface oxide layer and that without the surface oxide layer, are shown in Table 4.1 and Fig. 4.21. This comparison result show that the specimen without the oxide layers has ductility of 3.1 % which indicates a regain of 0.5 % ductility as a result of the removal of the oxide layer.

In the current work a comparison was made between two specimens, which were exposed for a 1000 hrs at 616 °C. The one with the oxide layer showed a ductility of 2.5 %. The removal of the surface layer has resulted in regain of the ductility to the values of 15 and 13.5 % for the specimens' thickness 1.32 and 0.58 respectively. The significant of these results in relation to the current work will be discussed in the following section.

IV.5 Oxygen in the bulk of β -21S

The work in the previous sections have resulted in two important conclusions

- By comparing the activation energy and that of oxygen, carbon, and nitrogen in β -21S, it was concluded that oxygen is the air element responsible for the loss of ductility during thermal exposure.

- The embrittlement of β -21S is a combination of surface effects due to the formation of surface oxides and internal one due to the formation of α phase.

This section will discuss the distribution of oxygen concentration in the interior of β -21S and will present a method for calculating the corresponding weight distribution

Distribution of oxygen in the interior of β -21S:

The oxygen concentration in the interior of a test specimen could be written as function of the depth x , as follows:

$$c = c_s (1 - \text{erf}(y)) \quad (2)$$

where c_s is the oxygen concentration at the specimen's surface (air/specimen interface), which is assumed to be 1.58 % for β -21S. this is calculated on the basis that c_s is 2 % weight of Ti, see Fig. 2.24 and Ti is 79 % weight in β -21S. the error function $\text{erf}(y)$ is written as:

$$\text{erf}(y) = \frac{2}{\sqrt{\pi}} \int_0^y e^{-y^2} dy$$

$$\text{where } y = \frac{x}{2\sqrt{Dt}}$$

t being the time and D is the diffusion coefficient. Equation 2 could then be plotted, using the computer routine listed in App. 10. Results are shown in Fig. 4.22 for the 1.0 mm thickness specimen at 650 °C as a function of the exposure time. Also, in the same figure, the maximum depth of the oxide surface layer for the same temperature is plotted. The intersection of this curve with each of the concentration curves shows the oxygen concentration distributed within the β -21S at the corresponding exposure time.

It should be mentioned here that this distribution represents the minimum possible concentration as the weight gain in the material's interior is 2/3 the total weight gain during the exposure process as it will be shown below.

The amount of oxygen, which diffused in the bulk, is calculated as the difference between the total weight gain and the amount of oxygen in the surface oxide layer, $(W_{O_2})_{\alpha}$. To find the amount of $(W_{O_2})_{\alpha}$, it was important to know the types and the volume fraction of the phases, which participated in the formation of the oxide layer. Fig. 2.15 is used to assist in defining the possible phases. Fig. 4.22 shows that the oxygen concentration across the oxide layer thickness is between 1.58 – 0.25 toward the bulk of the specimen. The possible phases for this range are $Ti_2 O$, $Ti_2 O + Ti O$, $Ti O$, and $\alpha + Ti_2 O$ phases across the oxide layer toward the bulk. The volume fraction of these phases was calculated with the aid of a thermal decoration process, which will be explained, later in this section. This process showed that the oxide layer could be considered from the point of view of the volume fraction as two phases. The first phase is a β phase while the second one is an α phase including all the titanium oxides mentioned above. Hence, to calculate the weight of oxygen in the bulk of β -21S, the following volume fraction procedure is applied.

$$W_{\alpha} = (V_{\alpha} / V) * W_b \quad (16)$$

where, W_{α} , V_{α} are the weight and volume of the oxide layer respectively. W_b , V are the total weight and volume of the test specimen. This equation is made with the assumption that the density of the oxide layer material and that of the bulk is the same. Furthermore, the volume fraction of α phase within the oxide layer is measured as

mentioned previously to be 34 % while the remaining is β phase. Since β -21S is 79 % titanium by weight, the weight of titanium in the oxide layer, W_{Ti} is then calculated as:

$$W_{Ti} = 0.34 \times (0.79 \times W_{\alpha}) \quad (17)$$

The weight of oxygen, W_{O_2} , in the oxide layer is calculated as

$$W_{O_2} = W_{Ti} \times (C_m) \quad (18)$$

Where (C_m) is the mean value of oxygen concentration in the oxide layer at a particular temperature, assuming that the composition of this case causing a range of titanium oxides.

By substituting Eqs. 16 and 17 in Eq. 18 one obtains:

$$W_{O_2} = [0.79 \times 0.34 \times (V_{\alpha} / V) \times W_b] \times (C_m) \quad (19-a)$$

This equation could be simplified into:

$$W_{O_2} = [M \times (2L / \delta) \times W_b] \times (C_m) \quad (19-b)$$

where M , is a constant while δ and L are the thickness of both the specimen and the oxide layer, respectively. Eq. 19-b is the required equation to calculate the weight of oxygen, which can diffuse in β -21S and form the oxide surface layer only. It should be noted here that the specimen's configuration is assumed to be rectangular.

The results of applying this method to estimate the amount of the weight of oxygen, which penetrated in the bulk of the specimen after 100 hours exposure, are shown in Figs. 4.23, and 4.24. The value of $(C_m)_{650^{\circ}C}$ which was used in this method was achieved by using 'quad8' (which is a numerical integration code) to calculate the area under the fitted curve of the maximum depth of the oxide layer which is shown in Fig. 4.22. The fitted curve equation is

$$C_m = 0.5 e^{-2.405x} + 0.8 e^{-0.054x} + 0.27 e^{-1.402x \exp(-11) \times x}$$

where x is the distance in the specimen's bulk measured from the surface. Fig. 4.24 shows the maximum and minimum possible oxygen weight gain curves, which could be diffused in the material. To plot these maximum and minimum curves it was assumed that the oxide layer consists only of Ti_2O or α phase, where the corresponding oxygen concentration at the specimen/air interface, c_s , are 2.0 and zero % for pure titanium, respectively. These values were re-scaled by a factor of 79 % to express the oxygen concentration value at β -21S' surface, see Fig. 2.15.

The curves shown in Fig. 4.24 determine the weight of oxygen in β -21S specimen bulk beyond the oxide layer due to the thermal exposure in air. The presence of oxygen at the surface and within the test specimen could not be detected with the SEM metalography analysis as shown in Figs. 4.25 – 4.32. for this reason a thermal decoration process was used to reveal this presence of O_2 . This decoration process is discussed later in this section under 'observation of oxygen in the bulk' subtitle.

The above analysis calculates the weight of oxygen within the exposed specimen at any temperature, allows the correlation of the oxygen weight gain concentration and the ductility loss. This is shown in Fig. 4.33 for the temperature range used in this study. This figure shows that the ductility is most affected at temperature near 600 °C. At this temperature the diffused oxygen weight in the bulk of β -21S is 0.062 %, which when added to the initial weight of oxygen in the alloy's composition (0.11 – 0.15 %) gives a critical weight percentage of oxygen in the range 0.172 – 0.212 %.

Bania and Paris [16] investigated the ductility loss of the heat-treated material due to an exposure range 510 – 616 °C and 1000 hours. They showed that a fully ductility occurs after removing the oxide layer. The current work investigation was for an exposure range 538 – 693 °C and 870 hours. The removed oxide layer from a specimen with exposure parameters 650 °C and 118 hours showed only a small value of ductility loss was regained.

The significance of these results could be further explained with the aid of Fig. 4.34. This figure shows the ductility-temperature relationship after exposure time of 1000 hours for the three different thickness 0.12, 0.39, and 1.0 mm used in the current study and two different thickness 0.58, and 1.32 mm used in the work of reference [8]. This figure shows two important observations. The first observation is related to the fact that the initial ductility (ductility before exposure) decreases as the specimen's thickness decreases. . This observation will be discussed in the embrittlement mechanism section. The second observation is that the loss of ductility increases as temperature increases. The later observation was further investigated by removing the oxide surface layers from two specimens with two different exposure parameters. The first specimen was exposed at 616 °C for 1000 hours. The removal of the surface resulted in complete recovery of ductility. The second set of specimens was exposed at 650 °C and 118 hours. The removal of the surface resulted in the recovery of 5 % of the initial ductility as shown in Fig. 4.35. In order to explain these results, the complimentary error function (cerf) was plotted for 1000 hours time to show the theoretical depth of penetration of the oxygen diffusion into the material as function of the temperatures 538, 600, and 650 °C, see Fig. 4.36. This figure shows two facts.

The first fact is that the depth of the oxygen penetration reaches 500 μm and 200 μm at 650 and 600 $^{\circ}\text{C}$ respectively. This means that the variations in microstructure at 650 $^{\circ}\text{C}$ is more pronounced than at 600 $^{\circ}\text{C}$ and therefore the removal of the oxide layer in the case of 650 $^{\circ}\text{C}$ would not be sufficient to regain exhausted ductility. The second fact is that the weight gain in the specimen after removing the oxide layers indicates that the oxygen weight gain in the 650 $^{\circ}\text{C}$ specimen is higher than in the 600 $^{\circ}\text{C}$. Furthermore, Fig. 4.33 shows that at 616 $^{\circ}\text{C}$ the critical oxygen weight gain percentage may be not reached yet, while at 650 $^{\circ}\text{C}$, the oxygen weight gain is higher than the critical value.

Observation of oxygen in the material's bulk

A thermal decoration process was applied. This process involves heating test specimens to a temperature equal or higher than the β transus temperature in order to transform the microstructure back into β phase. Therefore, if α phase is found in the specimen after the decoration process, this would indicate the presence of titanium oxides which are not recoverable by the re-heating process. The choice of the β transus temperature for this decoration process was therefore estimated 830 $^{\circ}\text{C}$. Fig. 4.37 shows a microstructure of an exposed specimen before decoration while Fig. 4.38 shows the same microstructure after decoration. This comparison shows the microstructure in the bulk of the specimen becomes a single phase of β . Also, Fig. 4.38 shows that the microstructure at the surface is still consisting of two phases. This result shows the oxygen in the specimen's bulk did not react with the alloy's elements, therefore upon heating to 830 $^{\circ}\text{C}$ all the α phase was transformed back into β phase.

However, at the specimen's surface where the two phases remained after the decoration process, the α phase could not transform due to the chemical bonding between the titanium and oxygen atoms.

Also, the depths of the two layers at the specimens' surfaces, which result from the thermal decoration process, were found to be correlated with the depths of the brittle fracture surfaces of the tensile specimens. This was done by comparing the thickness of the fracture surface layers' depths versus the two-phase microstructure surface layer of the thermally decorated specimens. Results of this comparison, see Figs. 4.39 – 4.42, showed that the depths of these layers of alpha case which have been measured after the tainting process versus the measured brittle layer of the fracture surface were equal for the same exposure parameters. This supports that the α case consists of " β " and " α which includes the titanium oxides" phases.

IV.6 Embrittlement Mechanism

The current work demonstrated that the embrittlement of β -21S alloy occurred in three different thermal conditions, which are the heat treatment in vacuum, the thermal exposure at temperatures up to 600 °C, and thermal exposure at temperature higher than 600 °C.

Embrittlement mechanism due to the heat treatment can be shown in the initial ductility value, which in turn was varied as function of the specimen's thickness. The cause of this embrittlement could be due to a martensitic transformation of β phase into athermal ω phase during the quenching process, which is responsible for the variation of the initial ductility while the embrittlement effect of the precipitated α

phase during the aging process is not responsible for that variation. Due to that enough time during the aging process the volume fraction of α phase in the different specimen's thickness should be the same, while due to the fast nature of ω phase formation it could be expected that the same amount will be transformed within the different specimen's thickness. As the same amount of ω phase will have less embrittlement effect on the thicker specimens, it should be expected that thicker specimens would provide higher ductility than thinner ones. The kinetics of ω phase transformation will be discussed.

Embrittlement mechanisms due to exposure in air could be divided as mentioned before into surface, and bulk mechanisms based on up to 600 °C or higher than this temperature respectively. Surface mechanism embrittlement was occurred by the formation of the oxide layer due to the enrichment of the surface layer with the diffused oxygen, which chemically was able to react with titanium. Bulk mechanism embrittlement was occurred by the precipitation of α phase at the cell boundaries and/or dislocations, which was encouraged by the existence of the diffused oxygen into the bulk. In addition, as a solute strengthener, dissolved O_2 tends to stabilize the bcc lattice. Therefore, during this mechanism it is suggested that O_2 accelerate the decomposition of β phase into $\alpha + \beta$ phases.

Another mechanism could cause the embrittlement and it might be added to the previous ones is the formation of isothermal ω phase. In order to investigate the formation of ω phase during the isothermal exposure process, samples from exposed specimens were proposed for transmission electron microscopy (TEM) examination.

The preparation of these specimens and their results are explained in the following section.

TEM sample preparation was done by cutting a conventional 3 mm discs from β -21S using the electric discharge machine (EDM). The results presented concern the samples that have been exposed to air at 600 and 650 °C for 80 and 500 hours respectively. The thickness of the cut samples were reduced from the both sides by a mechanical grinding to about 70 μm to avoid any surface effects. Electron transparent samples were prepared by jet polishing in a twin jet polisher. The electrolyte was a 10 % perchloric acid in glycerol and methanol solution at 40 V and 0 °C. The TEM has Philips CM20 which was operated at 200 KV. Results of the TEM work are shown in Fig. 4.43, which illustrate the change of diffraction pattern of the ω phase with temperature and time. The micrographs of Fig. 4.43-a and Fig. 4.43-b show the $\langle 113 \rangle$ zone exist at the interface α/β for the two exposed samples at 600 and 650 °C for 80 and 500 hours respectively. Extra spots noted I are visible in Fig. 4.43-b due to the aging and the long time of exposure at 650 oC for 500 hours. In order to highlight this transformation, the diffracted spot noted j on Fig 4.43-b is used to make a dark field image where the ω phase will appear in white contrast. The image reported in Fig 4.43-c shows clearly the presence of this brittle phase at the interface between α and β phases.

As shown above that ω phase is one of the martensitic phase that could be formed at relatively low temperature (< 450 °C). the $\beta \rightarrow \omega$ phase transformation occurs both thermally and isothermally as mentioned before. It is developed by

applying to pairs of adjacent $(110)_\beta$ planes in bcc lattice an equal and opposite shear in the $\langle 111 \rangle_\beta$ direction through a distance equal to $1/6$ of the separation of the $(111)_\beta$ planes ($d = a\sqrt{3}/2$, where a is the bcc lattice parameter). Displacements of A and B atoms by $\pm(1/6)d$ lead to the hexagonal structure of ω -phase. The shear force, which could cause the formation of ω -phase, could be due to the quenching, the aging, and / or plastic deformation during the sheet manufacturing process. The reason this second mechanism is strongly suggested, because generally in Ti-Mo alloys α -precipitation takes place elsewhere than near the ω -precipitate site during the aging process, which shows a very high possibility of the existence of ω phase after the quenching or the aging processes.

However, for further investigation it is recommended to measure the volume fraction of α and ω phases in the bulk. These measurements will support the previous suggestions of the embrittlement mechanisms.

IV.7 Influence of thermal exposure on fatigue crack growth and ΔK_{th}

The previous analysis shows that the exposure of β -21S in air affects the material's ductility, where it was also proved that the diffused oxygen is the main element lead to the degradation of that ductility. Also it shows that almost $2/3$ of the oxygen weight gain due to exposure went into the bulk of the specimen while the rest was arrested by the surface layer (α -case). The mechanical pickling proved that the amount of the oxygen, which dissolved in the bulk at a temperature higher than 600°C leads to an embrittlement mechanism, which cause the ductility degradation. Further,

it was proved that upon increasing the O₂ % in the bulk more than 0.21% of the β-21S the amount of the ductility degradation becomes substantial.

All these previous results proved that the ductility degradation due to exposure followed two different processes surface and bulk. However, it was questioned how does an intrinsic property as the threshold stress intensity range, ΔK_{th} , would response to each of the surface and bulk processes where it (ΔK_{th}) should meet temperatures higher than 600 °C.

Fig. 3.31, shows curves representing the relationship between the crack growth rate da/dN and the applied stress intensity factor ΔK for different exposed specimen as indicted in the figure. The general observation of these curves is that the crack growth rate of the exposed specimens is about 2 to 3 times higher than the growth rate of the unexposed specimen. Also, ΔK_{th} of the unexposed specimen was degraded from 4.5 MPa \sqrt{m} to about 2.8 MPa \sqrt{m} for all the specimens upon the exposure in air. A variation of ΔK_{th} exists between the exposed specimens, in the range of 2.7 - 3 MPa \sqrt{m} . The fatigue crack growth behavior observations were supported by Figs. 4.44 and 4.45, which show that the crack front across the specimen's thickness has different speed in the unexposed specimen but same speed in the exposed specimen respectively.

IV.7.1 Crack growth rate and thermal exposure in air

Figs. 4.44 and 4.45 show two different fronts of the crack growth rates. Fig. 4.44 shows the crack was faster in the middle of the cross section of the fatigue

fracture surface than in the outer surface layers. However, Fig. 4.45 shows that the difference of the crack growth rates was vanished. This was interpreted based on the energy required for the crack growth. This energy is function of the loading condition and the material ductility. The energy required for the crack growth in plane stress condition is higher than in plane strain condition. This energy is $G = K^2 / E_1$, where K is the stress intensity factor which can be calculated based on the specimen's geometry, E_1 is equal the elastic modulus E for the plane stress and $E / (1 - \nu^2)$ for the plane strain conditions, where ν is the Poisson's ratio. As mentioned above that Fig. 4.44 shows the crack front of the heat-treated specimen before the exposure. In this figure the crack front speed in the middle of the cross section of the specimen is faster than these ones at the edges. This showed that higher portion of the applied energy on the specimen was consumed at the specimen edges where the plane stress condition is controlling the crack growth, than in the middle of this specimen where plane strain is the controller. Fig. 4.45 shows the crack front for the central crack specimen which were exposed with 650 °C and 50 hrs. This figure shows that the crack front at the edges of the specimen accelerated itself to have the same crack growth rate as in the middle of the cross section of this specimen. This was interpreted based on two factors. First as the material becomes more brittle the energy required for fracture will be less. Second the energy in front of the crack is function of the stress intensity factor as discussed earlier. Therefore, as the embrittlement in Timetal 21S was higher close to the surface layers than in the middle of the specimen as it was explained before, so it should be expected that the fracture would be faster at the edges than in the middle. That explained how the crack front at the edges accelerated itself to reach

that in the middle. Further, as the energy is a function of the stress intensity factor K , it can be expected that to achieve the same crack length it will require less K for the brittle region than the other region, which has higher ductility. Therefore, it should be expected that the fatigue crack growth curve would be shifted to the left, as the material is embrittled. This explains the faster crack propagation in Fig. 3.31 for the Timetal 21S upon exposure in air, which found to be 2 to 3 times the crack propagation rate of the non exposed specimens. It should be noted that, matching between the small difference in the crack growth rate (which is 2 to 3 times), and that accelerated profile at the edges of the crack front of the exposed specimen which can be seen by comparing Fig. 4.45 versus Fig. 4.44.

IV.7.2 Threshold stress intensity range ΔK_{th} and the bulk changes

ΔK_{th} is one of a number of threshold-type parameters. It may be used where a pre-existing crack or notch in the material, to describe the growth/no-growth condition under high-cycle fatigue loading. So many mechanistic theories have been advanced to explain near-threshold behavior that any experimental data can be explained away by reference to one or the another of them. A considerable work of assimilation and comparison is required if one is to decide which approach is valid under which set of conditions. Defining the near - threshold behavior is out of the scope of the current work. However, it may be proposed that the fatigue threshold degradation could be interpreted based on the argument of Ritchie [25], which stated that, the oxidation effects on the slip character by decreasing the reversibility of slip and therefore tends to accelerate damage near the crack tip.

Table 4.1 – Elongation d obtained from the Stress-Elongation curves of 1.0 mm thickness at different aging parameters

| T (°C) | t (hrs) | d (%) |
|--------|---------|-------|
| 538 | 40 | 12.2 |
| | 100 | 11 |
| | 163 | 9.8 |
| | 862 | 8.5 |
| 600 | 40 | 11.1 |
| | 80 | 9.9 |
| | 150 | 8 |
| | 700 | 3.2 |
| 650 | 40 | 6.3 |
| | 85.5 | 3.6 |
| | 118 | 2.7 |
| | 500 | 0.0 |
| 693 | 40 | 1 |
| | 80 | 0.3 |
| | 186 | 0.0 |

Table 4.2 – Elongation d obtained from the stress-elongation curves of 0.39 mm sheet thickness at different aging parameters

| T (°C) | t (hrs) | d (%) |
|--------|---------|-------|
| 482 | 24 | 5.8 |
| | 111.5 | 5.25 |
| 538 | 20 | 5.9 |
| | 41.5 | 5 |
| | 116 | 4.6 |
| 650 | 5 | 4 |
| | 20 | 2.8 |
| | 80 | 2.2 |
| 693 | 12 | 1.5 |

Table 4.3 – Elongation obtained from the stress-elongation curves for sheet thickness 0.12 mm at different aging parameters

| T (°C) | t (hrs) | d (%) |
|--------|---------|-------|
| 482 | 20 | 0.9 |
| | 39 | 0.65 |
| | 50 | 0.42 |
| | 100 | 0.36 |
| 538 | 5 | 0.8 |
| | 52 | 0.35 |
| | 100 | 0.2 |
| 594 | 5 | 0.5 |
| | 15 | 0.4 |
| | 34 | 0.15 |
| 650 | 5 | 0.45 |
| | 10 | 0.12 |
| | 20 | 0 |
| 693 | 1 | 0.6 |
| | 2 | 0.13 |
| | 3 | 0 |

Table 4.4 – The natural logarithm of the exposure times, which were extracted from the d-t curves Fig. V.1 for the four arbitrary elongation values which were used to plot the $t - T$ relationship for that sheet thickness of 0.12 mm which is shown in Fig. V.8.

| T (°C) | 1000/T (1/°k) | ln(t) _{d=0.6} | ln(t) _{d=0.4} | ln(t) _{d=0.2} | ln(t) _{d=0.1} |
|--------|---------------|------------------------|------------------------|------------------------|------------------------|
| 482 | 1.32 | 3.13 | 3.56 | 4.17 | 4.60 |
| 538 | 1.23 | 2.89 | 3.46 | 4.09 | 4.38 |
| 594 | 1.15 | 2.59 | 2.99 | 3.38 | 3.82 |
| 650 | 1.08 | 1.00 | 1.60 | 2.07 | 2.31 |
| 693 | 1.03 | 0 | 0.26 | 0.69 | 1.09 |

Table 4.5 – The natural logarithm of the exposure times, which were extracted from the d-t curves Fig. V.1 for the four arbitrary elongation values which were used to plot the t – T relationship for that sheet thickness of 0.39 mm which is shown in Fig. V.9.

| T (°C) | 1000/T (1/°K) | ln (t) _{d=1.3%} | ln (t) _{d=1.0%} | ln (t) _{d=0.5%} | ln (t) _{d=0.2%} |
|--------|---------------|--------------------------|--------------------------|--------------------------|--------------------------|
| 483 | 1.3245 | 6.5000 | 6.5500 | 6.8000 | 7.0000 |
| 538 | 1.2330 | 6.4900 | 6.5400 | 6.7900 | 6.9900 |
| 650 | 1.0834 | 4.3944 | 4.6444 | 5.0689 | 5.4381 |
| 693 | 1.0352 | 3.1781 | 3.5264 | 4.0604 | 4.3567 |

Table 4.6 – The natural logarithm of the exposure times, which were extracted from the d-t curves Fig. V.1 for the four arbitrary elongation values which were used to plot the t – T relationship for that sheet thickness of 1.0 mm which is shown in Fig. V.10.

| T (°C) | 1000/T (1/°k) | $\ln(t)_{d=1.6\%}$ | $\ln(t)_{d=1.0\%}$ | $\ln(t)_{d=0.5\%}$ | $\ln(t)_{d=0.2\%}$ |
|--------|---------------|--------------------|--------------------|--------------------|--------------------|
| 482 | 1.3245 | 8.1000 | 8.2500 | 8.4500 | 8.7500 |
| 538 | 1.2330 | 8.0900 | 8.2400 | 8.4400 | 8.7400 |
| 600 | 1.1455 | 6.3500 | 6.5000 | 6.7500 | 7.0000 |
| 650 | 1.0834 | 4.8675 | 5.0626 | 5.2730 | 5.4381 |
| 693 | 1.0352 | 3.7612 | 3.9512 | 4.2047 | 4.4773 |

Table 4.7 – The activation energy as function of constants (b), and m for the three sheet thickness under research

| Specimen thickness (mm) | b | m | Q (kcal/mol) |
|-------------------------|--------|-------|--------------|
| 0.12 | 0.3315 | 22.05 | 58.5 |
| | 0.34 | | 57.7 |
| | 0.3666 | | 55.4 |
| 0.39 | 0.39 | 23.22 | 56.2 |
| | 0.379 | | 57.2 |
| 1.0 | 0.33 | 23.49 | 62.5 |
| | 0.39 | | 56.9 |
| | 0.379 | | 57.9 |

Table 4.8 – Transition temperatures (T_t) due to the thermal exposure of Timetal 21S sheets.

| T_t (for 0.12 mm) | T_t (for 0.39 mm) | T_t (for 1.0 mm) |
|---------------------|---------------------|--------------------|
| 569.1 | 589.0 | 546.7 |
| 569.1 | 538.1 | 548.0 |
| 574.4 | 575.2 | 548.0 |
| 578.1 | 568.8 | |

Table 4.9 – The mechanical properties of two sets of specimens with two different heat treatments as function of the exposure in air

| Heat treatment | Test condition | h* (mm) | UTS (MPa) | YS (MPa) | % Elongation | ΔK_{th} (MPa \sqrt{m}) | Ref. |
|-----------------|----------------|---------|-----------|----------|--------------|-----------------------------------|---------------|
| STA* | RT | 1.53 | 1365 | 1268 | 8.6 | 2.8 | [26] |
| STA | 170 °C | 1.53 | 1185 | 1068 | 10 | 2.0 | [26] |
| OA ⁺ | RT | 1.00 | 1020 | 960 | 12 | 4.5 | Current study |
| OA | RT | 1.00 | 1010 ± 20 | 990 ± 20 | Fig. V.1 | 2.8 | Current study |

*h is the specimen thickness.

*Solution treatment and aging of (851 °C / 0.5 hrs + 537 °C / 8 hrs) with air-cooled AC.

⁺Over aged heat treatment of (693 °C / 8 hrs + 650 °C / 8 hrs) with AC.

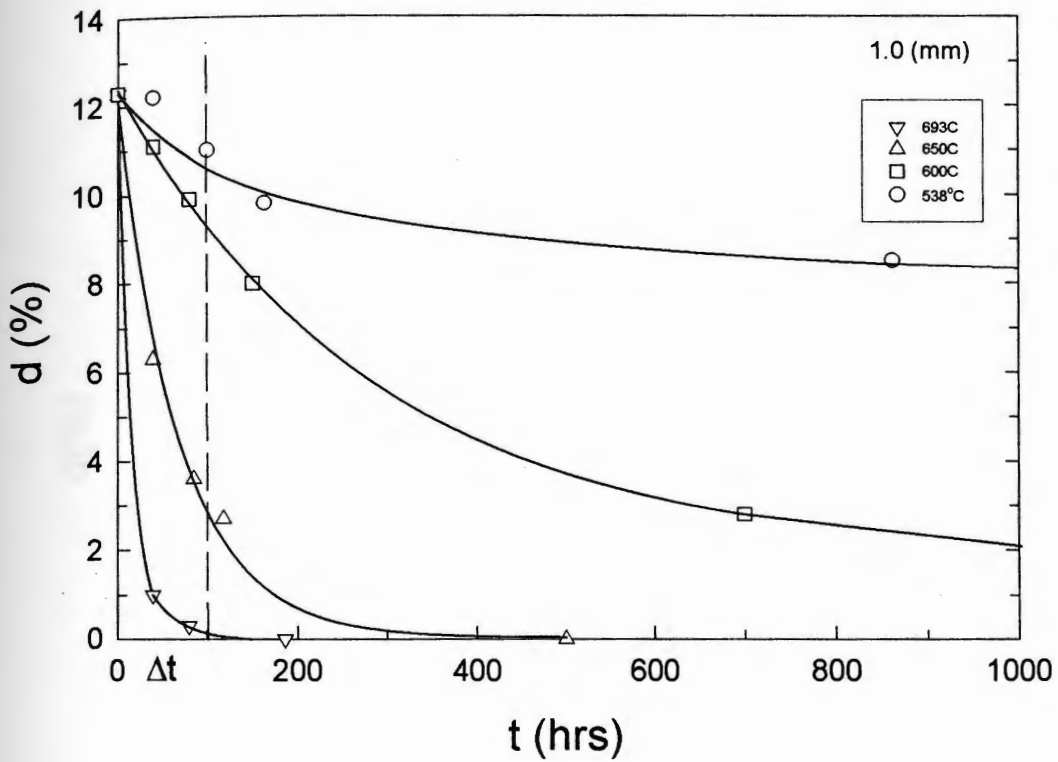


Fig. 4.1- The available elongation (d) of sheet specimens with 1.0 mm thickness after exposure time (t).

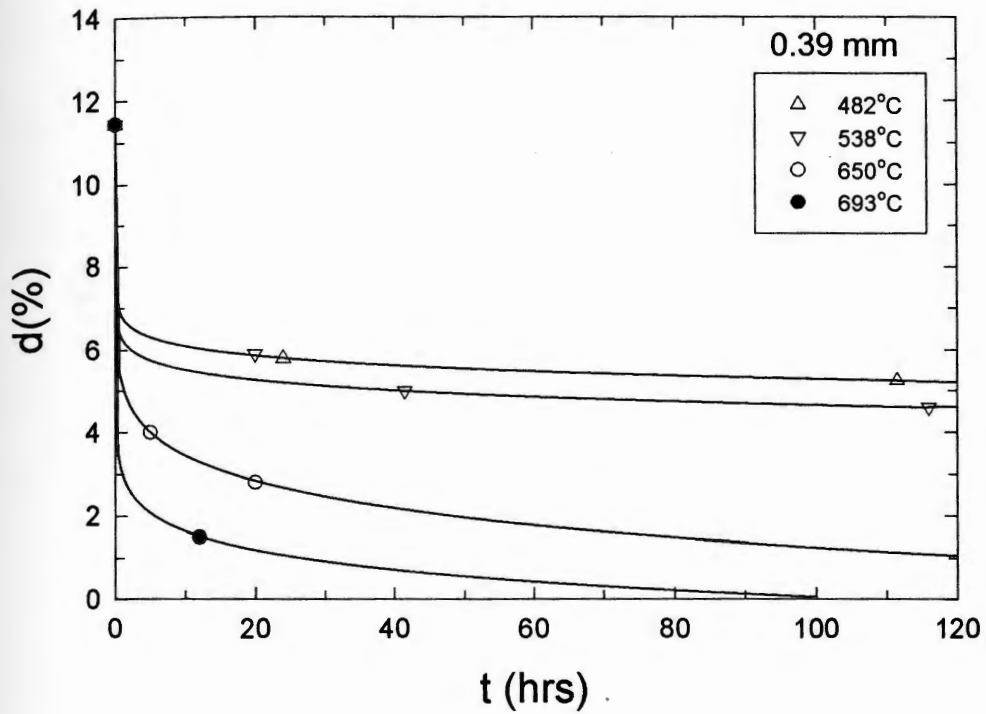


Fig. 4.2— The available elongation (d) of sheet specimens with 0.39 mm thickness after exposure time (t).

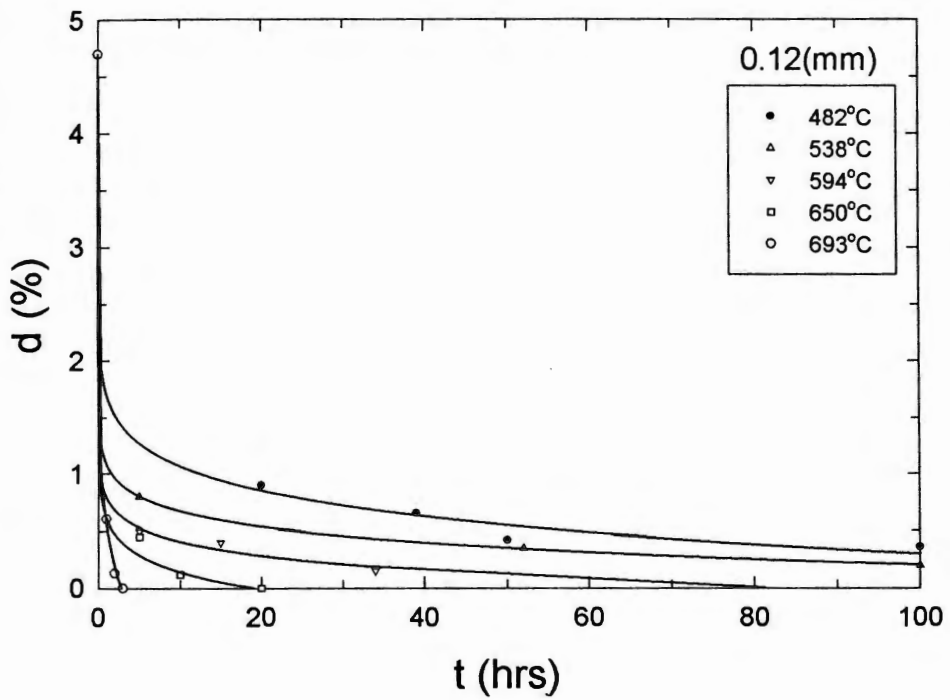


Fig. 4.3– The available elongation (d) of sheet specimens with 0.12 mm thickness after exposure time (t).

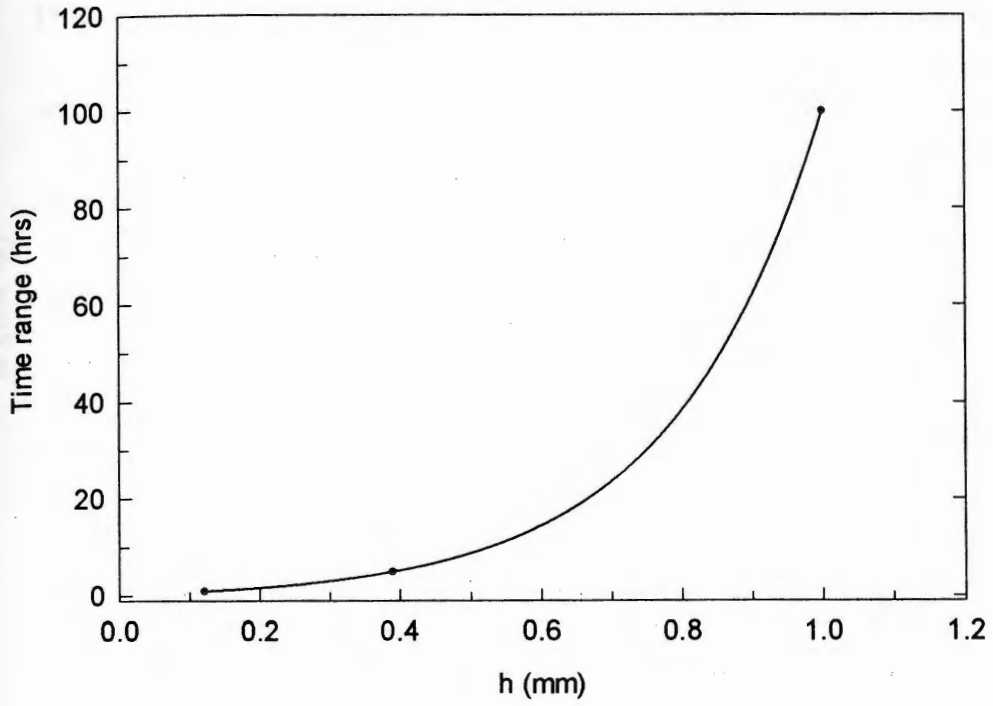


Fig. 4.4 – Time range of the fast rate of the loss of ductility as function of the specimen's thickness.

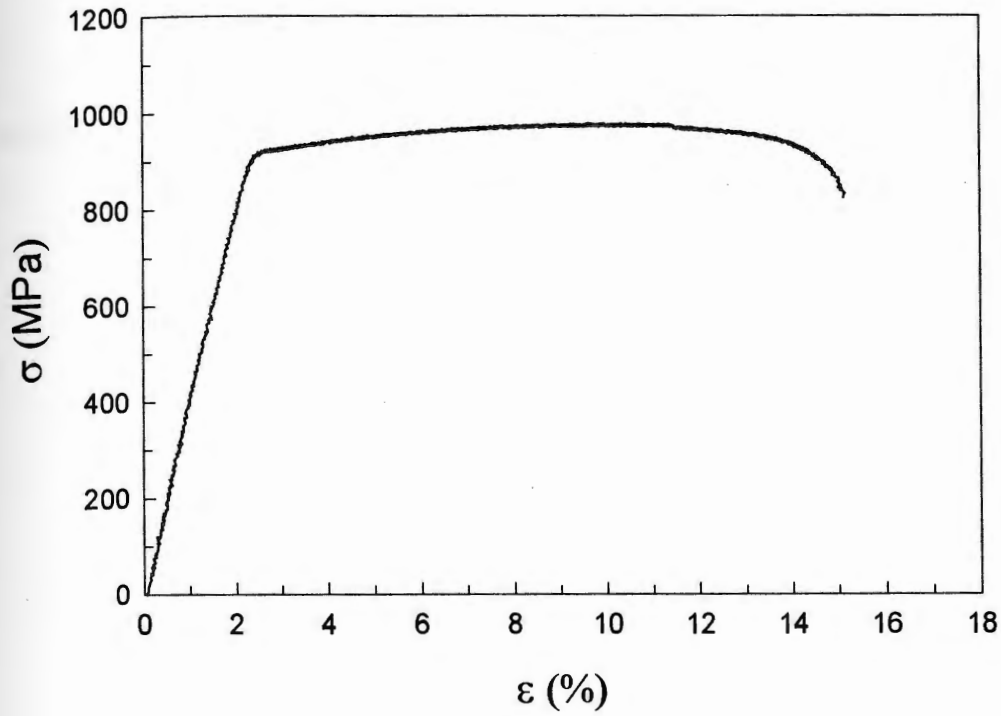


Fig. 4.5 – Stress strain relationship of 1.0 mm exposed β -21S specimen in vacuum for 120 hrs at 650 °C.

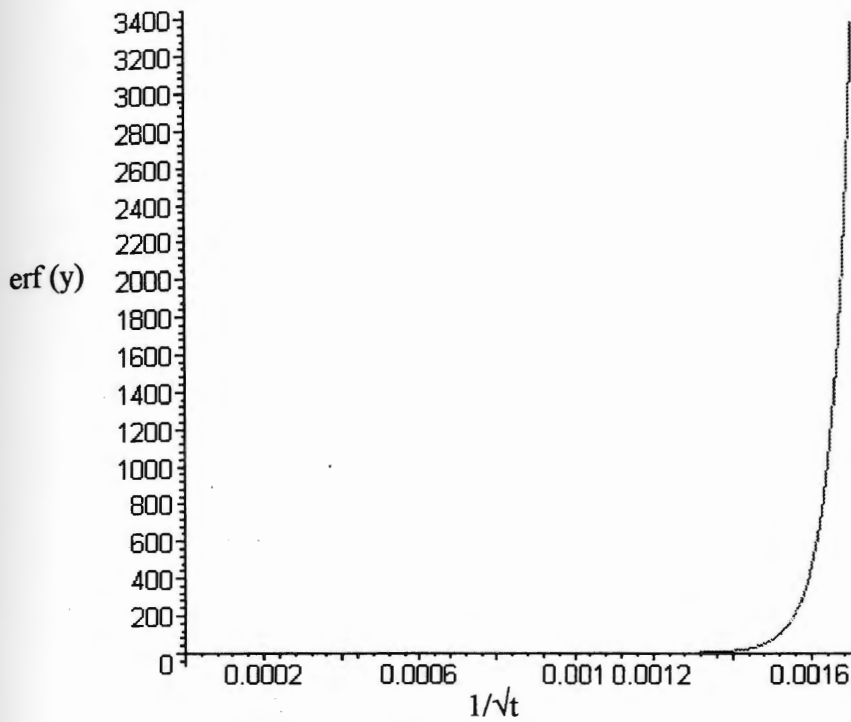


Fig. 4.6 – Shows the relationship between erf function (y-axis) and $1/\sqrt{t}$ where t is the time in sec., for the assumed value of the diffusion coefficient $D = 10^{-10} \text{ cm}^2 / \text{sec}$ and plate thickness of 0.1 cm during the first 100 hrs of exposure.

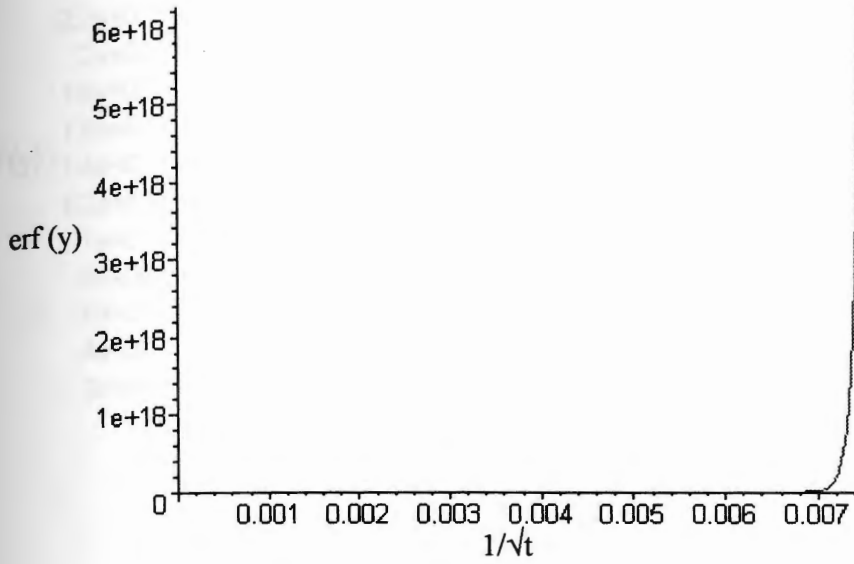


Fig. 4.7 – Shows the relationship between erf function (y-axis) and $1/\sqrt{t}$ where t is the time in sec., for the assumed value of the diffusion coefficient $D = 10^{-10} \text{ cm}^2 / \text{sec}$ and plate thickness of 0.039 cm during the first 5 hrs of exposure.

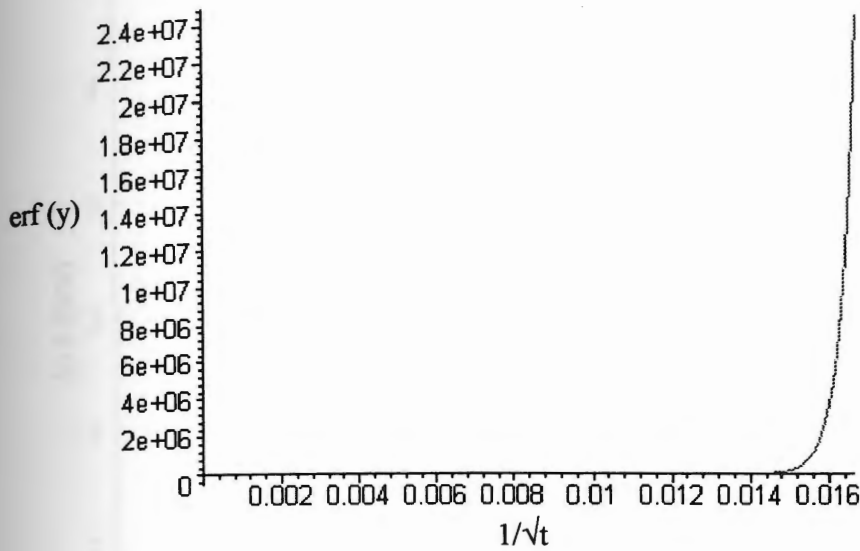


Fig. 4.8 – Shows the relationship between erf function (y-axis) and $1/\sqrt{t}$ where t is the time in sec., for the assumed value of the diffusion coefficient $D = 10^{-10} \text{ cm}^2 / \text{sec}$ and plate thickness of 0.012 cm during the first 100 hrs of exposure.

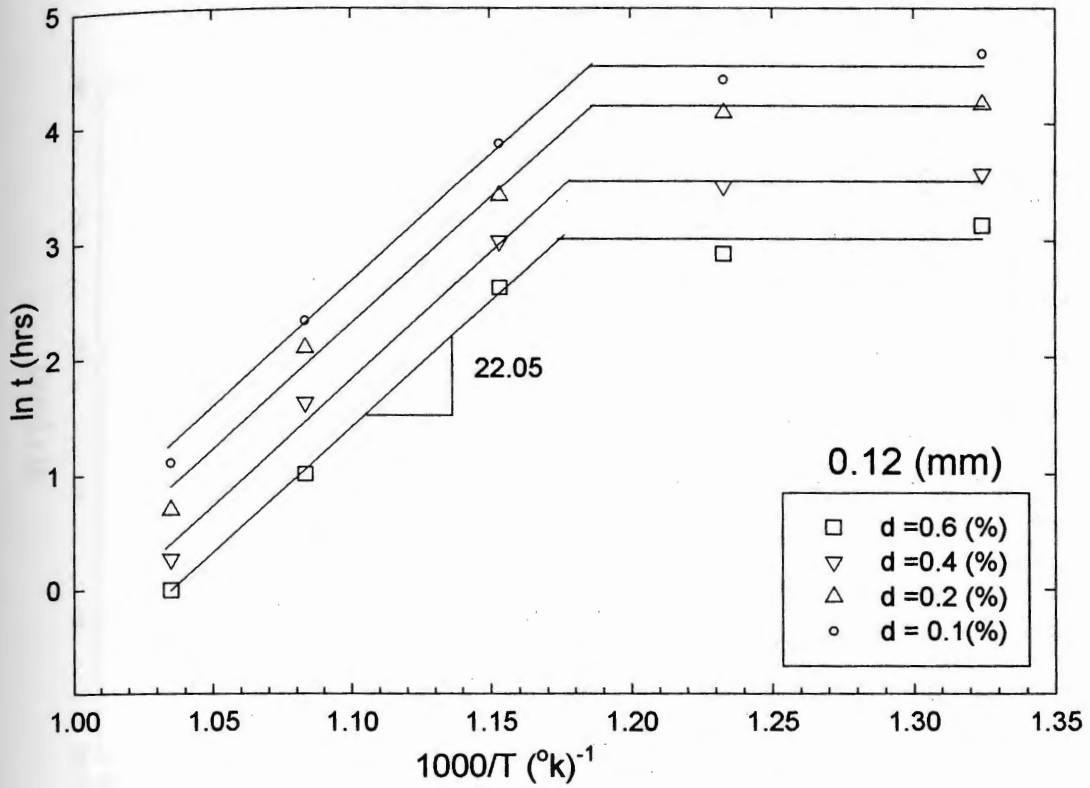


Fig. 4.9 – The exposure time – temperature relationship of 0.12 mm specimen for certain elongation (d) (d : the remaining elongation after exposure)

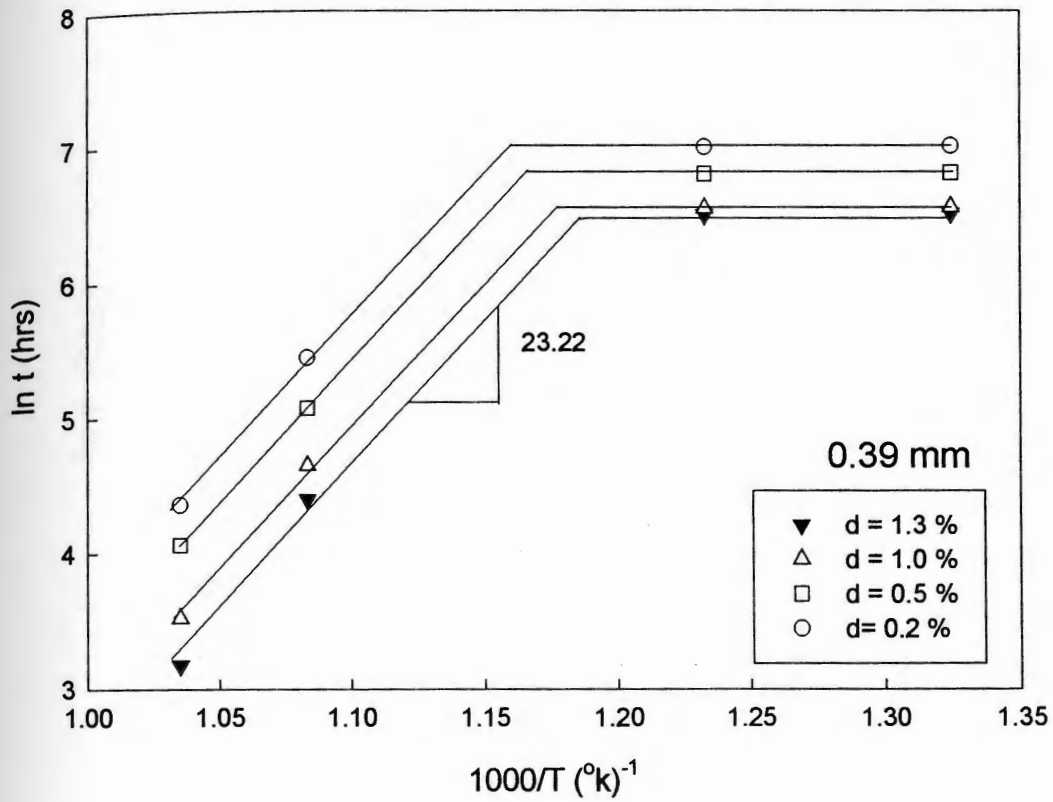


Fig. 4.10 – The exposure time – temperature relationship of 0.39 mm specimen for certain elongation (d) (d : the remaining elongation after exposure)

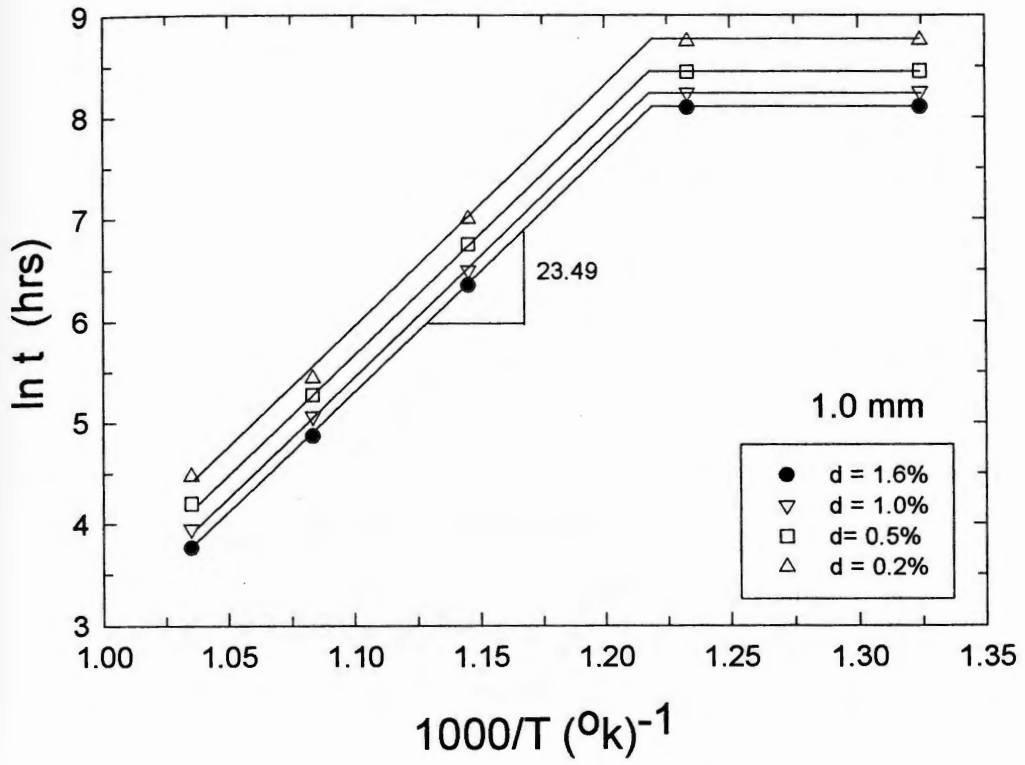


Fig. 4.11- The exposure time - temperature relationship of 1.0 mm specimen for certain elongation (d) (d : the remaining elongation after exposure)

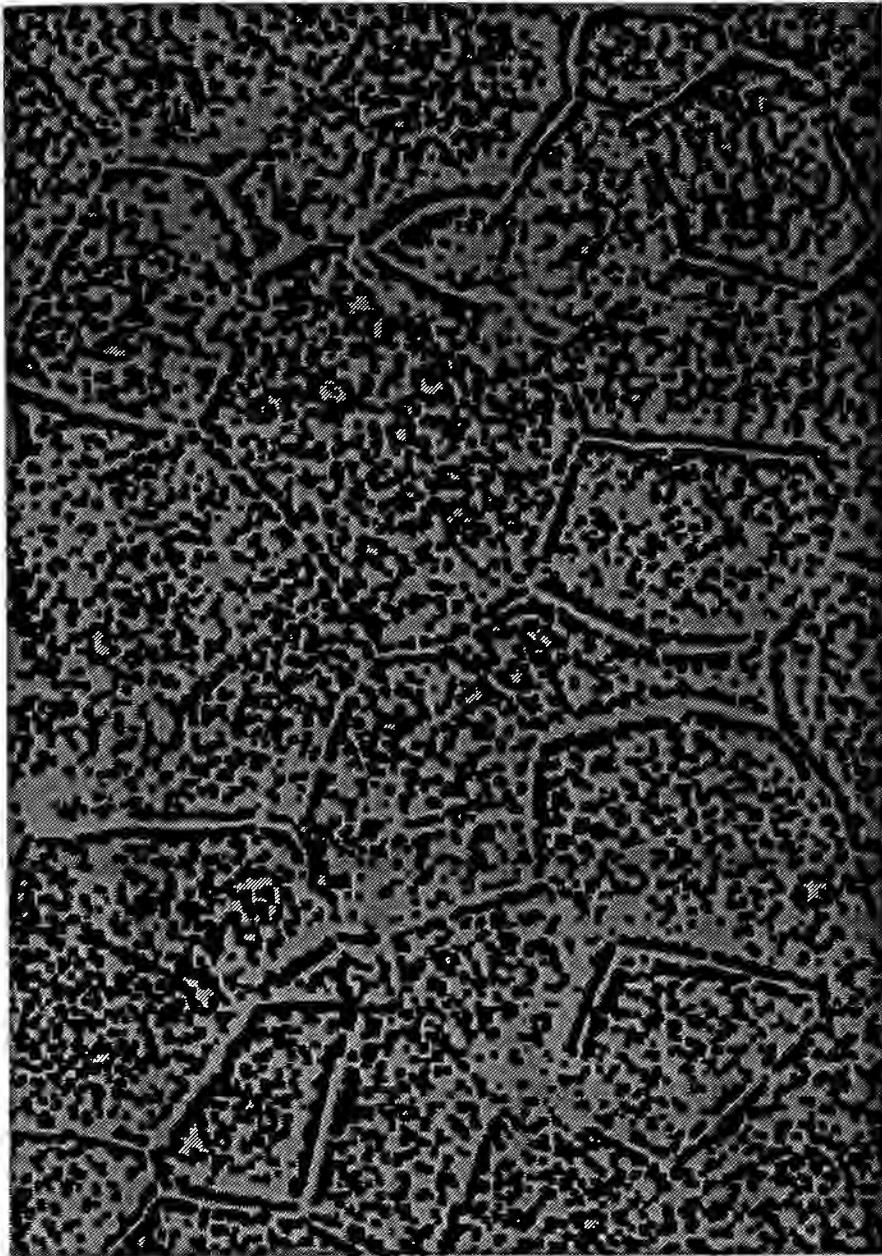


Fig. 4.12– Alpha phase to beta phase volume fraction ratio, where the red and black colors represent alpha-phase and beta-phase respectively.

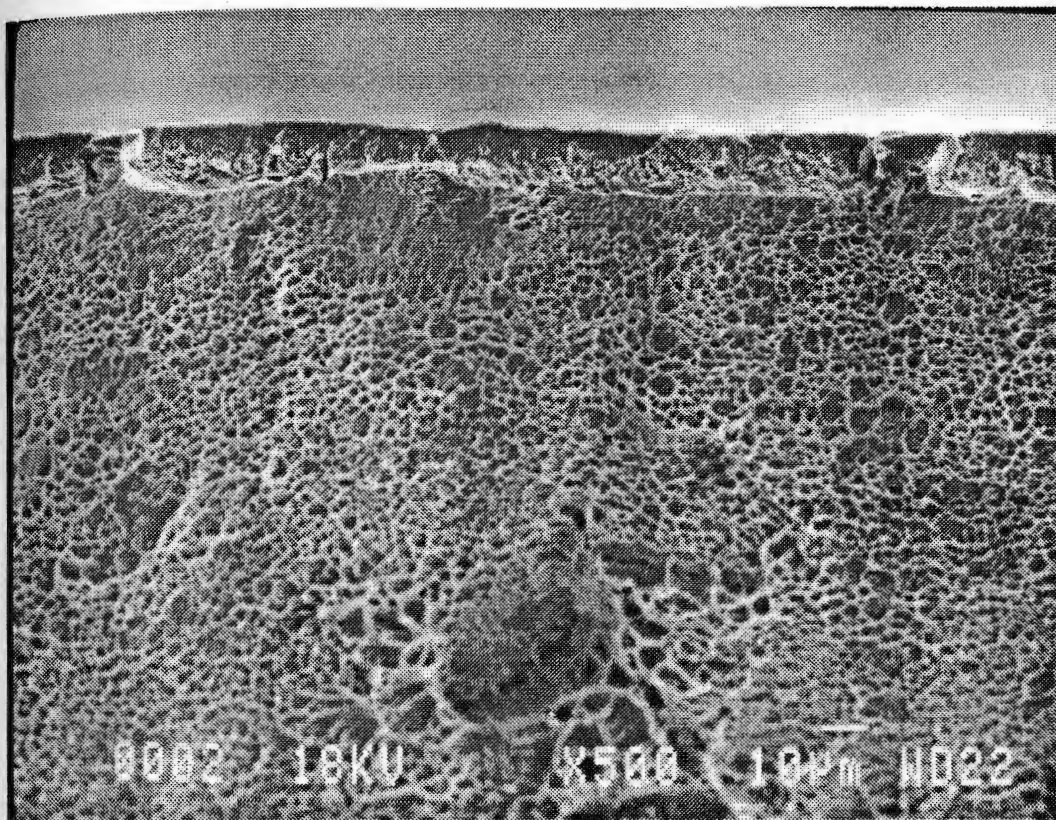


Fig. 4.13 – The fracture surface of 1.0 mm, tensile, and exposed specimen of Timetal – 21S with exposure parameters 538 °C, and 40 hrs.

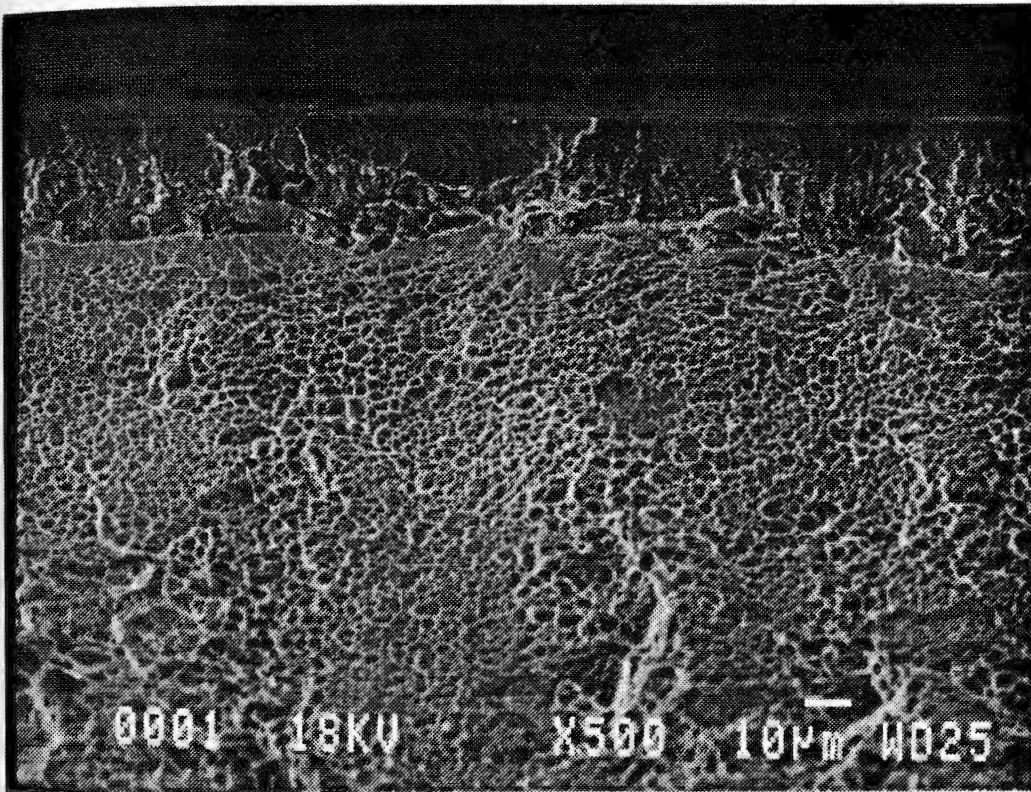


Fig. 4.14 – The fracture surface of 1.0 mm, tensile, and exposed specimen of Timetal – 21S with exposure parameters 538 °C, and 862 hrs

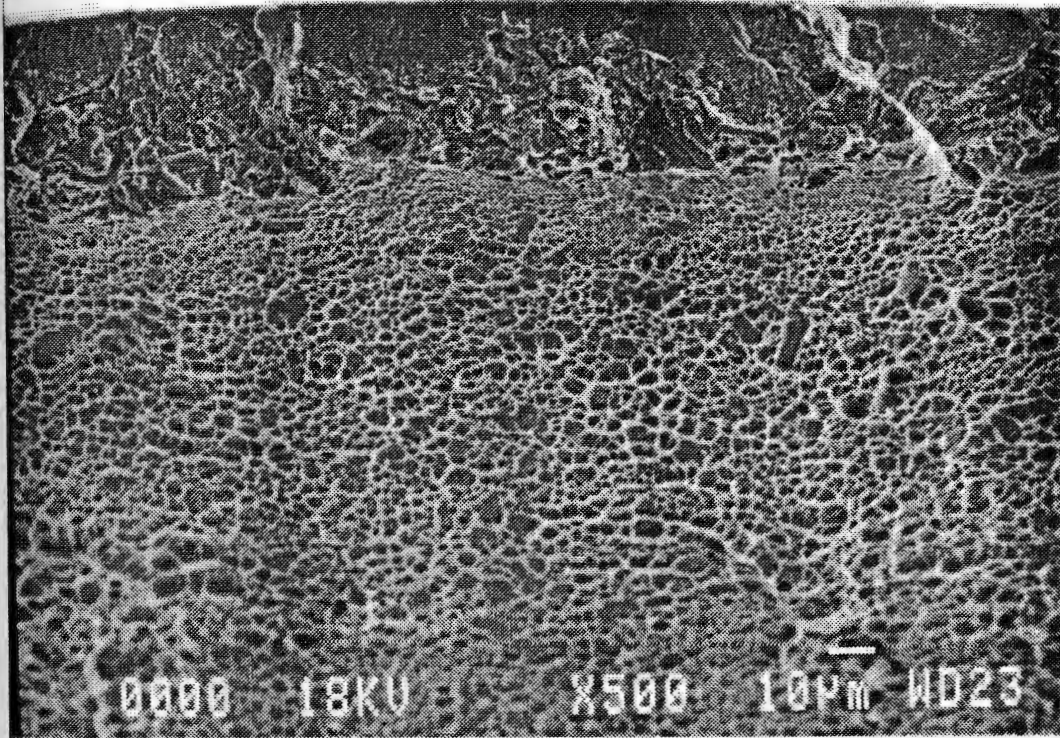


Fig. 4.15 – The fracture surface of 1.0 mm, tensile, and exposed specimen of Timetal – 21S with exposure parameters 650 °C, and 40 hrs

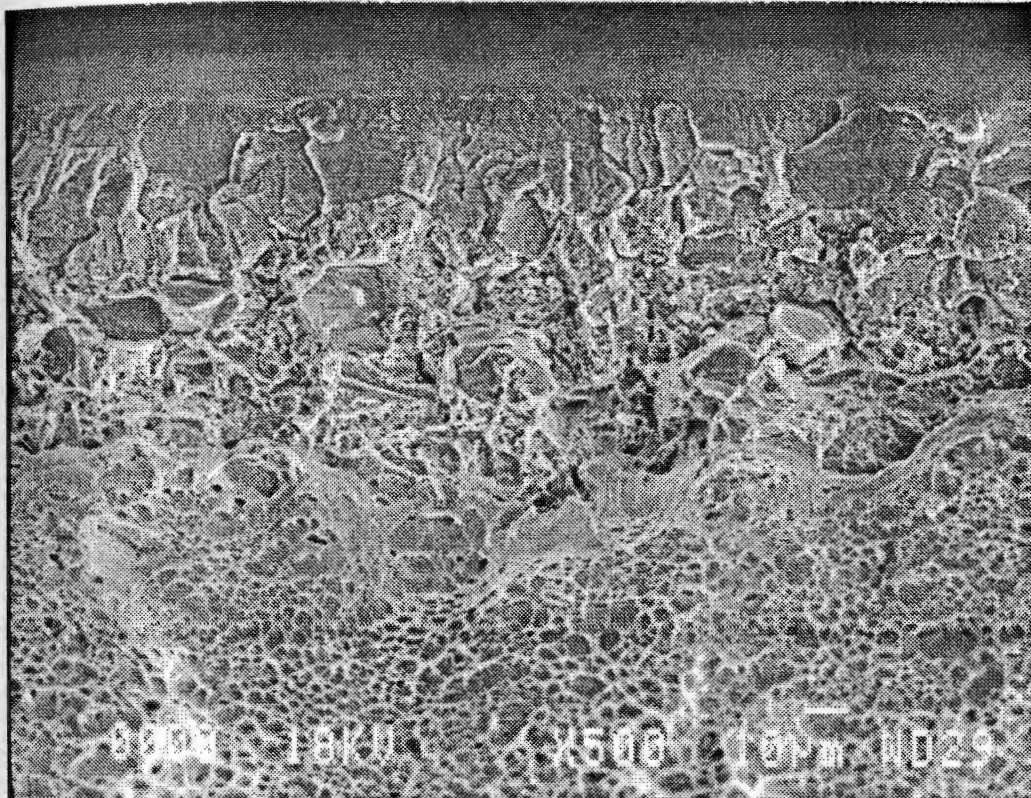


Fig. 4.16 – The fracture surface of 1.0 mm, tensile, and exposed specimen of Timetal – 21S with exposure parameters 650 °C, and 118 hrs

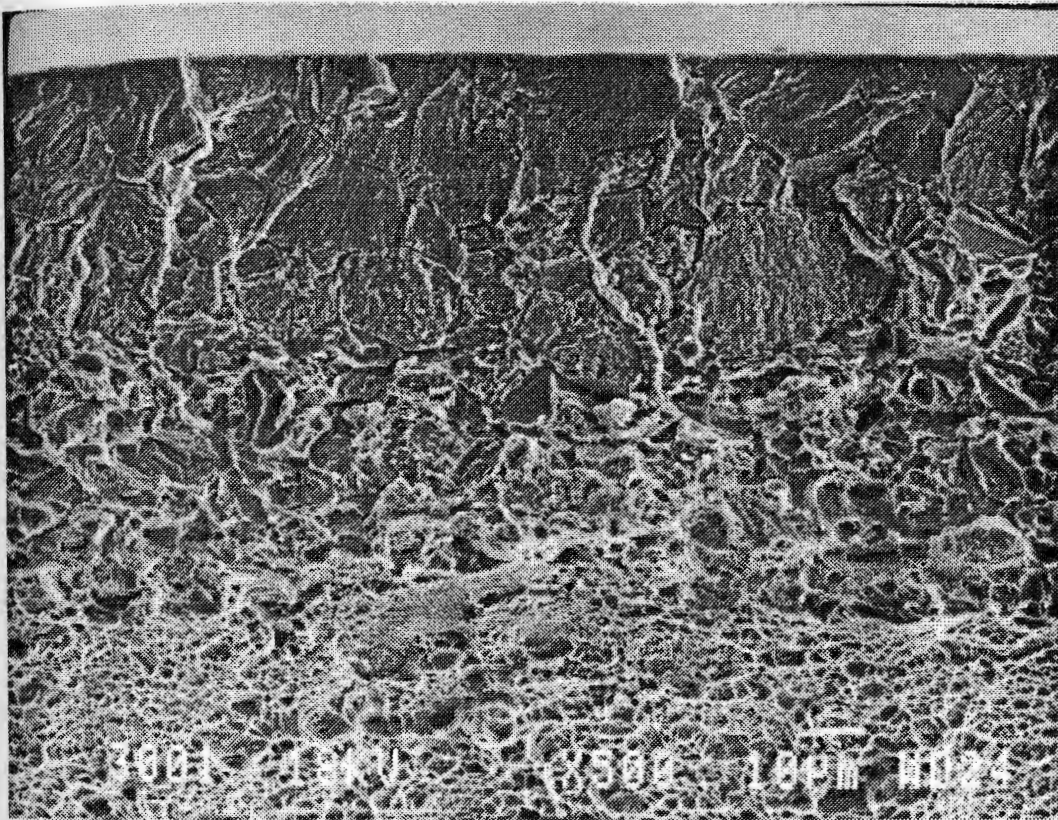


Fig. 4.17 – The fracture surface of 1.0 mm, tensile, and exposed specimen of Timetal – 21S with exposure parameters 693 °C, and 40 hrs

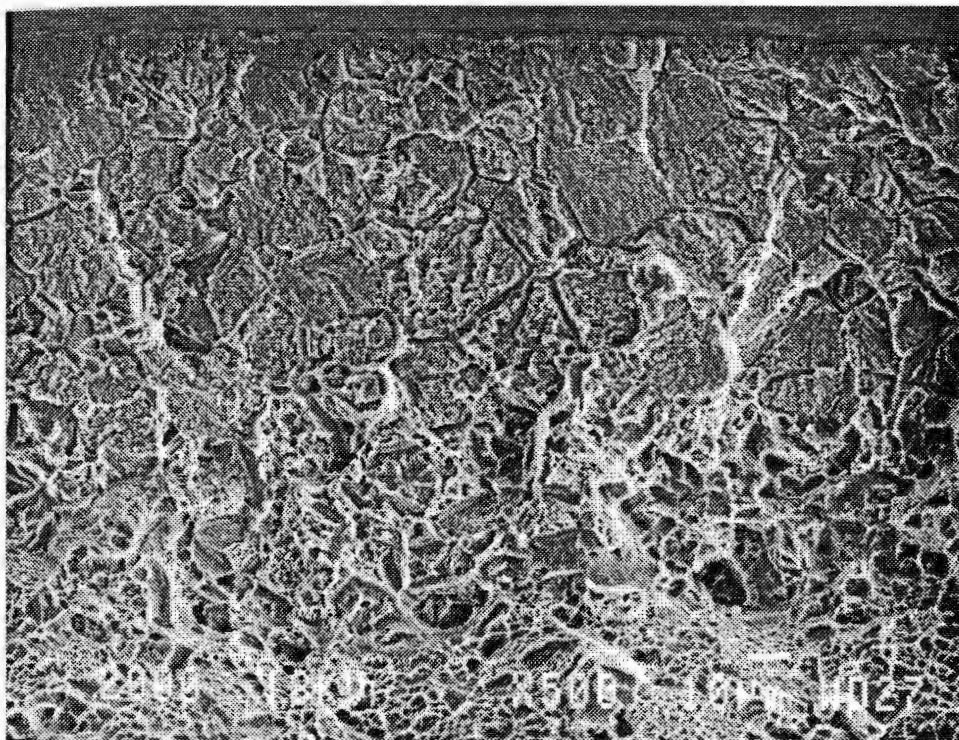


Fig. 4.18 – The fracture surface of 1.0 mm, tensile, and exposed specimen of Timetal – 21S with exposure parameters 693 °C, and 80 hrs

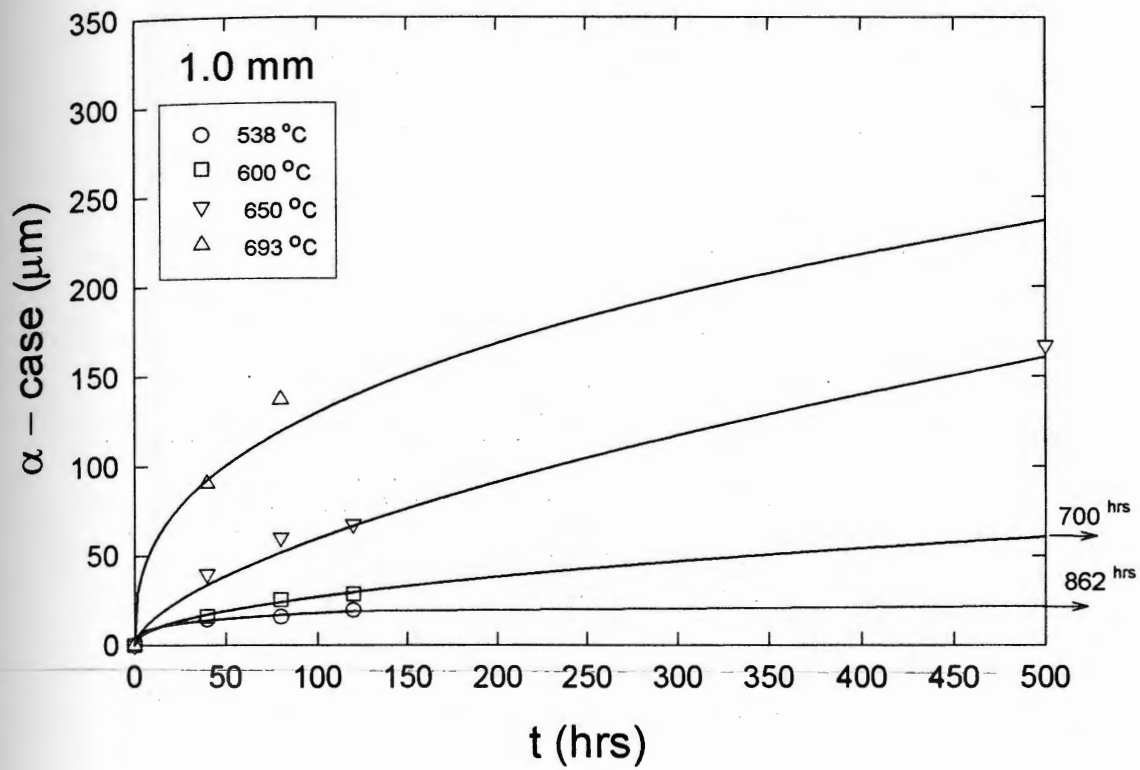


Fig. 4.19 – The effect of exposure parameters on the formation of alpha – case.

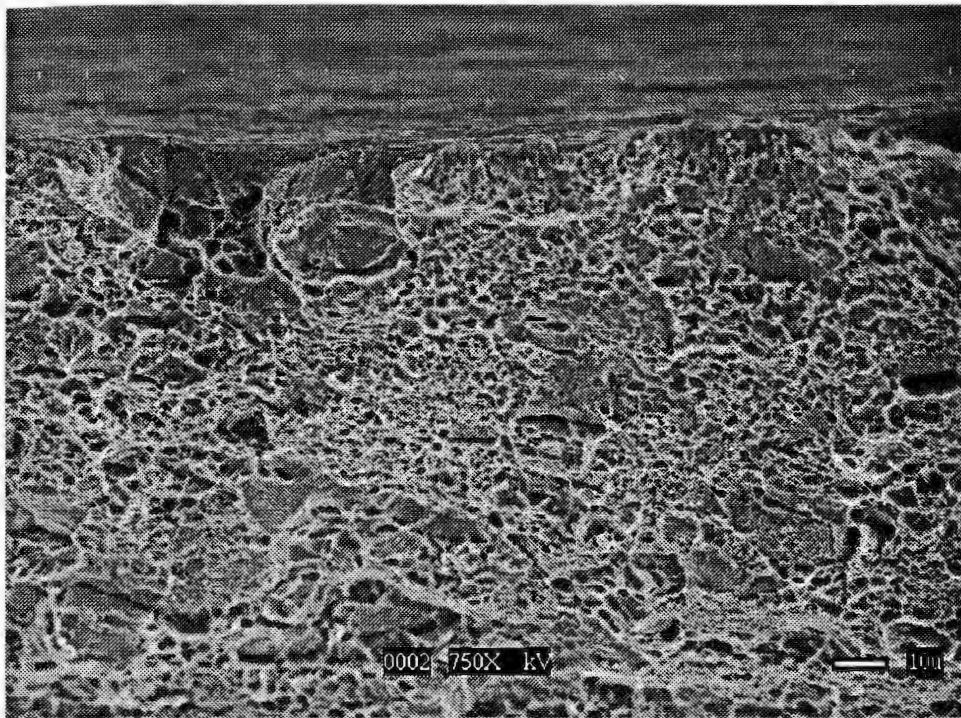


Fig. 4.20 – Specimen surface after the alpha - case layer is removed by the mechanical pickling of an exposed specimen with 118 hrs and 650 °C

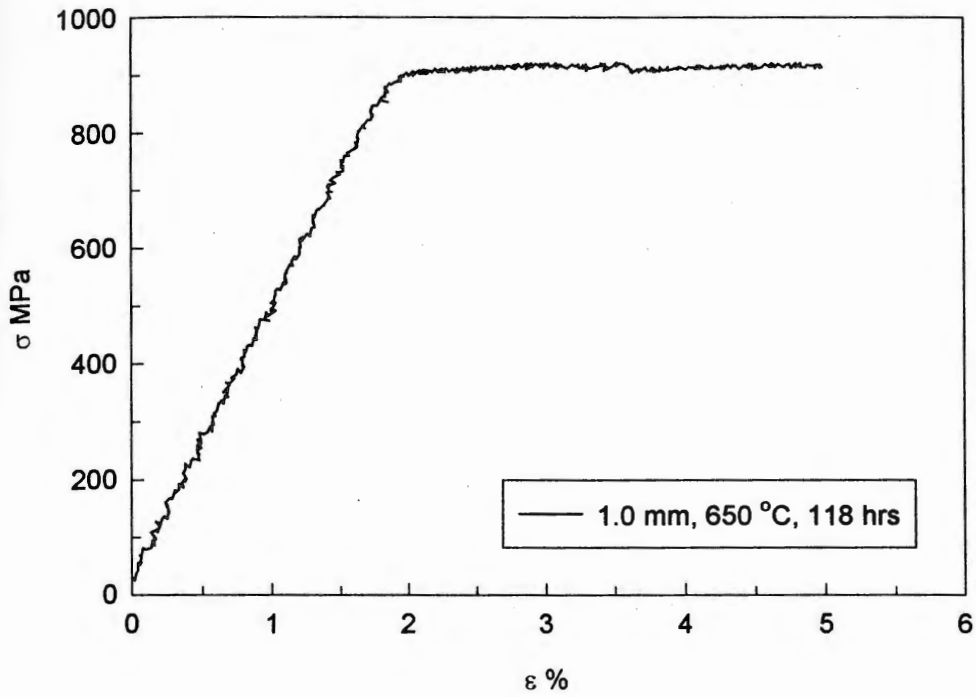


Fig. 4.21 - σ - ϵ relationship of 1.0 mm exposed specimen at 650 °C for 118 hrs after removing the oxide layer

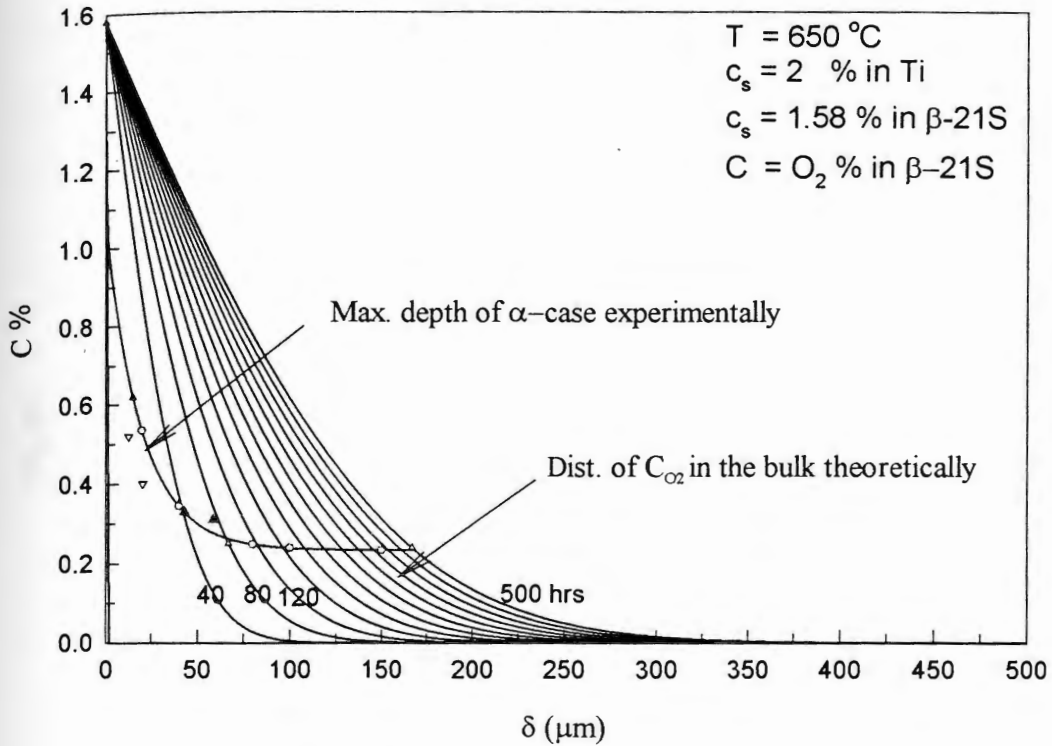


Fig. 4.22 – The distribution of the oxygen concentration (C) as function of the distance (x) measured from the surface of the test specimen and the maximum depth of oxygen penetration in the bulk of the specimen. Also, it shows the measured values of the alpha case in different specimens' thickness (0.12 and 0.39 mm) are in good agreement with 1.0 mm specimen thickness.

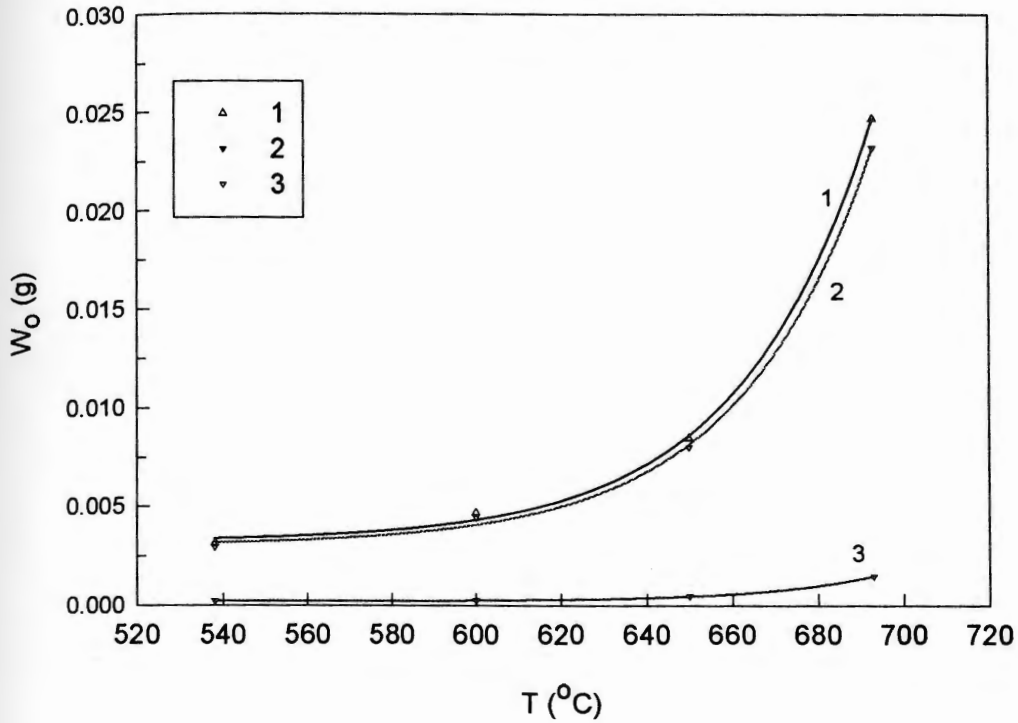


Fig. 4.23 – 1: total weight of oxygen diffused in the specimen, 2: weight of oxygen diffused in the specimen's bulk where the equivalent oxygen concentration in titanium is $C=0.5\%$, 3: weight of oxygen diffused in α -case where the equivalent oxygen concentration in titanium is $C=0.5\%$.

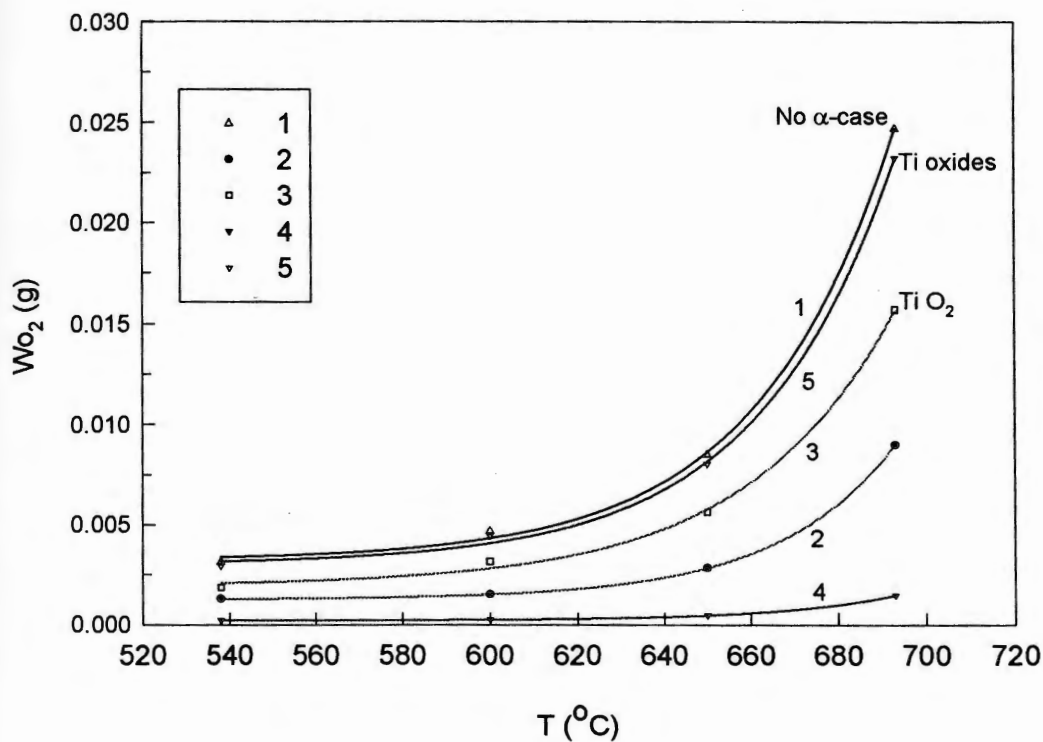


Fig. 4.24 – The weight gain in the bulk of the specimen at three cases of the surface layer; first, no oxide layer, second, oxide layer is TiO_2 , and third, oxide layer is titanium oxides. 1: total weight of oxygen diffused in the specimen. 2, 3: weight of oxygen diffused in oxide layer and in the bulk respectively where oxygen diffused in oxide layer and in the bulk respectively where the equivalent oxygen concentration in titanium is $C=0.5\%$.

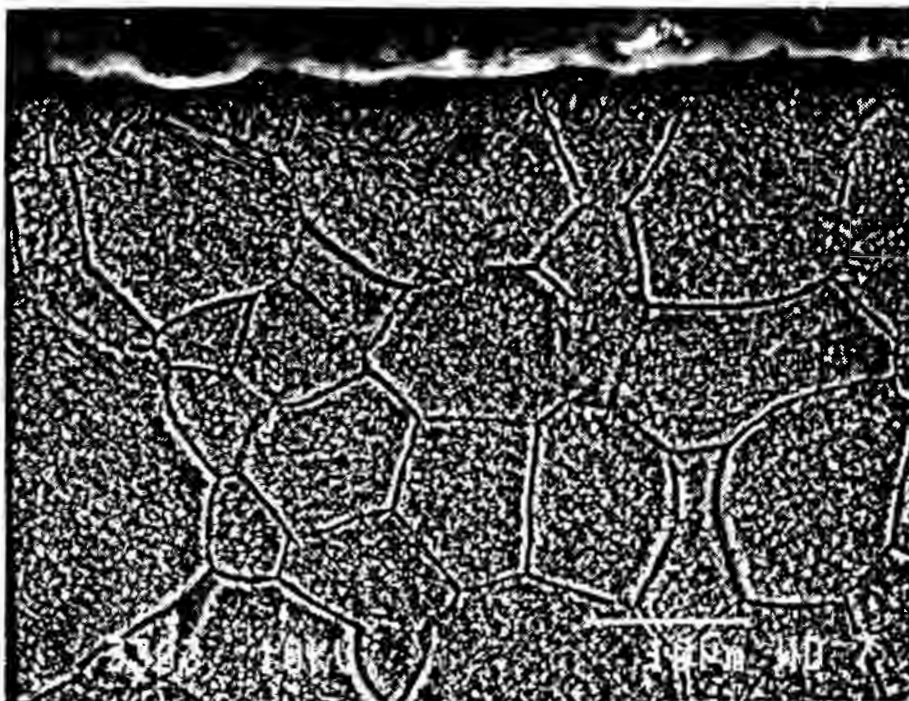


Fig. 4.25 – The microstructure at the surface of 1.0 mm heat treated specimen of Timetal 21S alloy

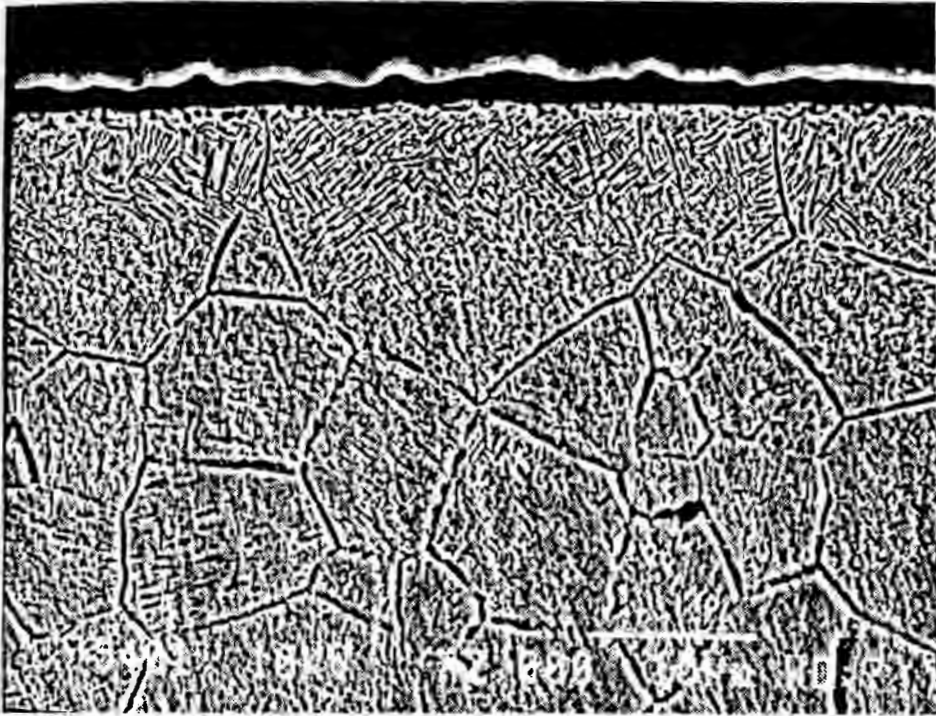


Fig. 4.26 – The microstructure at the surface of 1.0 mm Timetal – 21S exposed specimen with exposure parameters of 538 °C, and 100 hrs and magnification X 2,000.

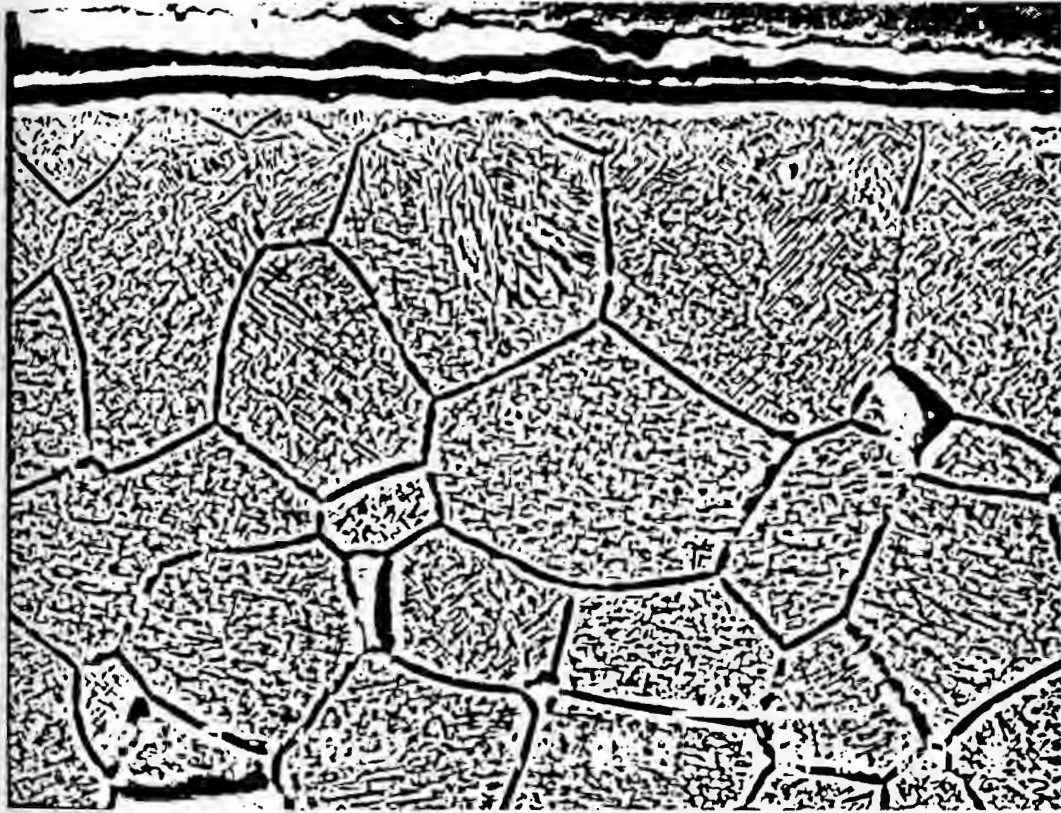


Fig. 4.27 – The microstructure at the surface of 1.0 mm Timetal – 21S expose specimen with exposure parameters of 650 °C, and 100 hrs.

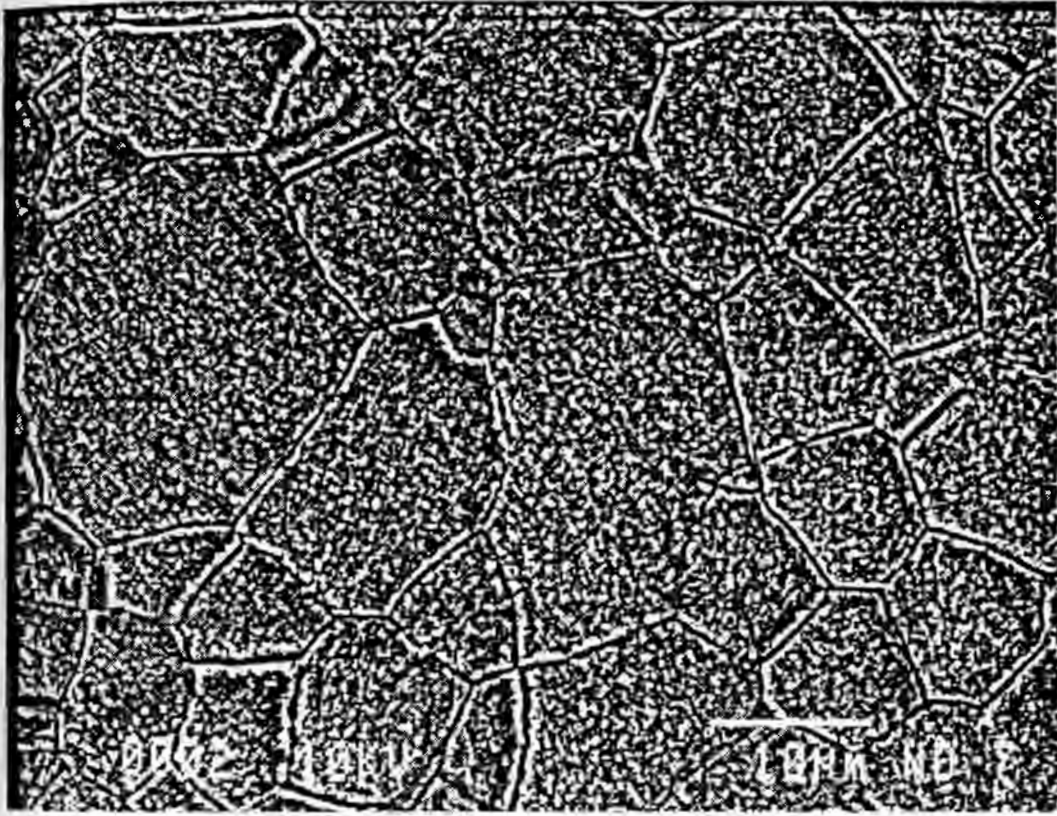


Fig. 4.28 – The microstructure in bulk of 1.0 mm heat treated specimen of Timetal – 21S alloy

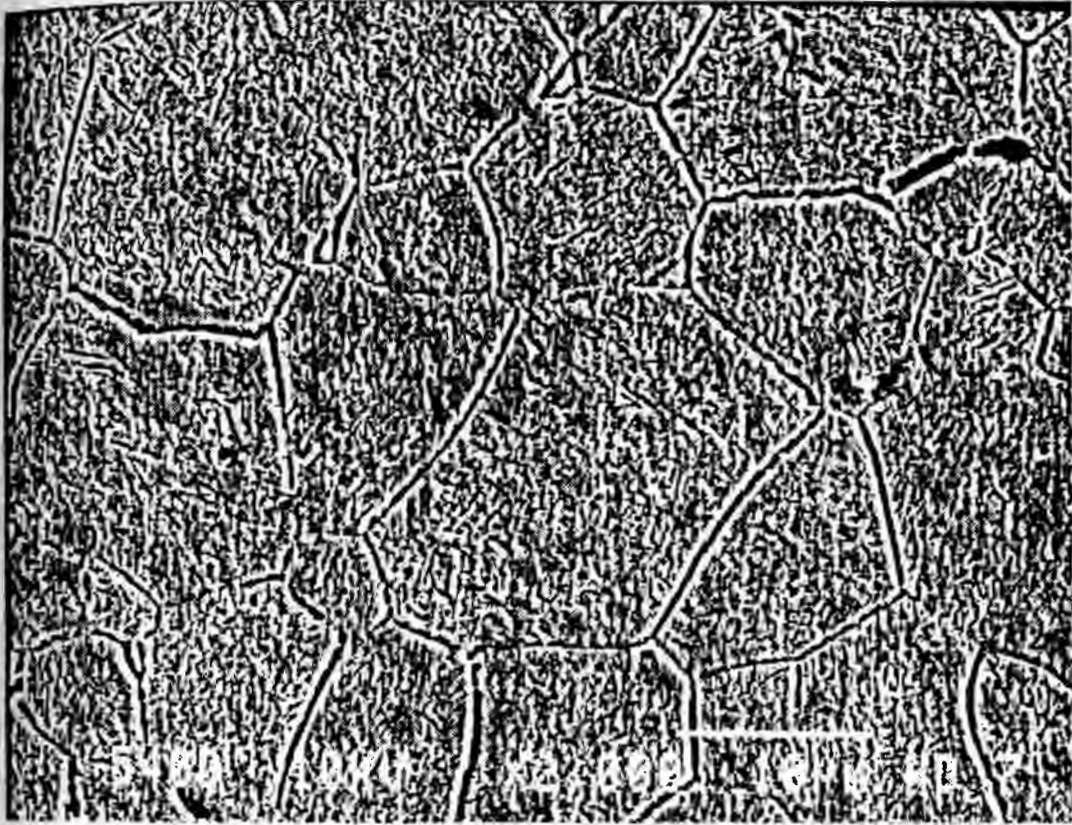


Fig. 4.29 – The microstructure in the bulk of 1.0 mm Timetal – 21S exposed specimen with exposure parameters of 538 °C, and 100 hrs.

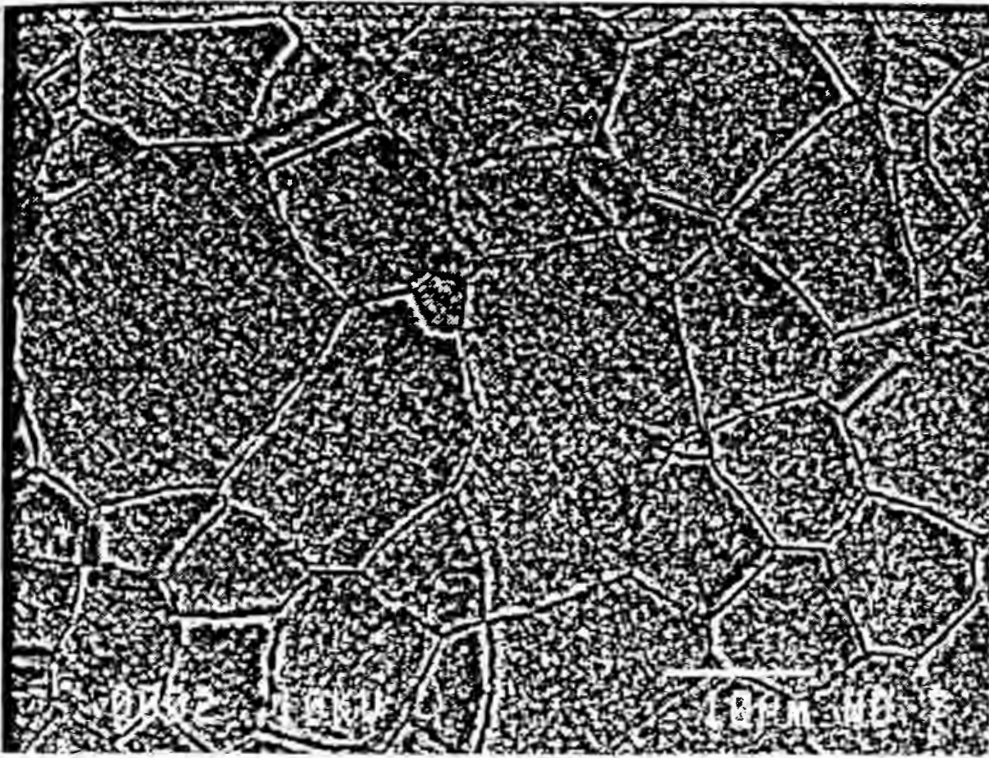


Fig. 4.28 – The microstructure in bulk of 1.0 mm heat treated specimen of Timetal – 21S alloy

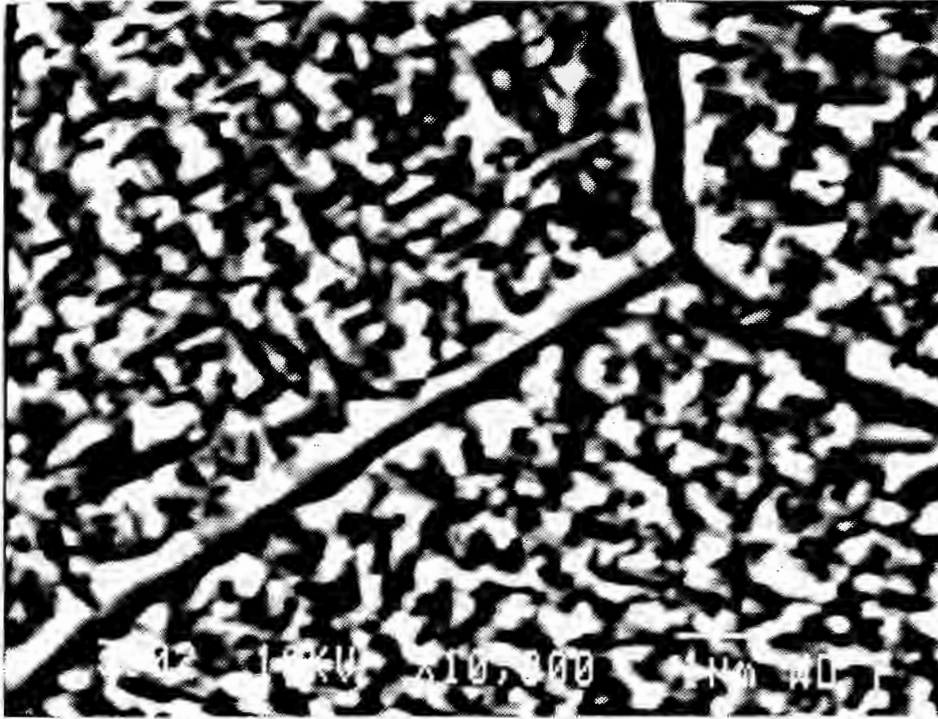


Fig. 4.31 – The microstructure in the bulk of 1.0 mm heat treated specimen with a magnification of X10,000

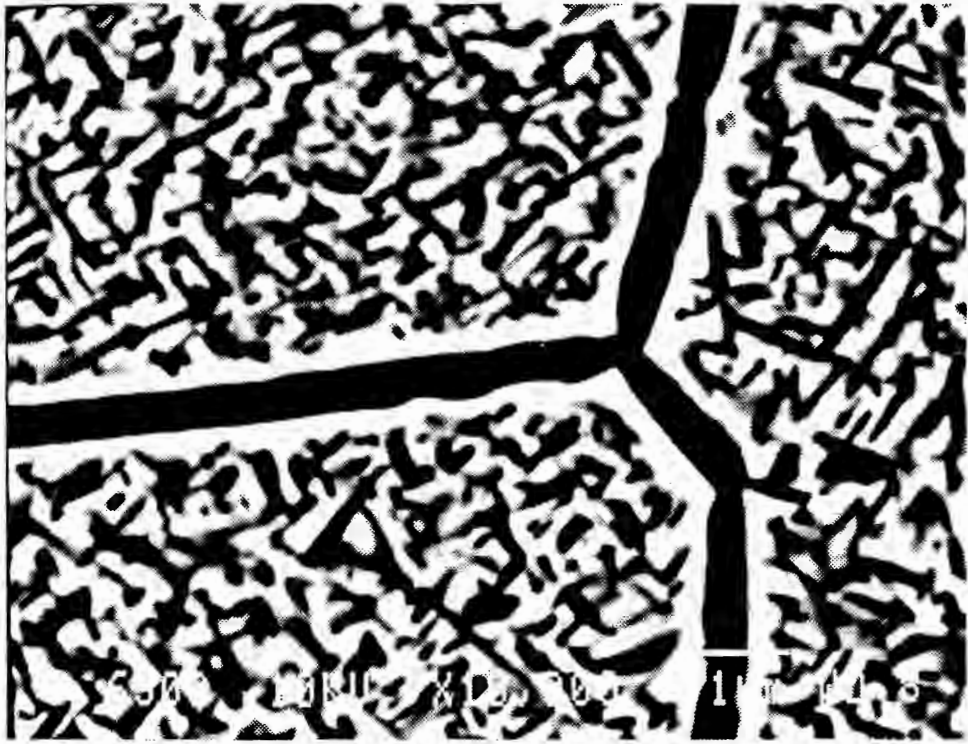


Fig. 4.32 – The microstructure in the bulk of 1.0 mm exposed specimen with exposure parameters of 650 °C, and 100 hrs, and a magnification of X10,000.

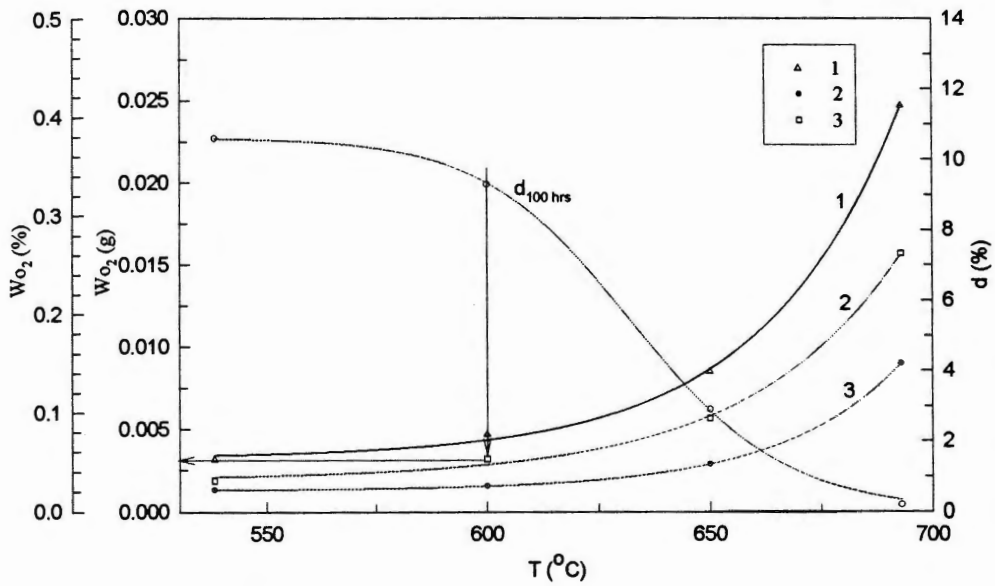


Fig. 4.33 - Vertical arrow from the beginning of the substantial loss of ductility to the horizontal arrow, which in turn pointing at the corresponding weight percentage of the diffused oxygen into the bulk of Timetal 21S. 1: total weight gain after exposure 650 °C /100 hrs. 2, 3: oxygen weight in the bulk and oxide layer (TiO_2) respectively after the same exposure.

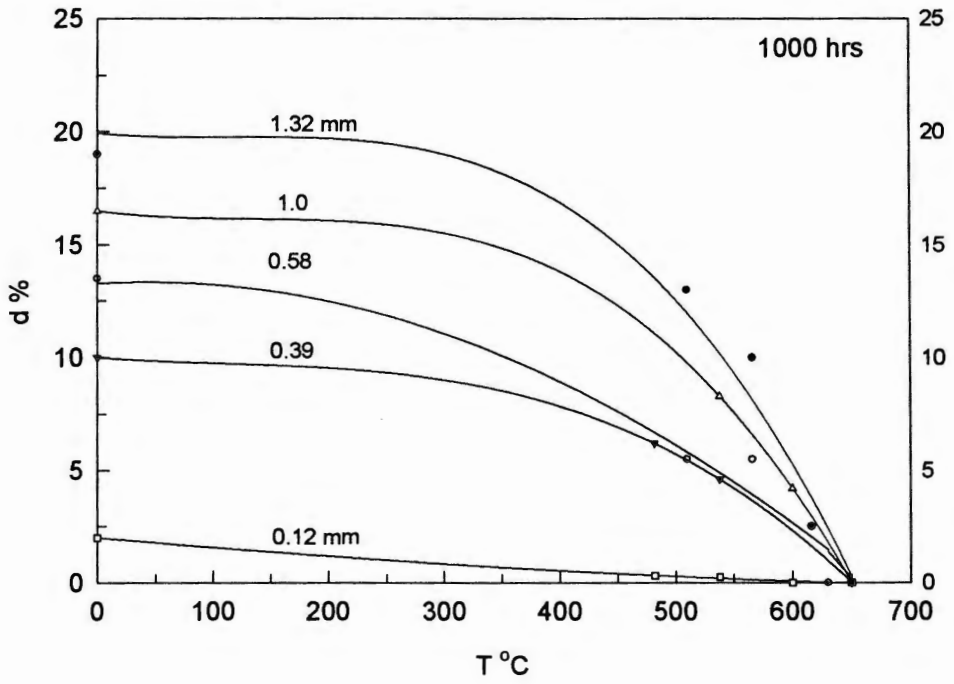


Fig. 4.34 – Ductility loss as function of temperature after exposure of 1000 hrs for β -21S sheet thickness of 0.12, 0.39, 0.58, 1.0, and 1.32 mm.

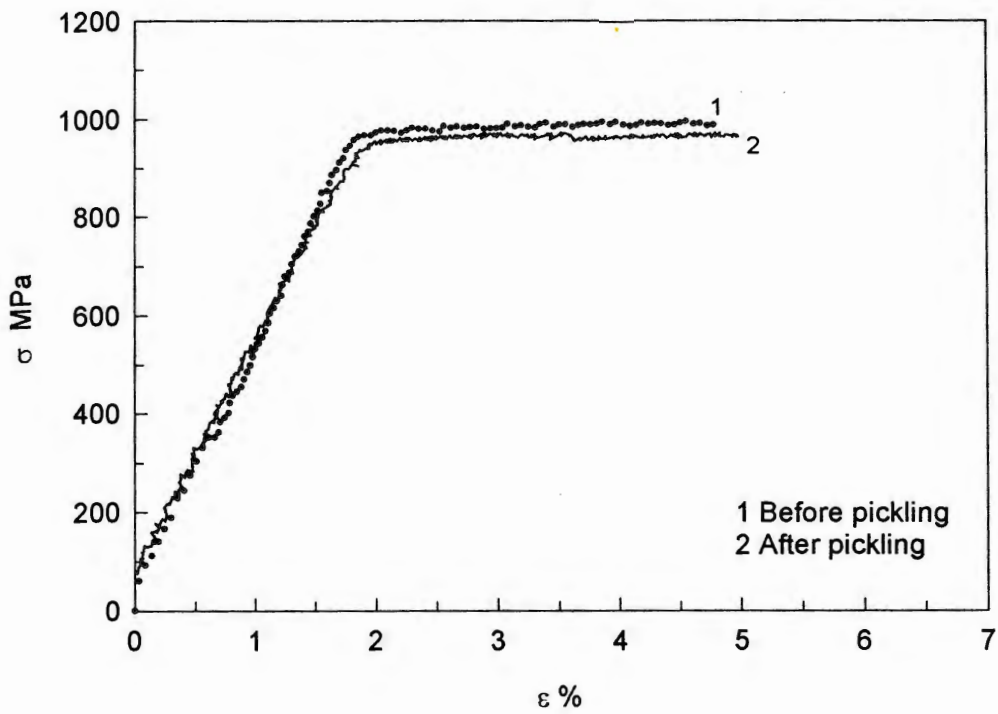


Fig. 4.35 – Stress-strain relationship of two exposed specimens at 650 °C and 118 hrs. 1: specimen before pickling, 2: Specimen after pickling

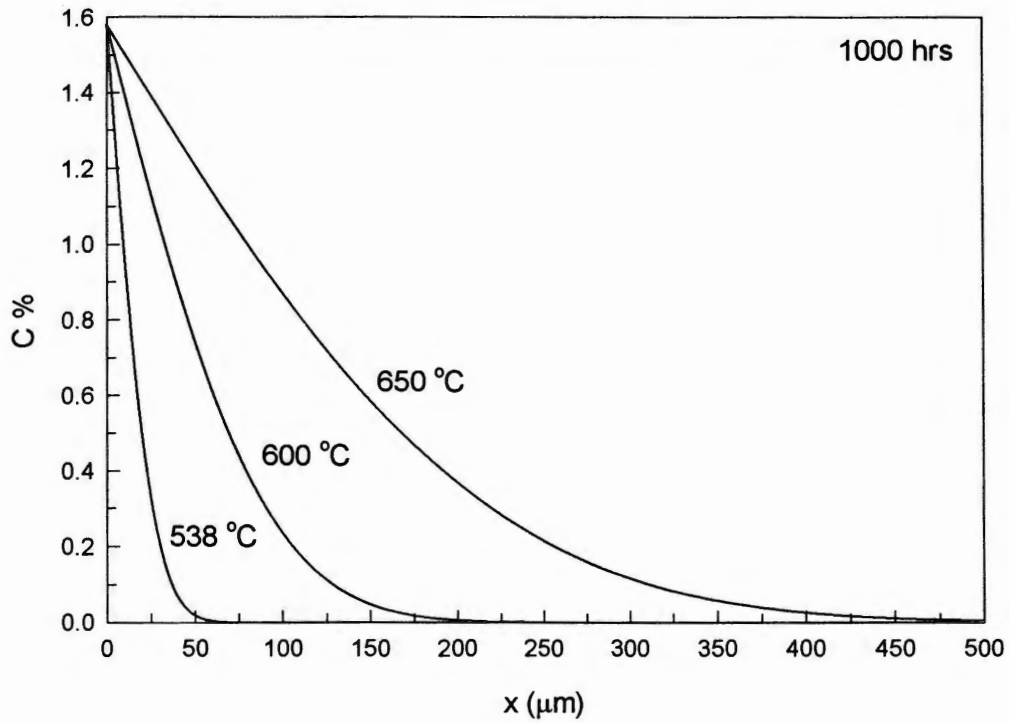


Fig. 4.36 – Theoretical Distribution of O₂ across the specimen's cross-section after exposure at 538, 600 , and 693 °C for 1000 hrs.

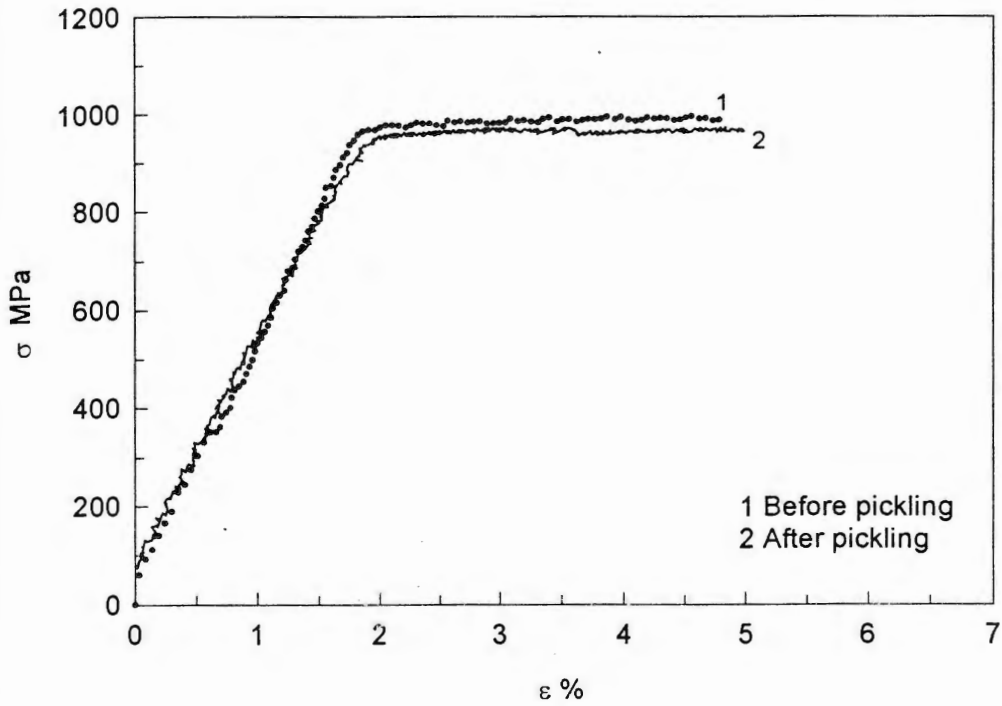
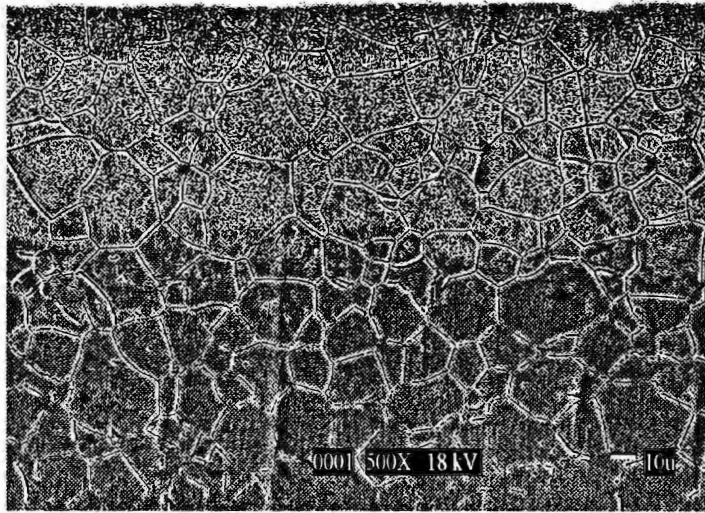
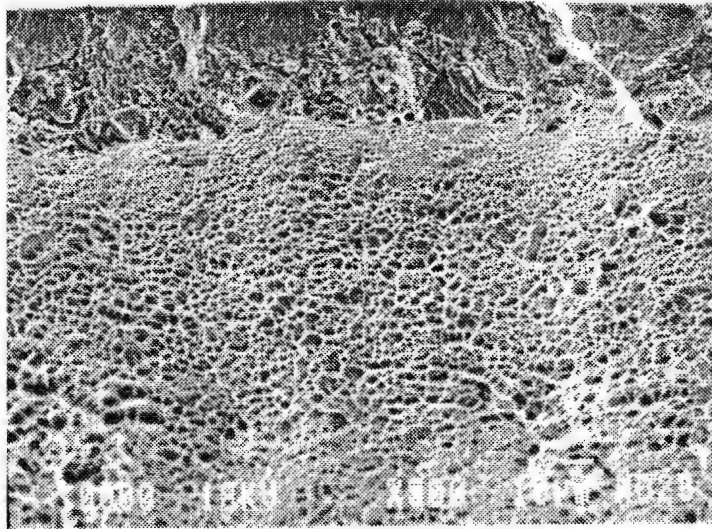


Fig. 4.35 – Stress-strain relationship of two exposed specimens at 650 °C and 118 hrs. 1: specimen before pickling, 2: Specimen after pickling



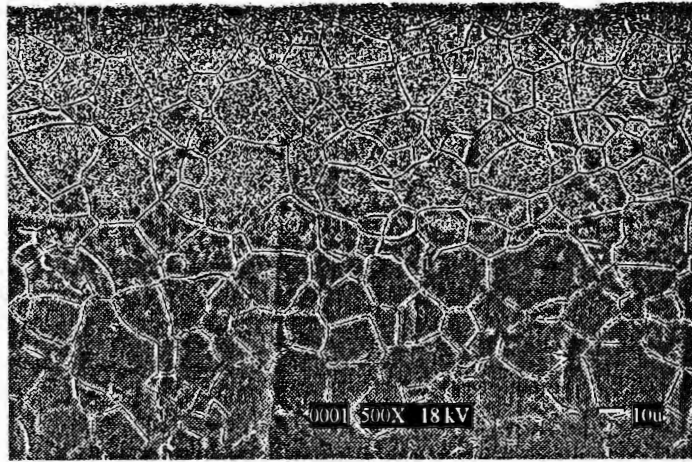
650 C - 40 hrs - 1 mm - (1R)

Fig. 4.38 – The distribution of Alpha phase after the decoration process in the exposed Timetal 21S specimen (with exposure parameters 650 °C, and 40 hrs) where the alpha phase distribution in the bulk disappeared.



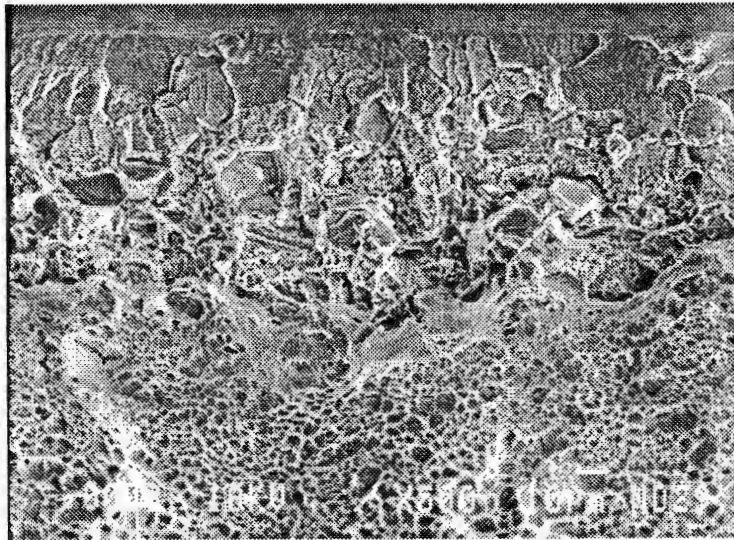
650 °C - 40 hrs - 1.0 mm

Fig. 4.39– The brittle tensile fracture surface to be compared with the alpha – case thickness in the following Fig. V.31 for the same exposure parameters



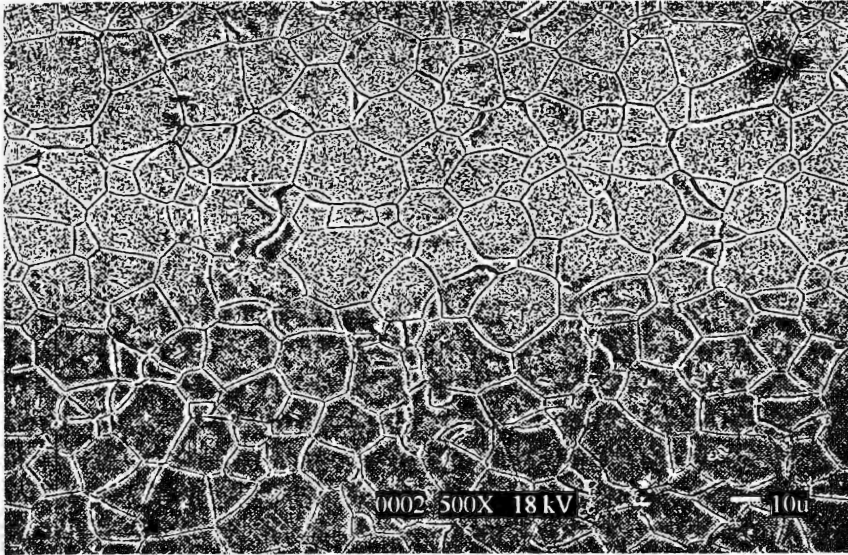
650 C - 40 hrs - 1 mm - (1R)

Fig. 4.40– The Alpha – case thickness layer to be compared with brittle tensile fracture surface in the previous Fig. V.30 for the same exposure parameters.



1.0 mm - 650 °C - 118 hrs

Fig. 4.41– The brittle tensile fracture surface to be compared with the oxide layer thickness in the following Fig. V.33 for the same exposure parameters.



650 C - 118 hrs - 1.0 mm

Fig. 4.42 – Shows the Alpha – case thickness layer to be compared with brittle tensile fracture surface in the previous Fig. V.32 for the same exposure parameters.

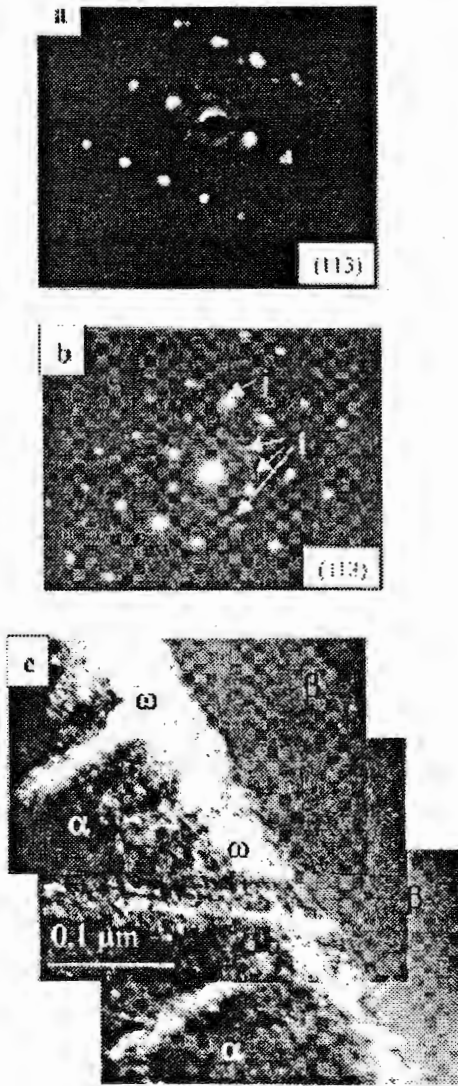


Fig. 4.43 - Characterization of ω phase in β -21S changes in (113) diffraction pattern with aging and exposure: a) 600 °C / 80 hrs; b) 650 °C / 500 hrs; c) dark field image for exposure 650 °C / 500 hrs.

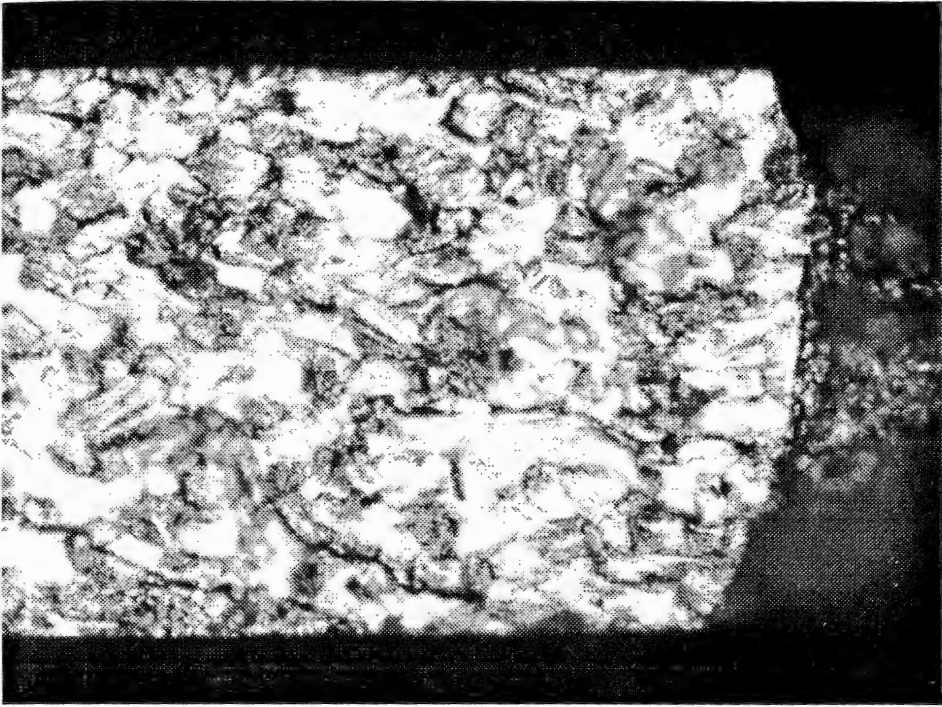


Fig. 4.44 – Shows the crack front of a center crack tension, 0.39 mm thickness, and heat-treated specimen due to a room temperature fatigue loading with a rate of 20 hz.

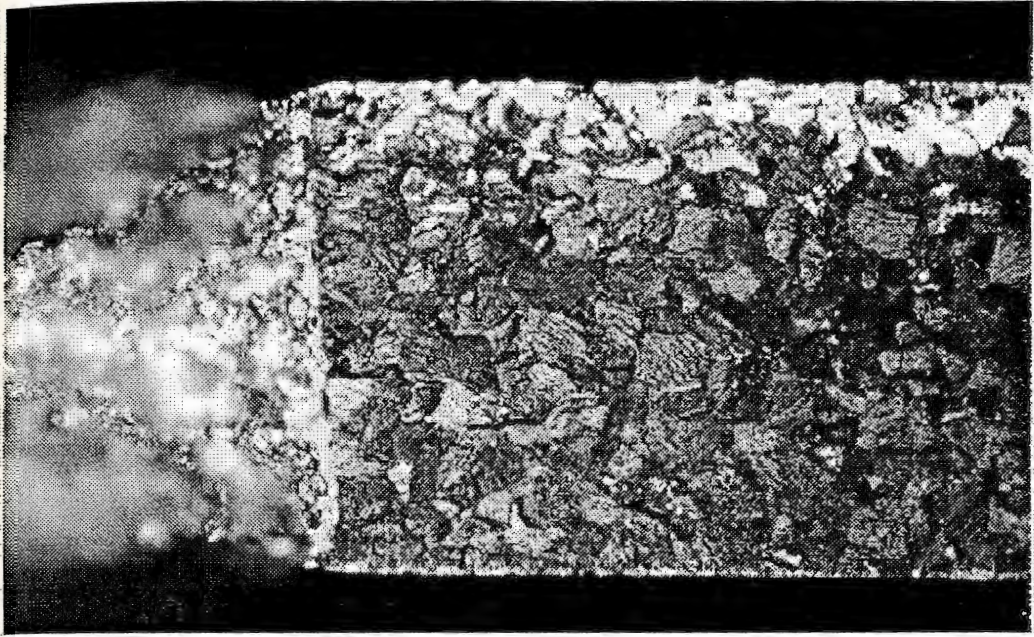


Fig. 4.45 – Shows the crack front of a center crack tension specimen with 0.39 mm thickness, and exposure of 538 °C and 40 hrs due to a fatigue loading with rate of 20 hz. X200

CHAPTER V: Conclusion and Recommendations

V.1 Conclusions

The recommended continuous operating temperature for Timetal 21S is below 540 °C. Application temperature for this alloy can, however, exceed this level, with attendant embrittlement due to oxidation. The present study examines the effects of exposures in air on the tensile ductility of fully aged Timetal 21S sheet specimens in temperature range 482 – 693 °C. In this thesis, the kinetics of the loss of tensile ductility is investigated as a function of exposure temperature and sheet thickness. The experimental embrittlement activation energies are estimated by determining exposure times at various temperatures to reach close to zero ductility at room temperature. The embrittlement kinetics is investigated for three different sheet thicknesses; 0.12, 0.39, and 1.0 mm. The morphology of the surface layer and changes in microstructure are examined using scanning electron microscopy (SEM) as a function of exposure conditions. Phase changes as a function of the exposure parameters are investigated using transmission electron microscopy (TEM). Kinetics of weight gain during exposure are also investigated. Results of this study show that two distinct embrittlement mechanisms exist within the temperature range mentioned above. At higher temperatures, >550 °C, the activation energy is 57 Kcal/mole indicating that the embrittlement process is controlled by diffusion of oxygen. Below 550 °C, the embrittlement activation energy approaches zero, a characteristic of a diffusionless athermal transformation. Furthermore, the SEM examinations reveal a protective oxide layer present only at temperatures higher than 550 °C. There is also

an indication of increased volume fraction of α phase in the vicinity of the surface.

TEM examinations reveal an increase of the isothermal ω phase as function of the exposure time increase. The current work results lead to these following conclusions:

- Thermal aging in vacuum does not degrade the ductility of an overage (OA) heat-treated specimen but thermal exposure (aging) in air environment does cause pronounced ductility loss.
- OA heat treatment provides better fatigue properties than the solution treatment and aging, STA heat treatment. Before any exposure, OA heat treatment provides better elongation and better ΔK_{th} on the expenses of the ultimate tensile stress (UTS) and yield stress (YS) in comparison to the STA heat treatment. After exposure, ΔK_{th} of the specimens with OA heat treatment is still higher than those specimens with STA heat treatment.
- Timetal 21S with OA heat treatment is stable during the exposure in the air up to 600 °C, but the level of the remained ductility depends on the contaminated volume fraction.
- Tensile stress of the OA heat-treated Timetal 21S was not affected up to exposure temperature 600 °C, but higher temperature than 600 °C caused a strength degradation. This indicated that the increase of the oxygen weight concentration more than 0.21 % in the bulk caused a decrease in the strength. That is because the increase of oxygen led to an increase of α -phase, which has less strength than β -phase, which is around 300 versus 800 MPa respectively.
- During the OA heat treatment the initial ductility is degraded due to a combination of two phases α and ω , however the variation of the initial ductility

as function of the specimen's thickness is due to the martensitic deformation of β $\rightarrow \omega$ phase.

- During the exposure process, loss of ductility has two different rates, fast and slow rates. Thicker specimens will take longer period of exposure time to reach the slow rates than thinner ones. Also, the ductility value at the starting time of the slow rate for the thicker specimen is higher than for thinner one. The interpretation of these behaviors is, during the same exposure time, the oxygen weight concentration, O_2 wt %, in the bulk of the thinner specimen will be higher than that O_2 wt % in the thicker specimen.
- 34 % fraction volume of α phase is the highest saturation value of α phase in the heat-treated Timetal 21S.
- Oxygen is the main element of air lead to the embrittlement of Timetal 21S. Activation energy of oxygen in Timetal 21S is 57.75 Kcal / mole. This activation energy agreed with the one extracted from the literature based on the values of the activation energy in both of α and β phases of titanium, which was found to be 57.46 Kcal / mole for β -21S alloy. These two values did not agree with the one published by Wallace [7] which shows a value of 41.2 Kcal / mole. However, one of the main causes of that difference could be the difference of the initial conditions of the specimens, such as the fracture volume of α phase, which in turn affects the amount of the diffused oxygen into the specimen because the diffusion coefficient is function of the phase type.
- The embrittlement process at exposure temperature higher than 600 °C is an internal process not surface embrittlement process. Removing the oxide layer from the

surface of an exposed specimen at 650 °C for 118 hours recovers only a small value of the ductility loss. The current work shows that the results of Parris and Bania [16] which showed that “the original ductility is restored after exposure by removing the oxygen contaminated surface layers” is only applicable up to around 600 °C only.

- The loss of ductility rate becomes substantial at a critical value around 0.21 % of O₂ wt % in the Timetal 21S, while Parris et al [16] show 0.25 %. The difference between the two critical values could be interpreted due to the method which used to introduce the oxygen into the material. First critical value (0.21 %) was calculated to define the O₂ wt % due to a diffusion process where the oxygen concentration varies across the material's cross section and another matters diffuse during the exposure process. In the other hand, the second critical value (0.25 %) was calculated for a material with a homogenous chemical composition where no gradient of the O₂ wt % neither a possibility of another matter diffusion.
- The oxide layer arrested around 1/3 of the diffused oxygen amount at any exposure parameters, this gives a very good advantage to β-21S by keeping the oxygen percentage in the bulk lower than 0.21 % up to a temperature close to 600 °C.
- The O₂ wt % at the alloy / air interface is estimated to be 1.58 %. The exact value depends on the chemical composition of the material after the exposure. Determining the chemical composition across the oxides-case layer will require some measurements.
- SEM fractography at the surface layer showed a brittle surface layer, this is because the existence of a chemical bond between O₂ and the contents of Timetal 21S.

- Diffusion coefficient, D , for the OA heat-treated specimens of Timetal 21S can be assumed constant during the exposure process.
- Any increase in the O_2 wt % more than the initial value of 0.15 % causes an increase of the crack growth rate 2 – 3 times and degrades the ΔK_{th} from 4.5 to 2.8 $MPa\sqrt{m}$.
- The change in ΔK_{th} was from 4.5 to 2.8 $MPa\sqrt{m}$ in the current study, and 2.8 to 2 in [26]. The difference between the two works could be due to the difference of the specimen's heat treatments, which are OA and STA respectively, which controls the material resistance to the oxygen diffusion.

VI.2 Future work

- Oxygen was found to be the main element of the air content diffused into the bulk of Timetal 21S and caused its embrittlement and strength degradation. Therefore, it will be very interesting to expose the material to oxygen only (not air) to find the effect of the other gases on the material's embrittlement, especially the activation energy and the critical value of the oxygen weight concentration.
- The evaluation of the oxygen concentration in the bulk depends on the chemical composition in the surface layer (oxides-case) of β -21S which was changed due to the exposure, therefore it is important to measure the exact chemical composition across this surface layer.

Appendix 1

A. 1 - Free – Energy

Free energy is a thermodynamic property of solids. In the solid solutions a spontaneous reaction frequently occurs in metallurgy (metal transformation), with a trend to lower the free energy

$$F = E + PV - TS$$

where F is the free energy, E is the internal energy, P is the pressure, V is the volume, T is the absolute temperature, and S is the entropy. The previous equation may be simplified due to the facts that most of the metallurgy reactions occur in constant pressure and temperature and the change in volume is very small. Thus the previous equation can be rewritten as follow

$$F = E - TS$$

It should be mentioned that $dS > dQ/T$ for any spontaneous reaction because it is irreversible reactions. Measuring dS is not of our interest at the moment.

Appendix 2

A. 2 - Moly Equation

Mo. Eq. = $1.0 * (\text{Wt. \% Mo}) + 0.67 * (\text{Wt. \% V}) + 0.44 * (\text{Wt. \% W}) + 0.28 * (\text{Wt. \% Nb}) + 0.22 * (\text{Wt. \% Ta}) + 2.9 * (\text{Wt. \% Fe}) + 1.6 * (\text{Wt. \% Cr}) - 1.0 * (\text{Wt. \% Al})$.

In the above equation the constant before each alloying element reflects the ratio of the β_c Table 2 for the moly baseline (i.e. 10 for titanium alloys) divided by the β_c for the specific element.

Example Timetal-21S which has a chemical composition of (15 Mo - 2.7 Nb - 3 Al - 0.2 Si)

Mo. Eq. for Timetal-21S = $1.0 * 15 + 0.28 * 2.7 - 3 * 1 + 0 * 0.2 = 12.756$

Appendix 3

A. 3- Random Walk

Two types of the random walk: (1) Random walk, (2) Correlated random walk will be discussed here to clear one picture of the nature of the diffusion mechanisms. Figs. II.20 and II.21 are representing the 'diffusion by a vacancy mechanism', and the 'diffusion by an interstitial mechanism' respectively which are examples of the two different types of the random walk.

The jump frequency tells, how often we may expect atoms to leave their normal positions, but it has nothing to say about the direction the atom will take for any particular jump. Fig. 20 shows that the impurity atoms in this hypothetical two-dimensional crystal can reach any of four interstitial positions by one unit jump. All of these four positions are completely equivalent, and the probability that the impurity will go to a particular one as a result of a particular jump is $\frac{1}{4}$. This means that the atom does not care which it jumps and it is purely a matter of chance which direction it takes. The reason for this is that the impurity atom spends such a long time between jumps (in vacancies compared to the time of one atomic vibration) that, after a jump, the impurity comes to equilibrium with the rest of the crystal before the next jump takes place. The preferential motion that resulted in the first jump is thereby lost, and the second jump again occurs at random (where the host atoms have the same probability as the impurity atom to move to the vacancy). All this is just another way of saying that the 100,000 or more atomic vibrations between jumps are enough to erase the atom's memory and it forgets from where it came. Actually, 100,000

vibrations are more than enough, since it only takes somewhere between 10 to 50 atomic vibrations to bring a distributed atom back to equilibrium.

The impurity atom accordingly takes a very haphazard path as it wanders through the crystal. This path is said to constitute a random walk; because a particular jump has no correlation with a previous jump, the motion is said to be uncorrelated.

Not all random walks are uncorrelated, however; for example, consider the motion of a substitutional impurity atom that jumps by a vacancy mechanism. In order to jump, the impurity must have a vacancy alongside it. After the jump takes place, a second jump would be uncorrelated with the first if the impurity had equal probability of making the second jump in any direction. But because we are dealing with a vacancy mechanism, this would require that the sites surrounding the impurity have equal probability of being vacant. But the jumping atom just came from a site that is now vacant, and “the time that elapses before this vacancy moves away is of the same order as the time between jumps”. Of all the sites surrounding the atom as it prepares to make its second jump, the site it came from has a higher probability of being empty than the others are. The two jumps are therefore correlated because the impurity atom is more likely to go back where it came from when it makes its second jump than to strike out in a new direction. If the degree of correlation is very high, the impurity atom jumps back and forth between two positions “many times before it moves” to some new position.

In such a case, the jump frequency of the impurity atom into a vacancy is much higher than the jump frequency of a host atom into a vacancy. A substitutional impurity atom is said to perform a correlated random walk. The degree of correlation

is important in understanding the detailed nature of the diffusion mechanism. So all the interstitial diffusion atoms perform a random walk not a correlated one.

Appendix 4

A. 4- Homogenous Point Defect

We have seen that atoms in both of the substitutional and interstitial diffusion they jump in a random walk pattern. Also we know that the free energy is a thermodynamic property, which controls the concentration of the vacancies and the interstitial atoms. Based on these two previous facts, one may now figure the importance of calculating the atom frequency r , which the atom has in performing the random walk in both of the substitutional and interstitial diffusions. Having in mind that the resultant motions for the homogenous point defect is zero.

Recall, that the change of the free energy (ΔF) in the metallurgy (where metal transform in a spontaneous reaction) can be assumed as:

$$\Delta F = \Delta E - T\Delta S$$

where ΔF = the change in the free energy due to introducing the vacancies or interstitial mixture within the pure metal atoms (or alloy atom), so one can write ΔF equal F_p where subscript here means the free-energy due to a point defect (vacancies or interstitial atoms etc.)

ΔE is the internal energy increase due to the vacancies or substitutional atoms, as shown in the free energy App. 6, which can be written as ' $n_p w$ '. Where n_p is the number of vacancies or interstitial atoms, w is the work required to introduce a vacancy or an interstitial atom into the pure metal lattice.

$$\Delta E = n_p w$$

ΔS is the increase of entropy (entropy of mixing) due to two reasons. The first is due to the presence of vacancies or interstitial atoms, as shown in mixing entropy (S_m) App. 7 and the second due to the vibrational entropy ($n_p s$)

$$S_m = - n k [C \ln (C) + (1- C) \ln (1- C)]$$

where n is total number of atoms ($n_A + n_B$), k = Boltzmann's constant, C = concentration of atom A, $(1 - C)$ = concentration of atom B, n_p = total number of vacancies or interstitial atoms, and s = vibrational entropy due to one vacancy or interstitial atom.

The above equation applies directly to the present problem (the presence of vacancies or interstitial atoms) if we consider mixing of lattice points, in which there are two types of lattice points: one occupied by atoms, the other unoccupied (in vacancies case) or occupied with the interstitial atoms. If one can imagine a box has two compartments, one filled with occupied lattice positions and the other filled with empty position (vacancies) or occupied interstitial atoms, as shown schematically in Fig. II.19-A, the corresponding mixed state in the box is shown in Fig. II.19-B

The present problem consists of mixing n_o objects of one kind with n_p of another kind, with a total number of (n_o+n_p) to be mixed. Therefore, one can make the following substitutions in the mixing-entropy equation:

$$n = n_o + n_p = 1$$

$$C = C_p = \frac{n_p}{n_o + n_p}$$

$$(1 - C) = C_o = \frac{n_o}{n_o + n_p}$$

where C_p is the concentration of vacancies or interstitial atoms, and C_o is the concentration of occupied lattice positions (the concentration of the pure metal). If the above quantities are set into the mixing-entropy equation, we have

$$S_m = -(n_o + n_p) k \left[\frac{n_p}{n_o + n_p} \ln \frac{n_p}{n_o + n_p} + \frac{n_o}{n_o + n_p} \ln \frac{n_o}{n_o + n_p} \right]$$

Simplifying the above Eq.

$$S_m = k [(n_o + n_p) \ln(n_o + n_p) - n_p \ln(n_p) - n_o \ln(n_o)]$$

The free-energy equation can be modified by the substitution for ΔE , ΔS . The free-energy equation for introducing vacancies or interstitial atoms may be now written as

$$\begin{aligned} F_p &= n_p w - (n_p s + S_m) T \\ &= n_p w - n_p s T - k [(n_o + n_p) \ln(n_o + n_p) - n_p \ln(n_p) - n_o \ln(n_o)] T \end{aligned}$$

As we recall, that the metallurgy reaction is spontaneous which in turn means that this system (the system which introduce the vacancies or interstitial atoms in the lattice) minimizing its free-energy to reach equilibrium for the system crystals. So, as a result to reach that equilibrium, the derivative of F_p with respect to n_p must equal zero, the temperature being held constant. Thus,

$$\frac{dF_p}{dn_p} = w - sT - kT \left[\frac{1}{(n_o + n_p)} + \ln(n_o + n_p) - n_p \frac{1}{n_p} - \ln n_p \right]$$

$$0 = w - sT - kT \left[\ln \frac{n_p}{(n_o + n_p)} \right]$$

$$\frac{n_p}{(n_o + n_p)} = e^{-\left(\frac{w-sT}{kT}\right)}$$

In general, it has been found that the number of vacancies or interstitial atoms (n_p) in a metal crystal is very small when compared with the number of atoms

$$\frac{n_p}{n_o} = e^{-\left(\frac{w - sT}{kT}\right)}$$

(n_o). Therefore the

above equation can be modified to give

If both the numerator and the denominator of the exponent of the above equation are now multiplied by N , Avogadro's number (6.03×10^{23}). It will define the energy required to accomplish an equilibrium reaction per or by introducing a mole of defect point (such as vacancies or interstitial atoms). Therefore the above equation can be modified to give

$$\frac{n_p}{n_o} = e^{-\left(\frac{Nw - NsT}{NkT}\right)} = e^{-\left(\frac{Q_f - sTN}{RT}\right)}$$

Where Q_f is the heat of activation, which is, the work required to form one mole of vacancies or interstitial atoms, N is Avogadro's number (number of molecules in a mole) = 6.03×10^{23} , k is Boltzmann's constant, and R is universal gas constant = 2 cal/(mole-°K)

But, the vibrational entropy is constant for constant temperature. Therefore the

$$\frac{n_p}{n_o} = e^{-\left(\frac{Q_f - sTN}{RT}\right)} = B e^{-\frac{Q_f}{RT}}$$

previous equation can be modified to give

where B is a constant equal $\exp(sTN/RT)$

So, we got the equation of the solubility (or the concentration) of vacancies or interstitial atoms in a pure atom system, which perform a spontaneous reaction to reach the equilibrium (minimum free energy).

So far nothing has been mentioned about how many jumps the atom makes per second (frequency) when the crystal in equilibrium in other words when the crystal contains an equilibrium number of vacancies or interstitial atoms.

It is found that the vibrational energy distribution of atoms in a crystalline solid is a 'Maxwell-Boltzman Distribution' where the probability 'p' that an atom has an energy equal or greater than a certain energy say q_0 as shown in Fig. II.22 which can be expressed as

$$p = A'e^{-\frac{q_0}{kT}}$$

where k is Boltzman factor, T is the temperature, and $A' = \text{Constant}$

This probability p should be proportional to the number of atom jumps per second r_p into a vacancy or interstitial site (having in mind we did not yet account for the existence of other atoms around the site)

$$r_p = Ae^{-\frac{q_0}{kT}}$$

where $A = A' \cdot N$ the proportionality constant, and N (Avogadro's number) now multiplies both the numerator and the denominator of the exponent of the above equation

$$r_p = Ae^{-\frac{Q_m}{RT}}$$

where Q_m is the energy (activation energy) required to move an atom into a mole of vacancies or interstitial sites.

Now, to get the average frequency per atom r . It is obvious that r_p (the frequency of atom into a vacancy or interstitial site) time n_p (the number of vacancy sites or interstitial atoms in a system) will give us the total frequency in the system as if only one atom exist. So, we must divide the previous result by the total number of atoms in the system

$$r = \frac{n_p}{n_o} r_p$$

$$r = B e^{\frac{Q_f}{RT}} * A e^{-Q_m/RT} = C e^{-\frac{Q_f+Q_m}{RT}}$$

In general, the rate, at which an atom jumps, or moves from place to place in a crystal, depends on two energies. Q_f , the energy required to *introduce* (form) a mole of vacancies or interstitial atoms into the alloy lattices. And Q_m , the energy barrier that must be *overcome* in order to move a mole of atoms into vacancies, such as the interstitial self-diffusion and the vacancy mechanisms, which are shown in Fig. II.20 and Fig. II.21. But, one must recall that there are another types of diffusion does not need the formation energy Q_f such as the interstitial impurity and the substitutional impurity diffusion (since the impurity atoms already have been existed as a result of different processes such as the manufacturing processes).

Appendix 5

A. 5- Diffusion in Nonhomogenous Concentration Crystal

This App. will show the change of a mater concentration as function of time and 1-D. The relationship represents what is so called Fick's second low.

Choose a rectangular parallelepiped in the crystal with dimensions as shown in Fig. II.24. Assume concentration distributions that vary in x-direction only. At time t the concentration in the parallelepiped is $c(t)$. At slightly later time $t+\Delta t$ the concentration has changed to some other value $c(t+\Delta t)$. The change in the number of atoms during time dt in this parallelepiped volume $\Delta x \text{ cm}^3$ is

$$\Delta x [c(t+\Delta t) - c(t)] \quad (1)$$

The only reason of the number of atoms have changed because the number entering at the left face is different than the number leaving the right – hand face. Let $J(x)$ be the flux of diffusing atoms at the left – hand face of this parallelepiped. $J(x+\Delta x)$ is the flux at the right – hand face. The increase of the number of atoms in the parallelepiped during time dt is

$$\Delta t [J(x) - j(x+\Delta x)] \quad (2)$$

equating Eq. 1 and Eq. 2 and dividing by $dx dt$ which gives

$$\frac{c(t+\Delta t) - c(t)}{\Delta t} = - \frac{J(x+\Delta x) - J(x)}{\Delta x} \quad (3)$$

If we take the limit as dx and dt approach zero, both sides of Eq. 3 reduce to the definition of a derivative and

$$\frac{\partial c}{\partial t} = - \frac{\partial J}{\partial x} \quad (4)$$

but the flux J can be expressed as function of the jump frequency term r (achieved in App. 4) as follow

Let $N(L)$ and $N(R)$ represent the number of atoms on the left and right faces in the parallelepiped respectively. r is the jump frequency.

$$J = a r [N(L) - N(R)] \quad (5)$$

where (a) is determined by the crystal structures.

Substituting in Eq. 5 for number of atoms N by the concentration c and assume the distance in the x -direction is L between the two faces

$$J = a r L [c(L) - c(R)] \quad (6)$$

Dividing $[c(L) - c(R)] = \Delta c$ by L and substitute for c as L go to Δx then take the limit as Δx approaches zero

$$\begin{aligned} \frac{c(R) - c(L)}{L} &= \frac{c(x + \Delta x) - c(x)}{\Delta x} = \frac{\Delta c}{\Delta x} \\ \lim_{\Delta x \rightarrow 0} \frac{\Delta c}{\Delta x} &= \lim_{\Delta x \rightarrow 0} \frac{c(x + \Delta x) - c(x)}{\Delta x} = \frac{\partial c}{\partial x} \\ \frac{\partial c}{\partial x} &= \frac{c(R) - c(L)}{L} \\ c(L) - c(R) &= -L \frac{\partial c}{\partial x} \end{aligned} \quad (7)$$

substituting Eq. 7 in Eq. 6 gives

$$\begin{aligned} J &= -a L^2 r \frac{\partial c}{\partial x} \\ J &= -D \frac{\partial c}{\partial x} \end{aligned} \quad (8)$$

what should be noted here that the diffusion coefficient D is function of the atom jump frequency Γ which in turn function of the temperature App. 4 and the diffusion mechanism (p.54 [X]).

Substituting Eq. 8 in Eq. 4, which gives what so called Fick's second law

$$\frac{\partial c}{\partial t} = \frac{\partial}{\partial x} \left(D \frac{\partial c}{\partial x} \right) \quad (9)$$

if D is not function of the concentration c , Eq. 9 can be simplified to give

$$\frac{\partial c}{\partial t} = D \frac{\partial^2 c}{\partial x^2} \quad (10)$$

Appendix 6

A. 6 - Example of Oxides Resistance

This example will show the manipulation of the different diffusion rates of the alloy's components to build a protective oxide layer against more oxidation at high temperature, the main steps (techniques) to achieve that goal, and the change of the scale composition during the initial oxidation.

Let us take Ni-9 Cr-6 Al wt. % alloy for demonstration.

In this case the alloying components form oxides with varying stability (recall the ambient partial pressure of oxygen versus the free energy required to form the oxide of pure metal): $\Delta G (\text{Al}_2\text{O}_3) < \Delta G (\text{Cr}_2\text{O}_3) < 3 \Delta G (\text{NiO})$.

Thus Al_2O_3 is the most stable oxide and NiO is the least one. Continuous scales of Al_2O_3 give the lowest oxidation rates, and thus it is desirable to adjust the alloy composition to obtain what is so called 'selective oxidation' of aluminum.

For Ni-Al alloys it is necessary to use alloy containing 10-20 wt. % Al in order to obtain continuous Al_2O_3 scales. However, for that alloy (Ni-Cr-Al) of our choice, a much smaller amounts of aluminum are needed to achieve the same effect. Thus our selected alloy (Ni-9Cr-6Al) produces continuous, protective Al_2O_3 scales at high temperatures (above 1100°C). This is illustrated in Fig. II.25 which compare the oxidation weight gain at '1 atm. O_2 and 1200°C ' for different alloys.

The explanations for this general type of oxide mechanism (in few words is, protector, displacement reaction, selectively oxidized) as follow:

One may consider that the chromium acts as a 'protector' to prevent internal oxidation of aluminum. During the very initial oxidation, oxides of all three components Al_2O_3 , Cr_2O_3 , and NiO , are formed. However if sufficient chromium present in the alloy, the initially formed NiO will be reduced by chromium through 'the displacement reaction' ' $3\text{NiO} + 2\text{Cr}(\text{in alloy}) \rightarrow \text{Ni}(\text{in alloy}) + \text{Cr}_2\text{O}_3$ '. In this manner a continuous layer of Cr_2O_3 is formed in the alloy. This in turn, reduces the oxygen activity at the scale/metal interface to such a low level that aluminum in the alloy can now be 'selectively oxidized' to build up a continuous Al_2O_3 scale.

At high temperatures and high oxygen pressures Cr_2O_3 will also gradually evaporate as CrO_3 , and the oxide left with a continuous, highly protective scale is Al_2O_3 .

Appendix 7

A. 7 - Mixing Entropy

Entropy (absolute entropy) is a measure of the energy that is no longer available to perform useful work within the environment. It can be called as the “randomness of the system” because it increases as the system goes from order to irregular or random fashion (i.e. vibrational-entropy).

In metallurgy (metal transformation), the free energy is the driving force for the diffusion of atoms, which occur with a spontaneous reaction, which in turn is an irreversible process which means increasing in the entropy. This total entropy production (increase) can be a result of the addition of different entropy productions such as vibrational-entropy, mixing-entropy etc. Mixing-entropy is the one of our interest, because it can be applicable directly in the diffusion in metals as shown in the App. 4 of “homogeneous point of defect”

Example: to show the derivation of mixing-entropy

Assume two different gases A and B under the same temperature and pressure in an insulated two compartments box, then the partition is lifted.

From the first law of thermodynamic

$$dE = dQ + dW$$

$$dE = 0$$

where dQ is heat absorbed by the system (A and B gases), dE = change in internal energy of the system, dW = work done on gases by the surrounding

from the driving force of diffusion

$$dF = dE - TdS$$

$$dF = 0 - TdS$$

from Boltzman's equation [$S = k \ln(p)$] of the relation between the probability of certain state (mixed or unmixed gases) and the entropy of the system at a given state

$$\Delta S = S_2 - S_1 = k \ln(p_2/p_1) \quad (1)$$

Where S_1 , and S_2 are entropy of unmixed and mixed gases respectively, and p_1 , and p_2 are probability of unmixed and mixed gases respectively

from the assumption of a perfect gases under same temperature and pressure, so the volume occupied by the gases must be proportional to the number of atoms in the gases. Thus

$$\begin{aligned} \left(\frac{n_A}{n}\right) &= \left(\frac{V_A}{V}\right) = C \\ \left(\frac{n_B}{n}\right) &= \left(\frac{V_B}{V}\right) = (1-C) \end{aligned} \quad (2)$$

where n_A , and n_B are the number of A and B atoms respectively, V_A , and V_B are volume originally occupied by gases A and B respectively, and C is the concentration of A

Since

$$p_1 = \left(\frac{V_A}{V}\right)^{n_A} * \left(\frac{V_B}{V}\right)^{n_B} \quad (3)$$

Assuming the mixing probability is the highest. Thus

$$p_2 = 1 \quad (4)$$

Substituting Eqs. 2, 3, and 4 in Eq. 1. As a result, we have

$$\Delta S = - k n C \ln(C) - k n (1-C) \ln(1-C)$$

if it is assumed that the total mixed gases is one mole. Thus

$$n = N \text{ (Avogadro's number)}$$

$$\Delta S = - R [C \ln (C) - (1-C) \ln (1-C)]$$

where R equal $k N$ (Universal gas constant), and ΔS is the mixing-entropy

Appendix 8

A. 8 - Equilibrium between Two Phases

The condition of equilibrium of a solid solution of one phase with two components (where the reaction occur under the same temperature and pressure as the original components at) is

$$n_A d\bar{F}_A + n_B d\bar{F}_B = 0 \quad (1)$$

where the subscript hold for the components A and B

$$d\bar{F}_A = \frac{\partial F}{\partial n_A} = \frac{dF}{dn_A} \quad (\text{partial molal of free energy})$$

Assuming the change in the free energy in A direction occurs while the amount of the free energy in B component still constant, based on that it is just an infinitesimal change amount in A direction (component).

However, for two phases α and β and two components A and B the free energy as follow

$$\begin{aligned} F^\alpha &= n_A^\alpha \bar{F}_A^\alpha + n_B^\alpha \bar{F}_B^\alpha \\ F^\beta &= n_A^\beta \bar{F}_A^\beta + n_B^\beta \bar{F}_B^\beta \end{aligned} \quad (2)$$

Let a small quantity (dn_A) of component A is transferred from the alpha phase to the beta phase. As a result of this transfer, the free energy of the alpha phase will be decreased, while that of the beta phase will be increased. The total free energy change of the system is the sum of these two changes and can be represented by the derivation of Eq. 2 with respect to n_A , then applying the equilibrium condition Eq. 1 on the system. Thus

$$\begin{aligned}
dF &= dF^\beta + dF^\alpha \\
dF^\alpha &= n_A^\alpha d\bar{F}_A^\alpha + dn_A^\alpha \bar{F}_A^\alpha \\
&= n_A^\alpha d\bar{F}_A^\alpha + (-dn) \bar{F}_A^\alpha \\
dF^\beta &= n_A^\beta d\bar{F}_A^\beta + dn_A^\beta \bar{F}_A^\beta \\
&= n_A^\beta d\bar{F}_A^\beta + dn \bar{F}_A^\beta \\
dF &= n_A^\beta d\bar{F}_A^\beta + dn \bar{F}_A^\beta + n_A^\alpha d\bar{F}_A^\alpha + (-dn) \bar{F}_A^\alpha \\
dF &= (n_A^\beta d\bar{F}_A^\beta + n_A^\alpha d\bar{F}_A^\alpha) + dn \bar{F}_A^\beta + (-dn) \bar{F}_A^\alpha
\end{aligned}$$

Applying the equilibrium condition where dF goes to zero. Thus

$$dF=0=0+dn (\bar{F}_A^\beta - \bar{F}_A^\alpha)$$

as dn is not zero, thus

$$\bar{F}_A^\beta = \bar{F}_A^\alpha$$

the above quite general result is not restrict to system of only two components or systems containing only two phases. In fact, it may be shown that, in the general case where there are M components with μ phases in equilibrium, the partial molal free energy of any given component is same in all phases.

Appendix 9

A. 9 – Definitions

Cold work: When the metal is plastically deformed at temperatures that are low relative to its melting point

e/a: The average group number or electron / atom

Eutectoid: It's the liquid phase of an alloy freezes to two solid phases

Flux of mater (J): The number of atoms moving in the positive x direction per second across a square centimeter.

Isomorphous: It's the liquid phase of alloy freezes to produce one single type of crystals.

Hardenability of a titanium alloy: Is a phrase that refers to its ability to permit full transformation of the alloy to martensitic phases or to retain beta to room temperature.

Soaking time: It is the time required for the solution treatment of an alloy based on the thickest component in the furnace. The rule is 20 to 30 min./in. of thickness. If the solution treatment at temperature is higher than the transus, one must watch for the grain growth.

Solid solution: It is the homogeneous mixtures of two or more kinds of atoms occur in the solid state

Thermal stable alloy: It is the ability of the alloy to resist changes of its mechanical properties. In alpha – beta titanium alloys, thermal stability is function of beta-phase transformation. During cooling from the annealing temperature, beta may transform and may, under certain conditions and in certain alloys, form the brittle

intermediate phase omega. So, a stabilization annealing treatment is required to produce a stable beta phase capable of resisting further transformation when exposed to elevated temperatures in service.

Hundredfold: Material resistance is increased 100 times.

Polytopic material: Material has the ability to change phases as function of the temperature changes i.e. titanium

Appendix 10

A. 10 - A Matlab code to plot the theoretical concentration of a diffused element in a material

```
% This code to plot the concentration of a diffused
element in a material
% based on the complimentary error function erfc(x)
function [R]=consent(D,t,ho,inc,h);
t=t';
for m=1:length(t)
    x1=ho:inc:h;
    x1=x1';
    x=x1./(2*sqrt(D*t(m,1).*3600));
    for n=1:length(x)
        y(n,1)=erfc(x(n,1));
    end
    x1=x1(:)*10000; % to change from cm to micrometer
    y=y(:).*0.02; % Assuming the maximum concentration
of                               Timetal 21S is 2%
    plot(x1,y)
    hold on
    end
    hold off
    R=1;
    % D the diffusivity in cm2/sec
    % t (hrs) the time in hours, for example t=10:20:110
will plot from 10 30 50 ...110 hrs
    % ho (cm) the surface it always put as zero (ho=0)
    % inc it how much increments of the distance in x-
axis you wish to see
    % h (cm) is the depth in the specimen as you want
    % example:T=650 C
    % D=3.9138e-011; t=10:20:110; ho=0; inc=0.0002; h
```

REFERENCES

- 1 - R. W. Schutz, "An Overview of Beta Titanium Alloy Environment behavior", RMI Titanium Company, 1000 Warren Avenue, Niles, Ohio 44446, 1993.
- 2 - T. A. Wallace, R. K. Bird, and K. E. Wiedemann, "The Effect of Oxidation on The Mechanical Properties of Timetal-21S", TMS Annual Meeting of Beta Titanium alloys, Denver, CO, 1993.
- 3 - R. K. Bird, T. A. Wallace, and R. K. Clark, "Mechanical Properties of Coated Titanium Beta - 21S After Exposure to Air At 700 and 800 °C", NASA Langley Research Center, Hampton, VA 23665 - 5225, 1992.
- 4 - W. M. Parris, "Beta - 21S, A High Temperature Metastable Beta Titanium", Products and Applications, proceedings of the Technical from the 1990 International Conference, Vol II, Titanium Development, 1990.
- 5 - T. A. Wallace, R. K. Clark, and K. E. Wiedemann, "Oxidation Characteristics of Beta - 21S in Air in the Temperature Range 600 to 800 °C", Proceedings of the Seventh World Conference on Titanium, San Diego, 1992.
- 6 - D. V. Ignatov, M. S. Model, L. F. Sokyriansky, and A. Ya. Shinyaev, "Parameters of Oxygen Diffusion in Alpha - and Beta - Forms of Titanium," Int. Conf. on Titanium, edited by R. I. Jaffee, and H. M. Burk, London, 1972.
- 7 - William P. Roe, Howard R. Palmer, and William R. Opie, "Diffusion of Oxygen in Alpha and Beta Titanium," Forty-First Annual Convention of the Society, Chicago, 1959.

- 8 - W. M. Parris and P.J. Bania, "Oxygen Effect on the Mechanical Properties of Timetal – 21S", Presented at the seventh conference on titanium, San Diego, 1992.
- 9 - X. Huang, J. Cuddy, N. Goel, and N. L. Richards, "Effect of heat treatment on the microstructure of a metastable β -titanium alloy," *Materials Engineering and Performance* 3, pp. 560-566, Aug 1994.
- 10 – Micheal R.L., "Engineering – In – Training Reference Manual," 7th Edition, 1990.
- 11 - P. J. Bania, "Beta Titanium Alloys and Their Role in the Titanium Industry", Timat, NV, 1993.
- 12 – Robert E. Reed – Hill, "Physical Metallurgy Principles," Litton Educational Publishing Inc., 1964.
- 13 - E. W. Collings, "Applied Superconductivity, Metallurgy, and Physics of Titanium Alloys", ISBN 0-306-41690-5, 1985.
- 14 – Per Kofstad, "High Temperature Corrosion," Elsevier Science Publishing Co., ISBN 1-85166-1549, 1988.
- 15 – L. A. Girifalco, "Atomic Migration in Crystals," Blaisdell Publishing Comp., Library of Congress Catalog Number 64-15976, 1964.
- 16 - B. Bavarian, et. al., "High Corrosion Behavior of Beta-21S Titanium Alloy", Paper No. 243, NACE Corrosion '93 Annual Conference, NACE, Houston, TX, 1993.
- 17 - H. G. Nelson, "Hydrogen - Induced Ductility – to – brittle Fracture Transition in Beta Titanium Alloys," Proceedings Summary of the 5th Workshop Publication, April 1993.

- 18 - K. Chaudhuri, and J. H. Perepezko, "Microstructure Study of the Titanium Alloy Ti – 15Mo – 2.7Nb – 3Al – 0.2 Si (Timetal 21S)," *Metallurgical and Materials*, Vol. 25A, June 1994.
- 19 - Bania, P. J. , Beta – 21S, "A High Temperature Metastable Beta Titanium Alloy", proceedings of the 1990 International Conference on Titanium Products Applications", Titanium Development Association, 1990.
- 20 - C. F. Yolton, F. H. Fores, and R.F. Malone, "Metal Tra" vol. 10A, pp. 132 – 24, 1979.
- 21 - Boyer and H. W. Rosenberg, " Beta Titanium Alloys" eds., AIME, Warrendale, PA., pp. 145-60, 1980
- 22 - E. Sokedai, H. Hashimoto, M. Hida, and H. Mabuchi, "Mater. Sci. Tech.", vol. 8, pp. 3 – 9, 1992.
- 23 - R. P. Gangloff, et. Al., "Environmentally Associated Cracking of High Strength Beta Titanium Alloys", Annual Report – Grant No. N0014 – 91 – J –4164, SEAS Report No. UVA / 525464 / MSE93 / 101, Univ. of Virginia, Oct. 1992.
- 24 - G. A. Young and J. R. Scully, " Effects of Hydrogen on the Mechanical Properties of Ti – Mo – Nb – Al Alloy", *Screpta Metallurgica*, Vol. 28, pp. 507 – 512, 1993.
- 25 - Unnam, J. Shenoy, R. N., and Clark R. K., "Oxidation of Commercial purity Titanium", *Oxidation of Metal*, Vol. 26, Nos. ¾, pp. 231 – 252, 1986.
- 26 - L. A. Glikman, V. I. Derybina, N. N. Kilgatin, I. A. Bytenskii, V. P. Teodorovich, and N.S. Teplov, "The Influence of Gas – Saturated Layers on the Strength and

- Plastic Properties of Titanium Alloys,” Titanium and Its Alloys, ed. I. I. Kornilov, 1966.
- 27 - Ghonem, Thompson, and Linsey, “Effect of Temperature and Frequency on Fatigue Crack Growth in Titanium Beta Monolithic Laminate,” 1992.
- 28 - Steven Ashley, “Boeing 777 Gets a Boost from Titanium” mech. Eng., vol. 115, pp 60 – 65, 1993.
- 29 - Z. Liu and G. Welsch, “Literature Survey on Diffusivities of Oxygen, Aluminum, and Vanadium in Alpha Titanium, Beta Titanium, and in Rutile,” metallurgical transaction A, vol. 19A, April 1988.
- 30 - Smithells, Colin J., “Metal Reference Book,” 4th Edition, ISBN 0408706279, 1967.
- 31 - E.W.Collings, “Applied Superconductivity, Metallurgy, and Physics of Titanium Alloys,” ISBN 0-306-41690-5, 1985.
- 32 - N. E. Paton and J. C. Williams, “Effect of Hydrogen on Titanium and its Alloys,” Titanium and Titanium alloys – Source Book, ASM International, Materials Park, OH, pp. 207.
- 33 - Suresh, S. and Ritchie, R. O, “Fatigue Crack Growth Threshold Concepts”, TMS – AIME, USA, p. 227, . 1983.
- 34 - Albertson, T. P., Stephens, R. R., and Bayha, T. D. “Fatigue Crack Growth of Two Advanced Titanium Alloys at Room and Elevated Temperature,” Elevated Temperature Effects on Fatigue and Fracture, ASTM STP 1297, R. S. Piascik, R. P. Gangloff, and A. Saxena, Eds., American Society for Testing and Materials, pp. 140 – 161, 1997.

BIBLIOGRAPHY

- Albertson, T. P., Stephens, R. R., and Bayha, T. D. "Fatigue Crack Growth of Two Advanced Titanium Alloys at Room and Elevated Temperature," Elevated Temperature Effects on Fatigue and Fracture, ASTM STP 1297, R. S. Piascik, R. P. Gangloff, and A. Saxena, Eds., American Society for Testing and Materials, pp. 140 – 161, 1997.
- Bania, P. J. , Beta – 21S, "A High Temperature Metastable Beta Titanium Alloy", proceedings of the 1990 International Conference on Titanium Products Applications, Titanium Development Association, 1990.
- B. Bavarian, et. al., "High Corrosion Behavior of Beta-21S Titanium Alloy", Paper No. 243, NACE Corrosion '93 Annual Conference, NACE, Houston, TX, 1993.
- Boyer and H. W. Rosenberg, "Beta Titanium Alloys" eds., AIME, Warrendale, PA., pp. 145-60, 1980.
- C. F. Yolton, F. H. Fores, and R.F. Malone, "Titanium," Metal Tra, vol. 10A, pp. 132 – 24, 1979.

- D. V. Ignatov, M. S. Model, L. F. Sokyriansky, and A. Ya. Shinyaev, "Parameters of Oxygen Diffusion in Alpha - and Beta - Forms of Titanium," International Conference on Titanium, edited by R. I. Jaffee, and H. M. Burk, London, 1972.
- E. Sakedai, H. Hashimoto, M. Hida, and H. Mabuchi, "Beta Titanium," Material Science Technology, vol. 8, pp. 3 - 9, 1992.
- E.W.Collings, "Applied Superconductivity, Metallurgy, and Physics of Titanium Alloys," Plenum Press, New York, 1986.
- G. A. Young and J. R. Scully, "Effects of Hydrogen on the Mechanical Properties of Ti - Mo - Nb - Al Alloy", Scripta Metallurgica, Vol. 28, pp. 507 - 512, 1993.
- Ghonem, Thompson, and Linsey, "Effect of Temperature and Frequency on Fatigue Crack Growth in Titanium Beta Monolithic Laminate," Material Science Technology., 1992.
- H. G. Nelson, "Hydrogen - Induced Ductility - to - brittle Fracture Transition in Beta Titanium Alloys," Proceedings Summary of the 5th Workshop Publication, April 1993.
- K. Chaudhuri, and J. H. Perepezko, "Microstructure Study of the Titanium Alloy Ti - 15Mo - 2.7Nb - 3Al - 0.2 Si (Timetal 21S)," Metallurgical and Materials, Vol. 25A, June 1994.

L. A. Girifalco, "Atomic Migration in Crystals," Blaisdell Publishing Comp., Library of Congress Catalog Number 64-15976, 1964.

L. A. Glikman, V. I. Derybina, N. N. Kilgatin, I. A. Bytenskii, V. P. Teodorovich, and N.S. Teplov, "The Influence of Gas – Saturated Layers on the Strength and Plastic Properties of Titanium Alloys," Titanium and Its Alloys, ed. I. I. Kornilov, 1966.

N. E. Paton and J. C. Williams, "Effect of Hydrogen on Titanium and its Alloys," Titanium and Titanium alloys – Source Book, ASM International, Materials Park, OH, pp. 207.

Per Kofstad, "High Temperature Corrosion," Elsevier Science Publishing Co., 1988.

P. J. Bania, "Beta Titanium Alloys and Their Role in the Titanium Industry", Timat, NV, 1993.

R. K. Bird, T. A. Wallace, and R. K. Clark, "Mechanical Properties of Coated Titanium Beta – 21S After Exposure to Air At 700 and 800 °C", NASA Langley Research Center, Hampton, VA 23665 – 5225, 1992.

Robert E. Reed – Hill, "Physical Metallurgy Principles," Litton Educational Publishing Inc., 1964.

- R. P. Gangloff, et. Al., “Environmentally Associated Cracking of High Strength Beta Titanium Alloys”, Annual Report – Grant No. N0014 – 91 – J –4164, SEAS Report No. UVA / 525464 / MSE93 / 101, Univ. of Virginia, Oct. 1992.
- R. W. Schutz, “An Overview of Beta Titanium Alloy Environment behavior”, RMI Titanium Company, 1000 Warren Avenue, Niles, Ohio 44446, 1993.
- Smithells, Colin J., “Metal Reference Book,” 4th Edition, Butterworth Hinemann, 1967.
- Steven Ashley, “Boeing 777 Gets a Boost from Titanium” mechanical Engineering, vol. 115, pp 60 – 65, 1993.
- Suresh, S. and Ritchie, R. O, “Fatigue Crack Growth Threshold Concepts”, TMS – AIME, USA, p. 227, . 1983.
- T. A. Wallace, R. K. Clark, and K. E. Wiedemann, “Oxidation Characteristics of Beta – 21S in Air in the Temperature Range 600 to 800 °C”, Proceedings of the Seventh World Conference on Titanium, San Diego, 1992.
- T. A. Wallace, R. K. Bird, and K. E. Wiedemann, “The Effect of Oxidation on The Mechanical Properties of Timetal-21S”, TMS Annual Meeting of Beta Titanium alloys, Denver, CO, 1993.

Unnam, J. Shenoy, R. N., and Clark R. K., "Oxidation of Commercial purity Titanium", Oxidation of Metal, Vol. 26, Nos. ¾, pp. 231 – 252, 1986.

William P. Roe, Howard R. Palmer, and William R. Opie, "Diffusion of Oxygen in Alpha and Beta Titanium," Forty-first Annual Convention of the Society, Chicago, 1959.

W. M. Parris, "Beta – 21S, A High Temperature Metastable Beta Titanium", Products and Applications, proceedings of the Technical from the 1990 International Conference, Vol II, Titanium Development, 1990.

W. M. Parris and P.J. Bania, "Oxygen Effect on the Mechanical Properties of Timetal – 21S", Presented at the seventh conference on titanium, San Diego, 1992.

X. Huang, J. Cuddy, N. Goel, and N. L. Richards, "Effect of heat treatment on the microstructure of a metastable β -titanium alloy," Materials Engineering and Performance 3, pp. 560-566, Aug 1994.

Z. Liu and G. Welsch, "Literature Survey on Diffusivities of Oxygen, Aluminum, and Vanadium in Alpha Titanium, Beta Titanium, and in Rutile," metallurgical transaction A, vol. 19A, April 1988.